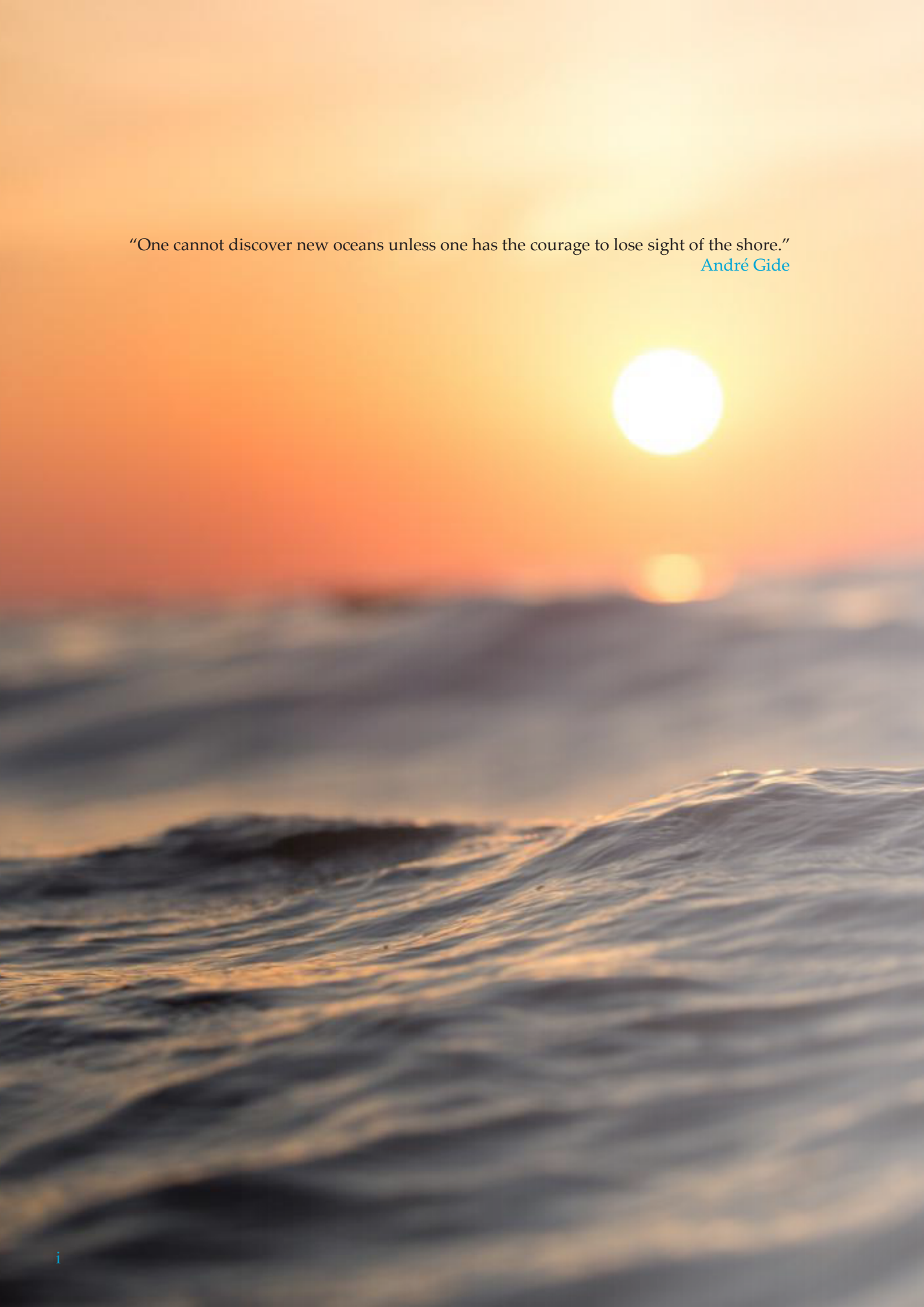


# Numerical Modelling of a Large Diameter Cold Water Pipe Installation for Land Based OTEC and SWAC

Machiel van der Veer  
Master of Science Thesis  
Offshore and Dredging Engineering



A photograph of a sunset over the ocean. The sun is a bright, glowing orb positioned in the upper right quadrant of the frame, just above the horizon. Its light creates a warm, orange and yellow glow across the sky. The sun's reflection is visible on the water's surface, appearing as a smaller, dimmer circle directly below the sun. The ocean waves are visible in the foreground, with their crests catching the light of the setting sun, creating a shimmering effect. The overall mood is serene and contemplative.

“One cannot discover new oceans unless one has the courage to lose sight of the shore.”  
André Gide

# Numerical Modelling of a Large Diameter Cold Water Pipe Installation for Land Based OTEC and SWAC

By  
Machiel van der Veer

in partial fulfilment of the requirements for the degree of

**Master of Science**  
in Offshore and Dredging Engineering

at the Delft University of Technology,  
to be defended on Thursday August 30, 2018

Thesis committee:  
**Prof. Dr. A. Metrikine**  
**Ir. J.S. Hoving**  
**Ir. B.J. Kleute**  
**Ir. J. Brugmans**

# Abstract

For remote islands with high energy prices in the tropics, Ocean Thermal Energy Conversion (OTEC) can be a reliable energy source to supply a renewable baseload for the energy grid. Also, due to the increasing cooling demand, there is a need for sustainable cooling around the equator. This can be supplied by seawater air-conditioning (SWAC). For the cold water supply of such projects, there is a cold water pipe required that could reach to a depth of up to 1000m. The cold water pipe material that is investigated in this thesis is high-density polyethylene (HDPE). The installation of these large diameter cold water pipes is challenging and requires careful attention, as it is one of the most expensive components of an ocean thermal energy project. A dynamic 3D geometrically non-linear Euler-Bernoulli model is developed that allows for large deformations. In this way, the lowering procedure, including lateral current actions on the pipe can be modelled in order to check the structural integrity of the pipe during installation. The model is validated by comparing it to scale model tests in MARIN, which results in a good comparison between the numerical model and scale model tests. Additionally, the model is compared to a geometrically non-linear Timoshenko beam model to estimate whether shear deformation plays a role for large diameter HDPE pipes. Both models showed a good comparison and the for the bending radii that are of interest, shear deformation is negligible. Making use of the numerical Euler-Bernoulli model, a case study is performed for a seawater air-conditioning project in Curaçao. Different installation methods are compared, where the subsurface current velocity is an important parameter. This velocity determines the required amount of ballast of the largest section of the pipeline. For high current velocities, the ballast is high, such that there are multiple holding points required along the pipe in order to make it sink in one piece without exceeding the design stress of HDPE. Ballast can be applied by means of concrete blocks along the pipeline. The pipe can be controlled during installation by either buoyancy modules or vessels with tug lines. Another option is to reduce the specific gravity of the pipe and to apply post ballasting by means of rock dumping. The best solution depends on site specific conditions, where detailed current velocity profiles are desired to choose the most cost effective solution. During installation, the currents will have an impact on the lateral deflection of the pipe, which can lead up to a deflection of several hundreds of meters if no measures are taken. Several vessels are required along the pipeline during installation to make sure the pipe is installed on the planned trajectory.



# Acknowledgements

I would like to thank all my supervisors for your guidance during my thesis. Firstly, Jeroen Hoving, who has always been available with motivating enthusiasm when I needed guidance. Not only during my thesis but also during the courses on arctic engineering, of which my trips to Spitsbergen has been a life changing experience. Andrei Metrikine, who was always able to quickly catch up with my work, challenge me and inspired me to work hard. From my bachelor onward I have learned a lot about dynamics from whom the students call the godfather of offshore engineering, where Jeroen Hoving would be the consigliere. Joost Brugmans, thank you for your enthusiasm, support and practical input. I was always looking forward to our meetings where you were able to provide me with new knowledge and insights. I must also thank Chris Keijdener, who has helped me with new insights during the start-up phase of my thesis. Berend Jan Kleute, who has not only provided me with valuable input during my thesis, but also during my project in Indonesia. It has been a pleasure to work with you on these challenges. I would like to thank my colleagues at Bluerise for the nice work environment. Especially Joost Kirkenier, who was always enthusiastic and motivating during both my thesis and the preparations of the project in Manado, Indonesia. Thanks to the fellow graduates at Bluerise for both the nice conversations and the sparring during the coffee breaks.

Furthermore, I would like to thank all my fellow students who have become truly good friends over the years. Without you I would not have come so far during my time at Delft University of Technology. Regarding this thesis, I have to especially thank Ikbal and Fabian for their motivation and their interest.

I must thank all my friends. You were able to take my mind off my thesis when it was needed and support me throughout my time at the university. Lastly, to my parents, their partners, my brother, Daphne, Marcel, Marie-Louise, my grandparents Willem, Cobie, and the rest of my family. Thank you for believing in me, everything you have done for me to get this far and your endless support.

Machiel van der Veer, August 16<sup>th</sup> 2018



# Thesis context

The worldwide energy demand is growing due to growing population, economies and electrification (EIA, 2017). It is projected that 40% of the rise in energy consumption is due to the growth in electrification, which is equal to the growth that oil took over the last twenty-five years (AIE, 2017). As stated at the climate conference in 2015, the Paris Agreement could be a turning point, should nations fully commit to cutting emissions (The Guardian, 2016).

At the end of 2016, REN21 estimated that 24.5% of the energy demand is provided by renewable energy. The renewable energy comes from hydropower (16.6%) followed by wind (4%), bio-power(2%), solar PV(1.5%) ocean energy, CSP and geothermal (0.4%) (Renewable Energy Policy Network, 2017). Policies increasingly continue to support renewable energy worldwide. According to the World Energy Outlook 2017, rapid deployment and falling costs of clean energy technologies are expected. Especially security and affordability of renewable energy is still a challenge. These are two of the three challenges of the “Energy Trilemma”, which is a trade-off between security affordability and sustainability. With wind and solar PV that are fluctuating over time, energy storage or fossil fuel backup is required to have energy security and to meet high peak demands.

## Ocean thermal energy conversion

Especially for remote islands with high energy prices, Ocean Thermal Energy Conversion (OTEC) could be a reliable energy source to supply the base load for an energy grid. OTEC uses the constant temperature difference in the ocean around the equator to produce energy. The surface water around the equator is the largest solar collector on earth. The surface water is warmed up to roughly 25-30°C. Together with cold deep seawater (5-7°C) at these locations, heat exchangers together with a working fluid are used to produce mechanical energy. This mechanical energy is then used to produce electricity. The temperature difference in the ocean must be at least 20°C. At many locations this is constantly available in the oceans, which could be used to provide electricity 24/7. The worldwide potential is 10TW, which is twice the world energy demand. However, most of the potential is in ocean remote from the energy demand and therefore is hard to deploy. Fortunately, there are plenty of locations around the world where the deep seawater is accessible relatively close to shore. Pipelines are used to pump up the cold deep seawater and the warm surface water to an OTEC plant, after which all water is discharged again.

The principle of OTEC has been around since 1881. The French physicist Jaques Arsene d’Arsonval came up with the working principle and Georges Claude, his pupil, even built an OTEC plant on Cuba. Unfortunately, this plant was destroyed by a storm. Due to the crisis in the 30’s and World War II, the interest in OTEC decreased. During the oil crisis of 1973 the interest in OTEC increased again but when the oil price decreased so did the interest in OTEC. Due to the interest in renewable energy technologies in combination with the decrease in costs in the offshore industry, interest has picked up again.



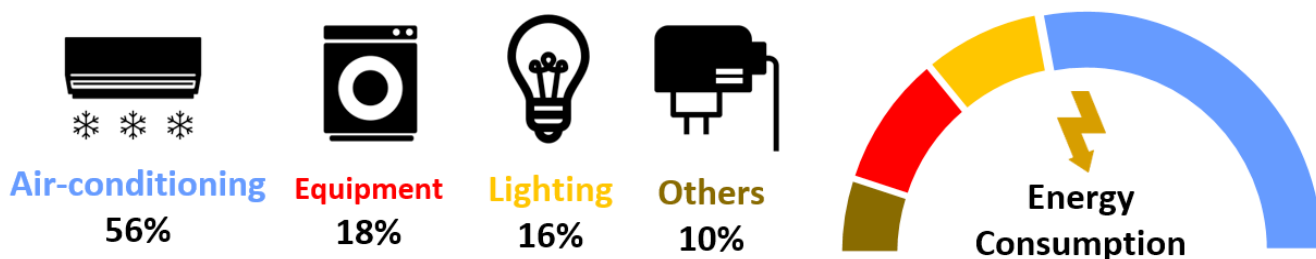
Cold water pipe installation in Cuba ▶  
(OTEC NEWS,2013)

Although this technology is still relatively expensive to implement, it is a growing market and there are several small scale plants built. By scaling up, the technology can make coastal areas in tropical regions more self-sustaining in the future. In this way, OTEC contributes to number 7 and 13 of the world sustainable development goals (United Nations, 2018). In remote areas such as Curaçao, fossil fuels are imported which results in high energy prices. Therefore, OTEC can be economically competitive, especially as this technology can be combined with seawater air-conditioning (SWAC). With SWAC, the cold deep seawater is pumped up and used together with heat exchangers to replace conventional chillers that run on fossil fuels.

### Seawater Air-Conditioning (SWAC)

Similar to the energy demand, the cooling demand is increasing in the tropics. According to the Netherlands Environmental Assessment Agency, the energy demand for cooling will overtake the energy demand for heating in 2060. Cooling systems of buildings are one of the largest energy consumers in tropical regions. Below the energy consumption distribution for a typical building in the tropics can be found. In these buildings, approximately 50% of the energy consumption is used for cooling. Economic growth might be related to the increase for demand of comfort. Which in tropical regions can be related to the demand of cooling (Adrian R KATILI, 2015).

With SWAC, the energy required for cooling can be reduced up to a factor 10. So instead of generating more renewable energy, one can also reduce the energy demand to become more sustainable. A reduction in the energy demand for cooling is a good starting point for tropical regions. Most SWAC plants are land based, which is also an option for an OTEC plant. One of the main challenges of land-based OTEC and SWAC is the cold water pipe (CWP) installation on a steep sloped seabed. When these plants are scaled up to 10-100MW, the pipe diameters become as large as 2.5-4m. These large pipe diameters have never been installed before in deep water and therefore require careful attention. This thesis focuses on a numerical model to analyse the installation of the large diameter cold water pipe for land based OTEC and/or SWAC.



Typical building energy consumption in tropical countries ▲



# Scope of work

This thesis is performed by a Msc. student from Delft University of Technology to gain more insight in the installation of the cold water pipe for ocean thermal energy systems. The thesis is performed for Bluerise and INTECSEA with supervision of Delft University of Technology. The research started in December 2017 and ended in August 2018. Some research has already been performed on the cold water pipe installation but still there are remaining challenges. For example, how the ballast and the environmental conditions are influencing the choice for the installation method. Furthermore, detailed dynamic modelling of the cold water pipe installation for the Curaçao project had not been performed before with sufficient accuracy for this stage of design. The deliverable is a numerical model that can be used to assess scenarios for the installation, where the most important parameters that influence the behaviour of the pipe are implemented. With this model, Bluerise has a tool that can be used to assess the requirements for the pipe installation for new projects, without the need to buy expensive third party software. In this way, both Bluerise and INTECSEA have an independent model that can be used to test scenarios and can be compared to third party software.

Literature and guidelines by researchers, HDPE pipe suppliers and the offshore industry are followed, including material safety factors. The data that is used for the case study is rough and solely acts as an indication for the aspects that play a role during installation. For this reason, no safety factors are applied for the environmental conditions. The case study should be interpreted as an indication for the project in Curaçao. Different data on the current profile along the coast would lead to different scenarios. No optimization is performed in this thesis.

# Reader's guide

The main report consist of ten chapters. In the first chapter, general background information is introduced. This background is both related to the relevance but also to the state of the art of the pipe installation for large diameter pipelines in deep water. Furthermore, the objective and approach that is used in this thesis is explained in this chapter. The second chapter gives background theory that is required to understand the challenge that is addressed. This includes theory on the pipeline material, installation and loading. Based on this theory, several numerical models are introduced in chapter three. These models are compared in chapter four, after which one of the models is compared to scale model tests in chapter five. Chapter six introduces a theoretical example to address the influence of hydrostatic pressure on the pipe behaviour in deep water. The model from chapter three is used in chapter seven for a case study for a pipe installation. Chapter eight, nine and ten are elaborating on the discussion, conclusion and recommendations.

The report contains appendices, of which appendix A contains a thorough derivation of the model. Appendix B elaborates upon the steps that are taken to verify the implementation of the model. Appendix C includes a derivation of the implementation of material damping in the geometrically non-linear model. Appendix E elaborates upon the interpretation of effective axial stress, which is related to the implementation of the hydrostatic pressure in the model. Appendix F shows the influence of the length scale of the elements in the model on the model results. Appendix G discusses the model that was used in a previous thesis on the subject. The rest of the appendices show additional results.

# Nomenclature

$\rho_p$	Pipe density	$N$	True wall force
$\rho_w$	Water density	$f_n$	Natural frequency
$s_g$	Specific gravity	$\sigma_l$	Longitudinal stress
$p_{internal}$	Internal pipe pressure	$\sigma_h$	Hoop stress
$a_a$	Air-fill ratio	$\sigma_r$	Radial stress
$d$	Water depth	$\nu$	Poisson's ratio
$w_{s,c}$	Submerged weight concrete	$\gamma$	Shear angle
$w_{s,p}$	Submerged weight pipe	$G$	Shear modulus
$D_i$	Inner pipe diameter	$T$	Tension
$\sigma_{burst}$	Burst stress	$m_p$	Pipe mass
$t$	Wall thickness	$m_a$	Added mass
$P$	Tension force	$k_d$	Seabed stiffness coefficient
$w_1$	Submerged weight	$c_d$	Seabed damping coefficient
$w_2$	Buoyancy of air-filled pipe section	$l$	Element length
$R_{min}$	Minimum allowed bending radius	$l_c$	Current element length
$E$	E-modulus	$k_r$	Rotation spring stiffness
$F_0$	Dimensionless Fourier number	$\alpha$	Relative angle between elements
$k$	Thermal conductivity	$F_M$	Equivalent moment force
$C_p$	Heat capacity factor	$\varphi$	Shear angle (global coordinate system)
$F_d$	Drag force	$W_s$	Submerged weight
$C_d$	Drag coefficient	$F_l$	Lift force
$v$	Velocity	$\mu$	Friction coefficient
$k$	Surface roughness	$\gamma_s$	Safety factor
$\dot{u}$	Fluid acceleration	$F_h$	Hydrodynamic force
$\rho_e$	Density external fluid	$W_{ac}$	Concrete weight in air
$\rho_i$	Density internal fluid	$W_{ap}$	Pipe weight in air
$S$	Effective axial force	$W_{dc}$	Displaced weight concrete
$p_i$	Internal pressure	$W_{dp}$	Displaced weight pipe
$p_e$	External pressure	$l_{c,ctc}$	Centre to centre distance concrete weights
$A_i$	Internal area	$F_r$	Resistance force
$A_e$	External area	$C_l$	Lift coefficient

## List of abbreviations

OTEC	Ocean Thermal Energy Conversion
SWAC	Seawater air-conditioning
HDPE	High density polyethylene
SDR	Outer diameter to thickness ratio
OD	Outer diameter
EB	Euler-Bernoulli
ODE	Ordinary differential equation

# Content

1	1 Introduction
2	1.1 Introduction to ocean thermal energy conversion (OTEC)
2	1.2 Introduction to seawater air-conditioning (SWAC)
2	1.3 Introduction to cold water pipe (CWP)
3	1.4 Research objective
3	1.4.1 Previous research
3	1.4.3 Objective
4	1.5 Approach and thesis structure 4
5	2 Theory
5	2.1 High density polyethylene
7	2.1.1 Material properties
7	2.2 HDPE pipe installation
8	2.2.1 Welding
8	2.2.2 Weighting
9	2.2.3 Installation methods
12	2.3 Temperature effects
13	2.4 Loading
13	2.4.1 Hydrodynamic drag force
14	2.4.2 Hydrodynamic inertia force
14	2.4.3 Total hydrodynamic loading
15	2.4.4 Hydrostatic pressure
16	2.4.5 Second order wave drift forces
17	2.4.6 Vortex induced vibrations
18	2.5 Stresses
18	2.5.1 Longitudinal stress
18	2.5.1 Shear stress
18	2.5.1 Hoop and radial stress
19	3 Model
19	3.1 Background
20	3.2 2D geometrically non-linear Euler-Bernoulli model
20	3.2.1 Pipe
21	3.2.2 Hydrodynamic drag and inertia force
22	3.2.3 Seabed
22	3.2.4 Material damping
23	3.3 3D geometrically non-linear Euler-Bernoulli model
23	3.3.1 Pipe
24	3.3.2 Hydrostatic loading
24	3.2.3 Hydrodynamic loading
24	3.2.4 Tug line and pulling tug
25	3.2.5 Summary
25	3.4 3D geometrically non-linear Euler-Bernoulli model
26	4 Comparison Timoshenko and Euler-Bernoulli models
29	5 Validation geometrically non-linear Euler-Bernoulli model
29	5.1 Scale model tests
30	5.2 Constant tension tests
31	5.3 Uncertainties VMQ silicon pipe
31	5.4 Model validation results
31	5.5 Discussion
34	5.6 Conclusion
35	6 Influence hydrostatic pressure on large diameter HDPE pipes in deep water
37	7 Case study Curaçao
37	7.1 Assumptions
38	7.2 Environmental conditions
38	7.2.1 Seabed
38	7.2.2 Surface currents
39	7.2.3 Subsurface currents
39	7.2.4 Waves

39	7.2.5 Wind
40	7.2.6 Extreme events
41	7.3 Ballast
43	7.4 Pulling force and controllability
44	7.5 Conventional installation method
45	7.6 Second installation phase
45	7.6.1 Extra vessels
48	7.6.2 Buoyancy modules
49	7.6.3 Comparison modified float and sink and hold and sink method
50	7.7 Influence currents
53	7.8 Residual lay stress
53	7.9 Local buckling
57	8 Discussion
57	8.1 Model
58	8.2 Case study
59	9 Conclusion
61	10 Recommendations
63	Bibliography
65	Appendix A Geometrically non-linear model derivations
65	A.1 2D geometrically non-linear Euler-Bernoulli model
65	A.1.1 Normal strain
69	A.1.2 Bending stiffness
72	A.1.3 Hydrostatic force
72	A.1.4 Hydrodynamic drag force
74	A.1.5 Hydrodynamic drag force
74	A.1.6 Hydrodynamic drag force
74	A.1.7 Hydrodynamic drag force
75	A.2 3D extension Euler-Bernoulli model
77	A.3 2D geometrically non-linear Timoshenko model
80	Appendix B Model verification
80	B.1 2D geometrically non-linear Euler-Bernoulli model
80	B.1.1 Axial stiffness
80	B.1.2 Bending stiffness
82	B.1.3 Hydrodynamic loading
83	B.2 3D geometrically non-linear Euler-Bernoulli model
84	B.3 2D geometrically non-linear Timoshenko model
85	B.4 Hydrostatic pressure implementation
87	Appendix C Material damping
87	C.1 Axial material damping
89	C.2 Material damping due to bending
91	C.3 Importance material damping
93	Appendix E Interpretation of effective stress and derivation for 1D equation of motion vertical pipe subjected to hydrostatic pressure
98	Appendix F Grid dependency
100	Appendix G Discussion on model van Nauta Lemke (2017)
102	Appendix H Additional results Timoshenko vs. Euler-Bernoulli
104	Appendix I Model validation results
107	Appendix J Additional results
112	Appendix K Preliminary sensitivity study

# 1 Introduction

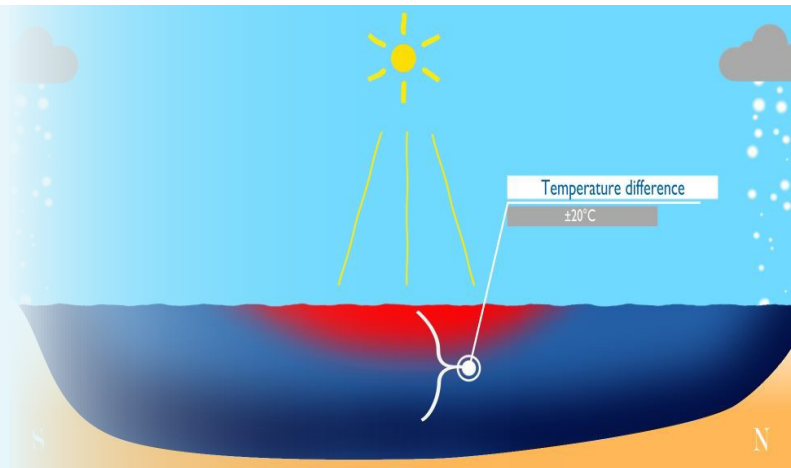
In this chapter, OTEC is introduced. After this, the challenges with the cold water pipe installation are introduced and the research that has been done so far is summarized. In the last section, the research objective is stated.

## 1.1 Introduction to ocean thermal energy conversion (OTEC)

An increased incentive for sustainability has accelerated the development of renewable energy technologies over the past years. Besides solar PV and wind energy, OTEC is an alternative method to produce sustainable and reliable energy. Around the equator, the constantly available temperature difference in vertical layers of the ocean can be used to produce energy. The surface water is heated up by the sun, while the colder deep seawater originates from the poles. At the poles, water cools down, sinks and slowly travels to the equator

In order to produce energy, cold deep seawater and warm surface water are pumped to the OTEC power plant. The warm surface water of roughly 25-30°C makes a working fluid with a low boiling point evaporate into a gas by making use of a heat exchanger. This vapor goes through a turbo-generator to produce energy. After passing the turbine, the working fluid goes through a heat exchanger and is condensed by the cold deep seawater of approximately 5-7°C. In this way the working fluid cycle is closed and the working fluid can be reused at the beginning of the closed cycle. All pumped up seawater is discharged into the sea again and part of the produced energy is used to pump up the seawater to keep the system self-sustaining.

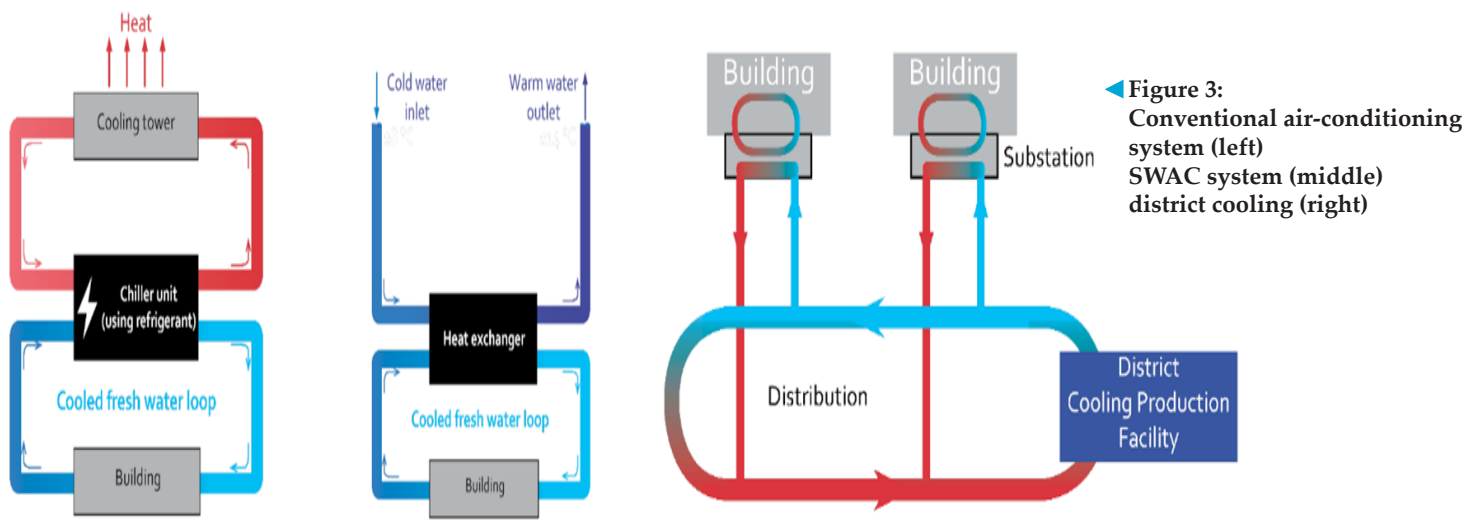
There are several options for a location of an OTEC plant. First of all, if the cold deep seawater is close enough to shore, shore based OTEC is an option. The cold and warm water is pumped up directly to shore through offshore pipelines. If the cold deep seawater is available far from shore, other options should be considered. For example, a jacket (shelf based) can be used as a support structure or floating structures such as a moored vessel, TLP, semi-submersible or spar can be used for locations further away from shore. Factors that are important for the location and substructure choice are: pipeline length, complexity, power cable length, type of substructure and maintenance costs. The options are schematically shown in Figure 2. For floating structures, the pipe is installed vertically down to reach the cold deep seawater. For shore-based OTEC the cold water pipe is longer as it is installed at or just above the seabed and also has to overcome a horizontal distance to reach the required water depth. Due to the friction losses in the pipe, the plant is less efficient as this requires more pumping power to keep the plant running. However, there are big advantages for land-based OTEC. The maintenance costs are lower, there is no expensive offshore substructure required and the cold deep seawater can be used for more purposes such as drinking water production and SWAC.



▲ Figure 1: Origin of temperature difference in the ocean around the equator. The cold water body, originating from the South Pole and North Pole travels slowly towards the equator, creating a temperature difference over depth



▲ Figure 2: Types of support structures for an OTEC plant



◀ Figure 3:  
 Conventional air-conditioning system (left)  
 SWAC system (middle)  
 district cooling (right)

## 1.2 Introduction to seawater air-conditioning (SWAC)

The cooling demand is increasing in the tropics. In large buildings in the tropics, approximately 50% of the energy consumption is used for cooling. SWAC can reduce the energy consumption for cooling up to a factor 10. With SWAC, cold deep seawater is used to replace conventional chillers in air-conditioning systems, shown on the left in Figure 3. The cold deep seawater is used to cool a fresh water loop that is used for air-conditioning. When more buildings or facilities can be cooled by deep seawater, district cooling can be used. Multiple buildings are connected to a freshwater loop that is cooled down in a district cooling production facility.

## 1.3 Introduction to cold water pipe (CWP)

In both cases of OTEC and SWAC, an offshore pipeline is required to pump up the (deep) seawater, see Figure 2. Especially offshore installation costs of the cold water pipe accounts for one of the larger slices of the CAPEX of a project. With an increasing interest in deep seawater applications, upscaling is inevitable. When the capacity of a plant is scaled up, more warm and cold seawater is required. This means that larger offshore pipes are required or the flow speed has to be increased. A higher flow velocity is not preferred because the wall friction increases with the flow velocity exponentially and sucking up of marine life must be avoided. Scaling up the pipe diameter decreases the required pumping power per  $\text{m}^3$  of seawater that is pumped. The reason for this is that the area of the pipe increases exponentially with the diameter, leading to lower wall friction losses per  $\text{m}^3$  water that is pumped. Thus, scaling up the pipe can make both a shore based OTEC and/or SWAC plant more economically feasible. In terms of efficiency of the system, it is more beneficial to install one large diameter CWP than multiple smaller pipes.

In 1930, the first on shore based OTEC plant of 22kW was built by Georges Claude in Cuba but was destroyed by a storm. It took Claude several attempts to install the CWP. Another attempt was to install the pipe in sections. The idea was to gently sink the last section of the pipe by deflating floats. However, due to a miscommunication between the people offshore, and a lack of communication technology, the pipe was sunk from the sea end first. The mooring cables were overloaded and the pipe installation failed. Eventually he managed to install the last pipe section but the operation time did not last for long. In 1935, Claude continued by building a ground breaking 1.2MW floating open cycle OTEC plant (Argonautes, 2012). In 1979, the first successful "Mini-OTEC" plant was built in the USA (Hawaii). This floating barge with a vertical CWP anchored to the seabed produced a net power output of 10kW. The polyethylene (PE) CWP was 660m long and had a diameter of 60cm. In 1981, the first successful shore based OTEC plant was built on Nauru, a Japanese island in the Pacific. The surface-tow method was used to install a PE CWP on the seabed. The segments were 10m long and were joint together by heat fusion to form longer 50m long pipe strings. After this, they were further joint together up to a length of 950m. The pipeline was hung on the main wire and the wire was towed by a towing boat with the pipelines floating on the sea surface, making use of floats. The pipe was stretched out in its proper position and the floats and wire were withdrawn to let the pipe sink to the seabed. The plant was supposed to provide 120kW but the net energy production was only 30kW. In 2001, a floating 1MW OTEC plant was developed in India. Unfortunately, the 1m diameter high density polyethylene (HDPE) CWP failed. In 2013, Saga University Japan built a 50kW plant. The plant is mostly used for research purposes on the use of deep seawater. In 2015, Makai Ocean Engineering successfully developed a 105kW shore based OTEC plant in Hawaii. The pipe diameter is 1.4m and is the largest cold water pipe installed to a large depth so far. Currently, the industry is scaling up and several plants up to 10MW are planned.

Due to the economic growth leading to an increase in cooling demand, SWAC is also a growing market. In 1986 the first SWAC installation was built in Hawaii for a cooling load of 50-80 tons. This plant was combined with the OTEC plant that was mentioned above. Since 1995, cold water from the Baltic Sea is used to cool properties in Stockholm. In 1999, a 1.6m diameter pipe of 3km was installed at a depth of 75m to provide Cornell University Campus in the US of sustainable cooling. Since May 2006, a 450 ton SWAC system is up and running in French Polynesia (Makai Ocean Engineering). Another example of a planned SWAC project is the Ocean Ecopark Curaçao that is being developed by Bluerise.

Besides SWAC and OTEC, there is more experience with large diameter pipe installations. An example is the 1.6m diameter HDPE pipe that transports water from Turkey to Cyprus over a span of 80km. This pipe is anchored to the seabed and is suspended 250m below the sea surface by anchors tied to the seabed.

It is evident that large diameter pipes are necessary for projects to have significant impact on sustainability. Bluerise estimates an ideal size of an OTEC plant to be 10MW, that would require a minimum diameter of 2.5m. For even larger plants, the pipe diameter can go up to 4m. As a reference, the biggest pipe laying vessel "Pioneering Spirit" can lay pipes up to 1.73m (68-inch) diameter. Installation of large diameter intake pipelines in deep water on a steep sloped seabed has never been performed before. The installation is a technical challenge that needs thorough attention.

## 1.4 Research objective

### 1.4.1 Previous research

Keesmaat (2015) looked into the deep sea installation of a large diameter HDPE CWP. The float and sink method, explained in section 2.2.3, was assessed using a static catenary model that neglected the bending stiffness of the pipe. This catenary model was validated by static FEM Orcaflex modelling. He concluded that the theoretical maximum pipe diameter that can be installed with the conventional float and sink method is 2.3m, with a pull tension of 350t. Keesmaat (2015) proposed an improvement of the float and sink method, other installation methods and different options for pipe materials. These recommendations were picked up by Van Nauta Lemke (2017) for further research. He evaluated different material options and installation methods taking into account both technical and non-technical aspects such as risks and costs. Van Nauta Lemke (2017) concluded that HDPE is still the best material for a large diameter CWP installation. The main reason was that it can be installed the quickest due to the long segment lengths that can be produced compared to other materials. By comparing six installation methods he concluded that it is best to install the pipeline in one segment. The float and sink method and the hold and sink method are most promising. These installation methods are explained in section 2.2.3. Van Nauta Lemke (2017) used a numerical 1st order Euler-Bernoulli beam to model the dynamics of the most promising single segment installation methods. This model includes stiffness in contrast to the catenary model that Keesmaat (2015) used. The model was validated with model scale tests at MARIN. The scale-model showed lower velocities than the numerical model predicted. However, the model behaves consistently under various types of loading. After several computations he concluded that it is best to first use the float and sink method until the pipe is filled with water and suspended under the water surface due to the tension force at the end of the pipe. After this, the tension is lowered and the installation is similar to the hold and sink method.

### 1.4.2 Objective

From the numerous possibilities for materials and installation methods, previous research converged to recommendations to use a certain installation method and material for the CWP. This is a good starting point for this thesis. One of the recommendations by Van Nauta Lemke was to take a closer look into the Euler-Bernoulli model that was used, as his numerical model might underestimate the bending stresses in the pipe. Furthermore, the modelling done so far was in still water. Environmental conditions will have an influence on the dynamics of the pipe, which should be taken into account. Van Nauta Lemke provided a good basis for a follow up research.

The main research question is:

**What is the preferred installation method for a large diameter HDPE cold water pipe for ocean thermal energy conversion and seawater air-conditioning?**

Sub questions that will be answered are:

*What is the influence of environmental conditions on the installation of the offshore pipeline?*

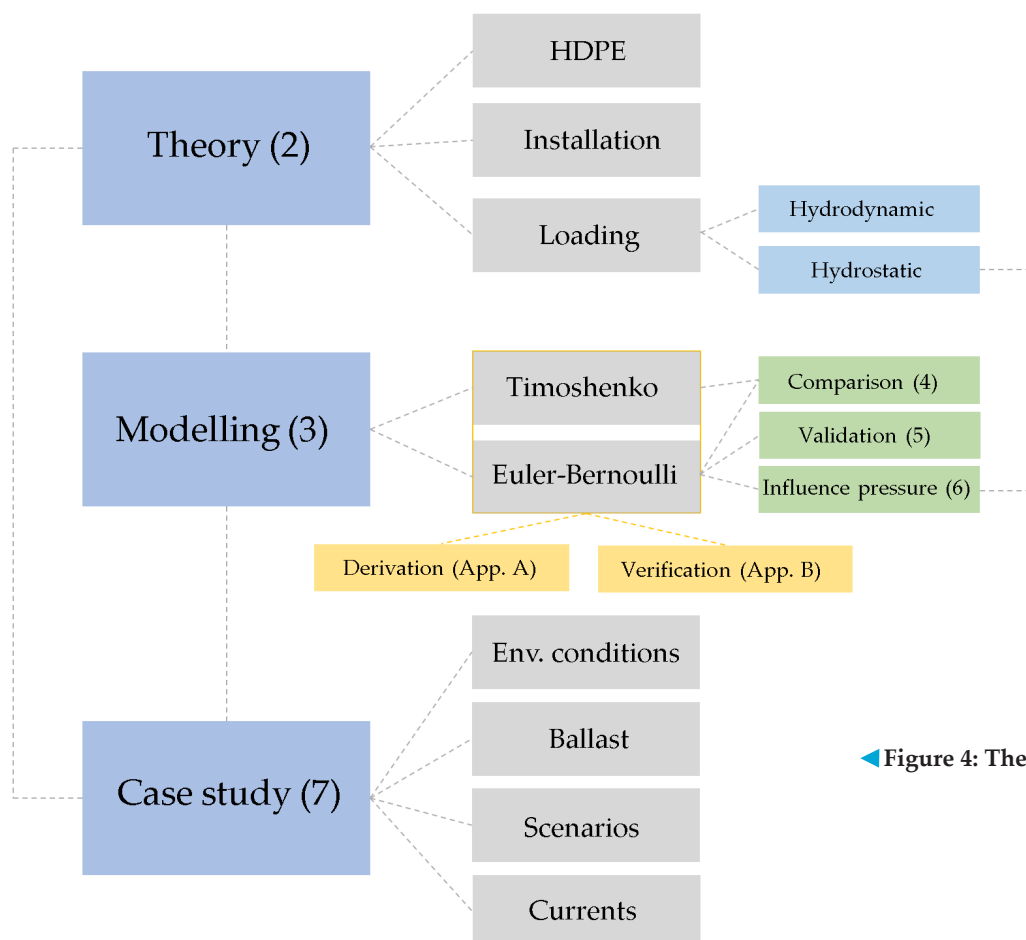
*How can the ballast, required for permanent condition, be implemented in the installation?*

*What is the influence of the shear strain on the pipe behaviour during installation?*

*What is the influence of the hydrostatic pressure on the pipe behaviour during installation?*

## 1.5 Approach and thesis structure

The first step to answer the questions in the previous section is a literature research. The background theory that is relevant for the installation is acquired. With this information, an Euler-Bernoulli model is developed. The model is built up from a simple 2d catenary, step by step to a 3d pipe with bending stiffness, submerged in deep water. During this procedure, every implementation in the model is verified by making use of theoretical examples. This model is compared to a geometrically non-linear Timoshenko model to see whether shear deformation is relevant to take into account for a large diameter HDPE pipe. This justifies the choice of the model that is used. Next, the 3D Euler-Bernoulli model is compared to scale model tests in order to validate the model. After the validation, a theoretical numerical example is worked out to get a feel for the influence of the hydrostatic pressure on the bending stiffness of the HDPE pipeline in large water depths. Lastly, a case study is performed for a seawater air-conditioning project in Curaçao. The environmental conditions are used to get an estimate of the amount of ballast that is required. Based on this input, different scenarios are worked out for the installation. A schematic overview of the structure of this thesis is given in Figure 4.



◀ Figure 4: Thesis structure

# 2 Theory

In this chapter, the theoretical background for this thesis is provided. Background for the pipe material and installation methods is given. Furthermore, the loading on the pipe is discussed.

## 2.1 High-density polyethylene cold water pipe

Keesmaat (2015) and Van Nauta Lemke (2017) considered a variety of materials for the pipe installation. They compared these materials on the following aspects:

- Material flexibility
- Material strength
- Density
- Surface roughness
- Resistance to fouling
- Resistance to corrosion
- Sensitivity to fatigue
- Thermal conductivity
- Material availability
- Environmental impact
- Maintenance & repair costs
- Transport

At this moment, all deep sea cold water pipes around the world are made of HDPE. HDPE pipes for land based water treatment plants are already proven for a diameter up to 1.6m diameter (Vega, 2003). The main reason is that the material is readily available and comes in a wide range of sizes. It is durable, flexible, non-corrosive, buoyant and can be easily welded together. Both Keesmaat (2015) and Van Nauta Lemke (2017) concluded that HDPE is the most favourable material. Mainly because of the short installation time due to the long pipe segments that are being produced. Following up on the thesis of Van Nauta Lemke, the material considered in this thesis is HDPE.

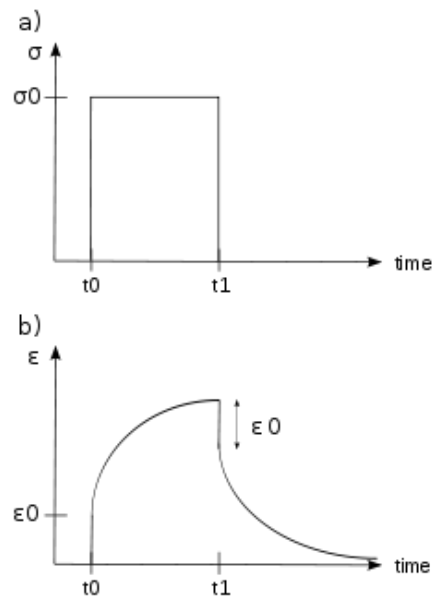
### 2.1.1 High density polyethylene

HDPE is a material that is used for a wide range of applications, for example plastic bottles, tanks and pipes. The material has a large strength to density ratio (Peninsula Plastics, 2018). It is commonly used for large diameter sewage pipes, submerged water outfall pipes or drinking water transport pipes.

Thermoplastics such as HDPE consist of very long chains of molecules. The chains form ordered crystallites when entangled together. Unordered areas form where different chains entangle together. In this way, molecules that are less branched will lead to a high density of the material. Due to the high degree of crystallinity, HDPE has a higher tensile strength than LDPE.

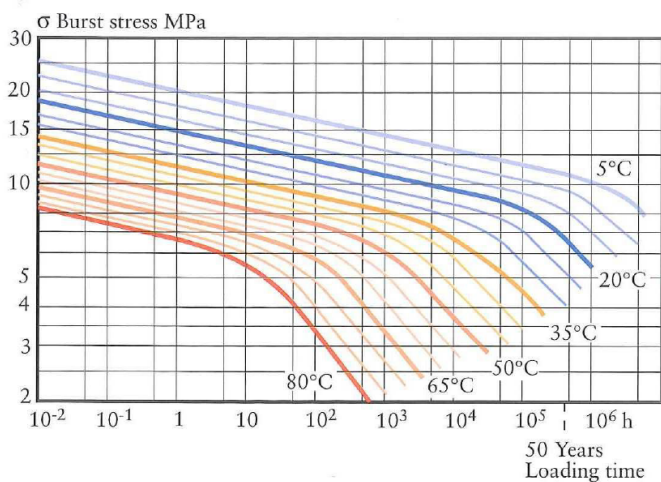
For plastics such as HDPE, the strain is not proportional to stress, and dependent on loading time. Also, creep will occur under loading. For most materials, the relation between stress and strain is linear up to a certain stress level. Hooke's law applies in this range. However, the conditions for plastics are different due to the different stress-strain relationship and the occurrence of creep. This means that the allowable design stress is dependent on the duration of the load. HDPE is a viscoelastic material where the types of strain occurring in the material can be characterized in 3 components. Namely, the elastic strain following Hooke's law, retarded elastic strain (primary creep) and viscous strain (secondary creep). The retarded elastic strain is the strain that recovers after  $t_1$  in Figure 5 and the secondary creep will not fully recover.

The design stress that is mostly used in ISO for plastics is for a design service life of 50 years. To define this design stress, laboratory tests are performed. The test results of the burst stress are usually plotted in a hoop stress-time log-log graph and extrapolated. Safety factors of 1.25-2.5 are used to obtain the design stress. The stress/time curve for type 1 HDPE pipes is given in the figures below. Figure 6 shows the stress time curve for HDPE pipes at different temperatures. Note that for lower temperatures the burst stress is higher. In the flat part of the curve, ductile failure is expected and brittle failure occurs in the steep part. This is also shown in Figure 7 where the open marks are tests where ductile failure occurs and the filled marks are tests where brittle failure occurred. Larger stress is required to achieve ductile failure as the binding forces of the crystallites in HDPE are very strong. Ductile failure happens in the non-crystalline regions of the molecules. The manufacturers have been improving HDPE the past years. For newer types of HDPE than the type 1 shown in Figure 6 and Figure 7, the “knee” in the graph, where the steepness of the curve changes, is no longer recognized. This means that it is most likely that all long term failures are ductile (Janson L.-E. , 2003).

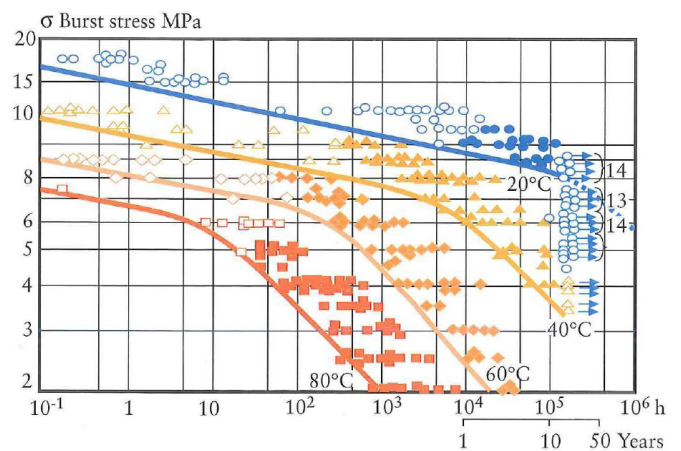


▲ Figure 5: Typical strain-time relation for HDPE subjected to constant stress (Wikipedia, 2018)

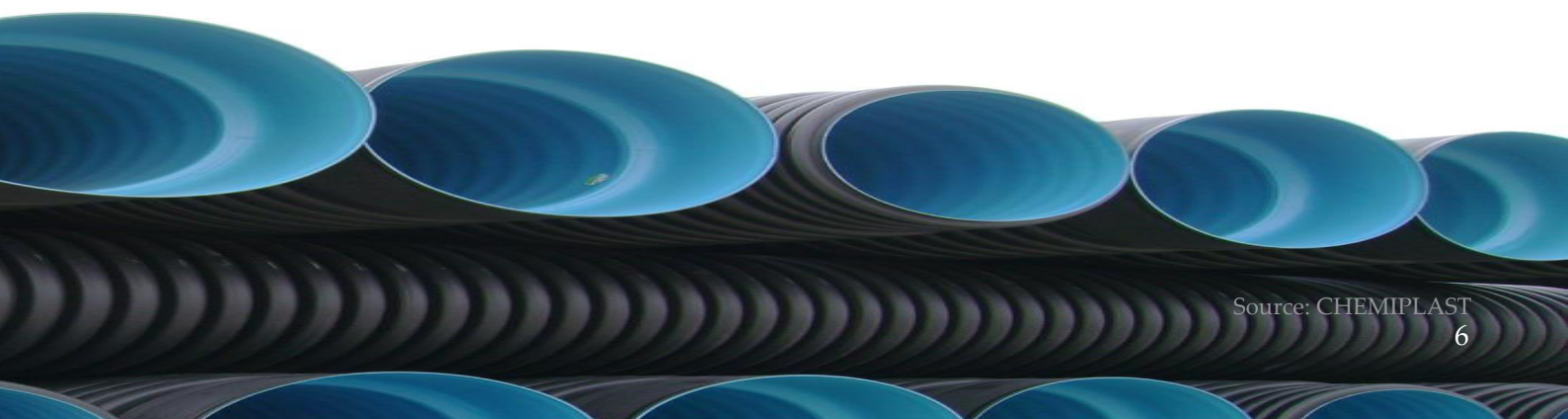
As can be seen in Figure 8, the stress strain/strain relationship is curved and dependent on the loading time. Unlike the elasticity modulus for linear elastic materials the elasticity modulus is not constant. For viscoelastic materials such as HDPE, the tangent of the stress strain curve is dependent on the loading time and the stress. This is called the creep modulus (if stress is constant) or relaxation modulus (if strain is constant) to point out that it is not an elastic modulus. Note that the decrease of the creep modulus over time modulus does not mean that the material gets weaker but only describes the creep or relaxation of the material. After tests it was shown that the creep modulus and relaxation modulus are more or less the same.

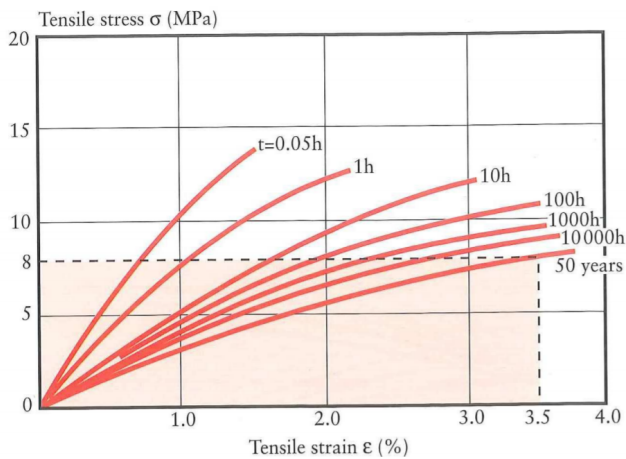


▲ Figure 6: Stress/time curve for HDPE pipe type 1, without safety factor (Janson L.-E. , 2003) HDPE pipe type 1, without safety factor (Janson L.-E. , 2003)



▲ Figure 7: Stress/time curve for HDPE pipe, type 1 including tests (Janson L.-E. , 2003)





▲ Figure 8: Stress-strain curves for HDPE type 1 at 20°C (Janson L.-E. , 2003)

the pipe wall at the end would bend inward. As the ends of these pipe sections have to be welded together, it is recommended that the frozen-in stresses are kept below 2.5MPa. The tests that have been performed to obtain the material properties included frozen-in stresses. It is recommended to discuss details regarding the frozen-in stresses with the manufacturer.

During the 1990's PE100 was developed. The resins for PE100 are produced in two reactors which causes two peaks in the molecular weight distribution graph. This creates a higher strength without decreasing the processability of the pipe. This method of manufacturing also results in a higher stress crack resistance (Janson L.-E. , 2003). This is a "third-generation" PE grade and has a minimum required strength of 10MPa. With a safety factor of 1.25, the design tensile stress of PE100 is 8MPa. A more conservative value of 1.6 is often used for submarine pipes (Pipelife, 2002), which leads to a design stress of 6.3MPa at 20°C.

### 2.1.2 Material properties

Material properties of HDPE were gathered from the CES Edupack database by GRANTA:

Density	947 - 955	kg/m <sup>3</sup>
Youngs modulus <sup>1</sup>	0.915 - 0.916	GPa
Youngs modulus after 50 years	150	GPa
Yield strength <sup>2</sup>	19,3 - 26,9	MPa
Elongation	170 - 800	% strain
Shear modulus	0.322 - 0.338	GPa
Poinsson's ratio	0.413 - 0.46	
Mechanical loss coefficient (tan delta)	0.0416 - 0.0437	
Thermal expansion coefficient	126 - 198	μstrain/ °C

▲ Table 1: Material properties HDPE (GRANTA, 2017)

- 1 The Young's modulus for initial linear-elastic part of the stress strain curve
- 2 Stress at first peak of the stress-strain curve, the Yield strength is time dependent stress strain curve

## 2.2 HDPE pipe installation

Currently, one of the largest diameter pipelines that is produced is 3.5m by the company Agru. The longest segments that were found by the author are 610m long segments with an outer diameter of 3.26m (Agru, 2018). There are other suppliers such as Kraih that supply segments up to an outer diameter of 4m but these pipes are made in segments of 6m. When considering long pipe segments, the flanged segments are buoyant and can be towed to the project location by tugboats, with a towing speed of 6-8 knots (Janson, 2003).

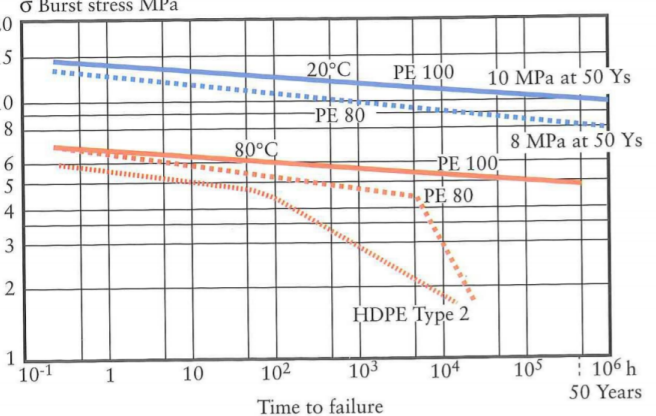
Another important aspect to consider are so called frozen-in stresses which are caused during the production of thermoplastic materials like HDPE. These stresses are caused during the cooling phase of the production. The pipe is often cooled in a cooling bath, where the outside of the pipe cools down while the inside is still warm. After some time, the inside of the pipe wants to contract while the outside is already contracted thermally. The external layer prevents the contraction of the inside layer and as a result, the inside of the pipe is in tension while the outside is in compression. Other cooling methods can cool the inside and outside of the pipe simultaneously, which leads to compression on the inside and outside of the pipe wall while the middle is still in tension. This frozen-in stress is both present in the circumferential and axial direction. If a pipe segment would be cut in the axial direction, the end of

the pipe segment would be cut in the axial direction, the end of

the pipe segment would be cut in the axial direction, the end of

### 2.1.2 Material properties

Material properties of HDPE were gathered from the CES Edupack database by GRANTA:



▲ Figure 9: Stress/time curve for PE80 and PE100 at 20°C and 80°C, without safety factor (Janson L.-E. , 2003)



▲ Figure 10: Pulling operation of 2m OD pipe segments from Norway to Colombia (Source: Pipelife)

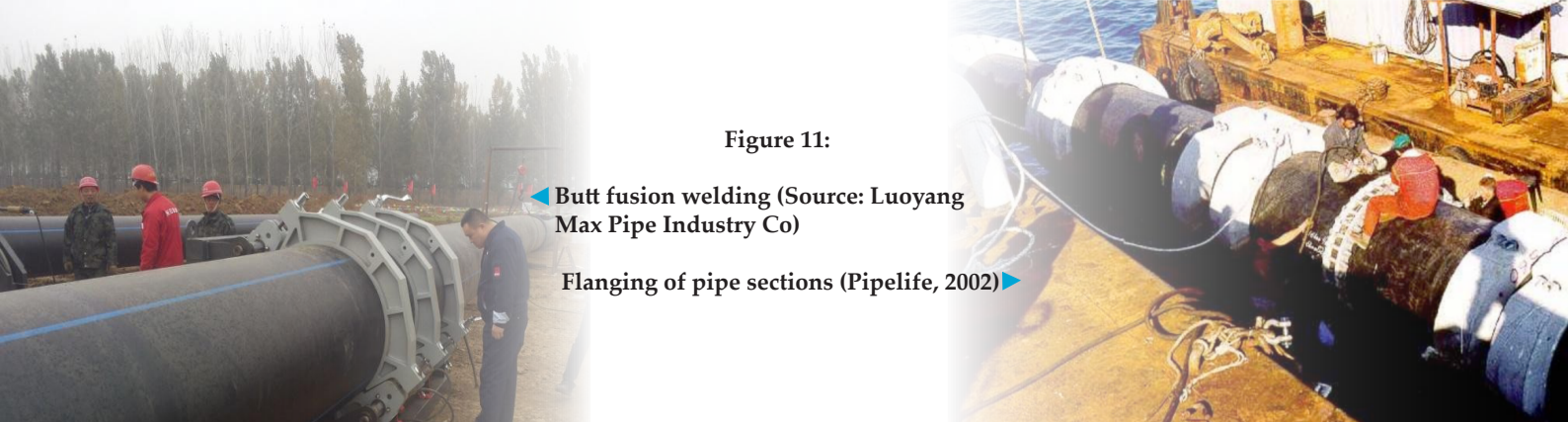


Figure 11:

◀ Butt fusion welding (Source: Luoyang Max Pipe Industry Co)

Flanging of pipe sections (Pipelife, 2002) ▶

## 2.2.1 Welding

On site, the separate pipe segments have to be connected to form one large pipe segment. This can be done by using flanges or by welding. For large diameter pipe, butt welding is a common jointing method. A welding machine with a heating element is used, which is shown in Figure 11. The pipe ends are accurately placed after which they are heated to their melting points of approximately 220°C. The pressure is controlled over different time segments with different pressures to optimize the weld. The time scales and chosen pressures are of major importance for the quality of the weld. If the quality of the weld is good, it should mean that the weld is about the same as the original pipe material. In practice this is not always the case. This is why the so called welding factor is introduced, which is 0.8-0.9 for good welds. However, this factor could get as low as 0.13-0.45 for unfavourable welding conditions (Janson, 2003). This welding factor is again related to the stress in the material. For higher stresses, the welding factor can drop. Note that there is a difference in welding in controlled conditions and on site welding. For very long pipe segments, it is often impossible to weld the pipe in controlled conditions. For example, frictional forces on the pipe, whether resting on the ground or on the sea, have to be taken into account in the welding pressure. Another welding method is electrofusion welding. In this welding method, special fittings are used with a heating element. These elements are used to weld the joint together. The choice for welding depends on the pipe manufacturer and contractor. It is recommended for long, large diameter HDPE pipes to use PE-flanges. This allows for loose metal back-up rings to transmit forces between the pipe sections. It should be noted that it is favourable to have long pipe segments. Longer pipe segments will mean less welding, which is especially time consuming for large diameter HDPE pipes.

## 2.2.2 Weighting

The density of HDPE is lower than the density of seawater. Which means that the pipe will be floating without any additional weighting. Therefore ballast has to be added to the pipe in order to make it sink and keep it stable on the seabed. The amount of ballast has to be chosen such that the pipe stays in place after installation. At the same time, the (empty) pipe must be able to float before installation. The weighting required is between approximately 25-100% of the displacement of the pipe, depending on the environmental conditions.

Concrete blocks are commonly used for the ballast of large diameter HDPE pipes. Once installed, these concrete blocks, shown in Figure 12, make the pipe float at a distance of more than a quarter of the diameter from the seabed and will decrease the lifting force on the pipe. The friction coefficient of the concrete blocks range from 0.2 (circular) to 0.8 (starred), depending on the design of the block (Pipelife, 2002). The concrete weights can be attached to the pipe both onshore or offshore, where the distance between the blocks depends on the specific requirements of the project. The distance can be adjusted to decrease the risk of pipe buckling. The blocks will also avoid torsion on the pipe. The centre of gravity can be chosen such that the blocks stay upright during installation. For locations with extreme environmental conditions, extra weights can be added after the installation. Figure 12 shows an example of concrete blocks connected to the pipe without any bolts or nuts, but it is also possible to connect them with bolts and nuts. The weights are then connected so tightly that the concrete blocks will not be able to move along the pipe. The force in the bolt recommended to be approximately is 2-3 times the weight of the concrete block in air (Pipelife Norge, 2002). Rubber lining is used to avoid damage by the concrete blocks to the pipe.

▼ Figure 12: Concrete weights to ballast the HDPE pipe (Krah, 2013)



The requirement of stability on the seabed determines the amount of required weighting. The force from currents and waves are decomposed in horizontal drag and inertia forces and a vertical lift force. The weight of the concrete blocks and the resulting horizontal friction have to balance the hydrodynamic loading.

The pipeline is often buried in the surf zone and in shallow water to avoid movement of the pipe due to wave loads as well as to protect against any third party interaction. Depending on the location, the pipeline is typically buried in water depths less than 10-15m.

The specific gravity is the ratio between the density of the pipe to the density of the seawater.

$$s_g = \frac{\rho_p}{\rho_w} \quad (1)$$

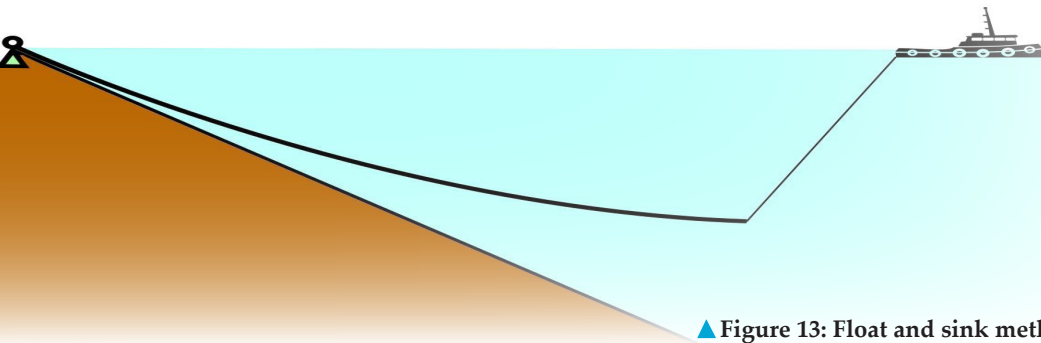
Where  $\rho_p$  is the density of the pipe and  $\rho_w$  is the density of seawater. A minimum specific weight of 1.1 is required for the permanent condition (Qiang Bai, 2014). This specific gravity allows to calculate the volume of the concrete blocks, when a certain distance between the blocks along the pipe is assumed. According to Janson (2003), weighting of 25-35% of the pipes displacement is sufficient due to the flexible design philosophy of the HDPE pipes.

### 2.2.3 Installation methods

One of the largest HDPE pipe diameters installed in the ocean is a 3000mm inner diameter pipe in Lima, Peru. The pipe was installed in different sinking strings, after which the strings were connected offshore by integrated flanges. The maximum water depth was 22m for this project. The largest diameter in deep water was a HDPE pipe of 1.4m diameter. Firstly, nine flanged segments of 300 meters were jointed together, after which it was installed by a controlled submergence process (Plastics Pipe Institute , 2001). There are many options for the controlled submergence process. The most promising installation procedures according to Van Nauta Lemke (2017) are described below.

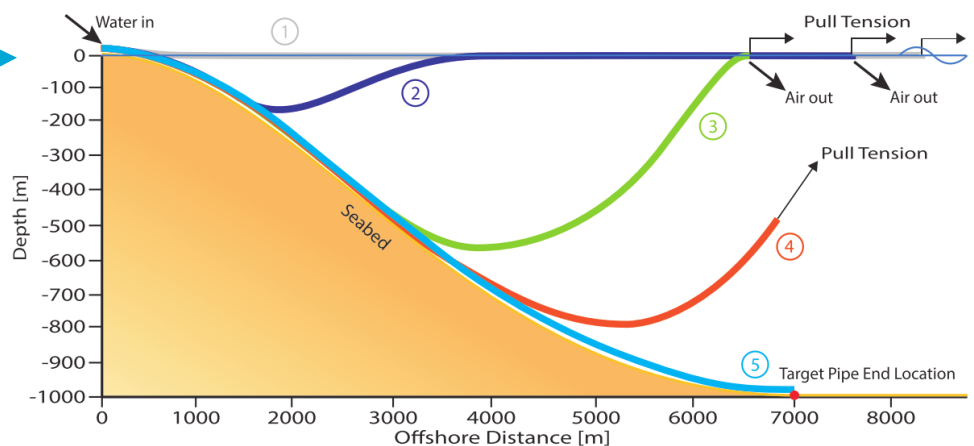
#### Float and sink method

Firstly, the pipe is filled with air in order to make it buoyant. A pulling tug pulls the pipe string to the installation location on the water surface. At the appropriate location, the tug applies pulling tension to the tug line that is connected to the pipe. On the shore end, the pipe is then filled with water to make it sink. The pipe will fill and bend, while the air filled section of the pipe is still buoyant, as shown in Figure 14. The tension force is maintained at the end of the pipe to limit bending of the pipe. A limiting factor is the amount of tension that has to be applied when to prevent buckling in the bending areas. This tension that is applied can become larger than the allowable stress of HDPE which means there is a limit. A recommended sinking velocity is 500m/hour (Janson, 2003).



▲ Figure 13: Float and sink method

Figure 14: Submerging process of the hold and sink method (Van Nauta Lemke, 2017)



### Hold and sink method

Another promising installation method is the hold and sink method. Multiple vessels can be used to hold the pipe in position. The pipe can already be filled with water instead of gradually filling it with water from the shore end, as long as there are enough vessels to hold the pipe on the water surface before installation. The vessels lower the pipe in a controlled way until the pipe is in the correct position. A tension could also be applied to the pipe end similar to the float and sink method. This method could reduce the amount of bending in the pipe with respect to the float and sink method. A disadvantage is that there are multiple vessels required which increases costs.

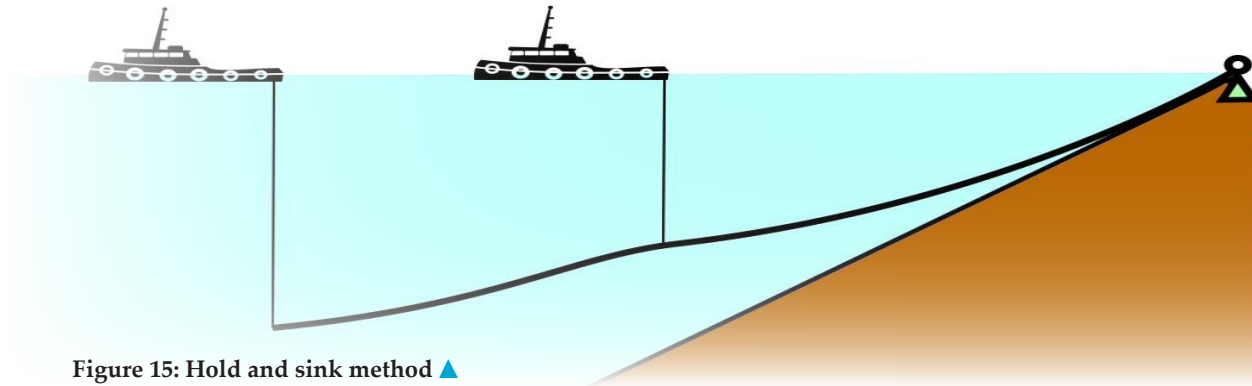
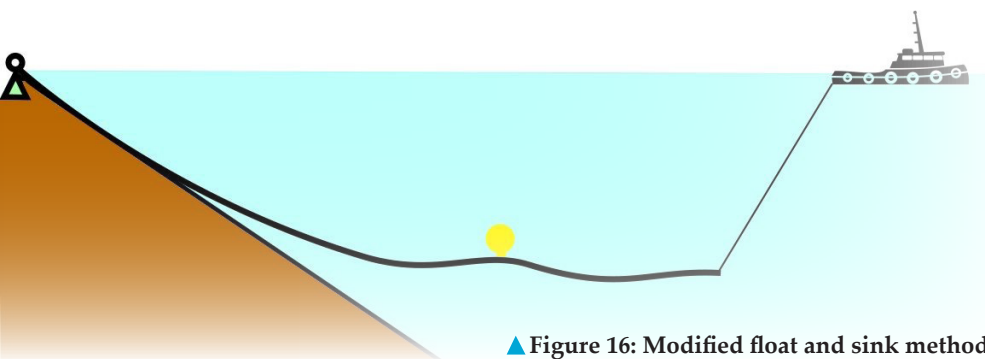


Figure 15: Hold and sink method ▲

### Modified float and sink method

The modified float and sink method is slightly different from the normal float and sink method with one pulling tug at the pipe end. Additional buoyancy modules are added along the pipe to limit the bending and increase controllability. These buoyancy modules can be disconnected by an acoustic release. These releases work on a certain frequency and can be released from the surface. This is a more expensive operation than the normal float and sink method.



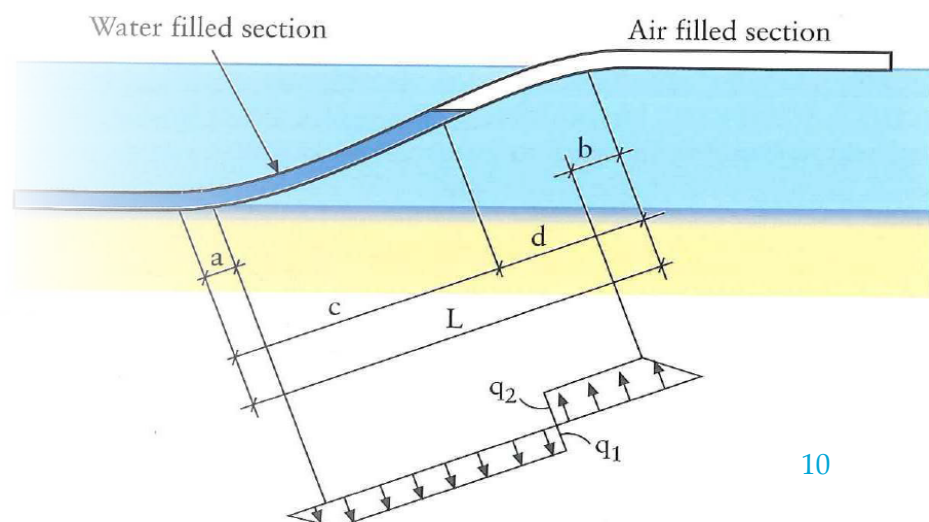
▲ Figure 16: Modified float and sink method

The total installation is expected to take approximately 3-5 days including the jointing of the pipe sections. These installation methods are expected to be in a weather window of approximately 12 hours.

### Sinking process

The pipe will be floating initially. The pipe is filled with water from shore in order to make it sink. In practice, it is likely that the first part of the pipe will be installed in a conventional sinking method, as shown in Figure 17.

Figure 17: Conventional sinking procedure ►



This sinking can be controlled by adjusting the air pressure in the air filled section of the pipe. By adjusting the tension at the end of the pipe, the sinking process must also be controlled in order to prevent buckling. The most important parameters for the sinking process are therefore the air pressure, pulling force and sinking velocity.

The internal air pressure balances the weight of the concrete collars. This pressure is caused by a compressor, which requires are certain capacity, depending on the conditions. This balance pressure is calculated by:

$$p_{internal} = a_a d \quad (2)$$

Where  $p$  is the internal pressure (mWC),  $a_a$  is the degree of air filling and  $d$  is the water depth. The degree of air filling is the ratio of the weight of the pipe and concrete weights to the buoyancy of the internal volume of the pipe. This is an indication of how much air would be needed inside the pipe to make it buoyant.

$$a_a = \frac{w_{s,c} + w_{s,p}}{\frac{\pi D_i^2}{4} \rho_w} \quad (3)$$

Here,  $D_i$  is the inner diameter of the pipe,  $w_{s,c}$  is the submerged concrete weight and  $w_{s,p}$  is the submerged pipe weight. An estimate of the maximum water depth can be made by using these formulas. Figure 9 shows that the burst stress for a 10 hour period is 8MPa for 35°C, including safety factor. It means that the maximum pressure in the pipe for the burst stress in the circumferential direction to be exceeded is:

$$p_{internal} = \frac{2t\sigma_{burst}}{D_{i,pipe}} \quad (4)$$

For a 3m pipe (SDR 23), this comes down to an internal pressure of 0.76MPa. Note that SDR is the diameter to wall thickness ratio. The amount of tension required for the conventional installation method is initially estimated by:

$$P_1 = w_1 R_{min} \quad (5)$$

$$P_2 = w_2 R_{min}$$

Where the maximum pulling force is the force that prevents buckling of the pipe.  $w_1$  and  $w_2$  are the submerged pipe weight per unit meter and the buoyancy of the air filled section of the pipe respectively.

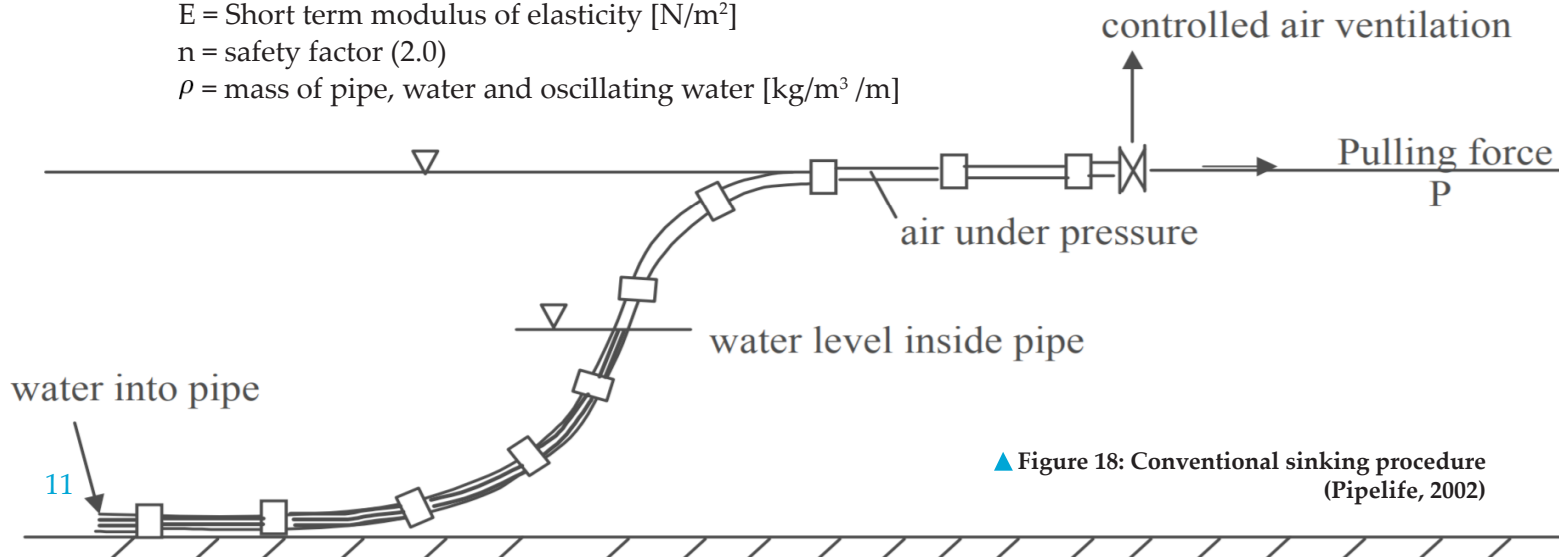
The amount of water entering the pipe is determined by the volume flow of water that is entering the pipe from shore.

Lastly, the sinking velocity is one of the key parameters during installation. There are three important aspects to keep in mind. Firstly, keeping the sinking velocity constant will limit the acceleration forces during installation. If the velocity is kept low, it will automatically mean that the accelerations cannot be very high either for a certain time step. Another reason for keeping the velocity low is the controllability of the installation. Corrections during the installation are easier when the pipe is installed slowly. Another reason for keeping the sinking velocity limited is the risk of oscillations. A rough estimate for the maximum sinking velocity for which the pipe has a risk to oscillate is estimated by (Pipelife, 2003):

$$v = \frac{\pi D^2}{25tH^2n} \left( \frac{E}{25SDR\rho} \right)^{\frac{1}{2}} \quad (6)$$

Where:

- D = Diameter [m]
- St = Strouhal number [-]
- H = waterdepth [m]
- E = Short term modulus of elasticity [N/m<sup>2</sup>]
- n = safety factor (2.0)
- $\rho$  = mass of pipe, water and oscillating water [kg/m<sup>3</sup> /m]



▲ Figure 18: Conventional sinking procedure (Pipelife, 2002)

This formula is conservative for smaller pipes. The sinking velocity obtained by this formula is plotted in Figure 19. The graph already indicates that this formula is not valid for large water depths, as the sinking velocity would have to be kept impractically low such that the installation would last at least 100 hours.

### 2.3 Temperature effects

It was already addressed that the strength of HDPE depends on the temperature of the material. This means that it is important to get a feeling for the range of temperatures that the material will be subject to during the installation.

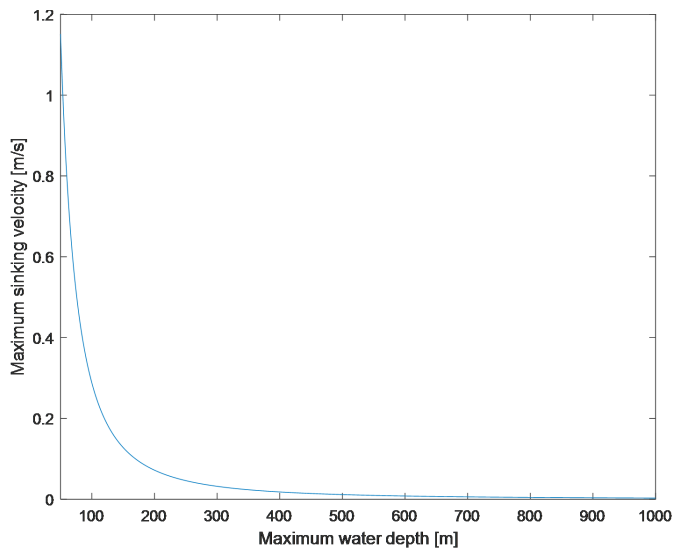
Something to keep in mind is that the pipe will be installed around the equator, which means that the pipe is most likely exposed to sunlight. An estimation of the maximum temperature that the pipe could get is made with the Stefan-Boltzmann law. This law states that the total heat that is radiated from a surface is proportional to the temperature of the surface by the power four (Encyclopaedia Britannica, 2018). The surface will heat up until the surface loses as much energy as the energy that is coming in from the sun. The assumption of the Stefan-Boltzmann law is that the material only loses heat through radiation. The formula is given by:

$$J = \sigma T^4 \quad (7)$$

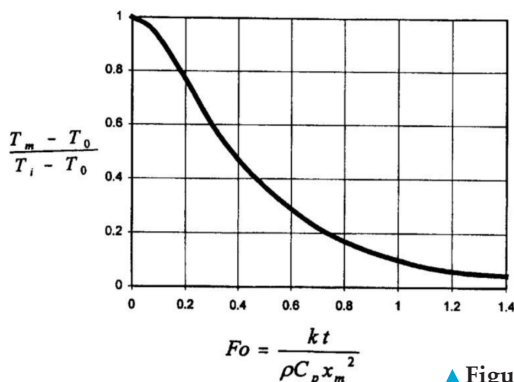
Where  $J$  is the heat flux,  $\sigma$  is the Stefan-Boltzmann constant which is equal to  $5.67E-8 \text{ Wm}^{-2}\text{K}^{-4}$ . The power of raw sunshine is around  $1\text{kW}$  per square meter (JC MacKay, 2008). This comes down to a wall temperature of  $90^\circ\text{C}$  when the pipe is subjected to a long period of sunlight. In practice, there are factors such as clouds and wind that can make the material cooler, which means that the temperature presented here is an upper limit.

When the pipe is submerged, the sea surface is expected to have a temperature of around  $30^\circ\text{C}$ , which will decrease to a minimum of  $5^\circ\text{C}$  when the pipe is submerged. If the pipe is assumed to heat up to a temperature of roughly  $80^\circ\text{C}$  onshore, it will be cooled down by the sea. Something to take into account is the time it would take for the pipe wall to reach a certain temperature which allows the pipe to have more favourable strength properties.

Using the chart in Figure 20, the time to cool a  $13\text{cm}$  pipe wall ( $3\text{m}$  OD,  $\text{SDR}=23$ ) from  $80^\circ\text{C}$  to  $35^\circ\text{C}$  when the pipe submerged at the sea surface takes around 30 minutes. If the pipe would be loaded for 3 hours when the pipe is either  $80^\circ\text{C}$  or  $35^\circ\text{C}$ , the burst stress would be  $7\text{MPa}$  and  $11.5\text{MPa}$  respectively (see Figure 6). Which is a  $164\%$  increase of the burst stress due to cooling down of the pipe. In this calculation it is assumed that the entire pipe is submerged to cool it down, which in practice is not necessarily the case. This means that more time would actually be required to cool down the pipe to  $35^\circ\text{C}$ . However, the assumption of a pipe heated by the sun to  $80^\circ\text{C}$  is rather conservative. This calculation is rough and should solely be interpreted to get a feel for the time span for the temperature effects on the burst stress during installation.



▲ Figure 19: Maximum sinking velocity vs. water depth according to formula Pipelife design guide (2003)



$$Fo = \frac{k t}{\rho C_p x_m^2}$$

▲ Figure 20: Plot to calculate the midplane temperature of a plate as a function of time and ambient temperature  $T_0$  (Strutt, 2002)

- $F_0$  = dimensionless Fourier number [-]
- $k$  = Thermal conductivity [ $\text{W}/\text{m}^\circ\text{C}$ ]
- $\rho$  = density of HDPE [ $\text{kg}/\text{m}^3$ ]
- $C_p$  = heat capacity [ $\text{J}/\text{kg } ^\circ\text{C}$ ]
- $x_m$  = distance from the surface to the middle of the plate [m]
- $T_m$  = Temperature in the middle of the plate [ $^\circ\text{C}$ ]
- $T_0$  = Ambient temperature around the plate [ $^\circ\text{C}$ ]
- $T_i$  = Initial temperature in the middle of the plate [ $^\circ\text{C}$ ]
- $t$  = Time [s]

## 2.4 Loading

To model the installation, a good understanding of the external loading on the pipe is essential. External loads on the pipe are primarily due to waves and currents. In a marine environment, there are many loading scenarios which are difficult to predict. One of the main advantages for HDPE pipes is the flexibility compared to steel or concrete pipes. Instead of using a large safety factor for other materials, the flexible pipe has the possibility to move when large forces are acting on the pipe. This also decreases the amount of seabed preparation that is required. Several types of loading are discussed below.

### 2.4.1 Hydrodynamic drag force

First of all, the pipe will experience drag forces when the pipes moves through a fluid. Where the fluid may move as a result of currents and waves. A relative velocity between the pipe and the surrounding water causes a quadratic drag force on the pipe. This is a result of the disturbance of the pipe in the flow, where the flow generally has been separated from the pipe. The resulting drag force is in opposite direction of the relative velocity between the pipe and the fluid and can be estimated by the drag part of the Morison equation. The resulting force per unit length of the pipe is the product between the stagnation pressure, the diameter per unit length and a dimensionless drag coefficient  $C_d$ .

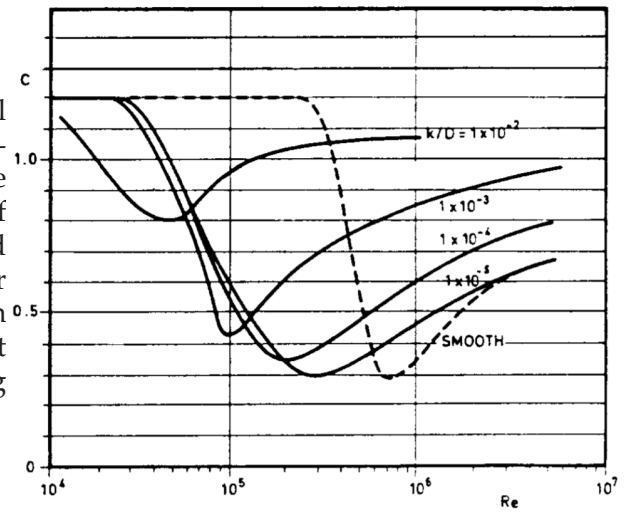
$$F_d = \frac{1}{2} \rho_w C_d D v |v| L \quad (8)$$

Where  $v$  is the relative velocity between the pipe and fluid. The drag coefficient of the pipe is dependent on the Reynolds number, Keulegan Carpenter number and the roughness of the pipe. For a current velocity in the range of 0.25-0.5m/s, as further described in chapter 7, the Reynolds number during installation is in the range of 400K-800K. This means that the flow is critical to supercritical. When an installation velocity of 0.1 m/s is assumed, the Reynolds number is 160K. The surface roughness of new HDPE is 0.007mm for (Marley Pipe Systems, 2010). However, due to transport of the pipe, the pipe can become less smooth. A reasonable assumption of the roughness is 0.02mm. According to Figure 21, the drag coefficient will be in in the range where the Reynolds number is in the range where the graph bends down. Following the line where  $k/D$  is approximately  $10^{-5}$ , it is between 0.3 and 0.5. Another way of estimating the drag coefficient is through DNVGL-RP-F105, where the basic drag coefficient is estimated by (DNV, 2017):

$$C_d = 0.65 \left( \frac{29}{13} + \frac{4}{13} \log_{10} \left( \frac{k}{D} \right) \right) \quad (9)$$

$$\begin{aligned} & ; \frac{k}{D} < 10^{-4} \\ & ; 10^{-4} < \frac{k}{D} < 10^{-2} \\ & ; \frac{k}{D} > 10^{-2} \end{aligned}$$

For HDPE, the drag coefficient according to this formula is 0.65. This drag coefficient has to be corrected for different situations, such as unsteady flow, seabed proximity, trenches. A drag coefficient of 0.65 coincides properly with the design guide by Pipelife (2002) that estimates the drag coefficient to be in the range of 0.5-1.2. Janson (2003) uses a drag coefficient of 0.7, which can be increased to 1.0 to take into account the concrete blocks along the pipe.



▲ Figure 21:  
Drag coefficient in steady critical flow regime for various roughnesses (DNV, 2014)

## 2.4.2 Hydrodynamic inertia force

Besides the drag force, there is an inertia force that is a result of the accelerating fluid particles near the pipe. The pressure gradient along the pipe in an undisturbed pressure field results in the so called Froude-Krilov force. The resulting inertia force for the pipe is equal to:

$$F_{FK} = \rho\pi R^2\dot{u} \quad (10)$$

Which is the mass of the displaced fluid times the acceleration of the surrounding fluid. This force can be present in both currents and waves. Since the pipe actually disturbs the flow, there is another force component. This results from the impermeable pipe that forces the fluid to move around it. The resulting force is given by:

$$F_{dist} = \rho\pi R^2\dot{u} \quad (11)$$

In waves, this force component is the result of a time-dependent build-up and break-down. This force is thus not present for a pipe in constant currents (Journée, 2001). The total inertia force on the pipe is given by:

$$F_I = F_{FK} + F_{dist} = 2\rho\pi R^2\dot{u} \quad (12)$$

Potential theory can be used for the water motion in undisturbed waves.  $F_{dist}$  is much more difficult to predict. The theoretical background used for the derivation of  $F_{dist}$  is no longer accurate because there are disturbances due to for example wakes in real flow. The inertia coefficient  $C_M$  is theoretically 2, where 1 comes from  $F_{dist}$  and 1 from  $F_{FK}$ .

$$C_M = 1 + C_a \quad (13)$$

In practice,  $C_M$  is estimated by laboratory tests.  $C_M$  is dependent on the surface roughness of the pipe, the Keulegan Carpenter number and the Reynolds number. The Keulegan Carpenter number in waves is estimated from equation (14), that is valid for deep water:

$$KC = \frac{2\pi\zeta_a}{D} \quad (14)$$

Where  $\zeta_a$  is the wave displacement amplitude. It is common practice that the maximum wave height during the installation weather window is below 1m (Pipelife Norge, 2002). This means that the KC number for the significant wave height of 0.55m is around 0.6. Making use of figure Figure 22, this leads to an inertia coefficient of 2.0.

Using DNVGL-RP-F107, the added mass coefficient  $C_a$  is 1 for both smooth and rough surfaces for free spanning pipelines. This value is valid in still water. Note that this coincides with the inertia coefficient of 2.0.

## 2.4.3 Total hydrodynamic loading

The total load on the moving pipe in currents and waves can be described by the relative velocity formulation. The relative velocity formulation is valid when  $r/D > 1$ , where  $r$  and  $D$  are the member displacement and the pipe diameter respectively (DNV, 2014).

$$f_n = \rho_w A a + \rho C_a A a_r + \frac{1}{2} \rho C_D v_r |v_r| \quad (15)$$

Here,  $a$  is the acceleration of the fluid,  $a_r$  is the relative acceleration of the fluid and the pipe.



### 2.4.4 Hydrostatic pressure

Besides the loading due to hydrodynamic pressures, there is also an influence of hydrostatic pressure on the pipe. According to Archimedes, this causes an upward force on the pipe known as the buoyancy force. This is based on the assumption that the pressure is acting on a closed surface. However, the pipe is not a closed surface. The internal and external pressure in the pipe can differ, depending on the conditions during installation. Consider a section of the pipe, shown in Figure 23, where an axial force  $N$  and external pressure are present.

The external pressure can be replaced by an enclosed area subject to external pressure in addition to the so called effective axial force. The first part is simply the buoyancy. The same can be done for the internal pressure, shown in Figure 24.

Combined, this leads to the effective axial force:

$$S = N - p_i A_i + p_e A_e \tag{16}$$

So, the true wall force can be computed by (Orcaflex, 2018):

$$N = S + p_i A_i - p_e A_e \tag{17}$$

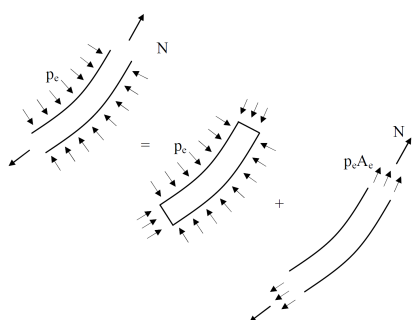
The effective axial force is a concept that caused a lot discussion and, as a result, clarification in literature. There are papers that claim that the effective axial force is a real force and papers that state that it is not. It is clear that the pressure fields acting on the inner and outer pipe wall result in a real force. This causes an equivalent distributed load along the pipe. Neto et al. (2017) believe that the effective tension is not a real force but a concept that is a result of mathematical manipulations. The effective stress is for example used to determine whether a pipe is subject to buckling risks instead of true stress (Collberg, 2005).

When the pipe is curved there is a force resulting from the integration of the pressure fields inside and outside of the pipe. This principle can cause the pipe to buckle due to internal pressure. Because the cold water pipe will be installed in deep water, which means there is high hydrostatic pressure, it is important to understand exactly how the behaviour of the pipe is affected by this pressure acting on both the inside and outside pipe wall.

The effective tension and weight definitions are helpful to understand the mechanical system, but this is not enough for solving it in for example a finite element model. Neto et al. (2017) derived a direct expression of the results of the pressure field integration along the pipe walls. The resulting equivalent load was derived for a generic curved pipe. The pipe was assumed to be a 3D curve in the Frenet coordinate system. Using Euler-Bernoulli assumptions, this allowed each cross-section to be tangential to this 3D curve. For the full derivation, one can read the clarifying paper by Neto et al. (2017). Firstly, an equivalent mechanical system was given which is a result of the pressure integration on the pipe lateral walls and resulted in a moment and force on an infinitesimal pipe element. Using first order Taylor series approximations, a force per unit length equivalent loading was found in order to apply in finite element models (Neto et al., 2017):

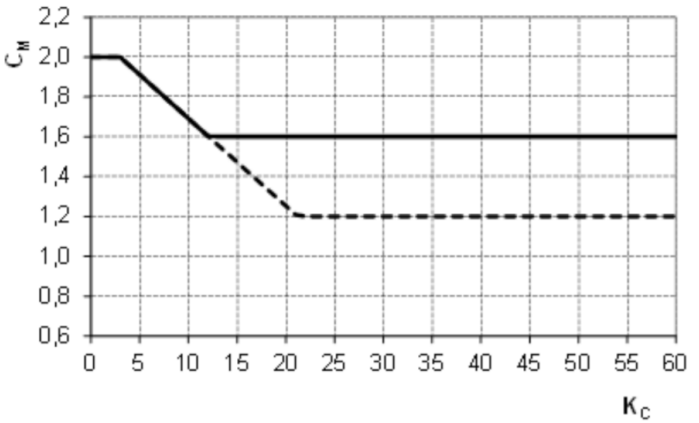
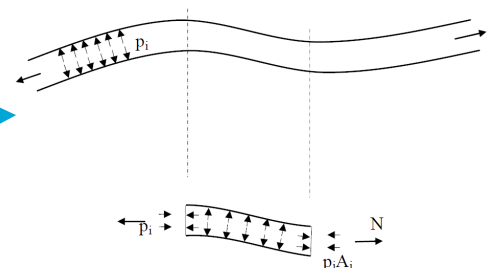
$$\vec{f}(s) = (\rho_i(s)\pi r_i^2 - \rho_e(s)\pi r_e^2)\mathbf{g} - (\rho_i(s)\pi r_i^2 - \rho_e(s)\pi r_e^2)\mathbf{g} * \mathbf{t}(s)\mathbf{t}(s) + (p_e(s)\pi r_e^2 - p_i(s)\pi r_i^2)\kappa(s)\mathbf{n}(s) \tag{18}$$

Where  $\mathbf{g}$  is the gravitation field vector,  $\mathbf{t}$  is a vector perpendicular to the cross-section in point  $s$  along the pipe.  $\mathbf{n}(s)$  is a unit vector pointing in the direction of the centre of curvature which lies in the osculator plane.



◀ Figure 23: Principle of effective axial stress (external pressure) (Collberg, 2005)

Figure 24: Principle of effective axial stress (internal pressure) ▶



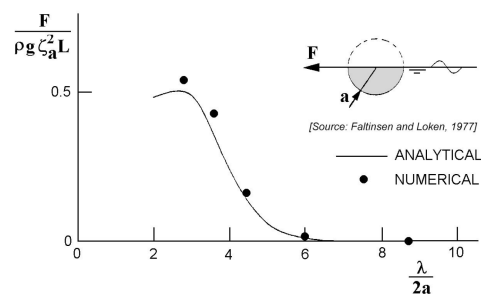
▲ Figure 22: Inertia coefficient as a function of KC for smooth (solid) and rough (smooth) cylinder. (DNV, 2014)

One can interpret the first term of equation (18) as the weight of the internal fluid per plus the buoyancy force, both per unit length. This force is always vertically directed and is related to the effective weight. To interpret the second term, imagine a completely vertical pipe, which would be the case in for a cold water pipe for floating OTEC. In this case, using only the first term in equation (18) would lead to a load per unit length in the vertical direction. This would be impossible as the pressures only act perpendicular to the pipe wall, in the horizontal direction. In reality, the vertical force due to the hydrostatic pressure on a vertical pipe is a result of the end cap pressure only. Due to this end cap force, the bottom of the pipe could even be in compression. With this in mind, the second term can be interpreted as a correction to the first term. For a vertical pipe, the dot product of  $\mathbf{g}$  and  $\mathbf{t}(s)$  is equal to the gravitational acceleration and if the pipe is not bent this will lead to a loading per unit length of the pipe which is equal to zero. A completely horizontal pipe without any bending is also a special case, where the dot product of  $\mathbf{g}$  and  $\mathbf{t}(s)$  is zero and there is only loading due to the weight of the internal fluid plus the buoyancy force. For any other orientations of the pipe, there will be a certain correction to the first term, depending on the state of the pipe section. The third term is a loading in the direction of the centre of curvature, or away from it, depending on the inside and outside pressures. This loading will only be present if the pipe has a nonzero curvature. If this force is directed towards the centre of curvature, it has a stabilizing effect on the pipe. When pointed away from the centre of curvature, for example for high internal pressure compared to external pressure, the resulting force is destabilizing the cold water pipe. Note that the higher the pressure, the more the bending will be either stabilized or destabilized. Besides equation (18), there will also be an end cap force resulting from pressure integration. This force will act on the cross-sectional area at the end of the pipe in the axial direction. More clarification on this topic is given in Appendix E. In this appendix, the equations of motion for a vertically hanging pipe and a horizontally submerged pipe are discussed in relation to the effective tension and true wall stresses.

### 2.4.5 Second order wave drift forces

When only considering first order wave forces, the pipe will on average stay in position in waves due to the circular motions of the water particles. However, irregular waves can exert a steady horizontal force on the pipe, known as the second order wave drift force. These drift forces are related to the square of the wave height. Within potential wave theory, the direct pressure integration method, introduced by Pinkster (1976) can be used. Using this method, the hydrostatic pressure, first order pressure and second order pressure are integrated over the wetted surface. This results in the hydrostatic fluid force, the first order oscillatory fluid force and the second order fluid force (Journée, 2001). For complex structures in waves, the second order fluid force can be expressed by quadratic transfer functions as a function of two different wave frequencies. In a similar way, Faltinsen and Loken (1978) computed the mean wave drift force on two-dimensional cylinders in regular waves, shown in Figure 25.

This graph can be used to calculate the mean wave drift force, proportional to  $\zeta_a$ . As stated before, the maximum wave height during installation is approximately 1m. An estimate of the significant wave height during the weather window is 0.5m. An average wave period for this significant wave height is estimated from wave data in Hato Bay in Curaçao, provided by Van Oord (2014). The location for this estimation is near shore at a water depth of 300m. The best months for the pipe installation, looking at the wave climate are October and November. In these months, the significant wave height of approximately 0.5m is not exceeded during 7-26% and 3-25% during October and November, respectively. Looking at the histogram charts, a typical mean zero-crossing wave period during these acceptable sea states is 2-7s. Using the dispersion relationship, this means that the wave length for most waves is approximated to be in the range of 60-750m, depending on the specific sea state. Using Figure 25, the significant wave drift force on the pipe that is floating on the sea surface will be negligible because the wave length divided by the diameter is larger than 20. Note that these approximations serve as an estimate of the effects of wave drift forces during installation.



▲ Figure 25: Horizontal drift forces on a cylinder (Journée, 2002) design guide (2003)

For this estimation, it is assumed that the waves are acting as beam waves. In reality, there are processes such as refraction that play a role near shore. It is expected that closer to shore, the wave direction is parallel to the axial direction of the pipe due to the change in bathymetry.

## 2.4.6 Vortex induced vibrations

To get an impression of the relevance of vortex induced vibrations (VIV), Reynolds number and the Strouhal number require attention. To avoid any means of vortex shedding during installation, the relative velocity between the pipe and the fluid must be kept limited such that the Reynolds number stays below approximately 40. For higher Reynolds numbers, the vortices in the wake will start separating and vortex shedding might occur. For a 3m diameter pipe, this would come down to a relative velocity between the pipe and the fluid of 10-5m/s which means that vortex shedding is inevitable.

The Strouhal number is the dimensionless ratio between the frequency of vortex shedding and the velocity of the flow and the diameter of the pipe. This number can be used to estimate the frequency of the vortices:

$$St = \frac{f_v D}{U} \quad (19)$$

Where  $U$  is the undisturbed flow velocity,  $f_v$  is the vortex shedding frequency and  $D$  is the diameter of the pipe. The Strouhal number for pipes is approximately 0.2 in most cases, see Figure 26.

In most situations where vortex shedding occurs, the vortices are randomly distributed in the wake of the pipe, such that the resultant lift force of all vortices is negligible with respect to the drag force. These lift forces can however play an important role when the vortex shedding frequency is approaching the natural frequency of the pipe. When the natural frequency is met by the vortex shedding frequency, the pipe will move crosswise to the flow, which disturbs the flow and will cause more vortices behind the pipe. The usually randomly distributed lift forces will be in phase, leading to more oscillations of the pipe (Journée, 2001). This process is called lock-in and has to be avoided. The relative velocity between the fluid and the pipe can be used to estimate the risk of vortex induced vibrations (VIV) during installation.

$$U_r = \frac{U}{f_n D} \approx \frac{1}{St} \quad (20)$$

From various experiments, it was shown that there is a risk of synchronization for relative velocities between 4 and 17 for a relative density of 1.2 (C.H.K. Williamson, 2007). The natural frequency of the pipe can now be used to determine the maximum velocity for the pipe installation for which there is no risk of VIV.

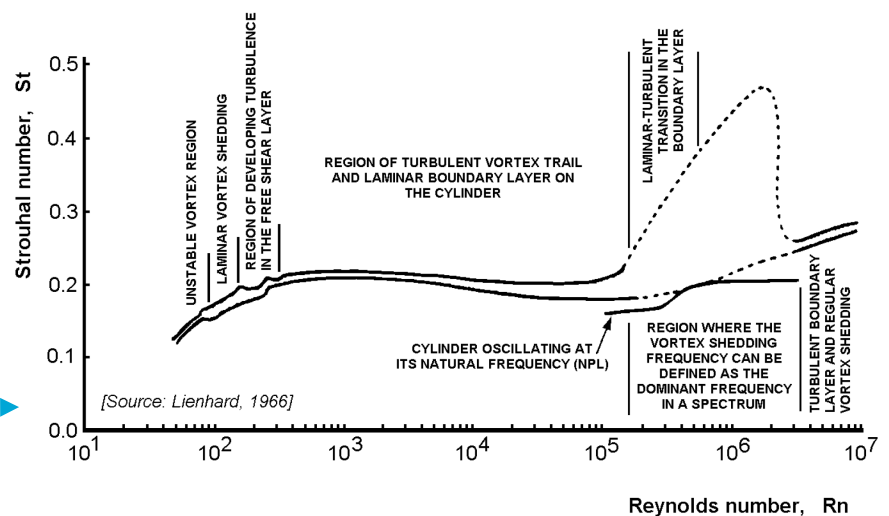


Figure 26: Reynolds number vs. Strouhal number (Lienhard, 1966)

## 2.5 Stresses

The loading described above will cause deformations of the pipe. This leads to stresses in the pipe which are categorized below.

### 2.5.1 Longitudinal stress

First of all, stress can be present in the pipe due to strain of the pipe in axial direction. The stress along the height of the cross-section is calculated by:

$$\sigma_l(z) = E\epsilon_l(z) \quad (21)$$

One of the causes of this strain is tension or compression in the axial direction of the pipe. Stress due to pure tension or compression is calculated by:

$$\sigma_{l,T} = \frac{T}{A} \quad (22)$$

Also, bending will cause the fibres to elongate. Stress due to pure bending is calculated with the following formula:

$$\sigma_{l,b}(z) = E\kappa z \quad (23)$$

Where  $z$  is the height along the cross section that is considered and  $\kappa$  is the curvature of the pipe. Furthermore, there is a stress in the axial direction due to the Poisson effect. The stress due to Poisson is calculated by:

$$\sigma_{l,p} = -\nu(\sigma_h + \sigma_r) \quad (24)$$

Where  $\nu$  is Poisson's ratio.  $\sigma_h$  and  $\sigma_r$  are the hoop and radial stress respectively and are described below. The total longitudinal stress is the sum of equations (22) till (24).

### 2.5.2 Shear stress

Besides the shear perpendicular to the cross-section of the pipe, there is a shear stress acting parallel to the cross section, which is the shear stress. For pure shear, the shear stress is given by:

$$\tau = \gamma G \quad (25)$$

Where  $G$  is the shear modulus and is given by:

$$G = \frac{E}{2(1 + \nu)} \quad (26)$$

This is valid for an isotropic material, which HDPE is. Note that  $E$  is time dependent for HDPE, which means that similarly the shear modulus is time dependent.

### 2.5.3 Hoop and radial stress

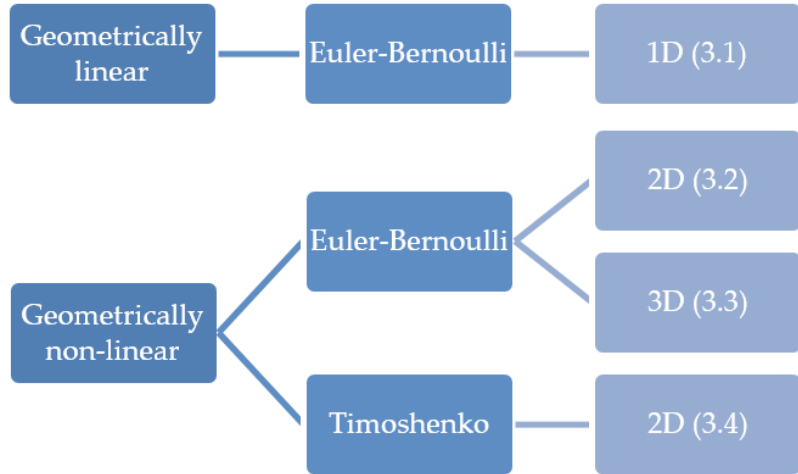
The hoop stress and radial stress were already briefly mentioned in section 2.5.1. In general, the hoop stress and radial stress for thick walled cylinders are calculated by Lamé's equations:

$$\sigma_h = \sigma_r = \frac{p_i r_i^2 - p_o r_o^2}{r_o^2 - r_i^2} + \frac{(p_i - p_o) r_o^2 r_i^2}{(r_o^2 - r_i^2) r^2} \quad (27)$$

Where  $p_i$  and  $p_o$  are the internal and external pressure and  $r$  is the radius of the pipe. For an internal and external pressure that are the same, the second term is equal to zero.

# 3 Model

This chapter discusses several models for the installation of the pipeline. Firstly, the geometrically linear Euler-Bernoulli (EB) model by Van Nauta Lemke (2017) is discussed. Geometrical linear means that the change in geometry is not taken into account. In section 3.2 and 3.3, a geometrically non-linear (GNL) model is derived in both 2D and 3D space. Lastly, the 2D GNL Timoshenko model by Keijdenner (2015) is reproduced in order to investigate the importance of shear deformation.



◀ Figure 27: Beam models and corresponding sections

## 3.1 Background

Several scenarios for the pipe installation were modelled by Van Nauta Lemke (2017). This model was available for the author of this thesis and is revised.

Van Nauta Lemke (2017) used an Euler Bernoulli beam model. An assumption for this model is that the cross section is perpendicular to the neutral axis. This model neglects shear strain and is valid for infinitesimal strains and rotations. The model used the following equation of motion:

$$EI \frac{\partial^4 w}{\partial x^4} - T \frac{\partial^2 w}{\partial x^2} + (m_p + m_a) \frac{\partial^2 w}{\partial t^2} + k_d(x)(w - d_{sb}(x)) + c_d(x) \frac{\partial(w - d_{sb}(x))}{\partial t} = \tau_{Morison}(x, t) - q_{grav}(x, t) + F_{installation} \quad (28)$$

External vessel forces are added on the right hand side for different installation scenarios. This model takes into account the following:

1. Restoring force due to bending stiffness
2. Restoring force due to tension
3. Inertia and added mass forces
4. Stiffness of the seabed
5. Damping of the seabed
6. Hydrodynamic drag force using the Morison equation
7. Gravity
8. Possible external forces

The beam was further discretized using finite difference. Van Nauta Lemke used a re-initialization in the model to correct for the limitations of small deflections and rotations of the Euler-Bernoulli beam theory that was used. This correction allowed to estimate the dynamics of the system for large deflections but resulted in several modelling errors, discussed in Appendix G. After a thorough revision of the work of Van Nauta Lemke, it is concluded that a geometrically non-linear model is required to allow for large deformations.

## 3.2 2D geometrically non-linear Euler-Bernoulli model

The pipe will have large deformations with respect to the sea surface during and after installation. To model the pipe with large deformations, a geometrically non-linear model is derived. This section summarizes the model. See Appendix A for a detailed derivation.

### 3.2.1 Pipe

The pipe is modelled by axial springs to take into account axial strain. Rotation springs are used to take into account the bending stiffness. A simplified figure of the model that was used for the pipe is shown in Figure 28.

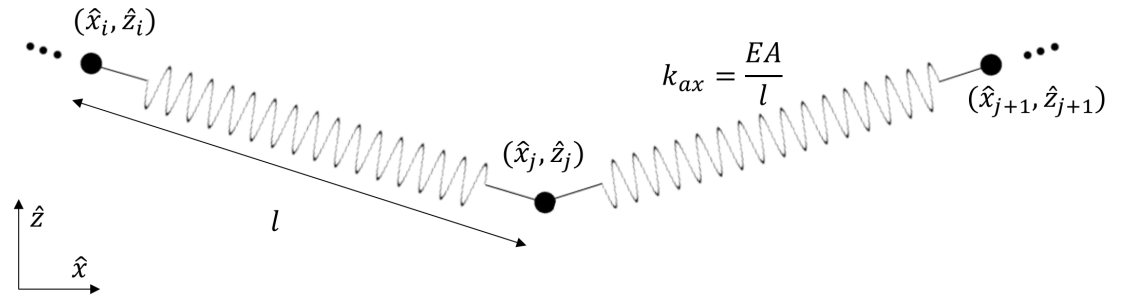
Figure 28: Element layout



The potential and kinetic energy are derived for a continuous piece of the pipe. This continuous piece of pipe is discretized using finite difference, where each element has two nodes. The Lagrangian approach is used to derive the equations of motion for the absolute nodal coordinates.

The degrees of freedom of the system are the nodal coordinates described in a global axis coordinate system rather than using the deformations as degrees of freedom. This allows to formulate the strain of the elements independently of the orientation of the element. In this way, the external forces on the nodes can easily be computed and added to the model in the correct direction (e.g. drag forces).

Figure 29: Axial springs for two elements (3 nodes)



Without the bending stiffness (rotation springs), the equation of motion for an element with nodes  $i$  and  $j$  is described in equation (29).

$$\begin{aligned}
 \frac{m_p}{4}(\ddot{x}_j + \ddot{x}_i) - \frac{\Delta x EA(l_c - l)}{l * l_c} &= F_{\hat{x}_i} \\
 \frac{m_p}{4}(\ddot{x}_j + \ddot{x}_i) + \frac{\Delta x EA(l_c - l)}{l * l_c} &= F_{\hat{x}_j} \\
 \frac{m_p}{4}(\ddot{z}_j + \ddot{z}_i) - \frac{\Delta z EA(l_c - l)}{l * l_c} &= F_{\hat{z}_i} \\
 \frac{m_p}{4}(\ddot{z}_j + \ddot{z}_i) + \frac{\Delta z EA(l_c - l)}{l * l_c} &= F_{\hat{z}_j}
 \end{aligned} \tag{29}$$

Where:

$$\begin{aligned}
 m_p &= \rho_p A_p l + \rho_w A_{ip} l \\
 l_c &= \sqrt{(\hat{x}_j - \hat{x}_i)^2 + (\hat{z}_j - \hat{z}_i)^2} \\
 \Delta x &= (\hat{x}_j - \hat{x}_i) \\
 \Delta z &= (\hat{z}_j - \hat{z}_i) \\
 \frac{\Delta x}{l_c} &= \cos(\alpha) \\
 \frac{\Delta z}{l_c} &= \sin(\alpha)
 \end{aligned} \tag{30}$$

The first term is the inertia force and the second force is the force resulting from the axial strain. This term can be interpreted as the elongation of the element  $(l_c - l)$  times the spring stiffness of the element  $EA/l$ , which gives the tension or compression force in an element. This is multiplied by the cosine or sine of the angle of the element, to account for the orientation of the force. The terms on the right hand side are the external forces on the nodes in a certain direction.

One of the assumptions of an Euler-Bernoulli beam is that the cross section is perpendicular to the neutral axis. This means that shear deformation is neglected. Rotation springs are added to take the bending stiffness into account. The moment in a node in the pipe can be defined by:

$$\begin{aligned} M &= k_r \alpha \\ \alpha &= \alpha_a + \alpha_b \end{aligned} \quad (31)$$

With the rotation spring stiffness:

$$k_r = \frac{EI}{l} \quad (32)$$

The moment is simply the curvature of the beam  $\alpha/l$  times the bending stiffness  $EI$ . The moment is decomposed into forces perpendicular to the neutral axis of the pipe, as shown in Figure 30.

$$F_{M_i} = \frac{EI}{l^2} \alpha \quad (33)$$

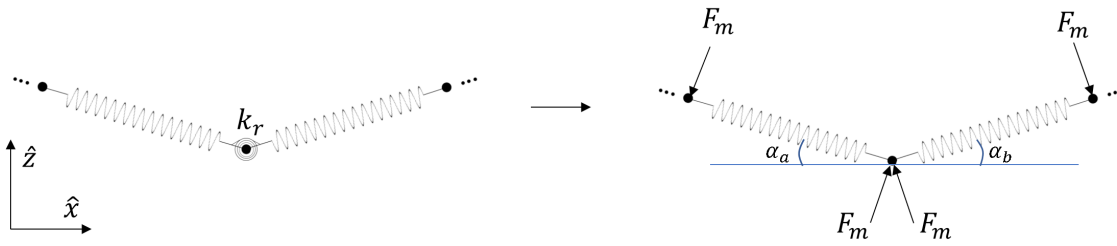


Figure 30: Replacement of rotation springs to forces perpendicular to elements

This perpendicular force can be decomposed into forces in the directions of the global axis coordinate system.

$$\begin{aligned} F_{\hat{x}_{i-1}} &= F_{M_i} \sin(\alpha_a) \\ F_{\hat{z}_{i-1}} &= -F_{M_i} \cos(\alpha_a) \\ F_{\hat{x}_{i+1}} &= F_{M_i} \sin(\alpha_b) \\ F_{\hat{z}_{i+1}} &= -F_{M_i} \cos(\alpha_b) \\ F_{\hat{x}_i} &= -F_{M_i} \sin(\alpha_a) - F_{M_i} \sin(\alpha_b) \\ F_{\hat{z}_i} &= F_{M_i} \cos(\alpha_a) + F_{M_i} \cos(\alpha_b) \end{aligned} \quad (34)$$

Where  $i-1$  and  $i+1$  are the nodes left and right of the rotation spring node  $i$ , respectively. The bending moment in the pipe is now decomposed into forces in the global axis coordinate system. For multiple elements, these forces are implemented in the equation of motion (29) to include the bending stiffness of the pipe. Note that the equation of motion for node  $i$  is dependent on the coordinates of node  $i$  and surrounding nodes  $i-1$  and  $i+1$ .

### 3.2.2 Hydrodynamic drag and inertia force

The relative velocity formulation (15) is used to incorporate the hydrodynamic forces due to the movement of the pipe through the water column. Due to the quadratic nature of the drag force, this force is not straightforward to decompose in the global  $x$  and  $z$  directions. The relative velocity for each node is calculated with respect to the water particle velocity. This velocity is decomposed in a velocity in the axial direction of the element and perpendicular to the element. This perpendicular velocity is used to calculate the drag force, perpendicular to the element. Vector projection is used to calculate the relative velocity perpendicular to an element. For a derivation, see equation (91) to (96) in Appendix A.

The first inertia term (Froude Krilov) from equation (15) is not taken into account in the equation of motion because there are no water particle accelerations in a stationary flow, which is considered in this thesis. The disturbance force, which is the term related to the added mass coefficient  $C_a$  is incorporated through the following equation:

$$\begin{aligned}
 F_{add\hat{x}_i} &= C_a \frac{\rho_w \pi R_p^2}{4} \Delta z (\ddot{x}_j + \ddot{x}_i) \\
 F_{add\hat{x}_j} &= C_a \frac{\rho_w \pi R_p^2}{4} \Delta z (\ddot{x}_j + \ddot{x}_i) \\
 F_{add\hat{z}_i} &= C_a \frac{\rho_w \pi R_p^2}{4} \Delta x (\ddot{z}_j + \ddot{z}_i) \\
 F_{add\hat{z}_j} &= C_a \frac{\rho_w \pi R_p^2}{4} \Delta x (\ddot{z}_j + \ddot{z}_i)
 \end{aligned} \tag{35}$$

The added mass is perpendicular to the element. Therefore, the terms  $\Delta x$  and  $\Delta z$  are the projection of the total added mass of the element in the  $x$  and  $z$  direction. Thus, the added mass is dependent on the state of the system.

### 3.2.3 Seabed

The pipe-soil interaction is important during both installation and operating conditions. The soil around the pipe is disturbed and difficult to predict because the changes in the strength and stiffness of the soil are highly dependent on the motions of the pipe. Soil sampling followed by in-situ and laboratory tests is required to evaluate the geotechnical parameters at a certain location.

For the conceptual design stage in this thesis, the seabed is modelled by springs and dashpots that activate as soon as a nodal coordinate crosses the seabed. The resulting seabed force is computed as a function of the nodal velocity and position with respect to the seabed. It is assumed that the pipe does not slide as soon as it is on the seabed.

### 3.2.4 Material damping

Material damping was added to the model. The material damping factor follows from a mechanical loss coefficient  $\tan\delta$  that typically has a value of 0.05 for polymer fibre materials (GrantaDesign, 2018). This coefficient is the ratio of the loss and storage modulus in a viscoelastic material and is obtained by material testing.

$$\tan\delta = \frac{E''}{E'} \tag{36}$$

Where  $E'$  is the storage modulus and  $E''$  is the loss modulus. The storage modulus is a measure of the stored energy and the loss modulus of the dissipated energy. The complex elasticity modulus is:

$$E^* = E' + iE'' \tag{37}$$

For linear dynamic systems, the stiffness matrix can be multiplied by the mechanical loss coefficient to obtain the damping matrix. However, there is no state independent stiffness matrix multiplication that can be used in order to obtain a similar damping matrix. A derivation of the state dependent damping terms in the equations of motion is given in Appendix C. This appendix also discusses the importance of the material damping, compared to damping due to drag forces. Based on the results, material damping is neglected in the model to keep computation time limited.

### 3.3 3D geometrically non-linear Euler-Bernoulli model

The pipe will have large deformations with respect to the sea surface during and after installation. To model the pipe with large deformations, a geometrically non-linear model is derived. This section summarizes the model. See Appendix A for a detailed derivation.

#### 3.3.1 Pipe

In order to take into account loads perpendicular on the pipe due to drag forces, the model is extended to 3D. The derivation is given in Appendix A.2. Similar to equation (29) in the two dimensional case, the equation of motion for the axial strain of a 3D element in a global axis coordinate system is given by:

$$\begin{aligned}
 \frac{m_p}{4} (\ddot{x}_j + \ddot{x}_i) - \frac{\Delta x EA (l_c - l)}{l * l_c} &= F_{\hat{x}_i} \\
 \frac{m_p}{4} (\ddot{x}_j + \ddot{x}_i) + \frac{\Delta x EA (l_c - l)}{l * l_c} &= F_{\hat{x}_j} \\
 \frac{m_p}{4} (\ddot{y}_j + \ddot{y}_i) - \frac{\Delta y EA (l_c - l)}{l * l_c} &= F_{\hat{y}_i} \\
 \frac{m_p}{4} (\ddot{y}_j + \ddot{y}_i) + \frac{\Delta y EA (l_c - l)}{l * l_c} &= F_{\hat{y}_j} \\
 \frac{m_p}{4} (\ddot{z}_j + \ddot{z}_i) - \frac{\Delta z EA (l_c - l)}{l * l_c} &= F_{\hat{z}_i} \\
 \frac{m_p}{4} (\ddot{z}_j + \ddot{z}_i) + \frac{\Delta z EA (l_c - l)}{l * l_c} &= F_{\hat{z}_j}
 \end{aligned} \tag{38}$$

Where:

$$\begin{aligned}
 m_p &= \rho_p A_p l + \rho_w A_{ip} l \\
 l_c &= \sqrt{(\hat{x}_j - \hat{x}_i)^2 + (\hat{y}_j - \hat{y}_i)^2 + (\hat{z}_j - \hat{z}_i)^2} \\
 \Delta x &= (\hat{x}_j - \hat{x}_i) \\
 \Delta y &= (\hat{y}_j - \hat{y}_i) \\
 \Delta z &= (\hat{z}_j - \hat{z}_i)
 \end{aligned} \tag{39}$$

Now, the bending stiffness is incorporated by a rotation spring as in equation (31), (32) and (33). However, in the three dimensional case, the angle  $\alpha$  is computed differently from the previous section. Say there are two elements in 3d space, where a, b and c are the distances between the nodes, shown in Figure 31. The cosine rule is used to determine the angle  $\alpha$  in equation (31) for two elements (3 nodes) in 3D space.

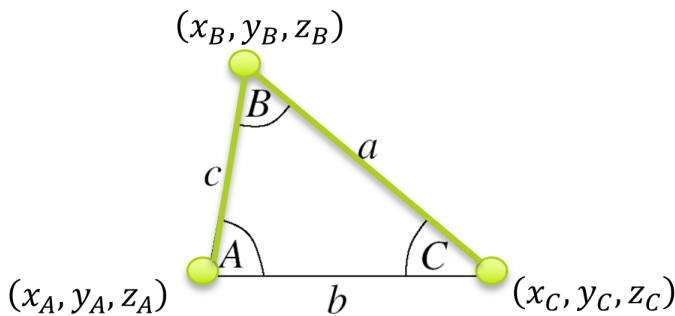
$$\alpha = \pi - \angle B = \angle A + \angle C = \arccos\left(\frac{b^2 + c^2 - a^2}{2bc}\right) + \arccos\left(\frac{a^2 + b^2 - c^2}{2ab}\right) \tag{40}$$

Equation (31) can now be used to compute the moment in the pipe. Next, the moment is decomposed in to forces perpendicular to the elements, similar to equation (34). However, the direction of the forces in three dimensional space are slightly more complicated. When torsion is neglected, the forces due to the decomposed moment are perpendicular to the elements in the plane of the three nodes. To obtain this direction in 3D space, vector projection is used. A schematization of the principle for two elements is depicted in Figure 32.

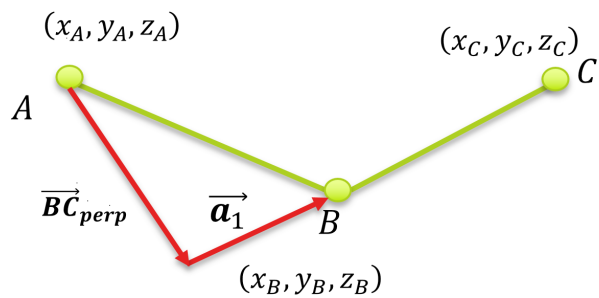
To get the perpendicular direction to element  $\overline{BC}$ , in plane ABC, the scalar projection of vector  $\overline{BC}$  on vector  $\overline{AB}$  is calculated by:

$$\alpha_1 = \frac{\overline{AB} * \overline{BC}}{|\overline{BC}|} \tag{41}$$

▼ Figure 31: Three nodes in 3D space



▼ Figure 32: Vector projection



This scalar projection is used to calculate the vector projection of vector  $\overline{AB}$  on  $\overline{BC}$ .

$$\overline{a_1} = a_1 \overline{BC}_{unit} \quad (42)$$

Where  $\overline{BC}_{unit}$  is a unit vector in direction of  $\overline{BC}$ . The vector perpendicular to element  $\overline{BC}$ , in the plane ABC can now be calculated by:

$$\overline{BC}_{perp} = \overline{AB} - \overline{a_1} \quad (43)$$

This vector is normalized and multiplied by the magnitude of the force to get the force vector in plane ABC perpendicular to element  $\overline{BC}$ .

$$F_{\overline{BC}_p} = \frac{\overline{BC}_{perp}}{|\overline{BC}_{perp}|} F_M \quad (44)$$

This procedure is applied to obtain all force vectors similar to the forces in Figure 32, but now in 3D space. The procedure to obtain force vectors perpendicular to the elements was verified in 3D drawing software with arbitrary nodes. Now, the moment in the pipe is decomposed into forces in the three dimensional global axis coordinate system and are a function of the degrees of freedom (nodal coordinates).

### 3.3.2 Hydrostatic loading

The influence of the hydrostatic pressure on the pipe was discussed in section 4.2.2, where an equation is given that can be implemented in the model. The first term in equation (18) is a force which can simply be added to the equation of motion of the pipe in the z-direction. The inside fluid density of the first term can be varied to model a section of the pipe that is filled with air. The second term of the equation contains the dot product between the vector  $\mathbf{g}$  and  $\mathbf{t}(s)$ , multiplied with  $\mathbf{t}(s)$ . The vector  $\mathbf{t}(s)$  is determined, which can be easily computed for a node in 3D space by normalizing vector  $\overline{AC}$  in Figure 32. In this way, the vector  $\mathbf{t}(s)$  is a vector in 3d space and has a cross-section perpendicular to the discretized neutral axis A-B-C in Figure 32. The third term of equation (18) contains the curvature  $\kappa(s)$ , which is already calculated in order to implement the rotation springs for bending into the equations of motion. Similar to the implementation of the rotation springs, the loading on a node due to the last term can be determined by means of vector projection. As an example, take the 2d case in Figure 30, where the sum of the 2 force vectors in the middle node can be normalized in order to obtain vector  $\mathbf{n}(s)$ , pointing towards the centre of curvature. The same principle is used in the 3 dimensional case. The magnitude of the external pressure in for example node i is calculated by:

$$p_{e_i} = \rho_w g \hat{z}_i \quad (45)$$

Now, all terms in equation (18) are determined in 3D space and by multiplying equation by the length of an element on obtains the load that can be added in the equations of motion. Note that the result of equation (18) is a vector and should be added in the correct direction. A verification of this implementation is given in appendix B, where the true wall stress is computed for a vertically hanging pipe. Chapter 6 discusses the influence of the third term in equation (18).

### 3.3.3 Hydrodynamic loading

The drag force is calculated similarly to the two-dimensional case except for extending the vectors in equations (91) up to (96) to 3D. The hydrodynamic inertia force is computed according to:

$$\begin{aligned} F_{add \hat{x}_i} &= C_a \frac{\rho_w \pi R_p^2}{4} \frac{\sqrt{dy^2 + dz^2}}{\sqrt{dx^2 + dy^2 + dz^2}} (\ddot{x}_j + \ddot{x}_i) = A_x (\ddot{x}_j + \ddot{x}_i) \\ F_{add \hat{x}_j} &= C_a \frac{\rho_w \pi R_p^2}{4} \frac{\sqrt{dy^2 + dz^2}}{\sqrt{dx^2 + dy^2 + dz^2}} (\ddot{x}_j + \ddot{x}_i) = A_x (\ddot{x}_j + \ddot{x}_i) \\ F_{add \hat{y}_i} &= C_a \frac{\rho_w \pi R_p^2}{4} \frac{\sqrt{dx^2 + dz^2}}{\sqrt{dx^2 + dy^2 + dz^2}} (\ddot{y}_j + \ddot{y}_i) = A_y (\ddot{y}_j + \ddot{y}_i) \\ F_{add \hat{y}_j} &= C_a \frac{\rho_w \pi R_p^2}{4} \frac{\sqrt{\Delta x^2 + \Delta z^2}}{\sqrt{\Delta x^2 + \Delta y^2 + \Delta z^2}} (\ddot{y}_j + \ddot{y}_i) = A_y (\ddot{y}_j + \ddot{y}_i) \\ F_{add \hat{z}_i} &= C_a \frac{\rho_w \pi R_p^2}{4} \frac{\sqrt{\Delta x^2 + \Delta y^2}}{\sqrt{\Delta x^2 + \Delta y^2 + \Delta z^2}} (\ddot{z}_j + \ddot{z}_i) = A_z (\ddot{z}_j + \ddot{z}_i) \\ F_{add \hat{z}_j} &= C_a \frac{\rho_w \pi R_p^2}{4} \frac{\sqrt{\Delta x^2 + \Delta y^2}}{\sqrt{\Delta x^2 + \Delta y^2 + \Delta z^2}} (\ddot{z}_j + \ddot{z}_i) = A_z (\ddot{z}_j + \ddot{z}_i) \end{aligned} \quad (46)$$

### 3.3.4 Tug line and pulling tug

Besides the pipe, there is a pulling tug and tug line added to the model. The equation of motion of the tug line is simply the catenary equation (38), where the properties of the tug line are included instead of those of the pipe. This tug line is connected to a vessel, that is modelled by a vertical mass spring system where the stiffness is modelling the buoyancy of the vessel.

### 3.3.5 Summary

Now that all forces in the equation of motion are derived, they can be implemented in MATLAB. The total equation of motion for one element becomes:

$$\begin{aligned}
 & \left(\frac{\rho Al}{4} + A_x\right)(\ddot{x}_j + \ddot{x}_i) - \frac{\Delta x EA(l_c - l)}{l * l_c} + F_{\hat{x},bend,i} = F_{\hat{x},drag,i} + F_{\hat{x},hs,i} + F_{\hat{x}_i} \\
 & \left(\frac{\rho Al}{4} + A_x\right)(\ddot{x}_j + \ddot{x}_i) + \frac{\Delta x EA(l_c - l)}{l * l_c} + F_{\hat{x},bend,j} = F_{\hat{x},drag,j} + F_{\hat{x},hs,j} + F_{\hat{x}_j} \\
 & \left(\frac{\rho Al}{4} + A_y\right)(\ddot{y}_j + \ddot{y}_i) - \frac{\Delta y EA(l_c - l)}{l * l_c} + F_{\hat{y},bend,i} = F_{\hat{y},drag,i} + F_{\hat{y},hs,i} + F_{\hat{y}_i} \\
 & \left(\frac{\rho Al}{4} + A_y\right)(\ddot{y}_j + \ddot{y}_i) + \frac{\Delta y EA(l_c - l)}{l * l_c} + F_{\hat{y},bend,j} = F_{\hat{y},drag,j} + F_{\hat{y},hs,j} + F_{\hat{y}_j} \\
 & \left(\frac{\rho Al}{4} + A_z\right)(\ddot{z}_j + \ddot{z}_i) - \frac{\Delta z EA(l_c - l)}{l * l_c} + F_{\hat{z},bend,i} = F_{\hat{z},drag,i} + F_{\hat{z},hs,i} + F_{\hat{z},g,i} + F_{\hat{z}_i} \\
 & \left(\frac{\rho Al}{4} + A_z\right)(\ddot{z}_j + \ddot{z}_i) + \frac{\Delta z EA(l_c - l)}{l * l_c} + F_{\hat{z},bend,j} = F_{\hat{z},drag,j} + F_{\hat{z},hs,j} + F_{\hat{z},g,j} + F_{\hat{z}_j}
 \end{aligned} \tag{47}$$

The first term is the inertia of the pipe plus the added mass. The second term is models the axial strain of the pipe. The third term is the force due to the bending moment. It must be noted that the bending force is included here and is a function the coordinates of the nodes next to node i and j, as described above. The bending forces are incorporated in the equation of motion of an element as a function of the coordinates of neighbouring elements. It is not a function of the degrees of freedom of the element itself, such as most other terms in equation (47). The first term on the right hand side of the equations are the drag force components. The second term is the hydrostatic pressure force which, similar to the bending force, is dependent on the curvature of the pipe and thus the surrounding elements. In the equations of motion in the z-direction, the gravity force is added which is a result of the weight in air. The last terms in the equation are possible external forces. An ODE solver in Matlab is used to solve the system of ODEs.

### 3.4 2D geometrically non-linear Timoshenko beam model

In order to incorporate shear deformation, the Timoshenko beam model by Chris Keijdener (2015) is remodelled. His model takes into account shear deformation and allows for large deformations. A continuum, depicted in Figure 33, is discretized with finite difference. The kinematic assumptions are based on Timoshenko beam theory. This means that the cross-section of the pipe stays straight but is not necessarily perpendicular to the neutral axis, in contrast to the Euler-Bernoulli beam theory. The h-s axis is the local coordinate system where s is the reference axis.  $\gamma_i$  and  $\gamma_j$  are the shear angles in nodes i and j in the local coordinate system.  $r_{1,n}$  is the distance between the neutral axis and the chosen reference system. In the case of a symmetrical cross-section, which is the case for the pipe, this distance is zero.  $\varphi_i$  and  $\varphi_j$  are the shear angles in the global coordinate system, where the relation between the two can be described by using the angle between the element and the global axis coordinate system,  $\alpha_n$ . The kinematic relationships, described in Appendix A.3, are used to obtain the potential and kinetic energy. Similar to the approach that was used by Keijdener (2015), the equations of motion are derived for the element layout, depicted in Figure 34. The derivation of the equations of motion can be found in Appendix A.3 and the paper by Keijdener (2015). The hydrodynamic and external forces are added with the same approach that was used for the GNL EB model and will not be repeated here for the sake of brevity.

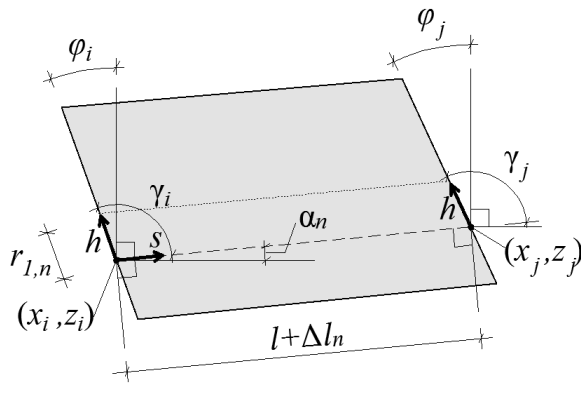
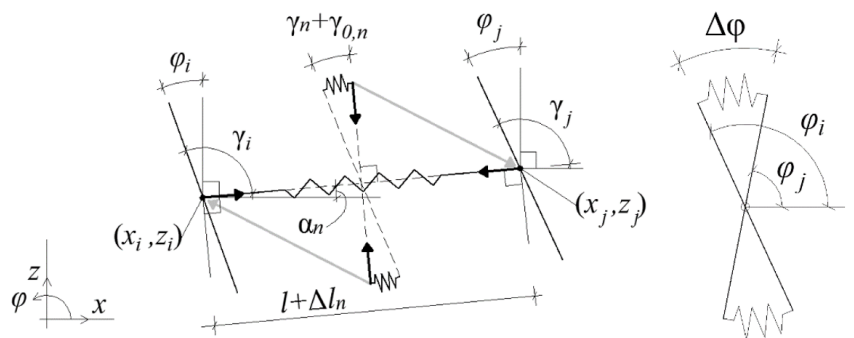


Figure 33: Non-prismatic, non-symmetric beam element (Keijdener, 2015)

Figure 34: Element layout: axial and shear springs (left) bending stiffness spring (right) (Keijdener, 2015)



# 4 Comparison Timoshenko and Euler-Bernoulli Models

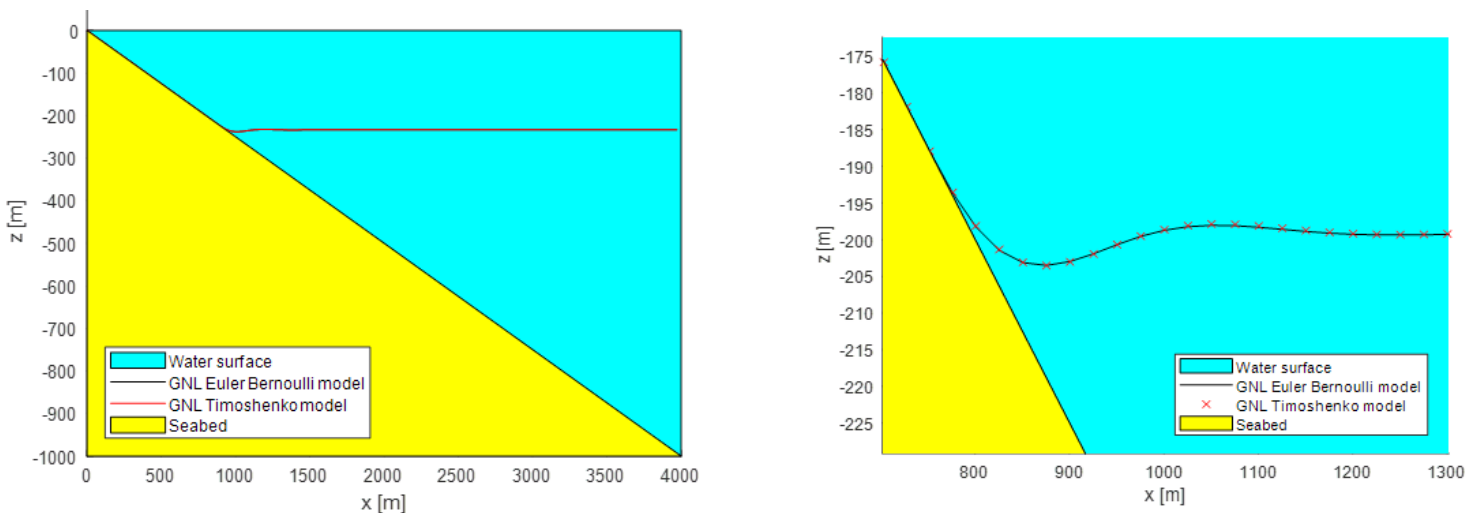
In the previous chapter, the GNL Timoshenko and GNL Euler-Bernoulli beam models are introduced. One of the research questions is whether shear deformation is important to take into account during the installation of large diameter HDPE pipes.

To investigate this, several freefall runs are done with both models, to compare the general behaviour of the pipe and the local behaviour where the pipe is bent. A freefall installation was modelled for a 4km long pipe, where it is initially held at the surface and submerged without any guidance. In this way, bending in the pipe is introduced where the pipe interacts with the seabed. The freefall for a 3m diameter pipe (SDR 23) with a specific gravity of 1.01 is shown in Figure 35. The left hand side of this figure shows the overall behaviour of the pipe for a specific time step. No noticeable difference of the general behaviour is observed during the full installation run. On the right hand side of the figure, the pipe section which is bent is shown in more detail. The solid black line shows the Euler-Bernoulli beam model and the red points show the Timoshenko model. Again, both models show the same bending behaviour. A minor difference was observed over time which is a result of different modes and natural frequencies of both models. Figure 36 shows the bending stress in a specific node over time. The same pattern was found in every node when comparing the bending stresses, where the stress peak of the EB model is slightly higher. One can observe the double curve, which is a result of the slight upward bending which can be seen on the right of Figure 35.

Figure 37 shows the shear stress by the Timoshenko beam model, which is a result of the shear deformation. The magnitude of the shear stress shows the same pattern as the bending stress. This means that during maximum bending, the shear deformation is at its maximum as well. However, the magnitude of the shear stress is smaller. The maximum bending radius during this freefall installation was 386m, which equals 128 times the pipe diameter. A typical rule of thumb for buckling is a minimum bending radius of 60 times the pipe diameter, including a safety factor of 2.

It is shown that the bending stresses during this freefall run with a specific gravity of 1.01 are already significant. To investigate the influence of shear deformation on a more heavily bent large diameter HDPE pipe, the same installation run is performed but with a specific gravity of 1.05. The corresponding bending stresses in a point along the pipe is shown in Figure 38. More results for a specific gravity of 1.05 and 1.1 are also shown in Appendix H. One can observe a similar pattern to the bending stresses for a specific gravity of 1.01. However, the difference in behaviour and consequently the bending stresses in the Euler-Bernoulli and Timoshenko beam models increases slightly. The shear stresses for the installation run with higher specific gravities remain within the same order of magnitude as the shear stresses for the freefall run with a specific gravity of 1.01.

Figure 35: Global (left) and local (right) behaviour of the pipe modelled by the GNL Euler-Bernoulli beam model and the Timoshenko beam model. L=4km, 161 nodes, D=3m, SDR=23,  $s^s=1.01$ ,  $\kappa=0.59$ ,  $G=313\text{MPa}$



**Bending stress comparison at s=1000m for a 4km, 3m diameter pipe SDR 23 during freefall installation sg=1.01**

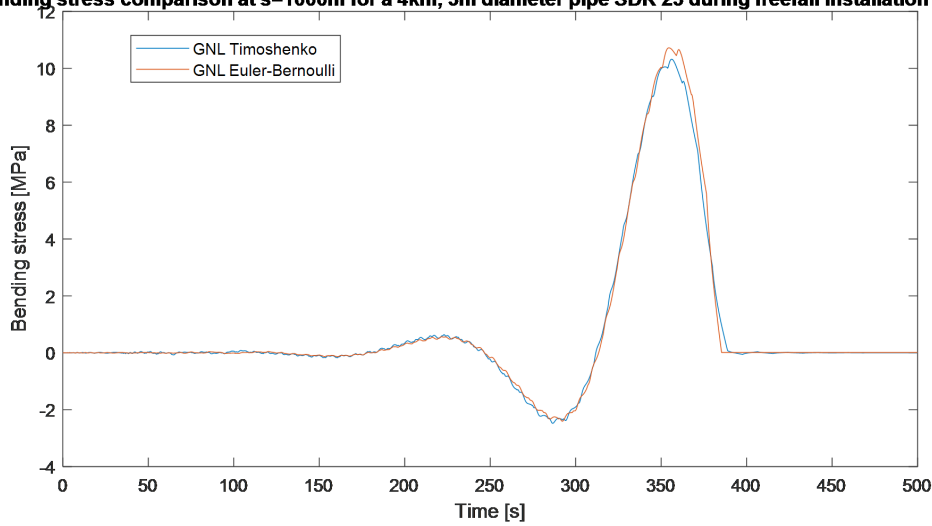
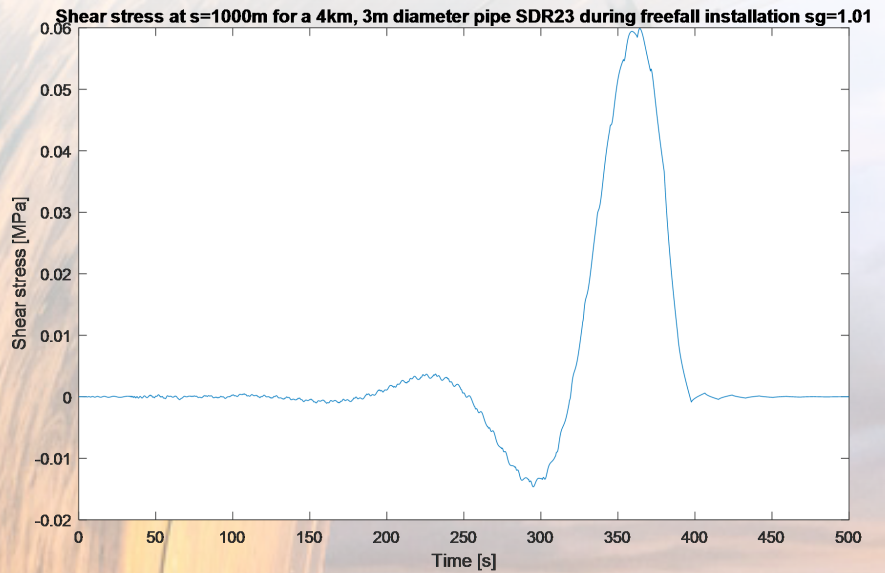


Figure 36:  
Bending stress in the pipe modelled by the GNL Euler-Bernoulli beam model and the Timoshenko beam model,  $sg=1.01$

Figure 37: Shear stress in the pipe modelled by the Timoshenko beam model,  $sg=1.01$



**Bending stress comparison at s=2000m for a 4km, 3m diameter pipe SDR 23 during freefall installation sg=1.05**

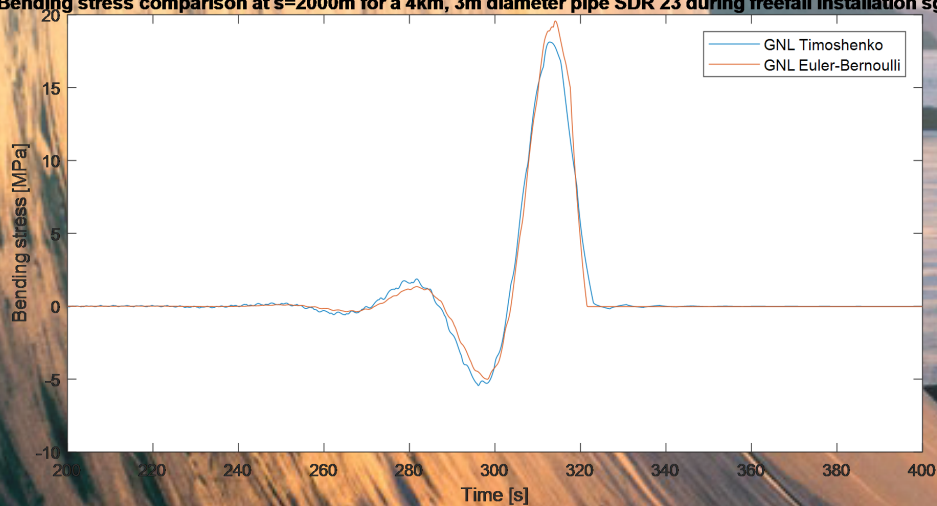


Figure 38:  
Bending stress in the pipe modelled by the GNL Euler-Bernoulli beam model and the Timoshenko beam model,  $sg=1.05$

## Intermediate conclusion

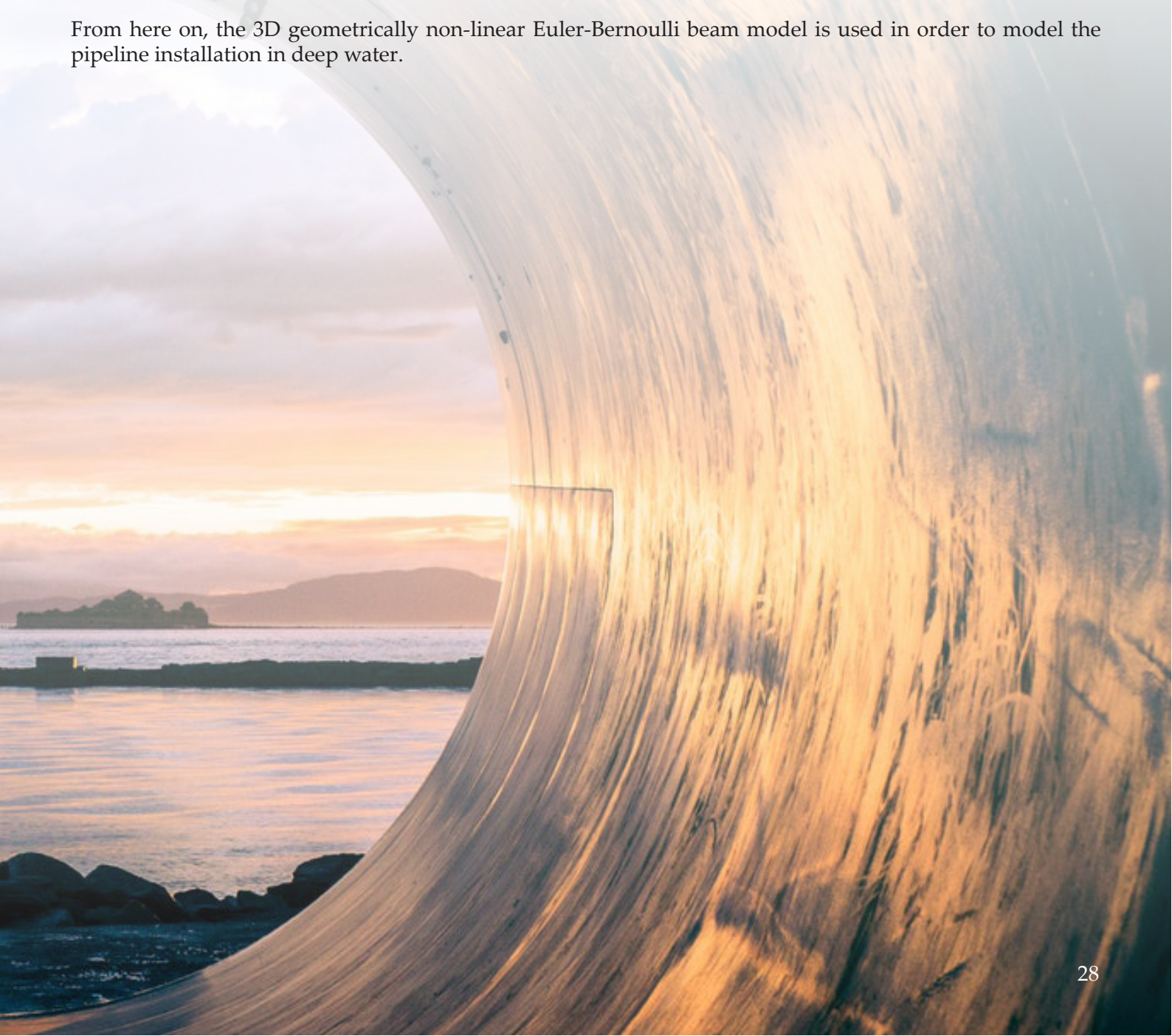
For a quick assessment whether Timoshenko beam theory is required, the following formula is often used:

$$\frac{EI}{\kappa L^2 AG} \ll 1 \quad (48)$$

Where  $\kappa$  is the Timoshenko shear coefficient and  $G$  is the shear modulus. When the entire length of the pipeline is used, this formula would be way smaller than one. However, Figure 35 shows that the bending occurs over a length that is significantly less than the entire pipeline length. Using the length of the pipe subjected to bending results in a value that is in the order of magnitude of  $10^{-4}$ .

From the comparison between the models, it is concluded that both beam models capture the general bending behaviour of the pipe. For an increasing curvature, the model results start diverging. This is a result of the shear deformation in the beam. This divergence occurs at relatively large curvatures that result in excessive bending stresses. For a specific gravity of 1.05 and 1.1, the bending radii are 170m and 144m respectively. For these bending radii, the pipe material would risk failure due to high bending stresses or buckling. Therefore, this region of deformation is of less interest for this study as the goal is to install the pipeline without failure. At lower bending radii, the models are similar and the stresses computed in the Euler-Bernoulli model are slightly higher, which means it is conservative. In all cases, the magnitude of the shear stress is negligible compared to the bending stresses. Also, the diameter which is used for the model comparison is already 3m, which is a significant diameter. In the projects for which a large diameter HDPE pipe installation in deep water is required, the diameter of interest is around 1.6m diameter, at the time that this thesis is published. Furthermore, the geometrically non-linear Euler-Bernoulli model is more straightforward to extend to 3D.

From here on, the 3D geometrically non-linear Euler-Bernoulli beam model is used in order to model the pipeline installation in deep water.



# 5 Validation geometrically non-linear Euler-Bernoulli model

Appendix B discusses the verification of the model. In order to validate the model, the geometrically non-linear Euler-Bernoulli model is compared to the scale model tests that were performed by Blue-  
rise and Delft University of Technology in January 2017.

## 5.1 Scale model tests

Both the hold and sink method and the freefall installation method were tested in the Marine Research Institute Netherlands (MARIN) basin (Van Nauta Lemke et al., 2017). The test setup is shown in Figure 39. The maximum depth to the modeled seabed is 2m with a horizontal length of 6m, leading to a 1/3 slope. The seabed was modeled with an aluminium truss with attached foam rubber mats. Five stepper motors combined with potentiometers and load cells are attached to the aluminium truss which can be seen in Figure 40. The potentiometers measure the velocity and displacement of the pipe and the load cell measured the force acting on the pipe. Furthermore, a tension is applied at the end of the pipe by a pulley which is located 12 meters from the end of the pipe. Furthermore, cameras are placed underwater and led lights are used to make the pipe visible.

The pipe was modelled by a silicon pipe. The specifications are given in Table 2. The E-modulus of the pipe was not specified by the manufacturer and was estimated from tests where the pipe was stretched with a certain force and the elongation was measured.

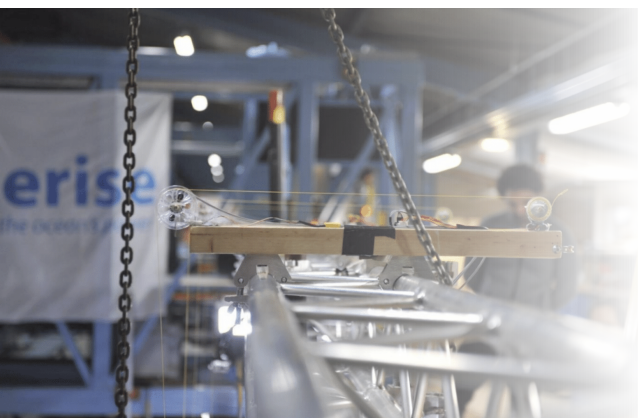


Table 2: Scale model pipe specifications

Material	VMQ Silicon
Length	5.35m
Inner diameter	25mm
Wall thickness	5mm
Density	1250kg/m <sup>3</sup>
E-modulus	3MPa

Figure 40: Stepper motors combined with potentiometers and load cells along the horizontal truss



Figure 39: Scale model test setup

## 5.2 Constant tension tests

The most straightforward tests that can be used to validate the model is the constant tension test. During these tests, the motor in Figure 40 was detached and a mass was attached to the rope in order to apply a constant vertical external force to certain points along the pipe. Additionally, a tension at the end of the pipe was varied. Figure 41 shows the test setup, where the points where vertical loading is applied are indicated with red dots and their corresponding numbers.

Table 3 shows the tests that are used for the comparison. There are measurements available for the five points in Figure 41. For the constant tension tests, the velocity and displacement of the rope that was connected to the pipe are the most interesting parameters. Interpreting solely the data would only lead to validation of the falling velocities and not the behaviour of the entire pipe. Due to the few measurement points that are available, which is less straightforward to interpret, it is more favorable to validate the model with video footage. The camera measurements were performed with a GoPro Hero 5 Black edition, in a resolution of 2704x1524 pixels.

In order to use the video footage, it needs to be corrected and processed. First of all, the camera was hung at a location on the water surface in order to maintain WIFI connection. Therefore, the camera has a relative displacement with respect to the scale model test. Furthermore, the lens distortion due to the submergence is removed by using Adobe After Effects, where a scaled plot of the seabed and pipe similar to the scale model test is used to calibrate the video material. As a first correction, the video material is corrected for its rotation when the camera was attached. This was corrected according to the horizontal details in the background wall, where an example of raw footage that was not yet corrected is shown in Figure 42. In order to remove the lens distortion, the curvature, vertical decentralization and horizontal decentralization were corrected in the lens distortion function in Adobe After Effects.

Test name	T.7.50.100	T.2.50.50	T.7.100.100
Loading points	2,4	1,3,5	2,4
Mass per point	50g	50g	100g
Cable tension	100g	50g	100g

Table 3:  
Scale model tests

Figure 41: Test setup and hanging points during scale model testing



### 5.3 Uncertainties VMQ silicon pipe

In the first case, when comparing the GNL EB model to the scale model tests, the numerical model seems to over-estimate the falling velocities. Similar results were found by Van Nauta Lemke (2017). To correct this, he increased the drag coefficient from 1.2 to 2.8. The reasoning behind this is that a smaller diameter reduces the Reynolds number which results in a higher drag coefficient. One of the reasons for the higher falling velocity in the scale model test that he mentioned was that the density and/or mass of the silicon pipe was not correct. Another reason could be that the dimensions of the pipe were deviating from what was stated by the supplier. Unfortunately, there was no pipe section from the model tests available for the author of this thesis to confirm this. Measuring the mass and the volume of a pipe section would clarify this. However, the GNL EB model allows to look at the problem from a static point of view. When a density of  $1250\text{kg/m}^3$  is applied in the numerical model, the pipe sinks to the seabed over its entire length. This was the case for a variety of tests that were considered. When analysing the video footage for the same tests, the pipe was floating for a large part when it was in static equilibrium. An example is shown in Figure 42 for a constant tension test. For this reason, the static equilibrium of scale model tests was matched with the numerical model in order to have a better estimation of the submerged weight. Note that the density of the VMQ silicon pipe is close to that of water, which means that small deviations of the density lead to a relatively large impact on the submerged weight. The CES EduPack database by GRANTA (2017) contains a variety of densities of VMQ silicon ranging from  $1020\text{-}1220\text{kg/m}^3$ , from which it can be concluded that the data that was provided by the supplier might not be spot on accurate. The density of the pipe in the numerical model that calibrated best with the static equilibrium of the scale model tests was  $1144\text{kg/m}^3$ , which leads to an 8% relative error to the density that was specified by the supplier of the pipe.

### 5.4 Model validation results

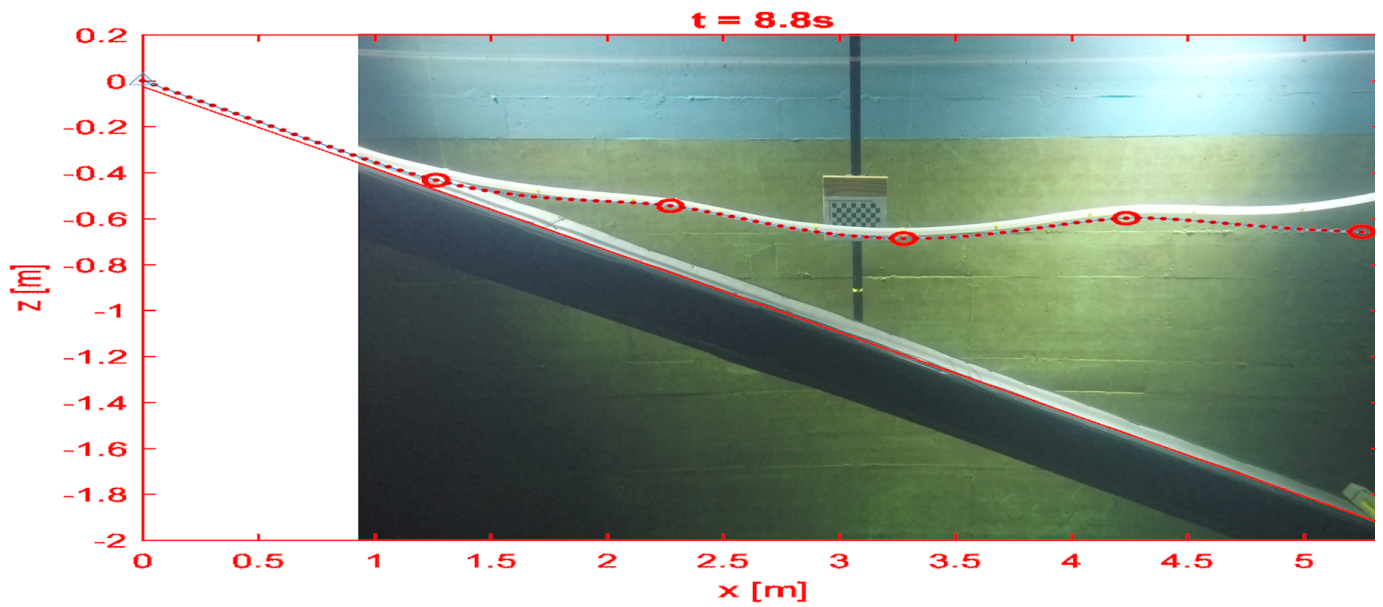
For the numerical model validation, the model was set up with the same values as the scale model tests. Only the density differs and is chosen equal to  $1144\text{kg/m}^3$ . The comparison between the video footage and the numerical model test is shown in Figure 43, Figure 44 and Figure 45. More comparison figures are shown in Appendix I.

### 5.5 Discussion

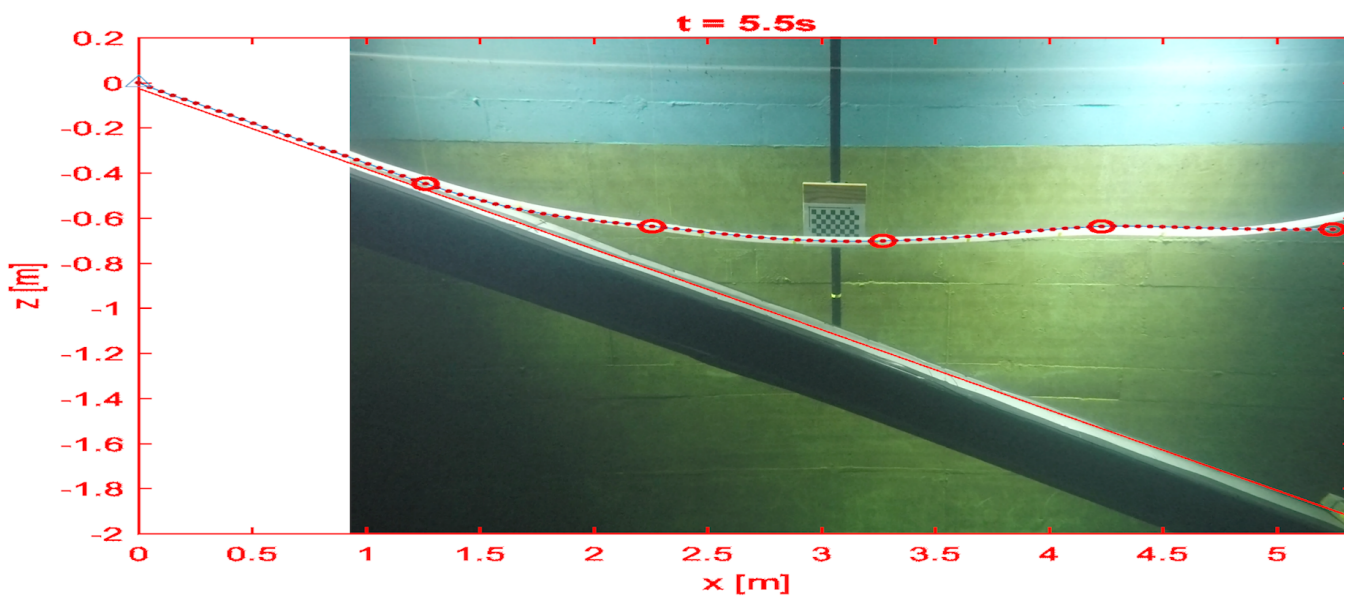
In order to conclude whether the model can provide a correct estimation of the pipe behaviour in reality, there are several things that have to be discussed. First of all, the density that is used to validate the model was different from what was specified by the pipe supplier. The density was chosen according to the static equilibrium of the model, and after implementing this density the falling velocities were very similar to what was observed during the scale model tests. A drag coefficient of 1.3 was used, which is a value that is empirically estimated according to the falling velocity during the model tests. This value is estimated as the pipe roughness is not measured and there were stickers placed along the pipe which could influence the drag coefficient. Furthermore, there were horizontal vibrations observed in the pipe during the scale model tests. According to Van Nauta Lemke (2017), the horizontal vibration frequencies are in the order of magnitude of the vortex shedding frequency,  $0.86\text{-}1.75\text{Hz}$ , calculated with equation (19). Thus, a drag coefficient of 1.3 seems reasonable, taking into account the extra friction caused by the stickers, ropes and potentially VIV related phenomena.

▼ Figure 42: End situation T.7.100.100

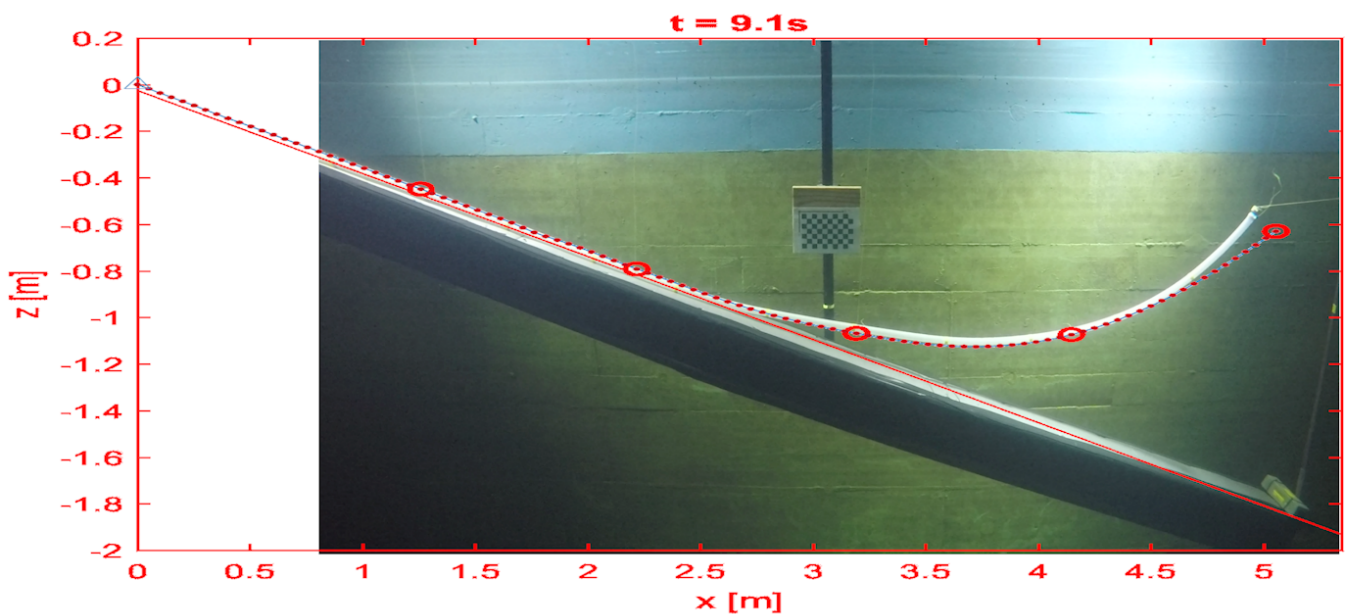




▲ Figure 43: Numerical model compared to scale model test T.7.50.100



▲ Figure 44: Numerical model compared to scale model test T.2.50.100



▲ Figure 45: Numerical model compared to scale model test T.2.50.50

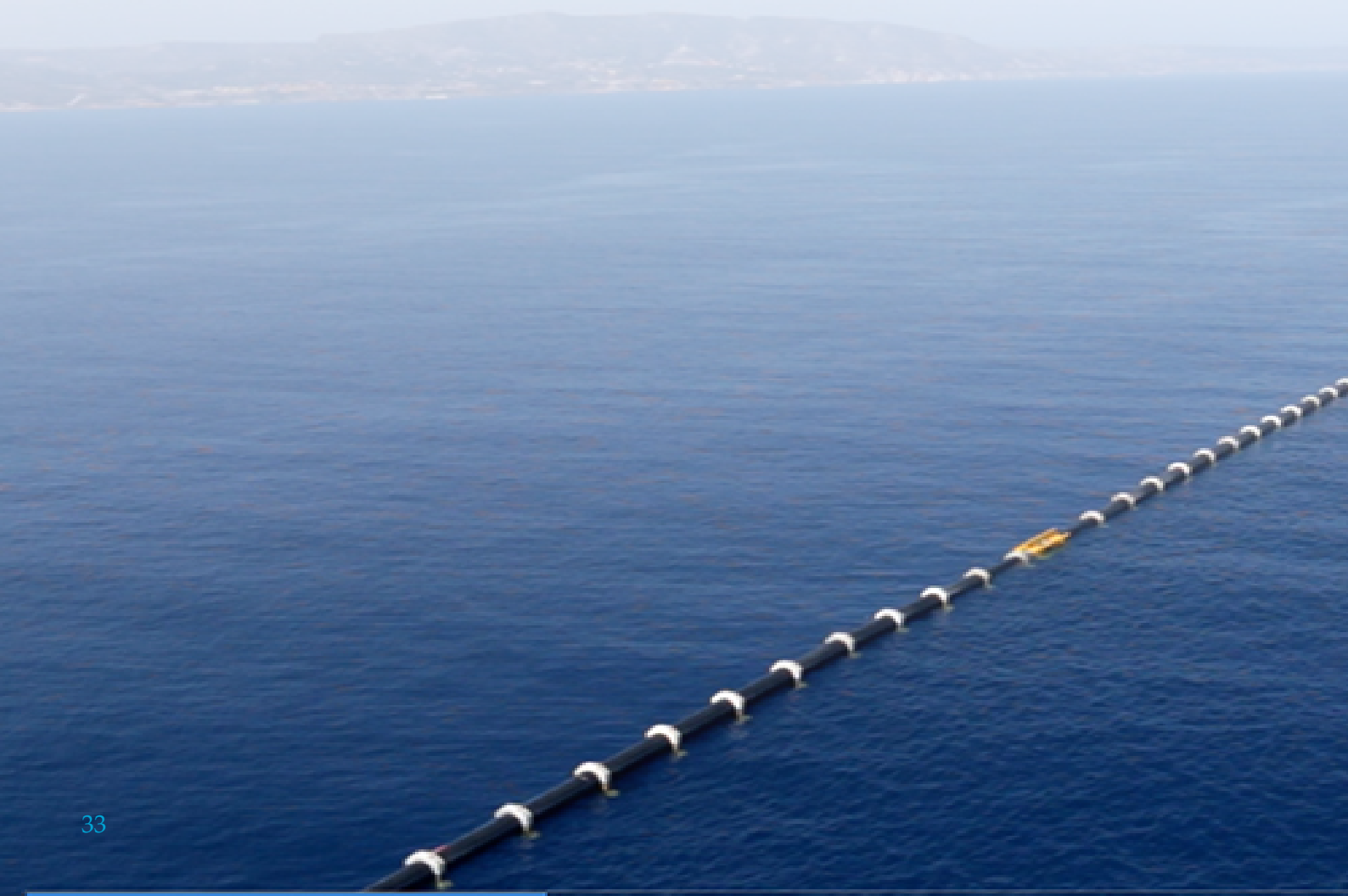
Another question that must be answered in order use the numerical on a larger scale is whether the scale model test performed at MARIN are representative for the full scale situation with a kilometers long pipe. The scaling that was used for the pipe properties in the scale model tests was based on the available dimensions of the concept basin. To keep the model test costs to a minimum, and being able to capture the installation on camera, the length of the silicon pipe was chosen as 5.35m. Additionally, the pipe properties were not scaled correctly as the preparation time for the experiments was limited. One of the main factors for choosing VMQ silicon is that the E-modulus is low and it has a density slightly higher than that of water. Due to the short preparation time span, these properties were not scaled to HDPE.

It is of less importance to scale back the properties to full scale because the material properties should have been scaled on beforehand to capture full scale effects of HDPE. On full scale, Reynolds scaling is taken into account when the numerical model is used with an appropriate drag coefficient which is dependent on  $Re$ .

There was some sort of pre-bending in the pipe, which was a result of the pipe being rolled up when it was supplied. One tried to get rid of this pre-deformation but unfortunately there was still a significant bending in the pipe, especially in the end of the pipe. This results in differences between the numerical model and the model scale tests that were performed. Especially the behaviour of the end of the pipe results in different behaviour, as can be seen in the figures above.

Furthermore, the initial conditions of the model scale test were slightly different from the initial conditions that were used in the numerical model. In the numerical model, the pipe was completely horizontal at the water surface, where in the model scale test the pipe was held at the surface at points 1-5 in Figure 42. As a result, the part between the hinge and point 1 was already slightly submerged and bent downwards before the pipe was released at points 1 till 5. Therefore, the beginning of the installation during the numerical model and scale model tests was slightly different until the influence of the initial conditions was damped out by the hydrodynamic drag forces.

Another discussion point is that the E-modulus of the VMQ silicon pipe was measured. One can argue that the pipe is visco-elastic and it is questionable until what extent this E-modulus is representative for the time scale in the scale model tests.



Lastly, the camera measurements were used to validate the model. There were measurements available but these measurements contained errors due to potentiometers that contained gaps in the measurements. During the freefall tests, there is nothing more that was measured at points 1 till 5 but the velocity and displacement, which was also captured by the cameras. The cameras and sensors show overall similar results. Although, lens distortion had to be removed in order to interpret the camera measurements. This could lead to minor errors, especially on the edge of the video footage. Fortunately, the pipe was tracked by markers and the distortion, especially in the middle of the footage, was limited. By means of adding a layer of the numerical model, without any distortion, and keeping track of the points where the forces are applied in full scale and numerical model, one can conclude that the distortion is nearly gone and one can safely interpret the camera measurements.

## 5.6 Conclusion

The main goal of the comparison between the numerical model and the scale model tests was to see whether the model is able to capture bending effects which are geometrically non-linear. The static equilibrium of the pipe and the falling velocity give a valid basis to assume that the density that was used in the test report is different from the actual density of the VMQ silicon pipe. However this cannot be confirmed by measuring the density as the piece of pipe is not available anymore.

When using a density that is estimated according to numerical model results, the falling velocities in the numerical model and the scale model are very similar. Especially when the behaviour that is a result of the initial conditions is damped out, the scale model and the numerical model show similar results. The dynamics and the bending effects are captured appropriately in the numerical model under different types of different loading. The static equilibrium at the end of the installation is also matching, except for the end of the pipe due to the pre-deformation in the VMQ silicon pipe. Overall, the numerical model captures the dynamic effects with satisfying accuracy.

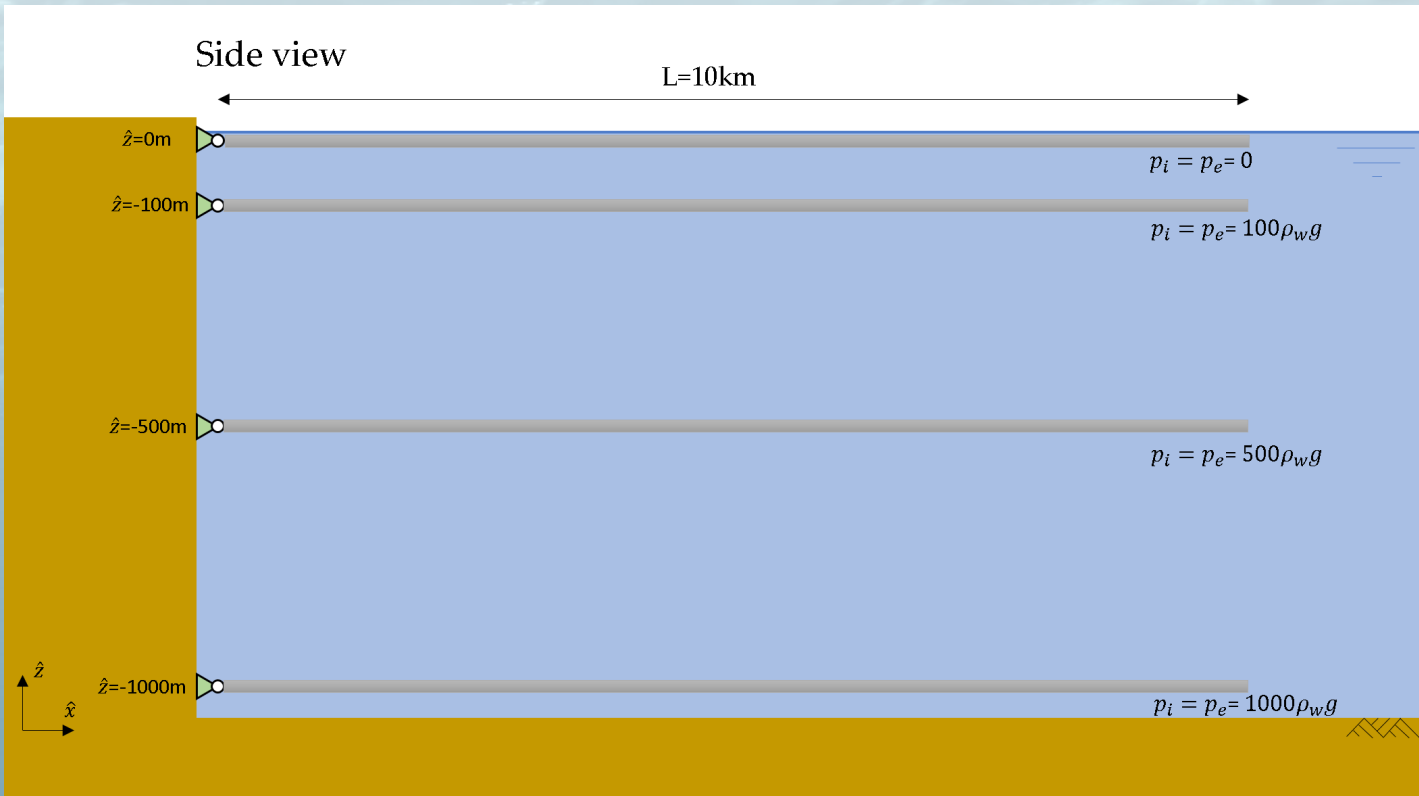


# 6 Influence hydrostatic pressure on large diameter HDPE pipes in deep water

The loading due to hydrostatic pressure on curved surfaces was introduced in section 2.4.4. The first two equations terms of equation (18) are dependent on the density of the inside and outside fluid and are related to the buoyancy of the pipe. The third term is related to the curvature of the pipe and the absolute pressure in and outside of the pipe. For ocean thermal energy applications, the pipe has to reach a certain depth where the water is cold enough. It is important to grasp the order of magnitude of the influence of the hydrostatic pressure on the bending behaviour of the pipe. In order to do this, a situation is modelled where only the third term of equation (18) remains, such that the first two terms cancel each other out. The situation that was modelled is shown in Figure 46 and Figure 47, where four pipes with a length of 10km are submerged and hinged to a wall. All four pipes are at a different depth, meaning all pipes are subject to a different internal and external pressure. All pipes are large pipes with a 3m outer diameter with SDR23. The specific gravity of the pipe is one, which means that there is zero loading in the vertical direction, because the sum of the first two terms of (18) and the weight in air is zero. All initial conditions of the pipe are such that the pipe is at rest, meaning that the end cap effects are taken into account in the initial conditions, and the pipe is already shortened at larger depths. Now, a 10kN force is applied in the positive y-direction for 10 seconds. The force is applied on the middle of the pipe such that the behaviour of the pipe is far away from boundary effects.

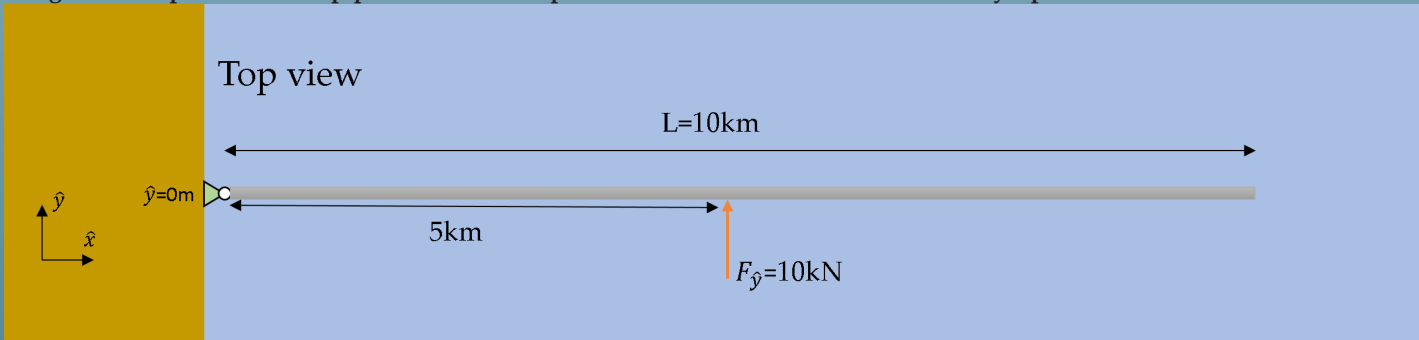
Firstly, the horizontal displacement after ten seconds is shown in Figure 48. Here, one can already see that the third term of equation (18) is important to take into account. Neglecting this term would lead to a result which is equal to the blue line for all four pipes at different water depths.

Note that the solutions look pointy, which is a result of a different x and y axis. To see what the influence is on the bending stresses, the bending stress in the middle of the pipe is shown in Figure 49. In larger water depths, the pipe will bend less. This is a result of the higher stiffness at higher pressures. The bending radii in this example are in the range that the pipe will bend during the installation procedure, which means that the depth at which the pipe will be subjected to loading will influence the dynamic response of the pipe significantly. The exact values of the plots are of less influence as during installation there are a variety of loading scenarios, and by taking into account the third term in equation (18), the pressure effects are captured.



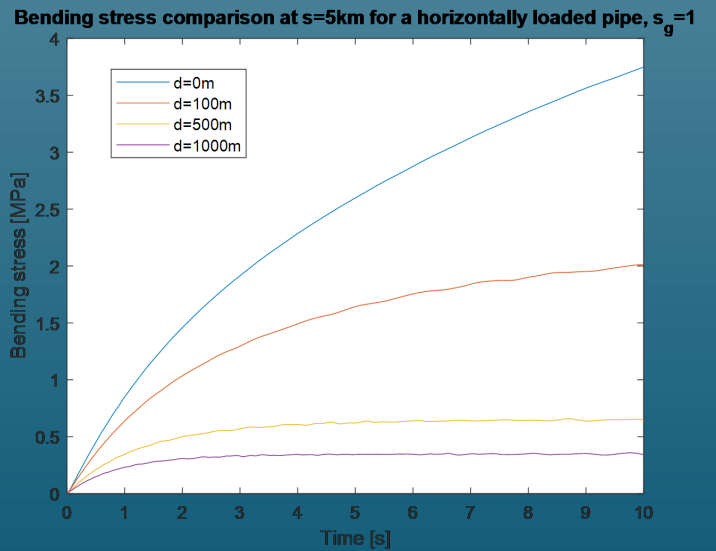
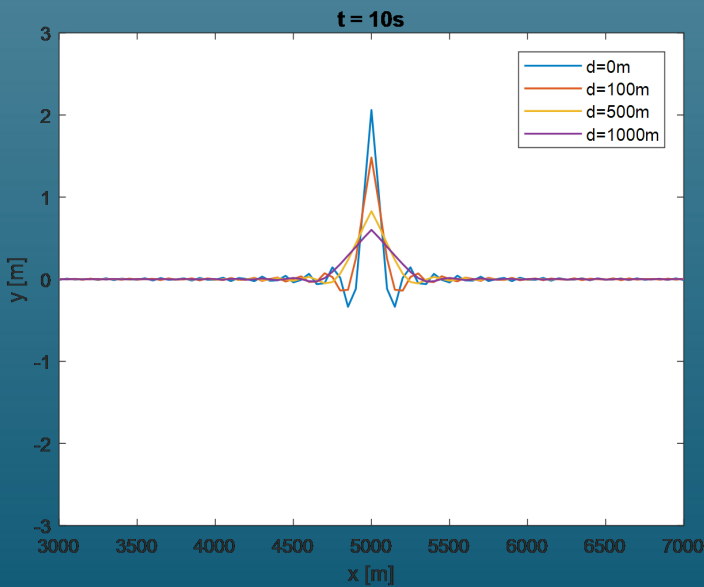
▲ Figure 46: Front view of four pipes at different depths loaded in the horizontal direction by a point load

▼ Figure 47: Top view of four pipes at different depths loaded in the horizontal direction by a point load



▼ Figure 48: Displacement of the pipes after 10 seconds of loading

▼ Figure 49: Bending stresses for pipes at different water depths loaded by a point load of 10kN



# 7 Case study Curaçao

In this chapter, the pipe installation for a 1.6m outer diameter pipe is assessed for a project in Curaçao. Firstly, a few assumptions are discussed. Next, the environmental conditions are presented. In section 7.3, the required ballast is analysed, after which the installation is analysed with the GNL Euler-Bernoulli model. In section 7.7, the influence of the current on the pipe installation is assessed. Sections 7.8 and 7.9 touch upon the residual lay tension and local buckling.

## 7.1 Assumptions

The model serves as a tool to assess different installation methods. In this stage of the design cycle there are several assumptions that have to be made. The assumptions that are used in the model runs are summarized below.

Firstly, there are several things that are neglected which should be noted:

- Local stress effects; due to pulling force, concrete blocks, and local forces
- Shear deformation; see chapter 4
- Torsion; concrete blocks can be designed such that torsion is limited
- Material damping; see appendix C
- Wind loading; low wind speeds expected during installation and small compared to current drag
- Vortex induced vibrations
- Time and temperature effects on material properties during installation
- Frozen in stresses due to production of pipeline
- Reduction of material strength due to welding
- Poisson effect
- Lift force; neglected during modelling
- Density gradient over water depth
- Sliding, settlement and erosion effects on the seabed; pipe is assumed to stay in position once it is on the seabed

Furthermore, the concrete blocks will have an influence on the drag force on the pipe. Therefore, the drag coefficient is estimated to be 1.0 (Janson, 2003), where the pipe itself would have a drag coefficient of approximately 0.7. In the model, the inertia effects of the concrete blocks along the pipe are taken into account by spreading the mass of the concrete blocks out over the pipe. This means that the mass in the mass matrix will be higher than the mass of solely the pipe including the water inside. The buoyancy force and gravity force of the concrete blocks are added as distributed loads. Extra parts along the pipe such as a diffuser at the end of the pipe are not taken into account.

It was stated before that both time and temperature have a significant influence on the material properties. As discussed in section 2.3, the temperature of the pipe during installation can vary significantly. It is assumed that the pipe temperature, when floating in the water, will not be higher than 35°C. This temperature is used to determine the design stress of 8MPa, for a loading time of 10 hours. The total design stress for HDPE pipes over the complete lifespan is 6.3MPa.

The cable that is attached to the pipe is connected to a vessel. It is assumed that the cable is made of Dyneema. The vessel is modelled as a moving boundary on the surface. The connection between the pipe, vessel and cable are not modelled in detail and are elements with different properties connected by a hinge.

$L_p$	7.2	km
$C_d$	1.0	-
$\rho_w$	1026.6	kg/m <sup>3</sup>
$\rho_p$	955	kg/m <sup>3</sup>
$SDR$	21	-
$D_o$	1.6	m
$E$	915	MPa
$C_a$	1.0	-
$C_d$	1.0	-

Table 4: Case study assumptions

## 7.2 Environmental conditions

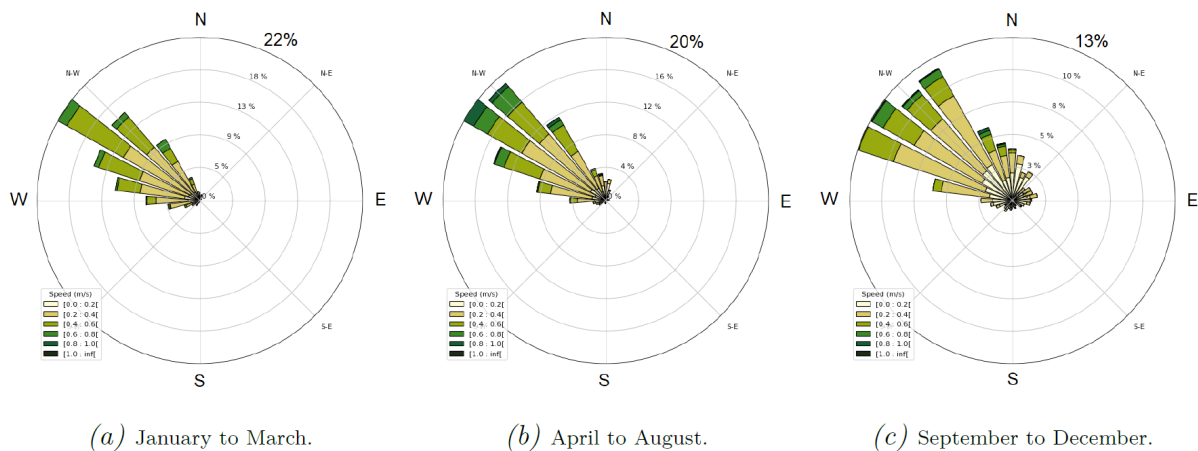
### 7.2.1 Seabed

The seabed slope is estimated from data by Bluerise. A crude estimate is made where the seabed slope is assumed to be linear between the elevation lines with an accuracy of 100m depth difference. The seabed slope is in the range of 1/3.7 to 1/10.6, depending on the distance from shore. Figures of the seabed that were used can be found in the figures in the end of this section and are not given here for the sake of brevity.

### 7.2.2 Surface currents

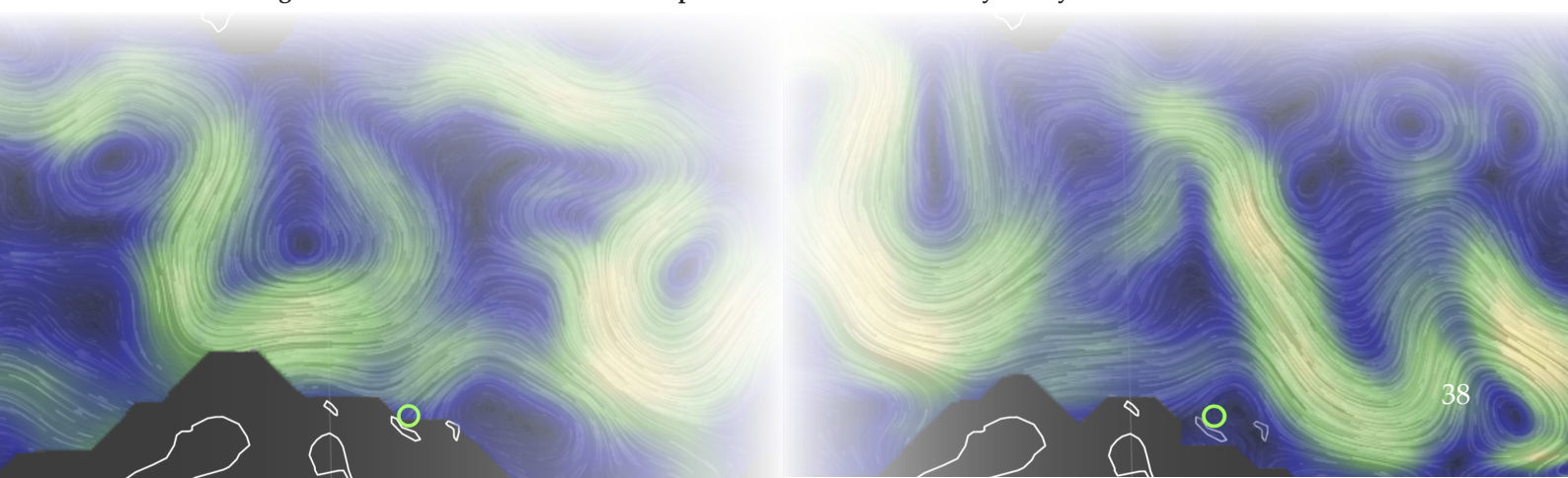
The surface current is caused by the wind along the Northern coast of Curaçao, where the air-port that would be cooled by SWAC is located. The dominant wind direction is towards the North-West. The current velocity is estimated from the Mercator Ocean Model based on data from 2007 to 2016. The rose plot for the surface current is shown in Figure 50. This figure shows that the current velocities are relatively low in the period September till December. A surface current during an installation weather window is therefore assumed to have a maximum of 0.4m/s and is directed towards the North-West. Wind forcing is one of the main drivers of the surface currents. From correlations found by De Jong (2017), this surface current would imply a wind velocity between 2.5-10m/s.

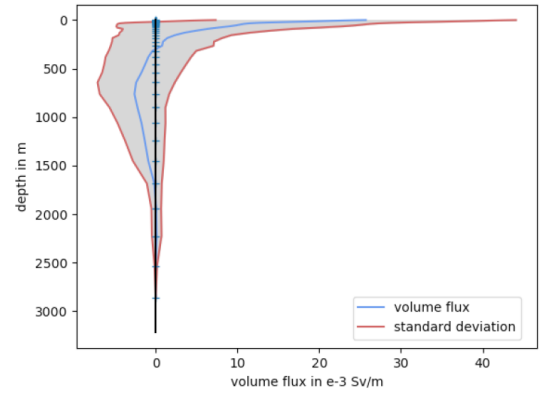
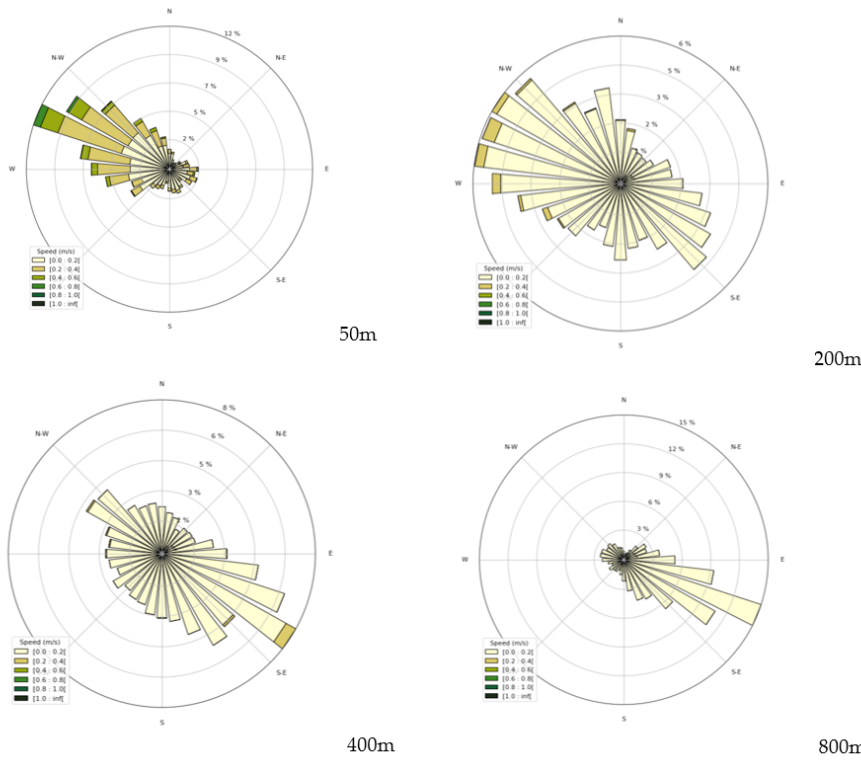
Data from Ocean Surface Current Analysis Real-time (OSCAR) is used to obtain a broader view of the surface currents around Curaçao. Data is obtained from various satellites and in situ measurements. The data has a 1/3 degree grid with a 5 day resolution. Figure 51 shows the surface current patterns around Curaçao for two random days. This figure shows that the variability in currents in Figure 50 is a result of eddies that are present North of the island, that are changing continuously over time. However, the direction is dominantly to the West due to the direction of the conveyor belt. This shallow current is something to bear in mind for both the permanent and installation conditions of the pipeline. Surface currents can be as low as 0.05m/s and get as high as 0.75m/s, which coincides with the data provided by the Mercator Ocean Model.



▲ Figure 50: Rose plot of surface current velocity North-East of Curaçao (de Jong, 2017)

▼ Figure 51: Surface current variability around Curaçao (Physical Oceanography Distributed Active Archive Center, 2018)  
The left and right hand side are the surface current patterns for two different days in a year





▲ Figure 53: Volume flux North-East of Curaçao averaged over 2007 to 2016 (de Jong, 2017)

◀ Figure 52: Subsurface current rose plots North-East of Curaçao for different depths (de Jong, 2017)

### 7.2.3 Subsurface currents

Besides the surface currents, there are subsurface currents present in deeper water. These are mainly driven by density differences in seawater bodies due to temperature and salinity gradients. Along the North-Eastern coast of Curaçao, these subsurface currents have a variable direction over depth. The deeper, the lower the current velocity. Rose plots for the subsurface currents at different depths are shown in Figure 52. From these figures it can be seen that the direction is unpredictable. This data is not detailed along the coast of Curaçao. This is the most detailed data available for the subsurface currents in this stage of design and is thus chosen as an estimate for the deep water currents. Figure 53 shows data that is averaged data over a time span of 9 years for the volume flux along the depth. In this figure, negative values are directed to the East and positive values to the West. This means that, looking at the blue averaged line, the currents are generally directed towards the West and are towards the East in deeper water. The profile in Figure 53 in combination with the magnitudes in Figure 52 can be used to determine a reasonable current profile during installation conditions.

### 7.2.4 Waves

Wave climate data by Van Oord shows that the September till November are the best months for the pipe installation. During these months, the significant wave height stays below or equal to 0.75m 15-20% of the time. A typical wave period for these sea states is 5s, where waves are coming from the North-East. Linear wave theory is used to obtain the maximum horizontal water particle velocity due to a wave in such a sea state, see Figure 54. From this figure, it can be seen that the influence of waves decreases with increasing water depth. Assuming a current profile based on Figure 52, hydrodynamic forces on the pipe due to waves can be neglected compared to those due to currents once the pipe is submerged below approximately 30m. Solving the differential equations for a random wave field slows down the model significantly and because the focus in this thesis is mostly on the behaviour of the pipe in deep water, wave loading is neglected.

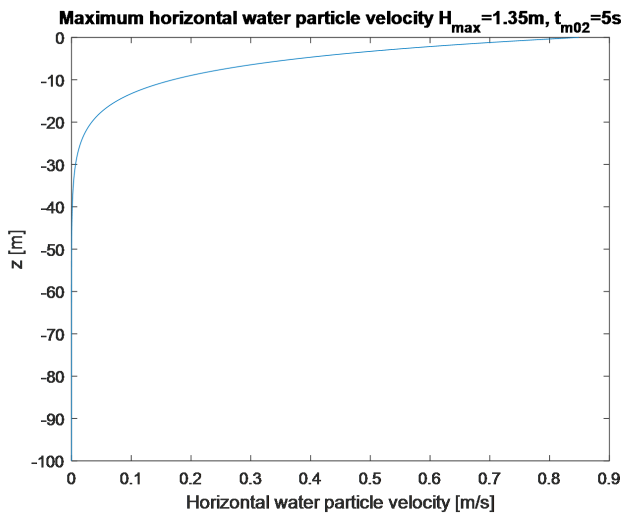
### 7.2.5 Wind

The wind direction is generally towards the West. The wind conditions are mildest in October, similarly to the wave conditions. According to data by Van Oord, the wind stays below 2.5-5m/s for 10-15% of the time. This wind will cause drag loading on the pipe and vessel(s). However, it is expected that the drag force on the pipe is negligible compared to the drag due to the current. As soon as the pipe is submerged, the wind will only influence the vessel, which is not modelled in a lot of detail in this thesis.

## 7.2.6 Extreme events

Wave climate data by Van Oord shows that the largest annual significant wave height that can be expected is 3m. However, this might not include extreme events such as hurricanes, as they might not be recorded in this data.

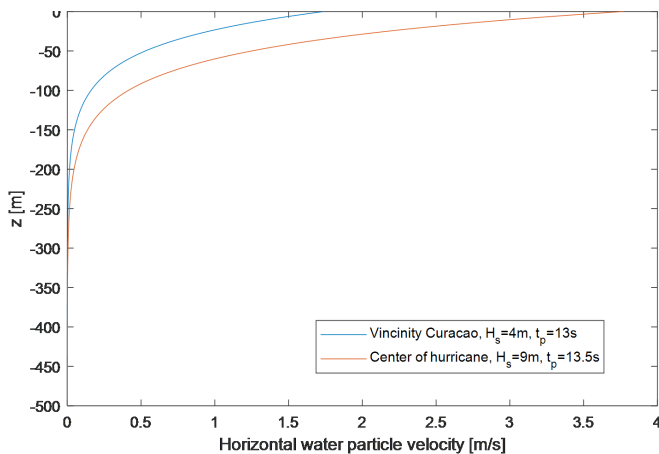
Curaçao is in the vicinity of the Atlantic hurricane belt, which makes a hurricane in Curaçao very rare, but possible. Generally, a hurricane hits Curaçao once every 100 years. Nonetheless, the environmental conditions on the island are affected by tropical storms and cyclones several times a year. To grasp a feel of the magnitude of the waves during these extreme events, hurricane Matthew is used as a reference, which is the last hurricane that took an unusual path and destroyed beaches at Curaçao. Note that detailed engineering for extreme events such as hurricanes are beyond the scope of this research. Figure 55 shows a picture of hurricane Matthew passing Curaçao.



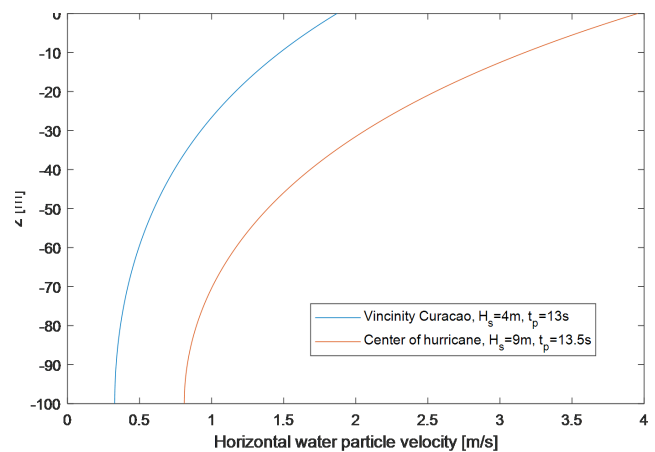
▲ Figure 54: Maximum horizontal water particle velocity over depth during mild sea state in Curaçao

According to hind cast data by WAVETECH III, the significant wave height in the centre of the hurricane was 9m with a period of 13.5s. Near Curaçao, the significant height reached 4m due to the hurricane passing by, with a period  $T_{m02}$  equal to 13 seconds. The horizontal maximum water particle velocity due to a waves by a hurricane event in deep and intermediate water depths are shown in Figure 56 and Figure 57 respectively.

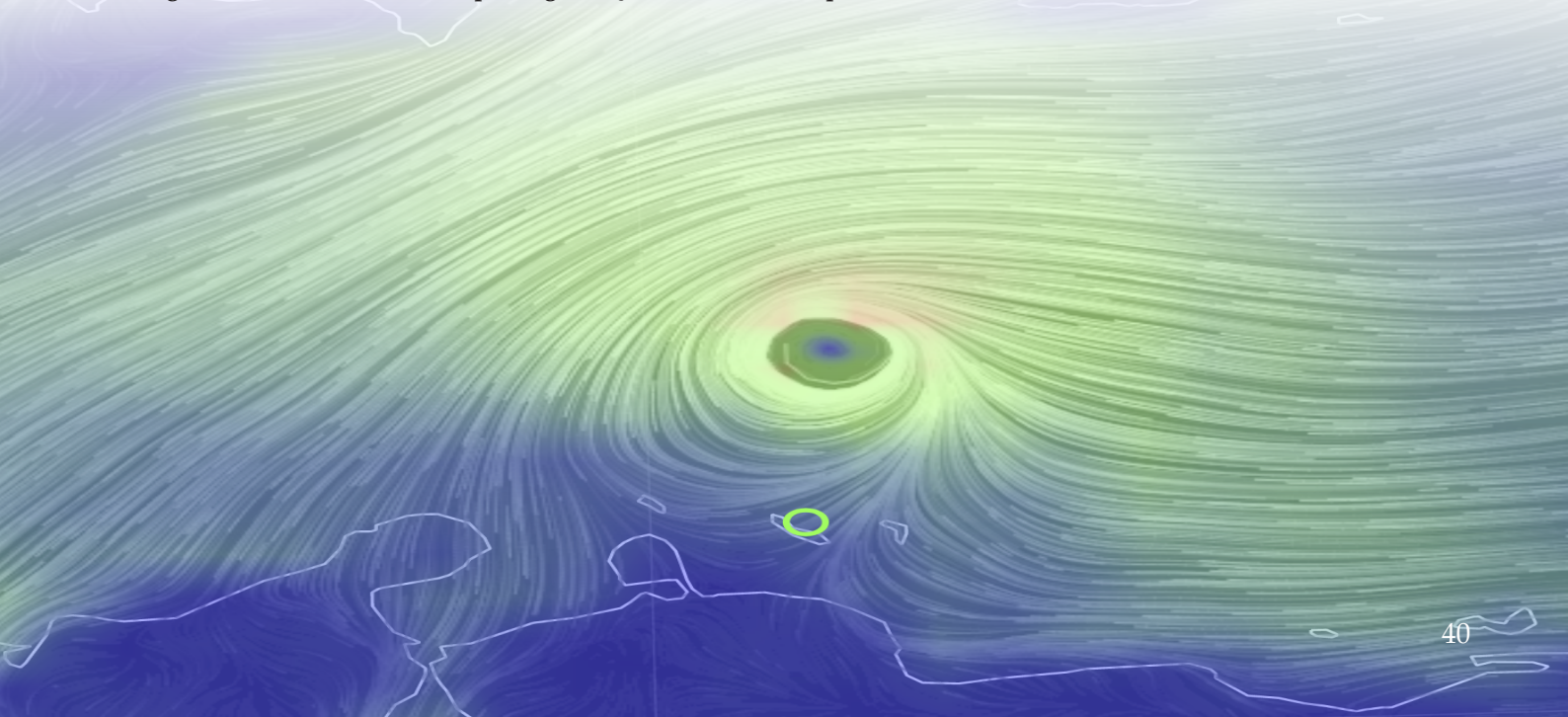
▼ Figure 56: Horizontal water particle velocity as a function of depth for deep water



▼ Figure 57: Horizontal water particle velocity as a function of depth for intermediate water depth



▼ Figure 55: Hurricane Matthew passing Curaçao on the 9th of September, 1016



### 7.3 Ballast

There are two conditions for the ballast: the installation condition and the operational condition. Ideally, the amount of ballast required for these conditions is the same, as this would reduce the need for expensive post-ballasting in deep water. An extensive ballast analysis is advised once detailed environmental data is available. Also, an extensive analysis is required for wave and current actions in the surf zone. For example, with non-linear wave theory. The current offshore industry has sufficient experience on this topic and this is assumed to cause no problems in shallower waters. For this stage of design, it is interesting to indicate the amount of ballast required in deeper waters, in which most of the pipe is located during operation.

From the previous section is clear that the influence of wave loading decreases with increasing depth during installation. However, for the operation conditions it is important that the pipe will also stay in place during extreme events such as hurricanes. From Figure 56, it is concluded that the waves will not cause significant loading on the pipe in depths larger than 200m, even during hurricanes such as hurricane Matthew. Thus, an estimation is required for depths larger than 200m. The absolute static requirement for lateral on-bottom pipelines based on the static equilibrium of forces is:

$$(W_s - F_l)\mu - \gamma_s F_h \geq 0 \quad (49)$$

Where  $\mu$  is the friction coefficient,  $W_s$  is the submerged weight,  $F_l$  is the lift force,  $F_h$  is the hydrodynamic drag force and  $\gamma_s$  is a safety factor. This safety factor is in the range of 0.93-2.54 for different locations (DNV-RP-F109). High safety factors are for cyclonic conditions. These could be used for the pipe in shallow water. It is not expected that cyclonic conditions will influence the flow in deep water significantly, and due to the flexible design philosophy of HDPE pipes, the pipes are allowed to move slightly during extreme events (Janson L.-E. , 2003). Therefore, a normal safety factor of 1.64 is used, which is a safety factor for sand and rock in cyclonic conditions in the Gulf of Mexico. This is relatively conservative as this safety factor is also used for wave conditions, and the current velocities in deep water are less volatile.

The specific gravity determines the submerged weight and is calculated by:

$$S_g = \frac{W_{ac} + W_{ap}}{W_{dc} + W_{dp}} \quad (50)$$

Where  $W_{ac}$  and  $W_{ap}$  are the weight of the pipe and the concrete weights in air, respectively.  $W_{dc}$  and  $W_{dp}$  are the displaced weight. Based on this formula, the dimensions of a concrete weight can be determined. The average area of concrete per unit length can be calculated by:

$$A_{c,av} = \frac{\rho_p A_p - S_g A_p \rho_w}{S_g \rho_w - \rho_c} \quad (51)$$

The concrete blocks can now be designed based on this average required concrete area per unit length. For the dimensioning, a rectangular block is assumed where the bottom has some extra width. The advantage of this layout is that the centre of gravity is lower than the centre of the pipe, which reduces the risk of torsion. The distance between the seabed and the pipe is assumed to be a third of the diameter.

To solve the stability check in equation (49), the seabed is assumed to be horizontal. This situation is shown in Figure 58. In this figure, the top figure shows the top view and the bottom figure shows the side view. In this figure  $l_{c,ctc}$  is the centre to centre distance between two adjacent concrete blocks,  $F_l$  is the lift force,  $W_{sp}$  is the submerged pipe weight,  $W_{sc}$  is the submerged concrete weight,  $F_h$  is the hydrodynamic force,  $F_r$  is the resistance force caused by friction between the concrete block and the seabed. The submerged concrete weight depends on the specific gravity, which determines the resistance force. The lift force is calculated by:

$$F_l = \frac{1}{2} \rho_w C_l D u^2 \quad (52)$$

Where  $u$  is the current velocity and  $C_l$  is the lift coefficient. The lift force is a result of pressures being lower on top of the pipe as the stream lines are converging. When the pipe is further away from the seabed, the lift force decreases. To be conservative, the lift force is assumed to be perpendicular to the seabed and a lift coefficient of 0.85 is used (Pipelife, 2002). In reality, the lift coefficient is expected to be lower, as the lift coefficient is 10% of the pipeline laying directly on the seabed when the gap between the pipe and the seabed is half the diameter. The hydrodynamic force in deep water only consists of the drag force due to subsurface currents. Morison equation is used with a drag coefficient of 1.0 to take into account the concrete blocks (Janson, 2003). Together with the current velocities from the previous section, equation (49) is used as a stability check. The friction coefficient  $\mu$  depends on the type of concrete block that is used, as discussed in section 2.2.2. The required specific gravity for different current velocities are shown in Table 5.

Table 5 shows that a specific gravity of 1.11 is reasonable for deeper water and a specific gravity of roughly 1.5-1.6 for shallower waters. These values are similar to the specific gravity that was used for the HDPE pipeline between Cyprus and Turkey, where the specific gravity in shallow regions is 1.3. It is expected that due to a combination of cyclonic conditions and the surface currents that are caused by the conveyor belt North of Curaçao, the specific gravity in shallow water is somewhere around 1.6 for a 1.6m diameter pipe. In reality, the pipe will be slanted as it is laying on a seabed slope. This is something to take into account for the stability requirement. Based on an estimate of a bathymetry maps, the slope is ranging from 1/4 to 1/11. Due to the varying seabed along the trace of the pipe, a conservative value for the seabed slope is used. Now, the forces acting on a pipe section between two concrete blocks is shown in Figure 59. In this figure,  $F_{HS1}$  and  $F_{HS2}$  are the first and second terms of equation (18),  $W_{ac}$  is the weight in air of the pipe section,  $W_{sc}$  is the submerged weight of the concrete and  $F_l$  is the hydrodynamic lift force. The forces can be decomposed into forces perpendicular to the seabed, such that the maximum friction force of the concrete block can be calculated. Now, a similar stability check can be performed like equation (49). Interestingly, for slopes up to  $\frac{1}{4}$ , this estimation of the required specific gravity results in similar values to those in Table 5. A reason for this is that for an increasing seabed slope, the force due to the hydrostatic pressure perpendicular to the seabed decreases per unit length of the pipe. Thus, although the perpendicular gravity force by the ballast, directed to the seabed decreases, so does the lift force due to the buoyancy of the pipeline. If the slope is increased more and more, a more noticeable higher specific gravity is required. For this calculation, it is assumed that the initial force caused by friction is zero, which in reality might not be the case because there can be forces parallel to the seabed that are caused by for example temperature effects, and residual lay tension in the pipeline. The only loading that is assumed to be applied parallel to the seabed is the hydrodynamic drag. Note that in the calculation above, the pipe was required to remain in place at all times. In reality, HDPE is allowed to move slightly as a result of extreme events as it is flexible (Janson, 2003).

Table 5:

Required specific gravity on horizontal seabed for 1.6m OD SDR21,  $\mu=0.6$

Current speed [m/s]	Specific gravity [-]
0.05	1.002
0.1	1.008
0.2	1.03
0.3	1.07
0.4	1.11
1.0	1.50
1.2	1.61

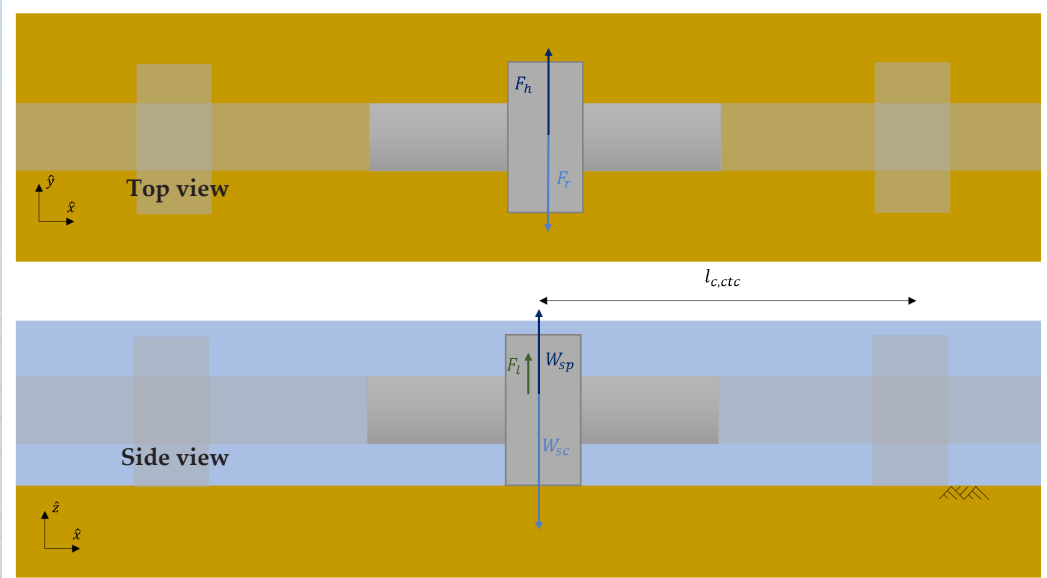


Figure 58: Pipeline on horizontal seabed

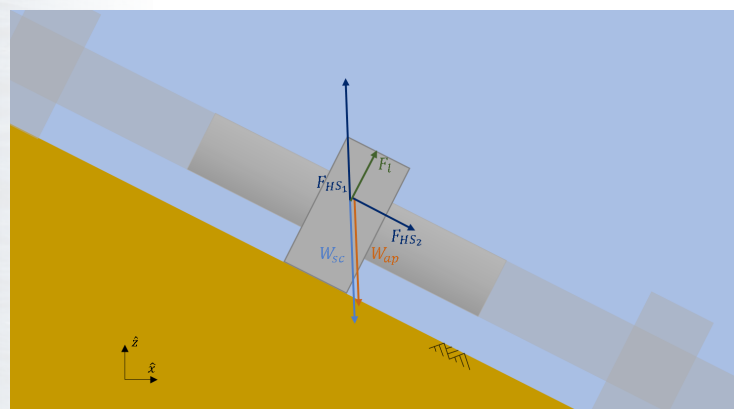


Figure 59: Pipeline section on a seabed slope

## 7.4 Pulling force and controllability

A starting point for the maximum pulling force that was used by Van Nauta Lemke (2017) and Keesmaat (2015) were the maximum pulling force that a large vessel could pull. In this thesis, the starting point for the maximum pulling force is the maximum stress that is allowed in the material. For that reason, Figure 6 is used. It is assumed that the pulling force is applied for 10 hours, and a conservative pipe temperature is chosen as 35°C. With a safety factor of 1.25 this leads to an allowable stress of 8MPa. An extra safety factor can be used to take into account dynamic effects and local stress effects. The maximum pulling force for different safety factors is plotted as a function of the pipe diameter in Figure 60.

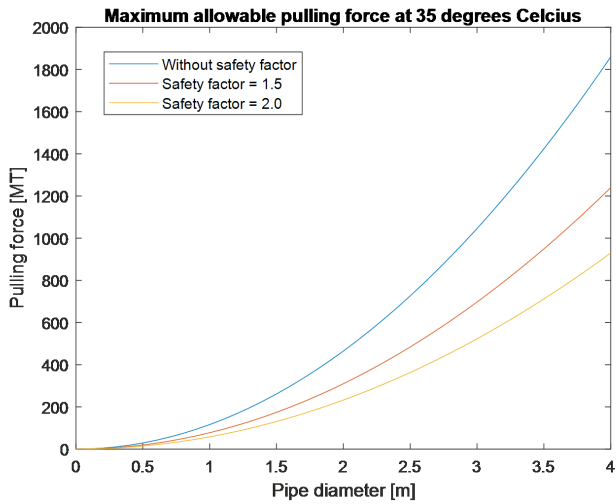


Figure 60: ▲ Pipe diameter (SDR 21) plotted against maximum pulling force

From Figure 60, an estimate of the allowable pulling force is made. This is a rough estimate because the stress in the pipe during installation will depend on many factors, such as hydrostatic pressure, currents, waves and so on. To get a feel for the controllability of the pipe, the pipeline is lowered with a constant tension at different specific gravities. The static equilibrium for a 1.6m diameter pipe subject to a 150MT pulling force is shown in Figure 61. Note that drag due to current is not taken into account yet. During all installation runs with this constant tension, the Von Mises stress stayed below the design stress of 8MPa. However, from this figure one can conclude that solely pulling with a tug that can deliver 150MT pulling force would not suffice. A reason for this is that one would want to be able to stop the installation or reverse it at some point if something goes wrong during installation. This is only possible for specific gravities lower than 1.01. This is a similar value to the value that Van Nauta Lemke (2017) used during model runs. Table 5 shows that this not desirable as the current velocities may get higher than 0.1m/s in deep water. These conditions can occur both during the installation and the permanent conditions, meaning that a certain minimum specific gravity would be needed during installation as well to keep the pipe on the seabed.

In practice, there are different stages during the installation that can be distinguished. Initially, the pipe will float on the sea surface. The pipe will be filled with water and submerged from shore while a large section of the pipeline can still be floating on the surface. In order to model this procedure, the vertical loading is increased from the nodes onshore towards nodes offshore. To estimate up until what depth this procedure is controllable, a certain pulling force resulting from Figure 60 is applied to the pipe. An equilibrium is sought for different specific gravities, where the pipe is only partially submerged. In this way, an estimate can be made up until what depth this stage of the installation process is reasonable to apply. This stage of the installation procedure is similar to the conventional installation method for large diameter HDPE pipes in shallower water, as described in section 2.2.3. However, in this calculation there is no internal air pressure applied yet, so the pipe is solely filled with water where it is submerged.

The maximum water filled 1.6m OD pipeline section, where the design stress of 8MPa is not exceeded, is shown in Figure 62. The limit for the first stage of the installation is shown for different specific gravities. The critical position for the Von Mises stress is the point along the pipe where it is bending downwards from the sea surface, on the overbend area. Note that, again, the horizontal and vertical axes are not equal in magnitude.

Figure 61: Pipeline section on a seabed slope



Static equilibrium with a pulling force equal to 150MT for a 1.6m diameter pipe SDR21

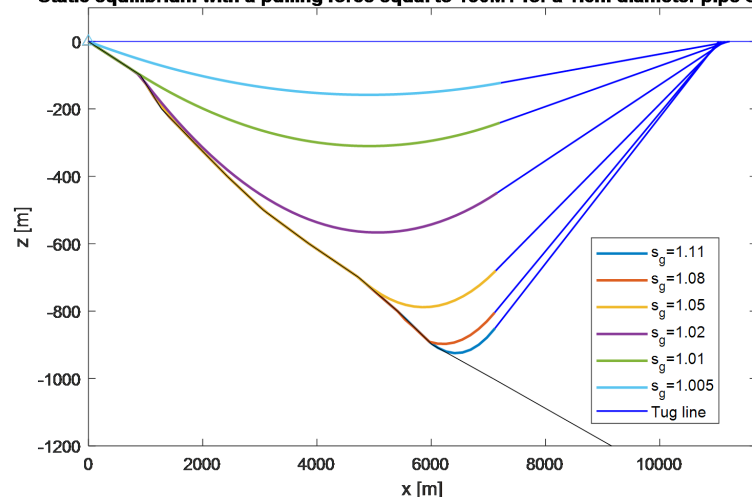
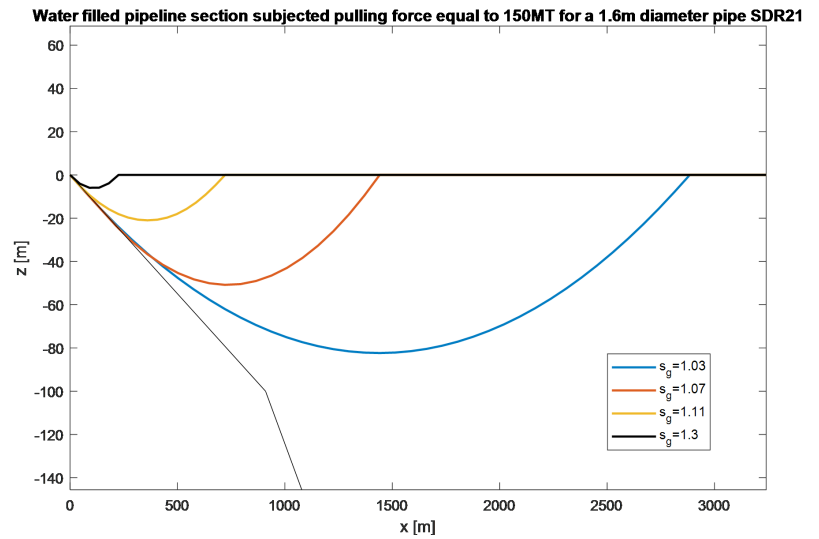


Figure 62 shows that for a lower specific gravity, the water filled section can be much longer. This results in a section that is submerged to a larger depth. A depth that can be reached by solely filling a pipe section is approximately 80m for a specific gravity that can cope with current velocities of 0.2m/s (blue line). If the ballast can withstand current velocities of 0.4m/s in deeper water, a pipe section of approximately 700m can be controlled, which is the yellow line. A more conservative specific gravity is plotted in black, which is a specific gravity that is more likely to be expected in the surf zone where there are hydrodynamic wave forces present. This figure shows that only 200m of the pipe can be submerged and filled with water while being under control without exceeding the design stress.



▲ Figure 62: Pipeline partially filled with water from shore, D=1.6m, SDR21, pulling force (150MT) pulling force

From the results presented above, one can conclude that using a single pulling tug with a tug line does not suffice to have full controllability during installation if ballast is taken into account and the pipe is filled with water. However, there is a certain amount of ballast that must be present during installation. This results in several options. The first option is to limit the ballast during installation and applying post-ballast. This is expensive in deep water and not necessarily preferred. Another option is to adjust the installation procedure by adding more tugs or buoyancy modules. This choice depends on several factors. The last option is to apply the conventional installation method, where air pressure is applied by a compressor as described in section 2.2.3 such that a part of the submerged pipe is filled with air. This last option is by far the cheapest option, however this method is challenging in large water depths.

### 7.5 Conventional installation method

In this subsection, the first stage of the installation is modelled, where the onshore pipe end is filled with water and air pressure is applied at the offshore end of the pipeline. In order to determine the amount of pressure required to obtain control over sinking of the pipe, the air fill rate is used. The air fill rate was introduced in equations (2) and (3). To see up to what depth the water should be pushed down according to this theory, the relationship between the specific gravity and air fill rate is shown in Figure 63. Thus, according to theory, the water has to be pushed down by the air-pressure for only 3% of the water depth to keep a pipe with a specific gravity of 1.11 from sinking.

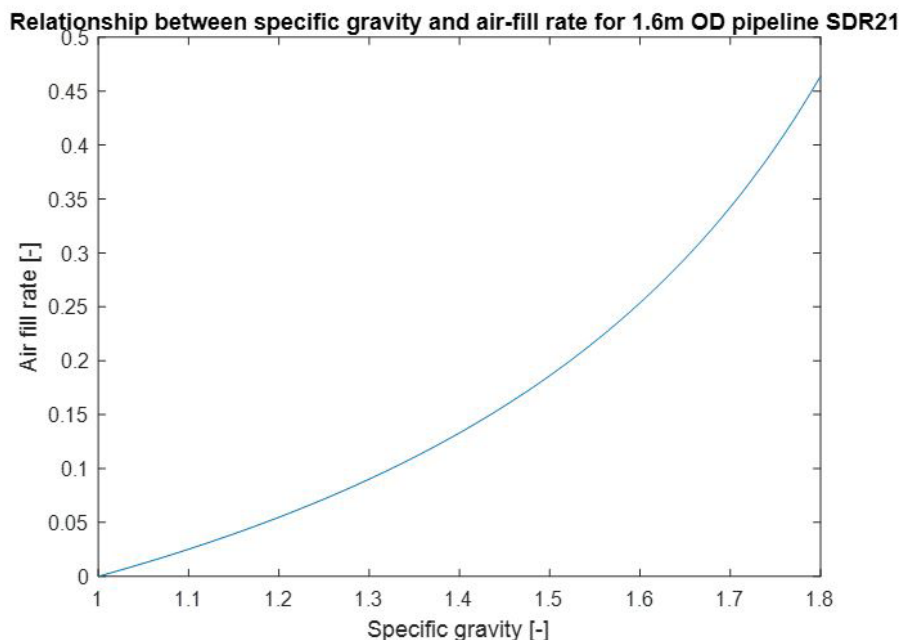


Figure 63: Air fill rate plotted against specific gravity

Submerging procedure conventional float and sink method, air fill rate=3%,  $s_g=1.11$ ,  $D_o=1.6\text{m}$ ,  $\text{SDR}=21$

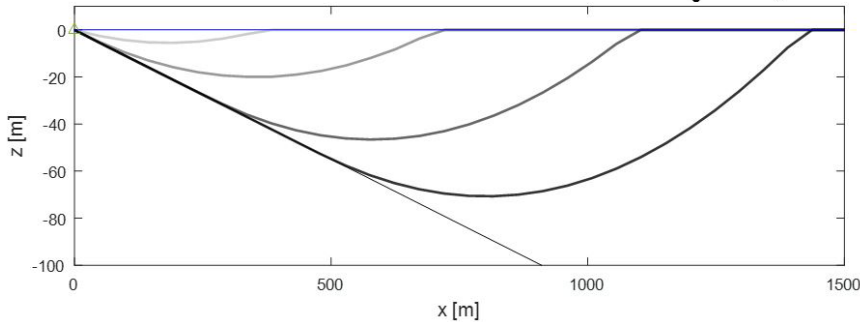


Figure 64:  
Submerging procedure conventional float and sink method

The dynamic GNL EB model is used to model this installation stage. The buoyancy force is adjusted according to the air-fill ratio together with a tension force at the end of the pipe. The Von Mises stress is checked in order to see whether the pipe is controllable up to a certain point. The first stage of the sinking procedure is shown in Figure 64. A constant tension of 150MT is applied to the pipe and the air pressure is controlled such that the 3% of the maximum water depth is filled with air. In this way, the pipe can be controlled properly by adjusting the tension and the air pressure. The black line in Figure 64 shows the stage where maximum allowable stress of 8MPa is reached. The limiting factor here is the bending stress on the surface. The air fill ratio is so low that the area where air filled section of the pipe contributes with an upward force is small. This means that the length of  $q_2$  in Figure 17 works over a relatively small pipe section. Therefore, there is no gradual bending, which could for example be achieved by an air fill ratio of 30%. One could choose to control the bending by making use of a structure such as a stinger.

This estimation is crude and there are more detailed models that can be used for this stage of the installation. Also, computation power limits the detail in which an air fill ratio of 3% can be modelled. It is of main interest what happens when the air pressure to control the buoyancy of the pipe can no longer be applied as the water depth is too large. From the estimation above it is clear that this method cannot be used for the entire submerging procedure and therefore, these results are used as initial conditions for the next stage of the installation.

## 7.6 Second installation phase

From Figure 61 and Figure 64 it is clear that there are measures required to maintain controllability during the entire installation procedure. The challenge is that the weight of the pipe including ballast is so high that it cannot be controlled with simply a tension at the end of the pipe. There are several options, that are discussed below.

### 7.6.1 Extra vessels

The use of extra vessels can be a solution to the controllability challenge. The downside of this solution is that it is expensive and requires a good communication between all vessels during installation. A big advantage is the increased controllability along the pipe, that could be required when environmental conditions are taken into account. Similar to the scale model tests, the vessels are modelled by a vertical force that is added to the pipe. This force is chosen such that a certain percentage of the remaining section that is not on the seabed yet, can be uplifted if required. The submerged weight per unit meter of the pipe including concrete blocks is equal to 460N/m. An estimate of the total vertical force that is required to keep the pipe from sinking is 3MN. Part of this force comes from the vertical component of the tension on the end of the pipe.

If the pipe is filled with air at first, there is a moment that the section of the pipeline at the surface has to be filled with water to continue to the second stage of the installation. If the pipe would be held at the surface at certain points while it is filled with water, the pipe will start bending. This was also observed in the scale model tests in MARIN, as discussed in chapter 5. The pipe is held at the surface at multiple points in the model, with a constant tension of 150MT to see how many holding points are required to stay below the design stress. The initial conditions from the previous subsection are used. Based on the previous section, it is assumed that the first holding point is at 20% of the pipe length from the onshore side of the pipe. This was the estimated length along the pipeline from shore end until where the conventional hold and sink method can be applied. The equilibrium situation for 15 holding points is shown in Figure 65. This equilibrium was modelled for several numbers of holding points, for which the stresses are plotted in Figure 66. These stresses occur in the point where the pipe is held on the surface. At the first holding point, the bending stress is higher than the stresses shown in Figure 66, which is a result of the down bending of the pipe where the first section is already resting on the seabed, as shown on the left hand side of Figure 65. This means that it is questionable whether the pipe can be installed up to the assumed point with the conventional float and sink method,

while holding it on the surface with vessels. An option could be to lower the pipe slightly at the first holding points in order to avoid excessive bending. In order to allow for some dynamic effects due to environmental conditions, there are approximately 20 holding points necessary to stay below the design stress. In this case, the vessels should be able to apply a vertical force on the pipe with a magnitude of 133kN per holding point, where the first point should be, if required during installation, able to deliver a higher force due to the section that is already lowered. The last holding point requires only half of that force, or might even be left out as there is a pulling tug at the end of the pipe.

Figure 65: Pipe filled with water held at the surface by vessels after the first stage of installation

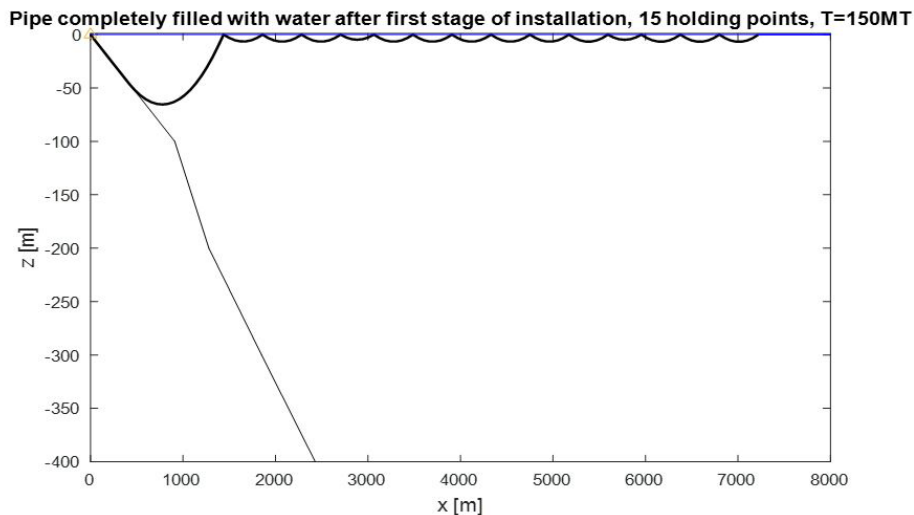
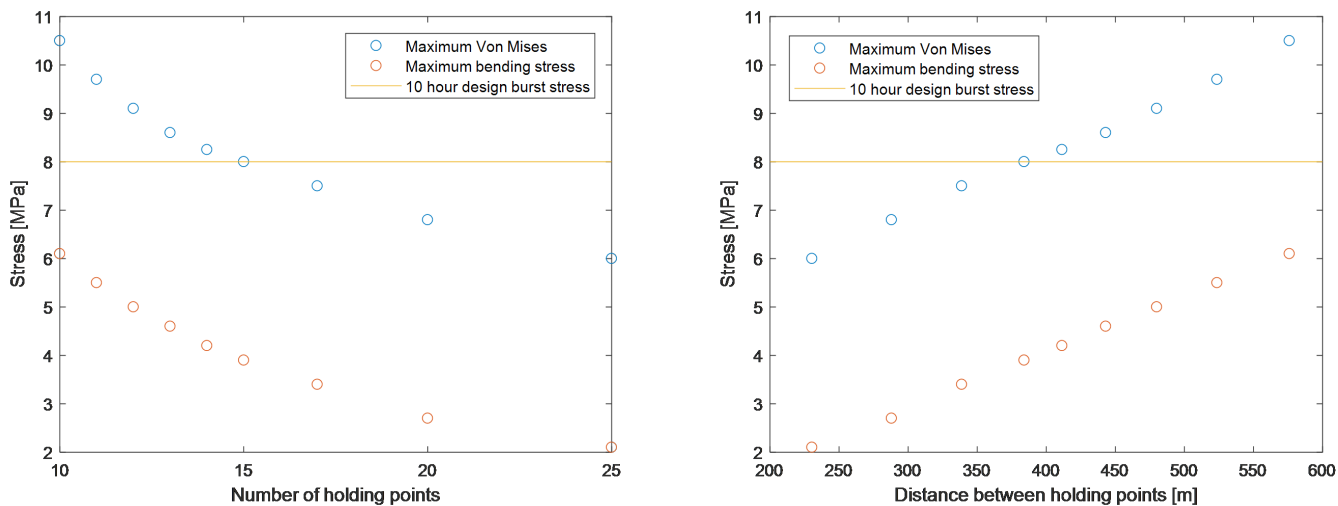


Figure 66: Maximum stress versus distance between holding points (left) and number of holding points (right)



Now, the hold and sink installation method is modelled with 20 holding points. The pipeline is lowered with a constant pulling force of 150MT. Upward forces at the holding points are added which are 133kN each, where the force on the last holding point is half the force. Every three minutes, there is a force released in order to make the pipe sink for the next pipe section. In practice, the force could be varied over time and the length of the line from the pipe to the tug can be increased such that no release is required, until the pipe is fully installed. The advantage is that the pipe installation could be reversed if required. The lowering procedure is shown in Figure 57, where the initial conditions resulted from the previous section.

The Bending stress along the pipe is plotted in Figure 68. At first, the pipe is held on the surface, at  $t=0s$ . With increasing time, the bending stress along the pipeline length decreases as the lowering points are released and the pipe is installed on the seabed. An interesting result is the peak that remains in time at a distance of roughly 1000m along the seabed. From Figure 67, one can see that the steepness of the seabed increases significantly at this point, leading to a bending force that is permanently present after installation.

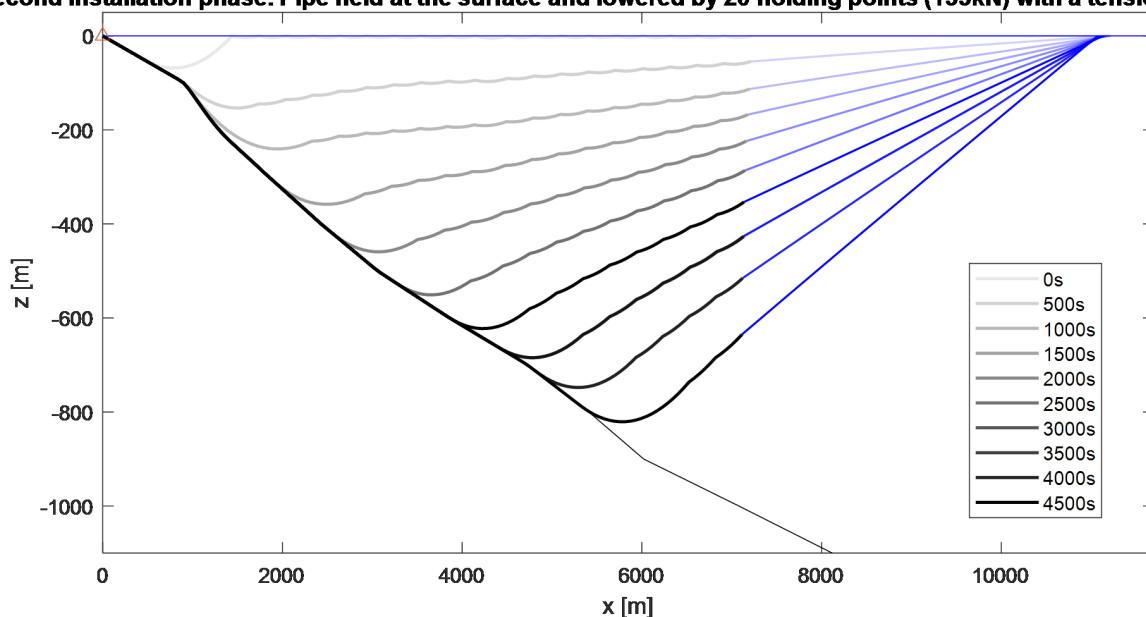
It is not enough to simply look at the stresses resulting from bending stresses. Failure of the pipe will occur as a result of combined stresses. The axial stress in the pipe is plotted in Figure 69. In the beginning, there is a tensile stress in the pipe which is about 4MPa, resulting from the constant 150MT pulling force. When the pipe is lowered, this true axial wall stress decreases as a result of the increasing hydrostatic pressure that acts on the pipe. Note that due to the way that the seabed is modeled, there is no slip and the stresses remain in the pipe when the pipe is installed on the seabed.

Maximum Von Mises stress as a result of the axial stress, bending stress and hoop and radial stress due to hydrostatic pressure is shown in Figure 70. Here, one can see that the stress stays well below the design stress of 8MPa. The maximum Von Mises stress occurs where the pipe is bending where the seabed slope increases. In practice, this can for example be avoided by seabed preparations.

This falling velocity is in the range of 0.2m/s. This is slightly higher than the recommended falling velocity of 500m/h by Janson (2003). In practice, this can easily be adjusted by lowering the pipe at a lower rate. Also, it is assumed to release a holding point every 3 minutes, where this can be done in a slower pace if required. This value was chosen to limit the computation time.

It is expected that the day rate of the vessels required would stay below 30,000\$ per vessel per day. Say the vessels have to travel from the Gulf of Mexico to Curaçao and back, including one day of installation, would lead to a 9 day payment of the day rate per vessel. This would come down to a price of around \$5.5 million, which includes mobilization and demobilization costs. Note that this is simply the day rate and there are no long tug lines and acoustic releases included in the price, which would increase the costs.

**Second installation phase. Pipe held at the surface and lowered by 20 holding points (133kN) with a tension of 150MT**



▲ Figure 67: Second installation phase: hold and sink method

Absolute bending stress in the pipe in all nodes

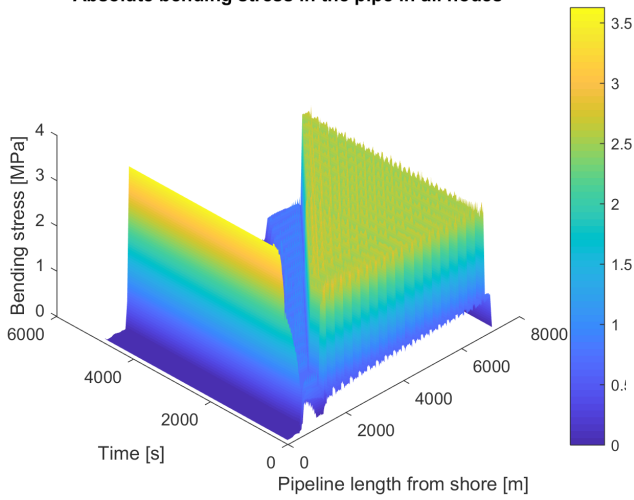


Figure 68: Stepper motors combined with potentiometers and load cells along the horizontal truss

Axial stress in the pipe in all nodes

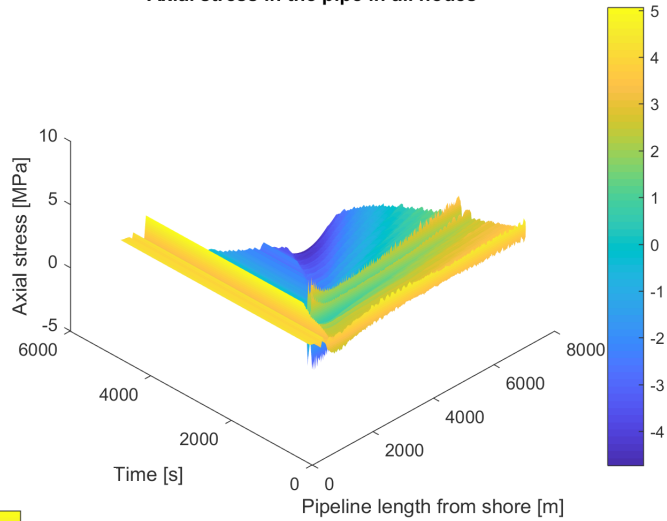


Figure 69: Pipe filled with water held at the surface by vessels after the first stage of installation

Maximum Von Mises stress in the pipe in all nodes

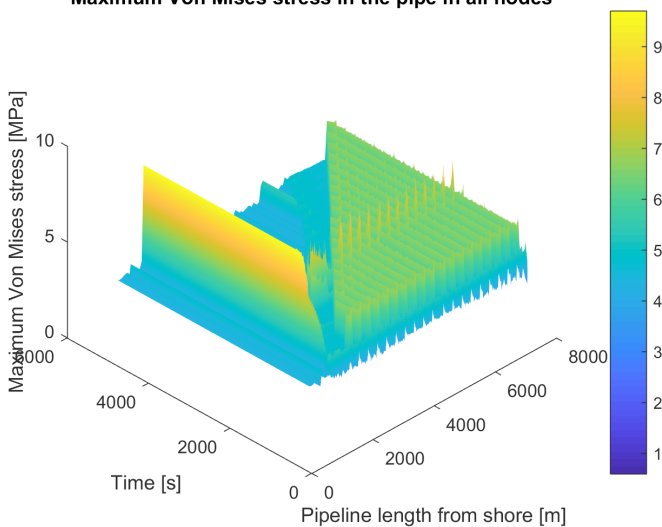


Figure 70: Stepper motors combined with potentiometers and load cells along the horizontal truss

### 7.6.2 Buoyancy modules

From the analysis in the section above it is clear that there are a lot of vessels required for the installation. If the pipe should be held at certain points, there is another option, which is to use buoyancy modules. The dynamic analysis would be similar to the procedure described in the section above and will not be repeated. The main difference is that there is no possibility to increase the upward force at a holding point, and there will be no lateral controllability to counter current actions on the pipeline.

The buoyancy modules should be able to deliver a buoyant force in deep water, which makes them expensive. An example are deep water hydro float buoys by DeepWater buoyancy (DeepwaterBuoyancy, 2018). These buoys have a diameter up to 1.58m and can deliver a buoyant force up to 1122kg per buoy. These buoys are \$27,520 per unit and together with an acoustic EdgeTech release on each point, including deck gear, this would come down to roughly \$6,8 million. This is the price if everything has to be bought new. No cost reduction is taken into account for buying in large quantities, which is expected to be the case if one would have to buy roughly 240 buoys. Also, there are not necessarily new buoys required. The contractor that will install the pipe might have similar buoyancy solutions readily available or can hire them for a lower price.

### 7.6.3 Comparison modified float and sink and hold and sink method

It is not straightforward to choose the cheapest and best installation method because there are many factors that play a role. The choice in a project would depend on the contractor, availability, environmental conditions and many more.

- Buoyancy module pros
  - ✓ Easy to modify
  - ✓ Less communication between vessels required because the acoustic release can be controlled from one point
  - ✓ Buoys are readily available
  - ✓ Buoys can be retrieved
  - ✓ No post-ballast required
  - ✓ Can be combined with vessels
  - ✓ Quick installation
  - ✓ Possible even spread of buoyancy modules over the pipe
- Buoyancy module cons
  - ✗ Expensive
  - ✗ Upward force cannot be increased during installation
  - ✗ No lateral controllability at holding points
  - ✗ Extra lateral drag loading due to buoyancy modules
- Vessel pros
  - ✓ Lateral stability against current actions
  - ✓ Could be done with relatively small vessels
  - ✓ Each vessel could have multiple tug lines attached to different points along the pipeline in order to decrease the required number of vessels
  - ✓ No post-ballast required
- Vessel cons
  - ✗ Good communication required between vessels
  - ✗ Tug lines required
  - ✗ Difficult to plan availability of all vessels
  - ✗ Dynamic effects between pipe and vessel motion due to wave loading
  - ✗ Expensive

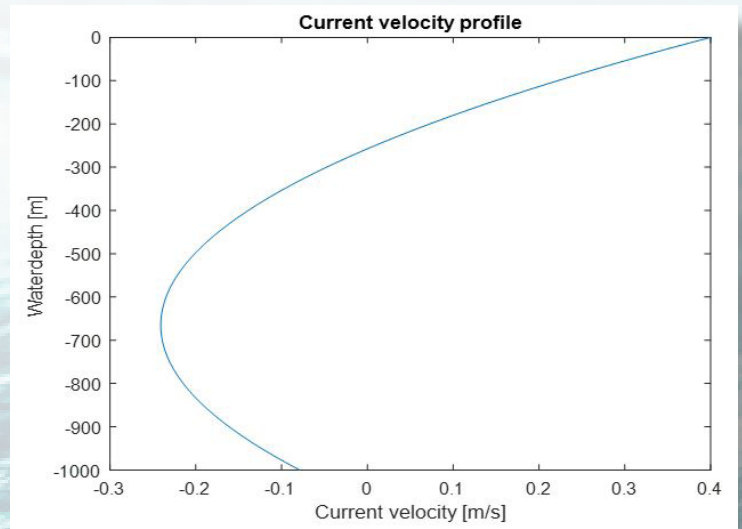
Another option is a combination between vessels and buoyancy modules. The choice on the installation method depends on many factors and is left to the company that is managing the project. Optimization in a further design stage should point out the cheapest installation method on the long term, taking into account the ballast costs. It is expected that post-ballasting is much more expensive than applying the ballast by means of concrete blocks and applying extra measures to keep the installation controlled. Detailed engineering in the surf zone should give more clarification on how much ballast is required. If a uniform specific gravity of 1.11 is applied along the entire pipeline length, the costs of the concrete blocks are expected to be in the range of \$400,000. This is based on a concrete price of 100\$ per cubic meter. Thus, a rough estimate of the total cost for the hold and sink method with vessels is around \$6 million. For buoys this would come down to roughly \$7 million. However, this could be cheaper, as the buoys are retrievable.

Say the pipe would be installed with a low specific gravity, there would not be a lot of vessels required. However, in this case, there would be post-ballasting required. For example by rock dumping. The 7,2km pipe has a total outside volume of 14476m<sup>3</sup>. Assuming a normal bulk density of 1.55ton/m<sup>3</sup>, there would be roughly 22 tonnes of rock needed. Say the vessel has an average rock dumping rate of 1000 ton/hr, the rock dumping would take approximately 22 hours. Additionally, the fall pipe must be built up and recovered, which takes approximately 1 hour per 60-70m water depth. This would come down to a total of 2-3 days. The day rate of a rock dumping vessel is estimated as \$100,000/day. Therefore, including the traveling time from the Gulf of Mexico and back, this would lead to a cost estimation of \$1 million. However, due to the currents it is questionable whether the pipe can be installed on the seabed for such a long time, without the pipe moving. Therefore, the possibility to reduce the costs during lowering and to apply post-ballasting really depends on the environmental conditions around the time of the installation.

## 7.7 Influence currents

The subsurface currents were discussed in section 7.2. In order to get a grasp of how the currents influence the installation, a current profile is applied during the same installation run as in section 7.6.1. A scenario for the current velocity over depth is given in Figure 71, where a positive current velocity is in the positive y-direction.

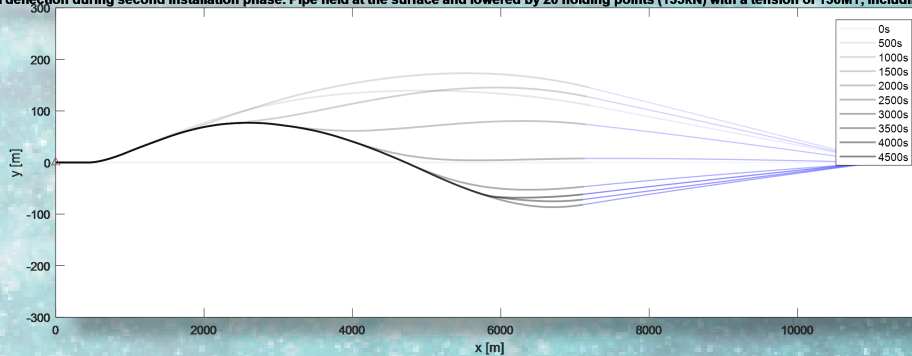
Firstly, it is assumed that the vessel keeps pulling in the positive x-direction and is able to stay at  $y=0\text{m}$ , meaning it will not deflect laterally. Also, no lateral correction force is applied at the holding points, which would for example be the case when the pipe is held by buoyancy modules. The results are shown in Figure 72 and Figure 73.



▲ Figure 71: Current velocity profile over depth

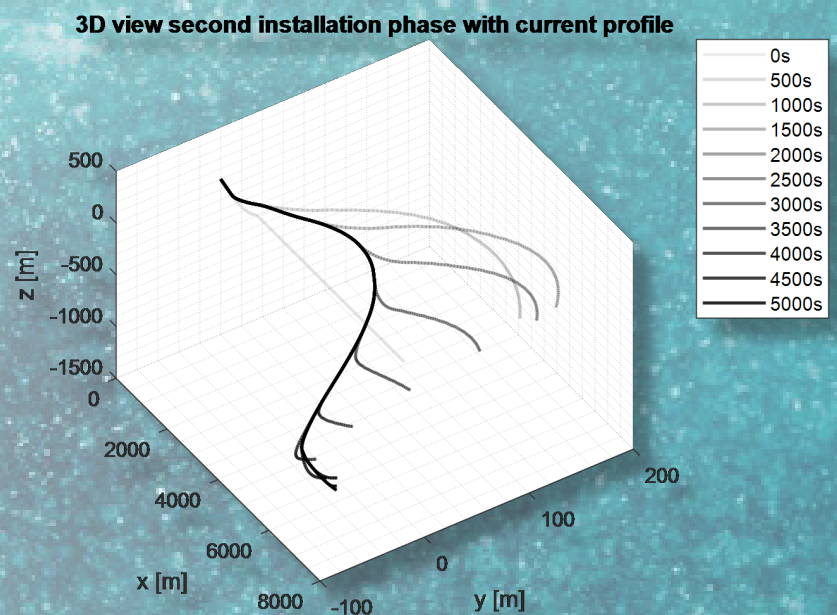
The stresses stay below the design stress of 8MPa. The stress plots can be found in Appendix J. In a time-span of several hours, there can be significant lateral deflections which is not desirable during installation. It is ought to install the pipe on a trajectory with a 10m placement accuracy. The final position of the tip of the pipe is 53m closer to shore due to the lateral displacement of the pipe. This means that the depth that is reached is 0.5m less, which is not necessarily a problem if one takes this into account on beforehand when determining the pipeline length.

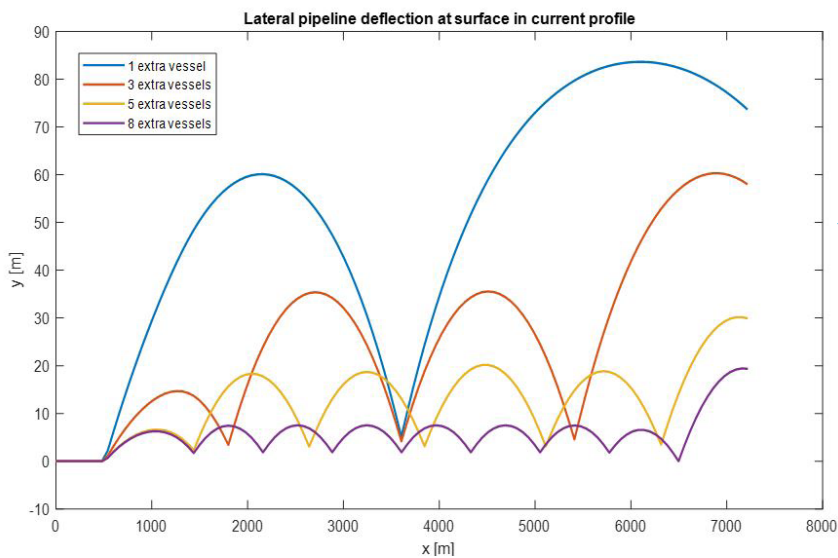
Lateral deflection during second installation phase. Pipe held at the surface and lowered by 20 holding points (133kN) with a tension of 150MT, including current profile



◀ Figure 72: Lateral deflection due to current profile

Figure 73: ▶  
3D view during sinking procedure



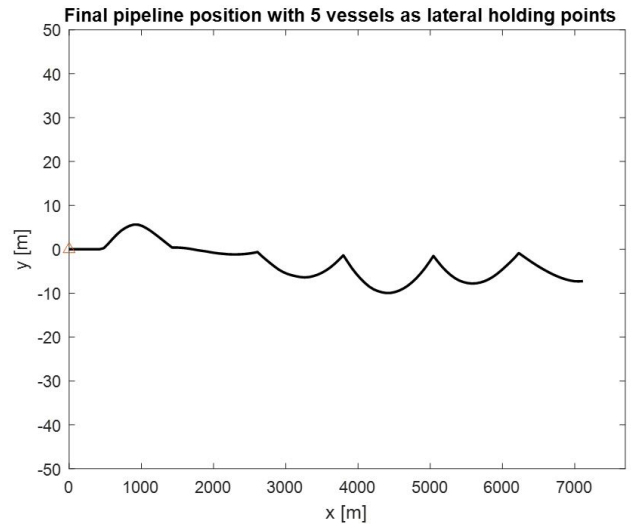


◀ **Figure 74:**  
Lateral pipeline deflection at the sea surface in current profile with a constant tension at the pipe end of 150MT

To be able to maintain controllability, the heading angle of the vessel could be changed in order to counteract this lateral displacement. Therefore, some redundancy must be built in for the pulling force of the tug. The amount of extra tension that would be required depends on the specific environmental conditions during a state of the installation. Due to the fact that the pulling tug is kilometres away from the point where the pipe interacts with the seabed, it can take tens of minutes before the lateral displacement of the pipe starts changing for the better. This is in a constant current profile such as the profile in Figure 71, but in reality the environmental conditions could be less predictable. Therefore, it might be more desirable to correct for lateral displacement closer to the touchdown point, for example at holding points. Instead of the lateral deflection that can lead up to hundreds of meters, adding lateral controllability along the pipe can decrease this. Several scenarios for different number of holding points are shown in Figure 74. One can see that adding a few vessels would decrease the lateral deflection of the pipe significantly. From this figure one can conclude that if there are several vessels, that can move laterally if required, the pipeline could be installed with enough accuracy. Something to bear in mind is the increasing bending stress due to this extra lateral controllability. When the pipe is at the surface, five holding points would mean that the maximum Von Mises stress is 8.5MPa, which is slightly higher than the design stress. A full lowering procedure is modelled where as an assumption, five extra vessels are used. Although more vessels would be more beneficial for the bending stress when the pipe is on the sea surface, it is expected that the bending will decrease with increasing depth. Thus, in total there are 20 holding points of which 5 are attached to a vessel. The other holding points can for example be buoyancy modules.

The final position for the installation with lateral controllability is shown in Figure 75. From this figure one can see that the lateral deflection stays limited and can will not exceed a deflection of 10m from the original route, which is assumed as  $y=0$ . Looking at the  $x$  coordinate, the first curve is towards the positive  $y$ -direction. This is the result of the current profile that is directed towards the North-West in shallower waters. For larger  $x$ , the pipe is in deeper water which is the reason for the bending towards the negative  $y$ -direction. Note the different scales for the  $x$ - and  $y$ -directions. Similar to Figure 73, Figure 77 shows a 3D plot of the sinking procedure. When comparing these figures one can see that the lateral controllability is significantly increased. The horizontal component of the force that the vessels would have to deliver to counteract the current forces are max 15MT per vessel if there are 5 vessels used. This is a reasonable bollard pull that a normal pulling tug would be able to deliver. This force is changing over time and its direction is determined by the state of the pipeline and the current velocity that it is subjected to at a certain depth. The Von Mises stress is plotted in Figure 76. Separate axial and bending stresses can be found in Appendix J. One can observe several things in the Von Mises stress over time. First of all, there is a large peak 1000m from shore, which is a result of the bending stress due to the change in bathymetry. Several other peaks can be observed that stay over time due to the bathymetry changes. The triangle of peaks in the right of the figure is the result of the bending stress due to the holding points. The bending stress at the holding points itself is slightly higher but is kept below 8MPa. Compared to Figure 70, there are some higher peaks that are the result of the extra bending due to the current velocity. Especially at the beginning, where the pipe is in shallow water in higher current velocities, there is an increase in the bending stress at the points where there is extra lateral controllability. Lastly, there is a peak that can be noticed far away from shore, at the last time steps. This is the result of the increased bending of the pipe when the last pipeline section is installed, by lowering the tension. Overall, the stresses are in the range of the design stress. Depending on the environmental conditions during the installation, extra measures could be taken to lower the bending stress in high currents and one should consider measures for the stresses due to the seabed bathymetry.

Final pipeline position with 5 vessels as lateral holding points **Figure 75:**



Maximum Von Mises stress in the pipe in all nodes

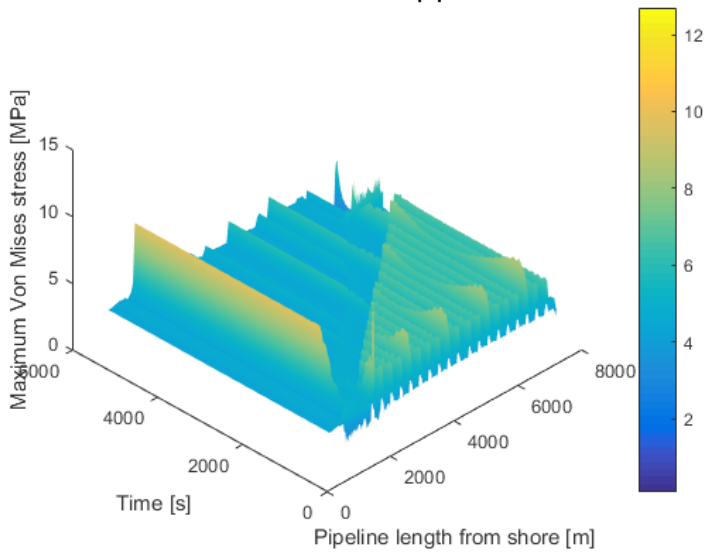
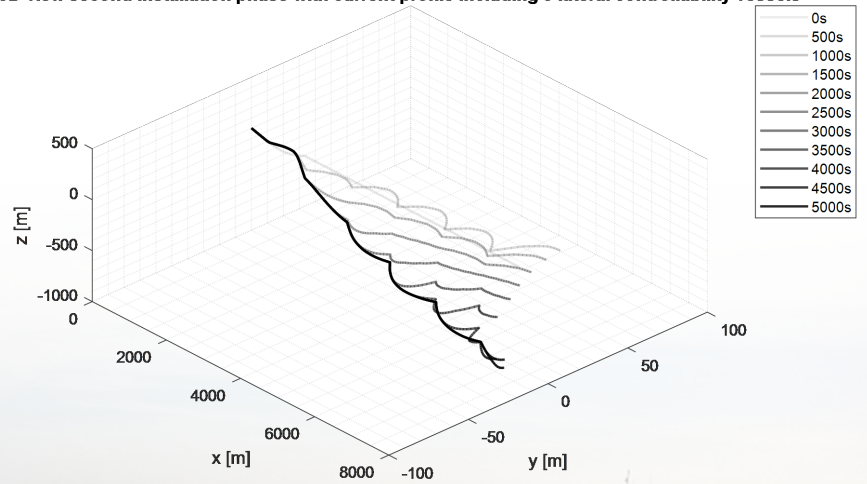
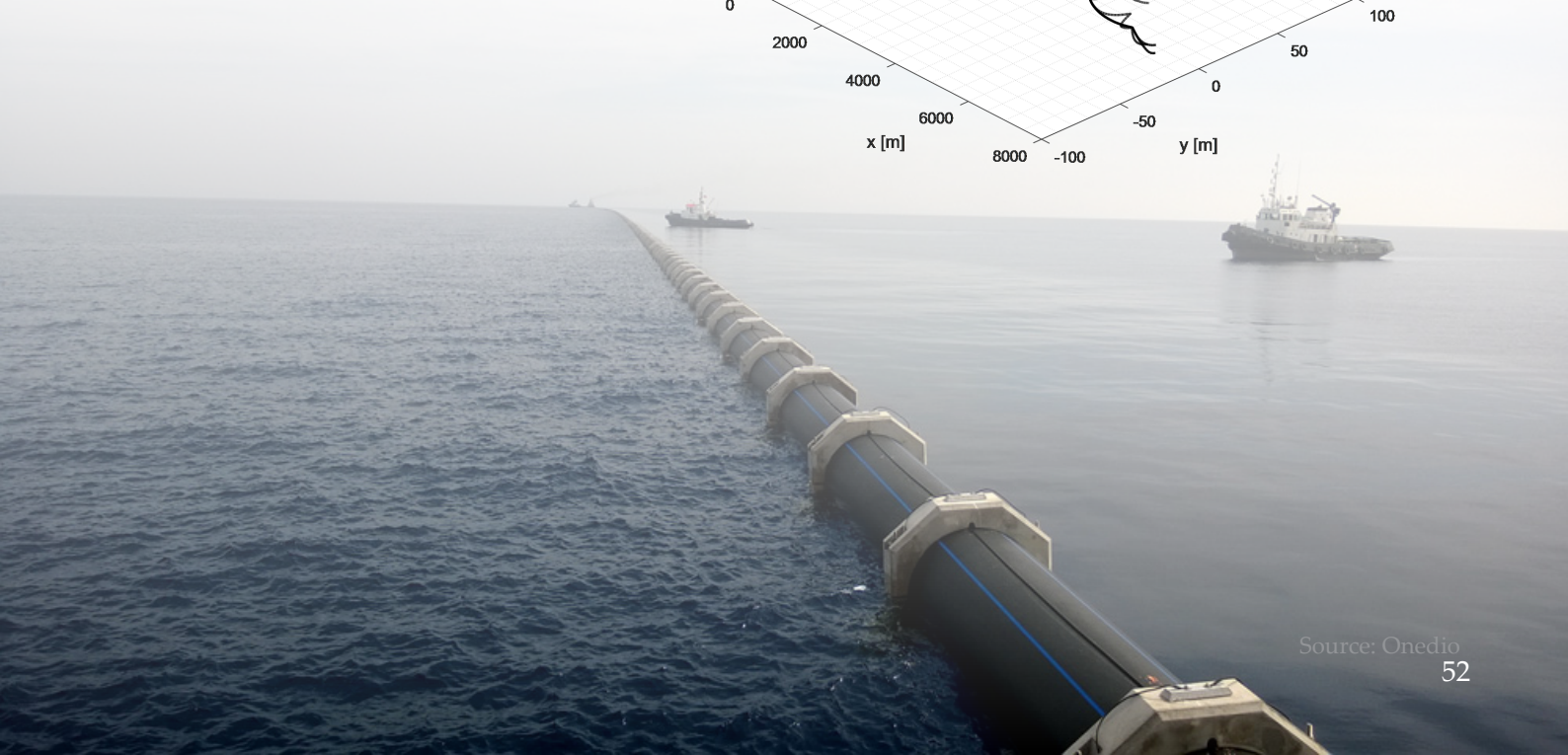


**Figure 76:** Maximum Von Mises stress in pipe during installation with current profile and 5 lateral holding points

3D view second installation phase with current profile including 5 lateral controllability vessels



3D plot pipe installation with current profile and 5 lateral holding points **Figure 77:**



Note that the amount of controllability that is desired partly depends on detailed data on the seabed conditions. For example, it might be desirable to avoid certain steep parts along the seabed at all costs, which means a more controlled installation is required. If the permits are not strict and there is a large margin where the pipe could be installed, there could be less need for controllability and the pipe can be controlled by means of a limited number of vessels.

### 7.8 Residual lay stress

When the pipeline is completely installed, there is residual lay stress in the pipe due to the tension that is applied in the pipe during installation. When the pipe temperature and internal pressure are the same as during installation, the effective residual lay tension is equal to the effective axial stress (DNV, 2007). The effective axial stress after installation on the seabed is calculated by the EB model. The true wall stress is corrected by the internal and external pressure according to equation (16).

The residual lay tension fluctuates around the tension that is applied at the end of the pipe (150MT). As a result of this tension, the pipe might slide on the seabed and search for an equilibrium. This strongly depends on the local bathymetry. On the long term, temperature effects can play a role. If the pipe is in operation, cold water will flow through the pipe where the water temperature outside the pipe is dependent on depth. These effects should be taken into account to assess the structural integrity of the pipe during installation. The operation conditions are however beyond the scope of this thesis.

### 7.9 Local buckling

For buckling, one can consider global buckling and local buckling. Global buckling implies buckling of the pipe as a bar in compression. During installation, the effective axial stress will not become negative, which means that global buckling will not occur. However, the pipe could buckle locally due to a deformation of the cross section. When a pipe is bent to a certain amount, buckling may occur due to a combination of a decreasing second moment of inertia and E-modulus. The second moment of inertia decreases due to ovalization of the pipes cross-section. The pipe is in a unstable state due to the decreased bending stiffness. The safety factor for buckling should be no less than 3 when buoyancy modules are used (Pipelife, 2003). This means that  $R/D_{min}=60$ . It must be made sure that this value will not be exceeded. In case of the installation run with the current profile, the bending radius stayed above 260m, which is 162 times the diameter of the pipe. Also, the pipe could buckle due to external over pressure.

$$p_e - p_{min} \leq \frac{p_c(t_1)}{\gamma_m \gamma_{sc}} \tag{54}$$

Where  $p_{min}$  is the minimum internal pressure that can be sustained. When the pipe is lowered, it is filled with water. Therefore, it is assumed that the internal pressure is equal to the external pressure (DNV-OSF101). This means that:

$$0 \leq \frac{p_c(t_1)}{\gamma_m \gamma_{sc}} \tag{55}$$

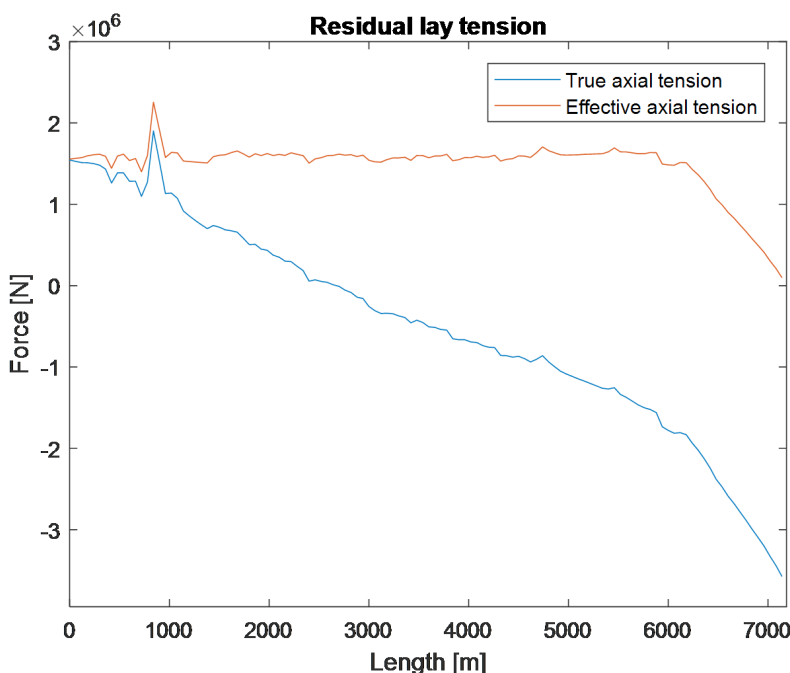


Figure 78: Residual lay tension

Where  $p_c(t_1)$  is the characteristic resistance against external pressure (collapse). It can be calculated according to:

$$(p_c(t) - p_{ei}(t))(p_c(t)^2 - p_p(t)^2) = \frac{p_c(t)p_{ei}(t)p_p(t)f_0D}{t}$$

$$p_{ei}(t) = \frac{2E\left(\frac{t}{D}\right)^3}{1 - \nu^2}$$

$$p_p(t) = \frac{f_y\alpha_{fab}2t}{D}$$

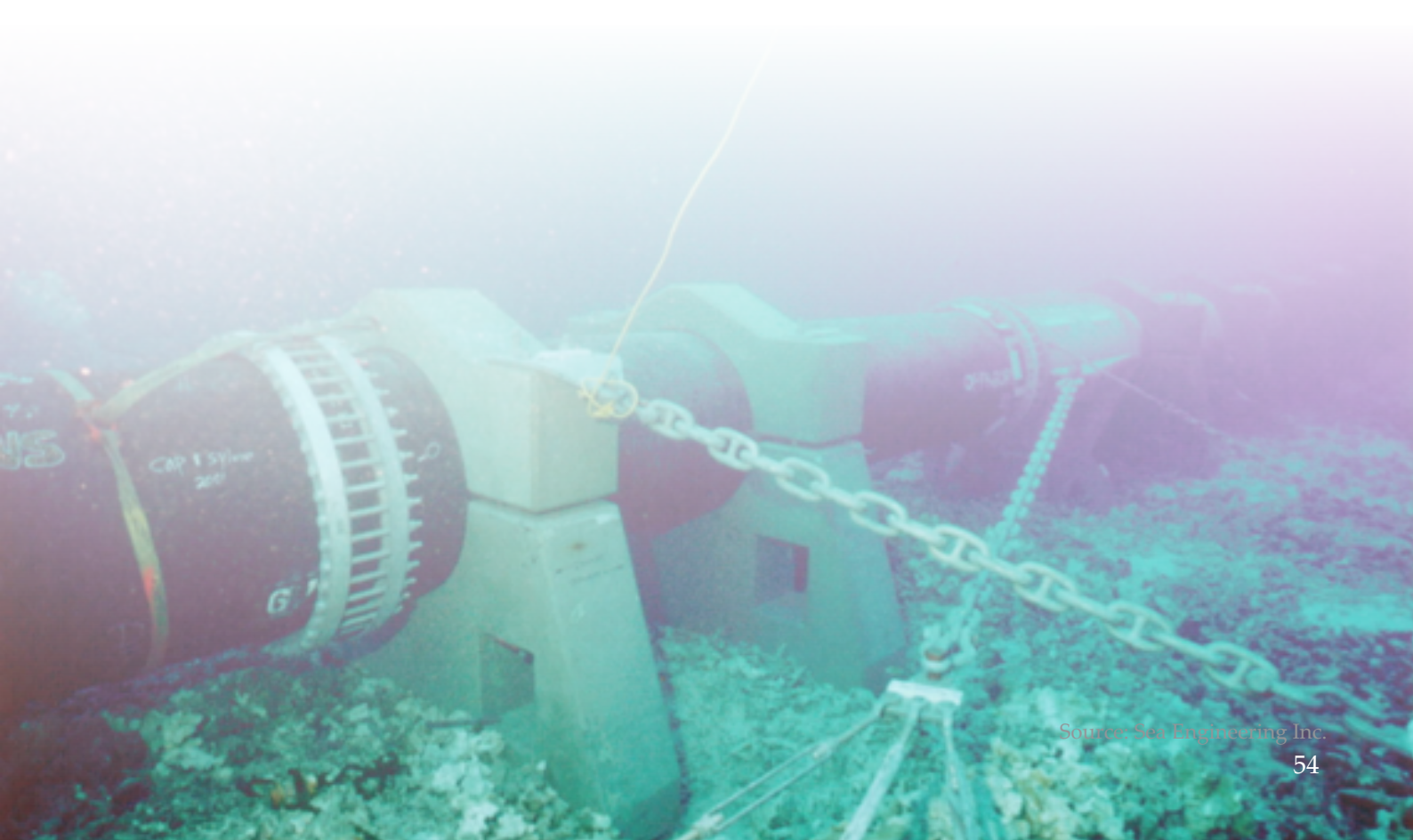
$$f_0 = \frac{D_{max} - D_{min}}{D}$$
(56)

Applying a fabrication factor  $\alpha_{fab}$  of 1.0,  $\gamma_{SC}$  equal to 1.14 and an ovality of 0.01, leads to a collapse pressure of 0.23MPa. As a reference, for an empty 1.6m OD pipe filled with air (ambient pressure), this would mean that the pipe could go down roughly 23m deep without local buckling. However, due to the fact the internal pressure equals the external pressure, there will be no local buckling collapse due to pressure.

The next stage is propagation buckling, which is not discussed in detail because local buckling must occur before this happens. In case there are buckling arrestors required, these can be chosen accordingly by calculating the propagation buckling criterion, which can be found in DNV-OSF101. If it is known how many holding points are required during installation, the buckle arrestors that can be added at these connection points can be designed accordingly. A detailed buckling analysis with finite element modelling including local stress effects is preferred for detailed design.

The allowable bending ratio in the beginning of this section did not take into account axial stress. The following local buckling criterion holds for a pipeline subjected to bending moment, pressure and effective axial force:

$$\left\{ \gamma_m \gamma_{sc} \frac{|M_{sd}|}{\alpha_c M_p} + \left\{ \gamma_m \gamma_{sc} \frac{S_{sd}}{\alpha_c S_p} \right\}^2 \right\}^2 + \left( \alpha_p \frac{p_i - p_e}{\alpha_c p_b} \right) \leq 1$$
(57)



Where:

$$\begin{aligned}
 \alpha_c &= (1 - \beta) + \beta \frac{f_u}{f_y} \\
 M_p &= f_y(D - t)^2 t \\
 S_p &= f_y(D - t)t \\
 \beta &= \frac{60 - \frac{D}{t}}{90}
 \end{aligned} \tag{58}$$

Note that the last term in (57) equals zero due to the hydrostatic pressure. For the design moment  $M_{sd}$ , the maximum moment that occurs in the pipe according to the EB model is used, combined with the maximum effective axial force  $S_{sd}$ . During the model run including the current profile, the maximum moment in the pipe equals 0.37MN. The maximum effective axial force equals 200MT.

If there is a lateral point load present, which is the case at the holding points during installation, the plastic moment  $M_p$  should be corrected. This is done according to the following formula:

$$\begin{aligned}
 M_{point} &= M_p \alpha_{pm} \\
 \alpha_{pm} &= 1 - \frac{D/t}{130} R/R_y \\
 R_y &= 3.9 f_y t^2
 \end{aligned} \tag{59}$$

Where R is the reaction force of the point load. When filling in these formulas, the value on the left hand side of equation (57) is equal to 0.86 which is smaller than 1. This means that the ultimate limit state criterion is satisfied. However, there still is some buckling risk. This is due to the fact that there can still be unforeseen dynamic effects, for example due to wave loading, that can influence the bending moment and effective axial force. However, the values that were used for the effective axial force and bending moment were the maximum values throughout the entire installation, which do not occur simultaneously.



# 8 Discussion

Before drawing a conclusion, one should understand the limitations of the research. Therefore the assumptions that were made during this research are discussed below.

## 8.1 Model

There are several assumptions that were made when modelling the pipeline installation. Firstly, effects due to torsion are neglected. In reality, there is a risk of torsion during installation as the concrete blocks could rotate. Also, the concrete blocks were assumed to be a distributed force. This means that there are no local stress effects taken into account, which could be a result of discrete concrete blocks along the pipe. The same goes for the flanges that can be used in combination with welds. Also, the additional drag loading due to the concrete blocks is taken into account by increasing the drag coefficient. This could be a crude representation of reality.

Wind and wave loading is not taken into account. Especially wave loading could influence the dynamics of the system. At certain frequencies, there could be a risk of resonance, when the pipe is in the first meters of water depth. This was neglected to reduce the computation time. In practice, wave and wind loading will be present.

Only the cable between the end of the pipe and the pulling tug was modelled. For simplicity, loading on other holding points along the pipeline length are modelled as forces, meaning that there is no cable and vessel modelled. Similarly, this keeps computation time limited. The vessel is also modelled as a moving boundary, meaning there are no details taken into account for the exact dynamics of the vessel. Especially when there is wave loading involved, there could be dynamic processes between the vessel and pipe that might play a role.

The seabed was modelled with springs and dashpots. It was assumed that as soon as an element is on the seabed, that it does not slide. In practice the pipe might slide due to residual tension, bathymetry and temperature effects.

Furthermore, the pipe is really long, which means that there are many nodes required to model the pipe with grid independence. Due to the large time span over which the installation should be modelled, there was a certain acceptable number of elements chosen. From the grid independency, discussed in Appendix F, it was shown that an element length of 50m already sufficiently, estimates the bending stress above 10MPa, which is already higher than the design stress of 8MPa. For a decreasing bending radius, there would be less nodes required to reach a grid independent solution. Still, no grid independent solution was found and the model will never precisely calculate the same for the exact same for a different number of nodes. However, the error resulting from the crude element length is limited.

Morison equation is used to determine the drag loading. Although this is a reasonable assumption, there are more detailed solutions such as diffraction software available to determine the hydrodynamic loading.

Also, the buoyancy of the pipe on the sea surface was not modelled in detail. In practice, this is a function of the depth of submergence when the pipe is only partly submerged. However, because the surface effects are not the focus of this research, this was not modelled in detail.

The connection to shore was modelled as a hinge. In practice this might be different, depending on how the pipe is connected onshore during installation.

The material properties are time dependent. This means that the behaviour of the pipe also depends on the loading time and the temperature, which was not modelled in detail. A constant E-modulus was assumed and viscoelastic effects were neglected.

The discussion on the model validation was already treated in chapter 5 and are not repeated for the sake of brevity.

## 8.2 Case study

First of all, the data that was available for the case study was crude. This means that the estimations in chapter 7 might be crude and serve as an indication of the requirements during installation. The specific gravity has a lot of influence on the forces and stresses in the pipe and the requirements to maintain controllability. If the currents never exceed a speed of 0.1m/s in deep water, this would decrease the costs of the hold and sink method significantly.

Furthermore, the specific gravity is assumed to be constant over the pipeline length. In practice, this will not be the case as this has to be designed based on a detailed bathymetry map and environmental conditions. The specific gravity will be much higher in the surf zone. Also, the installation in the surf zone is not modelled in detail, as there will be air pressure effects that play a role.

The conventional installation method, where air pressure is applied, was not modelled

Extra attachments such as a diffuser at the end of the pipe are not taken into account. In practice, this could lead to extra forces on the pipe end, but it is expected that this will not have an influence on the installation significantly.

The cost estimations are crude and serve as an indication. As stated in the previous section, there are many factors that play a role to choose the best installation method and this might be subject to change when there is more insight in the site-specific conditions.

Also, the pipe needs to be welded and might be connected with flanges. These details are not modelled, but could have an effect on the design stress. The welding factor was discussed in chapter 2 and should not be neglected in detailed design.

The conventional installation method (with air pressure), was not modelled in great detail in this thesis. This modelling was used as initial conditions for the second installation phase. There are detailed models available in the industry for HDPE pipeline installations. These showed that the pipe could be installed as deep as 280m for a pipeline with 1.6m outer diameter, SDR 26. This were results for the Turkey Cyprus project, where INTECSEA was involved in. However, it should be mentioned that for a different temperature and wall thickness, the allowed stress are different from the case study in this thesis.

Lastly, the buckling analysis used formulas from DNV-OSF101. These formulas are based on buckling for steel pipes. It is questionable whether these formulas apply for HDPE. However, all rules of thumb by HDPE pipe suppliers that were found in literature were not exceeded.

An important thing is to address the findings that are different from the previous work done on the cold water pipe installation. The main reason for the large differences that are observed with the thesis by Van Nauta Lemke (2017) is the temperature effects on the stress, in combination with time scale that the stress acts. Additionally, the weight of the pipe in this thesis is higher, as it was almost neutrally buoyant in the thesis by Van Nauta Lemke.

This work is a follow up and therefore the most promising installation methods were assessed. As it turned out that the lateral currents have a large impact on the installation, it could be more beneficial to use other installation methods such as the so called Brewers method, where the pipe is pulled down from attachment points on the seabed. These methods were not assessed in this thesis and might still be effective installation methods.

# 9 Conclusion

This thesis focusses on a preferred installation method for large diameter cold water pipes in deep water. A 3D numerical model is developed to estimate the stresses in the pipe during installation. The numerical model is easily adjustable and is able to take into account pressure effects and current actions in all directions. The model is compared to a 2D geometrically non-linear Timoshenko beam model. Model tests at MARIN were used to validate the 3D geometrically non-linear Euler-Bernoulli. In this comparison, it was shown that the numerical model is able to capture the sinking procedure in the pipe with satisfying accuracy. Furthermore, a case study for Curaçao showed that there pipe must have a higher weight than assumed by Van Nauta Lemke (2017). Together with the temperature and time dependent strength properties of HDPE, that are over-estimated by Van Nauta Lemke, leads to an increased amount of measures that have to be taken to control the pipe during installation. Firstly, the sub-questions of this research are answered, after which the main research question is answered.

*How can the ballast, required for permanent condition, be implemented in the installation?*

The amount of ballast is strongly dependent on the environmental conditions. The largest part of the pipe could require a specific gravity of roughly 1.1. This means that concrete blocks can be attached to the pipe, or post-ballasting can be applied. It is also important to have controllability during the entire installation procedure. Therefore, applying concrete blocks would mean that there are a number of holding points required along the pipe to limit the bending stresses. This can be done by either vessels or buoyancy modules with acoustic releases. The number of holding points depends on the pipe properties and the specific gravity of the pipe. Due to the drag loading resulting from subsurface currents, it is questionable whether post-ballasting is preferred. If the pipe has a low specific gravity the pipe could start moving in between the placement of the pipe and the post-ballasting, which is not favourable.

*What is the influence of environmental conditions on the installation of the offshore pipeline?*

The most important environmental condition that influences the installation are the current velocities. They determine the required amount of ballast which is an important parameter for the controllability during the lowering procedure. Currents also have a significant impact on the final position of the pipeline, if no measures are taken during installation. Solely controlling the lateral deflection of the pipe with a single pulling tug at the end of the pipe is not favourable. The timescale in which this vessel can correct is long, where the current profile is unpredictable over the length of the pipeline. One way of controlling the pipe would be to add multiple vessels along the pipe, that can counteract the current actions locally.

Other environmental loading such as wind actions and first and second order wave drift forces are not expected to play an important role during installation. However, if vessels that are connected to the pipe are used, one should carefully analyse the dynamic interaction between the vessel, cable and the pipe.



### *What is the influence of the shear strain on the pipe behaviour during installation?*

For large diameter HDPE pipes, shear strain is increasing when bending is increased. However, in the region of allowable bending stresses, there is not enough bending that shear strain plays a significant role. For bending stresses around 10MPa, the Timoshenko model and Euler-Bernoulli model showed similar behaviour for diameters up to 3m that were modelled. When conditions were modelled where more bending occurs, the models started diverging. However, these bending stresses are of lesser interest as they have to be avoided during installation. The shear stresses in the HDPE pipe are in the order of magnitude of 0.1MPa. Therefore it is reasonable to neglect this stress compared to other stresses. Overall, shear deformation will not influence the dynamics on a large scale significantly.

### *What is the influence of the hydrostatic pressure on the pipe behaviour during installation?*

The hydrostatic pressure has a stabilizing effect on the bending of the pipe with increasing depth. This will influence the natural frequencies of the pipe during installation, due to the state dependent additional stiffness. In deeper water, the pipe will be more stiff and bend less. This phenomenon should not be neglected for pipes in deep water and is incorporated in the model and taken into account during the case study.

Next, the main research question is answered:

### *What is the preferred installation method for a large diameter HDPE cold water pipe for ocean thermal energy conversion and seawater air-conditioning?*

The preferred installation method strongly depends on the environmental conditions. If the subsurface currents are low, the required ballast stays limited and the installation can be done with a small number of holding points, without expensive post-ballasting. However, if the subsurface currents are in the range of 0.2-0.4m/s, there is a significant risk that the pipe will not be stable on the seabed shortly after installation if there is not enough ballast applied. This means that there should already be sufficient ballast present during installation, which can be added by means of concrete blocks. Applying this ballast increases the required amount of holding points significantly, which increases the installation costs.

In this thesis, a specific case for Curaçao is investigated, with a 1.6m outer diameter. It is not the question whether the pipe can be successfully installed, but how cost-effective. The preferred installation method is strongly dependent on costs and therefore detailed data of subsurface currents is desired.

Both the hold and sink method with vessels, and the modified hold and sink method with buoyancy modules are decent options. They both have advantages and disadvantages, mostly related to controllability. If there are high current velocities expected during installation, it is preferred to use several vessels, as the lateral displacements due to currents can be countered locally. A combination where both vessels and buoyancy modules are applied as holding points is an interesting option. Optimization and more detailed data for a specific project should point out which method is cheapest and has the lowest risk for installation failure. Scenarios for different projects can be assessed with the tool developed in this thesis.



# 10 Recommendations

From chapter 9, it is clear that there is no clear convergence towards an installation method. The reason is that there is not enough detailed environmental data available with respect to the subsurface currents. Therefore, the most important recommendation is to obtain data for the specific project in Curaçao. If one finds out that there is a really low velocity subsurface current along the seabed, this would change the whole requirements for the installation and can greatly decrease the costs. The opposite holds if there are high subsurface currents present during the operational lifetime of the pipeline.

Chapter 8 discussed some limitations with respect to the model which means there is room for improvement. Firstly, the seabed was modelled with springs and dashpots. It would be better to implement a stick-slip boundary condition, or a more detailed soil model. This would also gain more insight in the residual lay tension in the pipe and the long term creep effects. Also, temperature and density effects could be taken into account, where a temperature profile could be added over depth and the material properties would change. A challenge is the time scale that plays a role, where the pipe material behaviour will not instantly react to the temperature changes when the pipe is sinking. Furthermore, torsion effects are not modelled. Especially when concrete blocks are applied to the pipe, there could be torsion effects due to the placement of the concrete blocks on an uneven seabed. It would be desired to know the order of magnitude of the stresses resulting from torsion.

The first stage of the installation, where air pressure is applied to the pipe is modelled with crude precision. It is advised to make use of third party software to optimize this installation phase and to gain more insight in the limits of this installation method. Keesmaat (2015) used a static model to investigate this, however there will be dynamic effects and an analysis is desired for the specific conditions of the project in Curaçao. A limitation for this installation method is the bending that occurs at the surface. One could think of a solution such as a stinger to limit the bending and to increase the workability of the conventional installation method.

As stated before, local stress effects are not taken into account. It is important to know how the stress is distributed locally, where a force resulting from for example a concrete block or the pulling tug is acting on the pipe. These local effects could introduce stresses much higher than the global stresses on the pipe.

The ballast in the surf zone was not estimated with much detail. It would be desirable to analyse extreme events such as hurricanes in more detail, in order to secure structural integrity over the lifespan of the pipeline.

VIV could play a role during installation. As discussed in the case study, it is expected that the falling velocity of the pipe can be controlled. However, there are current actions on the pipe that are less predictable. Additionally, the natural frequency of the pipe will change with increasing hydrostatic pressure. Therefore, there can potentially be situations where the natural frequency of the pipe, on a local scale, will be similar to the vortex shedding frequency. Although it is not expected that VIV will influence the installation of the pipe to a great extent, it might still be interesting to know in which situations there is a risk of VIV and what this would mean for the installation.

Janson (2003) stated that the pipeline is allowed to move due to the flexible design strategy for HDPE. In this thesis, the formulas that were used for the ballast are based on absolute stability of the pipe. There might be room for optimization and lowering the ballast, depending on how often the absolute static equilibrium on the seabed will be distorted and by what extent, locally and globally.

Another thing that is not considered in a lot of detail are local and global buckling effects. A buckling analysis should be applied which can also be used to optimize the concrete block distribution along the pipe. For this assessment, it is recommended to use finite element methods to model local behavior

One could also consider applying extra measures at the holding points to increase the friction on the seabed to increase the stability of the pipe once installed. A certain type of anchor can be used and installed at the holding points in order to make sure that the pipe will stay in position after installation. In this way, the required specific gravity could be lowered.



It is also interesting to see what the influence of the trajectory of the pipe would be to head losses in the pipe. For example, one could estimate how straight the pipe should be laid in order to have minimum effect on the long term efficiency of the OTEC or SWAC plant. If there is less precision required, this would lead to an easier and quicker installation.

Furthermore, it is recommended to consider different installation options. For example, based on the new insights from this thesis, the Brewers method could be reconsidered. Furthermore, other options for ballasting could be considered. An example is to attach an extra pipe to the HDPE pipe and fill it with grout after or during installation.

Lastly, it is desired to optimize costs and risks. The model developed in this thesis serves as a starting point and could be expanded to include costs. For example, the pipe wall thickness was based on an SDR equal to 21. This was provided by Bluerise. However, it might be desirable to increase the wall thickness such that a larger pulling force is allowed along the pipe. Some rough estimates for the sensitivity of certain parameters are presented in appendix K. A detailed sensitivity analysis could point out the most important parameters for installation optimization.

# Bibliography

- Abhay Ocean India. (2016). Technical Catalogue for Submarine Installations of Polyethylene Pipes. Mumbai.
- Adrian R KATILI, R. B. (2015). Space Cooling in Buildings in Hot and Humid Climates – a Review of the Effect of Humidity on the Applicability of Existing Cooling Techniques. The University of Nottingham.
- Agru. (2018). AGRULINE large diameter piping system.
- AIE. (2017). World Energy Outlook 2017.
- Alfredo Gay Neto, P. d. (2017). Hydrostatic Pressure Load in Pipes Modeled Using Beam Finite Elements: Theoretical Discussions and Applications. J. Eng. Mech.
- Argonautes. (2012). The pioneer OTEC operation: “La Tunisie”. Retrieved from <http://www.otecnews.org/2013/01/georges-claude-the-genius-gone-astray/george-claude-cuba1/>
- Brugmans, J. (2005). Parametric Instability of Deep-Water Risers. Delft.
- C. Keijdener, A. M. (2015). Deriving Simple Dynamic Discrete Element Models of Geometrically Nonlinear Timoshenko Beams. Crete, Greece.
- C. Keijdener, A. M. (2015). DERIVING SIMPLE DYNAMIC DISCRETE ELEMENT MODELS OF GEOMETRICALLY NONLINEAR TIMOSHENKO BEAMS.
- C.H.K. Williamson, R. G. (2007). A brief review of recent results in vortex-induced vibrations.
- Collberg, O. F. (2005). Influence of pressure in pipeline design.
- de Jong, H. (. (2017). Ocean current patterns and variability around Curacao for Ocean Thermal Energy Conversion. Delft.
- DeepwaterBuoyancy. (2018). Retrieved from DeepwaterBuoyancy: <http://deepwaterbuoyancy.com/>
- DNV. (2007). DNV-OS-F101 SUBMARINE PIPELINE SYSTEMS.
- DNV. (2014). ENVIRONMENTAL CONDITIONS AND ENVIRONMENTAL LOADS.
- DNV. (2017). Free spanning pipelines (DNVGL-RP-F105).
- DNVGL. (2017). Environmental conditions and environmental loads.
- EIA. (2017). International Energy Outlook 2017. U.S. Energy Information Administration.
- Encyclopaedia Britannica. (2018). Stefan-Boltzmann law. Retrieved from <https://www.britannica.com/science/Stefan-Boltzmann-law>
- GRANTA. (2017). CES EduPack 2017.
- GrantaDesign. (2018). CES EduPack.
- Janson. (1987). Submersion of plastic marine outfalls - Effect of non-linear material properties and ovalization of the cross-section. Stockholm.
- Janson, L.-E. (2003). Plastics pipes for water supply and sewage disposal. Stockholm: Borealis.
- JC MacKay. (2008). Sustainable Energy - Without the Hot Air. Retrieved from [https://www.withouthotair.com/c6/page\\_38.shtml](https://www.withouthotair.com/c6/page_38.shtml)
- Journée, M. (2001). Offshore Hydromechanics. Delft: Delft University of Technology.
- Krah. (2013). 3000mm PE pipes for deep water outfall pipeline. Retrieved from Plastics News: <http://www.plastics.gl/construction/mega-wastewater-treatment-plant/>
- Lienhard, J. H. (1966). Synopsis of Lift, Drag, and Vortex Frequency Data for Rigid Circular Cylinders. Washington.

- Makai Ocean Engineering. (n.d.). An Introduction to Seawater Air Conditioning. Kailua, Hawaii.
- Marley Pipe Systems. (2010). HDPE Design Considerations. Retrieved from <https://www.marleypipesystems.co.za/images/pdfdownloads/productbrochures/hdpe-design-considerations.pdf>
- Metrikine, A. V. (n.d.). Dynamics, Slender Structures and an Introduction to Continuum Mechanics. Faculty of Civil Engineering and Geosciences, Section of Structural Mechanics.
- Orcaflex, O. (2018). Line Theory: Line Pressure Effects. Retrieved from <https://www.orcina.com/SoftwareProducts/OrcaFlex/Documentation/Help/Content/html/LineTheory,LinePressureEffects.htm>
- OTEC NEWS. (2013). George Claude Cuba.
- Peninsula Plastics. (2018). Thermoforming Materials & Blends. Retrieved from <http://www.peninsulaplastics.com/thermoforming/thermoforming-materials/>
- Physical Oceanography Distributed Active Archive Center. (2018). OSCAR third degree resolution ocean surface currents. Retrieved from [podaac: https://podaac.jpl.nasa.gov/dataset/OSCAR\\_L4\\_OC\\_third-deg](https://podaac.jpl.nasa.gov/dataset/OSCAR_L4_OC_third-deg)
- Pipelife Norge. (2002). Technical Catalogue for Submarine Installations of Polyethylene Pipes.
- Pipelife. (n.d.). World record for towing the line. Retrieved from Pipelife: <http://www.pipelife.com/com/news/573-world-record-for-towing-the-line.php>
- Plastics Pipe Institute . (2001). 3,000 FEET UNDER THE SEA. Retrieved from [https://plasticpipe.org/pdf/3000\\_feet\\_under\\_the\\_sea.pdf](https://plasticpipe.org/pdf/3000_feet_under_the_sea.pdf)
- Polymer Properties Database. (2015). TYPICAL POISSON'S RATIOS OF POLYMERS AT ROOM TEMPERATURE. Retrieved from [polymerdatabase.com: http://polymerdatabase.com/polymer%20physics/Poisson%20Table.html](http://polymerdatabase.com/polymer%20physics/Poisson%20Table.html)
- Qiang Bai, Y. B. (2014). Subsea Pipeline Design, Analysis and Installation.
- Renewable Energy Policy Network. (2017). Renewables 2017 Global Status Report - Infographics. Retrieved from <http://www.ren21.net/status-of-renewables/global-status-report/renewables-2017-global-status-report-infographics/>
- Strutt, J. V. (2002). BASIC HEAT TRANSFER AND SOME APPLICATIONS IN POLYMER.
- Takács, G. R.-I. (2012). Model Predictive Vibration Control. London: Springer.
- Techet, A. (2016). Derivation of Added Mass around a Sphere.
- The Guardian. (2015, October 26). World set to use more energy for cooling than heating. Retrieved from The Guardian: <https://www.theguardian.com/environment/2015/oct/26/cold-economy-cop21-global-warming-carbon-emissions>
- The Guardian. (2016, October 5). Paris Climate deal a 'turning point' in global warming fight. Retrieved from <https://www.theguardian.com/environment/2016/oct/05/obama-paris-climate-deal-ratification>
- Tidal Energy Today. (2017, June 19). Global map of OTEC plants comes to light. Retrieved from TidalEnergyToday.
- United Nations. (2018). Sustainable Development Goals. Retrieved from <https://www.un.org/sustainabledevelopment/sustainable-development-goals/>
- Van Nauta Lemke, K. H. (2017). Land-Based OTEC tests at MARIN.
- Vega, L. (2003). Ocean Thermal Energy Conversion Primer. Marine Technology Society Journal.
- Welleman. (2013). CTB2210 Constructiemechanica 3. Delft: TU Delft.
- Wikipedia. (2018). Viscoelasticity. Retrieved from Wikipedia: <https://en.wikipedia.org/wiki/Viscoelasticity>

# Appendix A

## Geometrically non-linear model derivations

This appendix presents the derivation of the geometrically nonlinear models that are used in this thesis. Firstly, the Euler-Bernoulli model is derived in 2D, after which it is extended to 3d. The system is modeled as elements with springs between the nodes to take into account axial elasticity and rotational springs are added to model the bending stiffness. A representation of the model is shown in Figure 27 in the main report. The last part of this appendix presents the derivation of the GNL Timoshenko model by Keijdener (2015). The degrees of freedom are described in a global axis coordinate system.

### A.1 2D geometrically non-linear Euler-Bernoulli model

#### A.1.1 Normal strain

As a first step, the strain of the beam in the axial direction is modeled. The derivation below results in a dynamic catenary model with springs in between two adjacent nodes. The starting point for the derivation is a generic piece of a continuous pipe along the neutral axis  $s$  in the global coordinate system, shown in Figure 79. The neutral axis is in the center of the beam because the cross-section of the pipe is symmetrical. The blue line indicates the cross-section, which is assumed to be perpendicular to the neutral axis.

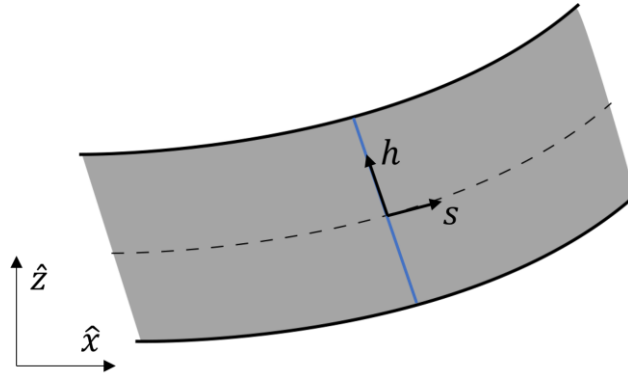


Figure 79: Continuous section of an Euler-Bernoulli beam with the cross section (blue) perpendicular to neutral axis

The Lagrangian for this continuous pipe section is given below:

$$L = P - K = \frac{1}{2} \int_{s-\frac{l}{2}}^{s+\frac{l}{2}} \int_{A(s)} (\rho V(s, h)^2 - \sigma(s, h) \varepsilon(s, h)^2) dA ds \quad (60)$$

Both the cross-section and the loading are assumed to be symmetric with respect to the x-z plane. The potential energy of a piece of the continuous beam due to axial strain is given by equation (61).

$$P_\epsilon = \frac{1}{2} \int_{s_n - \frac{l}{2}}^{s_n + \frac{l}{2}} \int_{A(s)} \sigma(s, h) \epsilon(s, h) dA ds \quad (61)$$

The continuous system can be discretized by using finite difference. With two nodes per element, the  $s$  dependency is removed by introducing equation (62) and (63):

$$x_j - x_i = l \frac{\delta x(s)}{\delta s} \Big|_{s=s_n} + O(l^2) \quad (62)$$

$$\frac{x_j + x_i}{2} = x(s) \Big|_{s=s_n} + O(l) \quad (63)$$

The same applies for all other properties such as  $z$ ,  $\sigma$  and  $\epsilon$ . Now the potential energy becomes:

$$P_{n,\epsilon} = \frac{l}{2} \int_A \sigma(h) \epsilon(h) dA \quad (64)$$

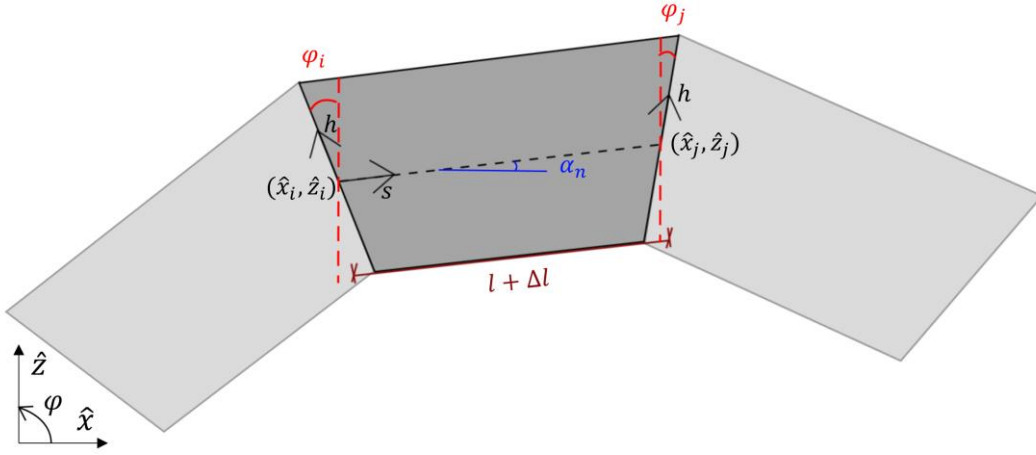


Figure 80: Discretized beam element with two adjacent elements

From Figure 80, the following kinematic relations are derived. In this figure,  $h$  is the axis along the cross section on nodes  $i$  and  $j$ .  $\varphi_i$  and  $\varphi_j$  are the angles between the cross sections in nodes  $i$  and  $j$  and the global  $\hat{z}$ -axis. Note that due to the assumption that the cross section is perpendicular to the neutral axis,  $\varphi_i$  and  $\varphi_j$  are a function of the angle  $\alpha_n$  and the angles  $\alpha$  of the adjacent elements  $n + 1$  and  $n - 1$ .

$$\begin{aligned} \hat{x}_i(h) &= x_i - h \sin(\varphi_i) \\ \hat{z}_i(h) &= z_i - h \cos(\varphi_i) \\ \hat{x}_j(h) &= x_j - h \sin(\varphi_j) \\ \hat{z}_j(h) &= z_j - h \cos(\varphi_j) \end{aligned} \quad (65)$$

Using these relations, the strain can be defined as a function of  $h$ :

$$\epsilon(h) = \frac{\Delta l_n(h)}{l} = \frac{1}{l} \left( \sqrt{\Delta X_n^2(h) + \Delta Z_n^2(h)} - l \right) \quad (66)$$

This means that the cross-section integral is equal to:

$$P_{n,\epsilon} = \frac{l}{2} \int_A \frac{E}{l^2} \Delta l_n^2(h) dA \quad (67)$$

Similar to the approach taken by Keijdener (2015), the squared elongation as a function of height is estimated by a Taylor series expansion around the center of the cross-section. In this way, the cross-section integral captures the same amount of energy as the potential energy equation (67) but it is truncated at a certain order  $\omega$  that equals the order of geometrically non-linearity. After this step, the solution is sought in such a way that the same amount of energy is captured by a number of springs between the nodes with a certain offset. He concluded that setting  $\omega$  equal to 1 already gives sufficiently accurate results when the same approach was used for a Timoshenko beam, which will be described in A.3. For this model,  $\omega$  is also set to 1 leading to a first order geometrically non-linear Euler-Bernoulli beam model. The solution for the cross-section integral in equation (67) is approximated by (Keijdener, 2015):

$$P_{n,\epsilon}^{(1)} = \frac{l EA}{2 l^2} (B_{n,0} + r_1 B_{n,1}) \quad (68)$$

Where  $r_1$  is the offset of the local s-axis to the neutral axis. The solution for the discrete spring system can be written as:

$$\hat{P}_{n,\epsilon}^{(1)} = \frac{l EA}{2 l^2} \sum_{q=1}^{Q_\epsilon} k_{n,q} (\hat{B}_{n,0} h^0 + \hat{B}_{n,1} h^1) \quad (69)$$

$k_{n,q}$  is a dimensionless scaling factor and  $h_{n,q}$  is the offset of the spring with respect to the reference axis.  $r_1$  is zero due to the fact that the pipe is symmetric with respect to the neutral axis. For a single axial spring in between two nodes, as shown in Figure 29 in the main report, this leads to the following set of equations:

$$\begin{cases} k_n h_n^0 = 1 \\ k_n h_n^1 = r_{1,n} \end{cases} \quad (70)$$

$h_n$  is zero for a pipe with a symmetric cross section and  $k_n$  is equal to 1. So the potential energy, equation (69) results in:

$$\begin{aligned} \hat{P}_{n,\epsilon}^{(1)} &= \frac{EA}{2} \int_l \left( \frac{\sqrt{(\hat{z}_j - \hat{z}_i)^2 + (\hat{x}_j - \hat{x}_i)^2} - l}{l} \right)^2 ds \\ &= \frac{EA}{2l} \left( \sqrt{(\hat{z}_j - \hat{z}_i)^2 + (\hat{x}_j - \hat{x}_i)^2} - l \right)^2 \end{aligned} \quad (71)$$

Now that the potential energy due to the axial elongation is determined, the kinetic energy can be defined:

$$K = \frac{\rho A}{2} \int_{s-\frac{l}{2}}^{s+\frac{l}{2}} (\dot{x}(s)^2 + \dot{z}(s)^2) ds \quad (72)$$

$$K = \frac{\rho A l}{2} (\dot{x}_n^2 + \dot{z}_n^2) \quad (73)$$

Where according to equation (63):

$$\dot{x}_n = \frac{\dot{x}_i + \dot{x}_j}{2} \quad (74)$$

$$\dot{z}_n = \frac{\dot{z}_i + \dot{z}_j}{2}$$

So that the total kinetic energy in the discretized form is described by:

$$K = \frac{\rho A l}{2} \left( \left( \frac{\dot{x}_i + \dot{x}_j}{2} \right)^2 + \left( \frac{\dot{z}_i + \dot{z}_j}{2} \right)^2 \right) = \frac{1}{8} \rho A l (\dot{x}_i^2 + 2\dot{x}_i\dot{x}_j + \dot{x}_j^2 + \dot{z}_i^2 + 2\dot{z}_i\dot{z}_j + \dot{z}_j^2) \quad (75)$$

Now both the kinetic energy and the potential energy of the element for elongation are derived. The equations of motion for the nodes of an element are derived from the Lagrangian.

$$L = K - P = \frac{1}{8} \rho A l (\dot{x}_i^2 + 2\dot{x}_i\dot{x}_j + \dot{x}_j^2 + \dot{z}_i^2 + 2\dot{z}_i\dot{z}_j + \dot{z}_j^2) - \frac{EA}{2l} \left( \sqrt{(\hat{z}_j - \hat{z}_i)^2 + (\hat{x}_j - \hat{x}_i)^2} - l \right)^2 \quad (76)$$

As an example, the equation of motion for the degree of freedom  $\hat{x}_i$  follows from Lagrange's equation:

$$\frac{d}{dt} \left( \frac{\delta L}{\delta \dot{\hat{x}}_i} \right) - \frac{\delta L}{\delta \hat{x}_i} = F_{\hat{x}_i}$$

$$\frac{d}{dt} \left( \frac{\delta L}{\delta \dot{\hat{x}}_i} \right) = \frac{\rho A l}{4} (\dot{x}_j + \dot{x}_i) \quad (77)$$

$$\frac{\delta L}{\delta \hat{x}_i} = -\frac{EA}{l} (\hat{x}_i - \hat{x}_j) \left( \frac{\sqrt{(\hat{z}_j - \hat{z}_i)^2 + (\hat{x}_j - \hat{x}_i)^2} - l}{\sqrt{(\hat{z}_j - \hat{z}_i)^2 + (\hat{x}_j - \hat{x}_i)^2}} \right)$$

So the total equation of motion for  $\hat{x}_i$  equals:

$$\frac{\rho A l}{4} (\ddot{x}_j + \ddot{x}_i) + \frac{EA}{l} (\hat{x}_i - \hat{x}_j) \left( \frac{\sqrt{(\hat{z}_j - \hat{z}_i)^2 + (\hat{x}_j - \hat{x}_i)^2} - l}{\sqrt{(\hat{z}_j - \hat{z}_i)^2 + (\hat{x}_j - \hat{x}_i)^2}} \right) = F_{\hat{x}_i} \quad (78)$$

$$\Delta x = \hat{x}_j - \hat{x}_i$$

$$l_c = \sqrt{(\hat{z}_j - \hat{z}_i)^2 + (\hat{x}_j - \hat{x}_i)^2} \quad (79)$$

$l_c$  is the length of the element including strain. Equation (79) can be written in a more compact way by substituting equation (79) in equation (78).

$$\frac{\rho Al}{4} (\ddot{x}_j + \ddot{x}_i) - \frac{\Delta x EA(l_c - l)}{l * l_c} = F_{\hat{x}_i}$$

$$\frac{\rho Al}{4} (\ddot{x}_j + \ddot{x}_i) + \frac{\Delta x EA(l_c - l)}{l * l_c} = F_{\hat{x}_j}$$

$$\frac{\rho Al}{4} (\ddot{z}_j + \ddot{z}_i) - \frac{\Delta z EA(l_c - l)}{l * l_c} = F_{\hat{z}_i}$$

$$\frac{\rho Al}{4} (\ddot{z}_j + \ddot{z}_i) + \frac{\Delta z EA(l_c - l)}{l * l_c} = F_{\hat{z}_j}$$
(80)

This means that the stiffness term is dependent on the state of the pipeline. Consequently, it is not possible to construct a linear stiffness matrix in order to solve the system. Note that by this single spring between two nodes, bending effects proportional to EI cannot be included. This is included in the next section.

### A.1.2 Bending stiffness

Next, the bending stiffness of the pipe is implemented in the model. As mentioned before, the assumptions for an Euler-Bernoulli beam are used. This means that the cross-section is perpendicular to the neutral axis such that  $\varphi_i$  and  $\varphi_j$  in Figure 80 are a function of the orientation of the adjacent elements. The contribution of the bending stiffness in the equation of motion is derived below.

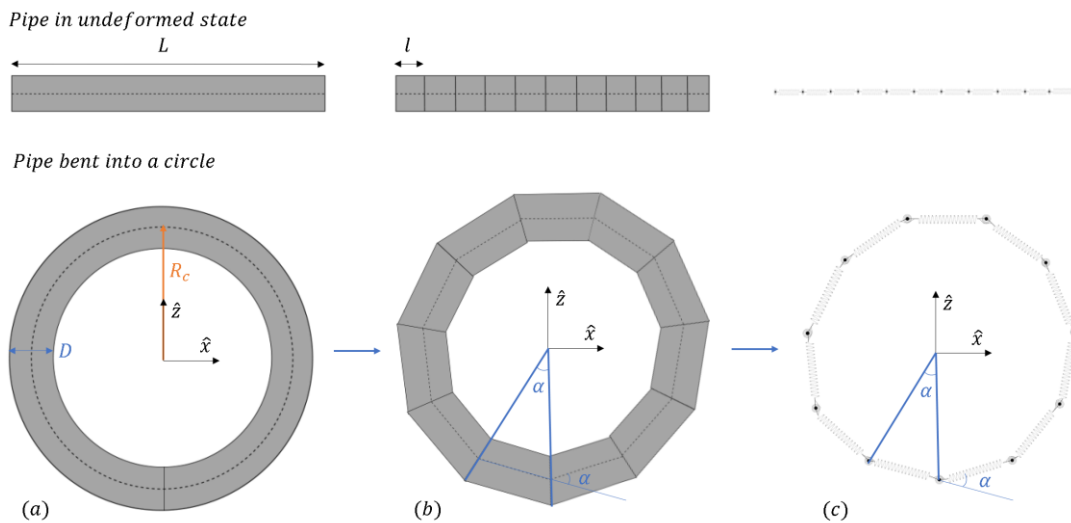


Figure 81: Pipe with length L bent into a circle (a) continuous pipe section (b) pipe discretized in elements (c) model

Firstly, imagine a continuous pipe bent in a full circle with radius  $R_c$  as depicted in Figure 81 (a). The pipe has a cross-section  $A$  and length  $L$ . This means that the length of the middle, outer and inner fibers are:

$$\begin{aligned}
 L_0 &= 2\pi R_c \\
 L_{outer} &= 2\pi \left( R_c + \frac{D}{2} \right) \\
 L_{inner} &= 2\pi \left( R_c - \frac{D}{2} \right)
 \end{aligned} \tag{81}$$

Where  $D$  is the cross-sectional diameter of the pipe. So the strain on the outside and inside of the pipe is defined by:

$$\begin{aligned}
 \varepsilon_{outer} &= \frac{L_{outer} - L_0}{L_0} = \frac{2\pi \left( R_c + \frac{D}{2} \right) - 2\pi R_c}{2\pi R_c} = \frac{D}{2R_c} \\
 \varepsilon_{inner} &= -\varepsilon_{outer} = -\frac{D}{2R_c}
 \end{aligned} \tag{82}$$

The strain over the height of the cross-section (as a function of  $z$ ) is:

$$\varepsilon(z) = \frac{z}{R_c} \tag{83}$$

The moment in the cross section can now be written as:

$$\int_{-\frac{D}{2}}^{\frac{D}{2}} \int_{-\frac{D}{2}}^{\frac{D}{2}} \sigma z \, dz dy = \int_{-\frac{D}{2}}^{\frac{D}{2}} \int_{-\frac{D}{2}}^{\frac{D}{2}} \left( E \frac{z}{R_c} \right) z \, dz dy = \frac{EI}{R_c} \tag{84}$$

So, if the pipe is inclined at one side and this moment is added at the end of the pipe, it should bend in a full circle. This is used to verify whether the springs were correctly added in the MATLAB model. The moment can be written as:

$$M = \frac{2\pi EI}{L_0} \tag{85}$$

This principle can be used to add rotational springs to the nodes to include bending stiffness. The principle is shown in Figure 81 (a) and (b). The moment in a node due to the bending stiffness is calculated as:

$$M = k_r \alpha \tag{86}$$

With the rotational stiffness:

$$k_r = \frac{EI}{l} \quad (87)$$

This formula can be interpreted as the curvature of the beam multiplied by the bending stiffness EI. The rotational spring can be decomposed in forces on the nodes, perpendicular to the element as shown in Figure 82.

$$\begin{aligned} F_{i-1}l + F_{i+1}l &= 2M \\ F_m l &= M \\ F_M &= \frac{M}{l} = \frac{EI}{l^2} \alpha \end{aligned} \quad (88)$$

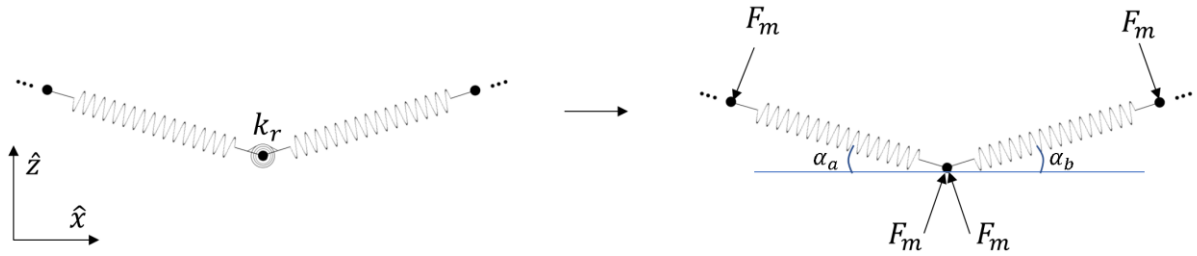


Figure 82: Two adjacent elements with forces due to bending moment

Because a global coordinate system is used, the angle  $\alpha$  can be written as a function of the node coordinates  $\hat{x}_{i-1}$ ,  $\hat{x}_i$ ,  $\hat{x}_{i+1}$ ,  $\hat{z}_{i-1}$ ,  $\hat{z}_i$  and  $\hat{z}_{i+1}$ .

$$\begin{aligned} \alpha &= \alpha_a + \alpha_b \\ \alpha_a &= \text{atan}\left(-\frac{\Delta y_1}{\Delta x_1}\right) \\ \alpha_b &= \text{atan}\left(\frac{\Delta y_2}{\Delta x_2}\right) \end{aligned} \quad (89)$$

Now the forces can be added to the model by taking into account that they are perpendicular to the neutral axis of the element.

$$\begin{aligned} F_{\hat{x}_{i-1}} &= F_M \sin(\alpha_a) \\ F_{\hat{z}_{i-1}} &= -F_M \cos(\alpha_a) \\ F_{\hat{x}_{i+1}} &= F_M \sin(\alpha_b) \\ F_{\hat{z}_{i+1}} &= -F_M \cos(\alpha_b) \\ F_{\hat{x}_i} &= -F_M \sin(\alpha_a) - F_M \sin(\alpha_b) \\ F_{\hat{z}_i} &= F_M \cos(\alpha_a) + F_M \cos(\alpha_b) \end{aligned} \quad (90)$$

The forces on node  $i$  are opposite to balance the force equilibrium. These forces can now be added to the equation of motion (80) of an element. Note that in MATLAB, the `atan2` function must be used in order to take into account bending in all angles, i.e. making it possible to bend the pipe into a full circle.

### A.1.3 Hydrostatic force

The implementation of the hydrostatic force was discussed in section 2.4.4 and 3.3.2 in the main report. The force vector resulting from formula (18) is obtained for each node by multiplying the force per unit length by the element length. In order to show how the direction of the hydrostatic force was calculated, the calculation of vectors  $\mathbf{t}$  and  $\mathbf{n}$  in equation (18) is clarified. Two neighboring elements are shown in Figure 83. In order to calculate  $\mathbf{t}$ , vector  $\overrightarrow{AC}$  simply must be normalized, which implies that the vector  $\mathbf{t}$  is perpendicular to the discretized neutral axis ABC. Unit vector  $\mathbf{n}$  is calculated by normalizing the unit vector that was used for the force decomposition shown on the right hand side in Figure 82. The two red vectors  $\mathbf{F}_m$  are summed and normalized to obtain the vector pointing to the centre of curvature. The same is done in the 3D case by extending the vectors to 3D.

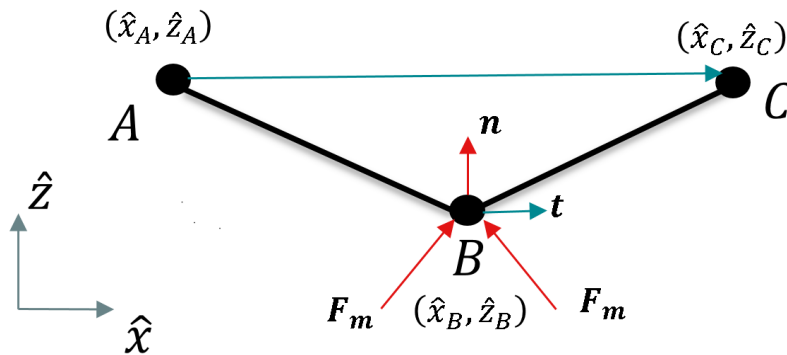


Figure 83: Calculation of unit vectors  $\mathbf{t}$  and  $\mathbf{n}$

Furthermore, an end cap force is added on the pipe end in the axial direction of the pipe. This force can be decomposed in the  $x$ ,  $y$  and  $z$  direction based on the state of the pipe.

### A.1.4 Hydrodynamic drag force

The relative velocity formulation (15) is used to incorporate the hydrodynamic forces. Due to the quadratic nature of the drag force, this force is not straightforward to decompose in the global  $\hat{x}$  and  $\hat{z}$  directions. Figure 84 is used to implement this in the two-dimensional space. Firstly, it is assumed that the velocity  $\dot{x}_i$  and  $\dot{y}_i$  in node  $i$  is representative for half of the element, which is the solid black line in Figure 84. Similarly, the water particle velocity  $u_i$  and  $w_i$  are calculated at the location of node  $i$ . The relative velocity vector can be computed by:

$$\vec{v}_r = \vec{u}_i + \vec{w}_i - \dot{\vec{x}}_i - \dot{\vec{z}}_i \quad (91)$$

The drag force is perpendicular to the element. Therefore, the relative velocity is projected on the element by vector projection. Take the axial direction of the element  $\vec{n}$ . The scalar projection of the relative velocity vector is calculated by:

$$v_{r_{par}} = \frac{\vec{v}_r \cdot \vec{n}}{|\vec{n}|} \quad (92)$$

This scalar projection is used to calculate the vector projection of vector  $\vec{v}_r$  on  $\vec{n}$ .

$$\vec{v}_{r_{par}} = v_{r_{par}} \vec{n}_{unit} \quad (93)$$

Where  $\vec{n}_{unit}$  is the unit vector in the axial direction of the element. The vector  $\vec{v}_{r_{perp}}$  perpendicular to the element is calculated by:

$$\vec{v}_{r_{perp}} = \vec{v}_r - \vec{v}_{r_{par}} \quad (94)$$

Now the magnitude of the drag force on node  $i$  can be calculated:

$$F_{Di} = \frac{1}{2} \rho_w C_d D \frac{1}{2} \sqrt{(\hat{x}_j - \hat{x}_i)^2 + (\hat{z}_j - \hat{z}_i)^2} |\vec{v}_{r_{perp}}|^2 \quad (95)$$

Where the total force vector in  $\hat{x}$  and  $\hat{z}$  direction is determined by multiplying the magnitude of the force by the unit vector of  $\vec{v}_{r_{perp}}$ .

$$\vec{F}_{Di} = F_{Di} \frac{\vec{v}_{r_{perp}}}{|\vec{v}_{r_{perp}}|} \quad (96)$$

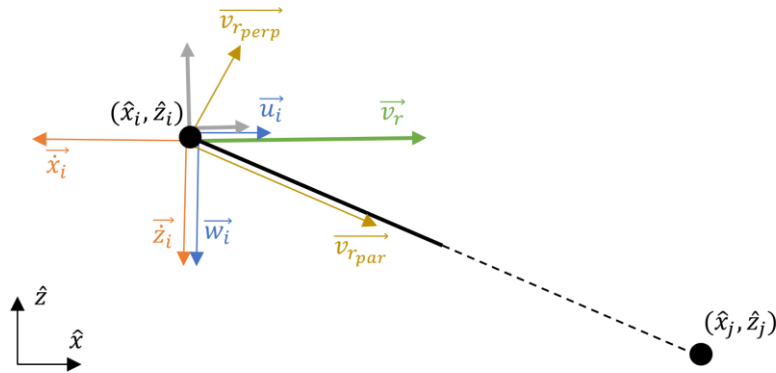


Figure 84: Principle of relative velocity formulation in 2D space

The same procedure holds for the drag force on node  $j$ . Note that the drag force perpendicular to the element could have also been calculated by using sines and cosines. However, this procedure is explained here because a trivial procedure is used for the relative velocity formulation in 3d space.

### A.1.5 Hydrodynamic inertia force

When the pipes moves through a fluid, some fluid will also move around it. The same goes for the acceleration of the fluid. The direction of this so called added mass is also state dependent. The hydrodynamic force can be found by integrating the pressure over the area of an element of the pipe (Techet, 2016). For the one dimensional case this results in:

$$m_a = \rho_w \pi R^2 l \quad (97)$$

It is assumed that the pipe is in an infinitely large body of fluid, far away from boundaries. This assumption is increasingly incorrect when the pipe gets closer to the seabed. For an element in the two dimensional space, the added mass terms are given by:

$$\begin{aligned} F_{add \hat{x}_i} &= C_a \frac{\rho_w \pi R_p^2}{4} \Delta z (\ddot{x}_j + \ddot{x}_i) \\ F_{add \hat{x}_j} &= C_a \frac{\rho_w \pi R_p^2}{4} \Delta z (\ddot{x}_j + \ddot{x}_i) \\ F_{add \hat{z}_i} &= C_a \frac{\rho_w \pi R_p^2}{4} \Delta x (\ddot{z}_j + \ddot{z}_i) \\ F_{add \hat{z}_j} &= C_a \frac{\rho_w \pi R_p^2}{4} \Delta x (\ddot{z}_j + \ddot{z}_i) \end{aligned} \quad (98)$$

So for a horizontal element  $\Delta z$  is zero and as a result there is only mass in the z-direction. Note that the first inertia term (Froude Krilov) from equation (15) is not taken into account in the equation of motion because there are no water particle accelerations in a stationary flow, which will be considered in this thesis.

### A.1.6 Material damping

The material damping derived above was compared to the magnitude of the drag force for a conservatively large value of the damping ratio  $\tan \delta$ . Model runs with and without material damping showed that the influence of the material damping is negligible compared to the damping resulting from the hydrodynamic drag force. More on material damping can be found in Appendix C.

### A.1.7 Seabed

The foundation soil interaction is important for the pipe during both installation and operating conditions. The soil around the pipe is disturbed and difficult to predict because the changes in the strength and stiffness of the soil are highly dependent on the motions during the pipe installation. Laboratory tests or in situ tests are required to evaluate the soil properties at a certain location.

For the conceptual design stage in this thesis, the seabed is modelled by springs and dashpots that activate as soon as a nodal coordinate crosses the seabed. The resulting seabed force is computed as a function of the nodal velocity and position with respect to the seabed. It is assumed that the pipe does not slide as soon as it is on the seabed.

## A.2 3D extension GNL Euler-Bernoulli model

This section summarizes the extension from 2D to 3D. Firstly for the pipe, after which the implementation of the hydrodynamic forces is discussed.

As the loads in lateral direction due to the currents and waves are expected to influence the pipe deflection during installation significantly, the model is extended to 3D. Therefore, a derivation similar to the 2D case was applied, starting from equation (99) similar to equation (76).

$$L = K - P = \frac{1}{8} \rho Al (\dot{x}_i^2 + 2\dot{x}_i\dot{x}_j + \dot{x}_j^2 + \dot{y}_i^2 + 2\dot{y}_i\dot{y}_j + \dot{y}_j^2 + \dot{z}_i^2 + 2\dot{z}_i\dot{z}_j + \dot{z}_j^2) - \frac{EA}{2l} \left( \sqrt{(\hat{z}_j - \hat{z}_i)^2 + (\hat{y}_j - \hat{y}_i)^2 + (\hat{x}_j - \hat{x}_i)^2} - l \right)^2 \quad (99)$$

The derivation results in similar equations of motion to the 2D model. The equations of motion for the axial elongation are:

$$\begin{aligned} \frac{\rho Al}{4} (\ddot{x}_j + \ddot{x}_i) - \frac{\Delta x EA (l_c - l)}{l * l_c} &= F_{\hat{x}_i} \\ \frac{\rho Al}{4} (\ddot{x}_j + \ddot{x}_i) + \frac{\Delta x EA (l_c - l)}{l * l_c} &= F_{\hat{x}_j} \\ \frac{\rho Al}{4} (\ddot{y}_j + \ddot{y}_i) - \frac{\Delta y EA (l_c - l)}{l * l_c} &= F_{\hat{y}_i} \\ \frac{\rho Al}{4} (\ddot{y}_j + \ddot{y}_i) + \frac{\Delta y EA (l_c - l)}{l * l_c} &= F_{\hat{y}_j} \\ \frac{\rho Al}{4} (\ddot{z}_j + \ddot{z}_i) - \frac{\Delta z EA (l_c - l)}{l * l_c} &= F_{\hat{z}_i} \\ \frac{\rho Al}{4} (\ddot{z}_j + \ddot{z}_i) + \frac{\Delta z EA (l_c - l)}{l * l_c} &= F_{\hat{z}_j} \end{aligned} \quad (100)$$

Where:

$$l_c = \sqrt{(\hat{z}_j - \hat{z}_i)^2 + (\hat{y}_j - \hat{y}_i)^2 + (\hat{x}_j - \hat{x}_i)^2} \quad (101)$$

To include the bending stiffness in three dimensions, a different approach is used to determine the direction and magnitude of the bending force. Vector projection and the cosine rule are used to determine the direction and the force direction and magnitude in 3D space and is explained in section 3.3 in the main report. The moment in the pipe is decomposed into forces in the three dimensional global axis coordinate system and are a function of the degrees of freedom (3D nodal coordinates).

The hydrodynamic drag force uses the same procedure as explained for the 2D case. Equation (91) to (96) are also valid for the 3D case, when the vectors are extended from two dimensions to three.

The hydrodynamic inertia force for the 3D model is similar to equation (98):

$$\begin{aligned}
F_{add\hat{x}_i} &= C_a \frac{\rho_w \pi R_p^2}{4} \frac{\sqrt{dy^2 + dz^2}}{\sqrt{dx^2 + dy^2 + dz^2}} (\ddot{x}_j + \ddot{x}_i) = A_x (\ddot{x}_j + \ddot{x}_i) \\
F_{add\hat{x}_j} &= C_a \frac{\rho_w \pi R_p^2}{4} \frac{\sqrt{dy^2 + dz^2}}{\sqrt{dx^2 + dy^2 + dz^2}} (\ddot{x}_j + \ddot{x}_i) = A_x (\ddot{x}_j + \ddot{x}_i) \\
F_{add\hat{y}_i} &= C_a \frac{\rho_w \pi R_p^2}{4} \frac{\sqrt{dx^2 + dz^2}}{\sqrt{dx^2 + dy^2 + dz^2}} (\ddot{y}_j + \ddot{y}_i) = A_y (\ddot{y}_j + \ddot{y}_i) \\
F_{add\hat{y}_j} &= C_a \frac{\rho_w \pi R_p^2}{4} \frac{\sqrt{\Delta x^2 + \Delta z^2}}{\sqrt{\Delta x^2 + \Delta y^2 + \Delta z^2}} (\ddot{y}_j + \ddot{y}_i) = A_y (\ddot{y}_j + \ddot{y}_i) \\
F_{add\hat{z}_i} &= C_a \frac{\rho_w \pi R_p^2}{4} \frac{\sqrt{\Delta x^2 + \Delta y^2}}{\sqrt{\Delta x^2 + \Delta y^2 + \Delta z^2}} (\ddot{z}_j + \ddot{z}_i) = A_z (\ddot{z}_j + \ddot{z}_i) \\
F_{add\hat{z}_j} &= C_a \frac{\rho_w \pi R_p^2}{4} \frac{\sqrt{\Delta x^2 + \Delta y^2}}{\sqrt{\Delta x^2 + \Delta y^2 + \Delta z^2}} (\ddot{z}_j + \ddot{z}_i) = A_z (\ddot{z}_j + \ddot{z}_i)
\end{aligned} \tag{102}$$

## Summary

Now that all forces in the equation of motion are derived, they can be implemented in Matlab.

The total equation of motion for one element becomes:

$$\begin{aligned}
\left(\frac{\rho Al}{4} + A_x\right) (\ddot{x}_j + \ddot{x}_i) - \frac{\Delta x EA(l_c - l)}{l * l_c} + F_{\hat{x},bend,i} &= F_{\hat{x},drag,i} + F_{\hat{x},hs,i} + F_{\hat{x}_i} \\
\left(\frac{\rho Al}{4} + A_x\right) (\ddot{x}_j + \ddot{x}_i) + \frac{\Delta x EA(l_c - l)}{l * l_c} + F_{\hat{x},bend,j} &= F_{\hat{x},drag,j} + F_{\hat{x},hs,j} + F_{\hat{x}_j} \\
\left(\frac{\rho Al}{4} + A_y\right) (\ddot{y}_j + \ddot{y}_i) - \frac{\Delta y EA(l_c - l)}{l * l_c} + F_{\hat{y},bend,i} &= F_{\hat{y},drag,i} + F_{\hat{y},hs,i} + F_{\hat{y}_i} \\
\left(\frac{\rho Al}{4} + A_y\right) (\ddot{y}_j + \ddot{y}_i) + \frac{\Delta y EA(l_c - l)}{l * l_c} + F_{\hat{y},bend,j} &= F_{\hat{y},drag,j} + F_{\hat{y},hs,j} + F_{\hat{y}_j} \\
\left(\frac{\rho Al}{4} + A_z\right) (\ddot{z}_j + \ddot{z}_i) - \frac{\Delta z EA(l_c - l)}{l * l_c} + F_{\hat{z},bend,i} &= F_{\hat{z},drag,i} + F_{\hat{z},hs,i} + F_{\hat{z},g,i} + F_{\hat{z}_i} \\
\left(\frac{\rho Al}{4} + A_z\right) (\ddot{z}_j + \ddot{z}_i) + \frac{\Delta z EA(l_c - l)}{l * l_c} + F_{\hat{z},bend,j} &= F_{\hat{z},drag,j} + F_{\hat{z},hs,j} + F_{\hat{z},g,j} + F_{\hat{z}_j}
\end{aligned} \tag{103}$$

The first term is the inertia of the pipe plus the added mass. The second term is models the axial strain of the pipe. The third term is the force due to the bending moment. It must be noted that the bending force is included here and is a function the coordinates of the nodes next to node  $i$  and  $j$ , as described above. The bending forces are incorporated in the equation of motion of an element as a function of the coordinates of neighboring elements. It is not a function of the degrees of freedom of the element itself, such as most other terms in equation (47). The

first term on the right hand side of the equations are the drag force components. The second term is the hydrostatic pressure force which, similar to the bending force, is dependent on the curvature of the pipe and thus the surrounding elements. This term is implemented similarly tot the implementation in 2D, discussed in A.1.3, but now the resulting force vector is a vector in 3D space. The resulting force vector is again decomposed in the  $\hat{x}$ ,  $\hat{y}$  and  $\hat{z}$  direction and added in the equations of motion above. In the equations of motion in the  $\hat{z}$  direction, the gravity force is added which is a result of the weight in air. The last terms in the equation are possible external forces. An ODE solver in MATLAB is used to solve the system of ODEs.

### A.3 2D geometrically non-linear Timoshenko model

As the Euler-Bernoulli model derived above does not take into account shear deformation, a geometrically non-linear Timoshenko beam is derived similarly to the derivation of Keijdener (2015). The cross sections in nodes  $i$  and  $j$  are not necessarily perpendicular to the neutral axis and are thus degrees of freedom.

The kinetic energy follows from the following equation:

$$K = \frac{\rho l}{2} \int (\dot{x}_n^2 + \dot{z}_n^2) dA$$

$$\dot{x}_n = \frac{1}{2} (\dot{x}_i - h \cos(\varphi_i) \dot{\varphi}_i + \dot{x}_j - h \cos(\varphi_j) \dot{\varphi}_j) \quad (104)$$

$$\dot{z}_n = \frac{1}{2} (\dot{z}_i - h \sin(\varphi_i) \dot{\varphi}_i + \dot{z}_j - h \sin(\varphi_j) \dot{\varphi}_j)$$

The kinetic energy is defined below.

$$K = \frac{I \rho l}{8} \left( (-\cos(\varphi_i) \dot{\varphi}_i - \cos(\varphi_j) \dot{\varphi}_j)^2 + (-\sin(\varphi_i) \dot{\varphi}_i - \sin(\varphi_j) \dot{\varphi}_j)^2 \right) + \frac{1}{8} \rho A l (\dot{x}_i^2 + 2\dot{x}_i \dot{x}_j + \dot{x}_j^2 + \dot{z}_i^2 + 2\dot{z}_i \dot{z}_j + \dot{z}_j^2) \quad (105)$$

The potential energy for the elongation, bending and shear are defined by:

$$\hat{P}_{n,\epsilon} = \frac{EA}{2l} \left( \sqrt{(\hat{z}_j - \hat{z}_i)^2 + (\hat{x}_j - \hat{x}_i)^2} - l \right)^2$$

$$\hat{P}_{n,b} = \frac{l EI}{2 l^2} \phi_x^2 = \frac{EI}{2l} (\varphi_j - \varphi_i)^2 \quad (106)$$

$$\hat{P}_{n,\gamma} = \frac{LAG\kappa}{2} \gamma_n^2 = \frac{LAG\kappa}{2} \left( \text{atan} \left( \frac{z_j - z_i}{x_j - x_i} \right) - \frac{\varphi_i}{2} - \frac{\varphi_j}{2} \right)^2$$

Making use of Figure 80, the following Lagrangian is defined:



Note that the mass matrix is state depending. Besides this mass matrix, the derivation results in a non-square centrifugal matrix times a vector of the rotational velocities squared. From the implemented model it showed that this non-square centrifugal matrix could be neglected as the resulting forcing is in the order of 10E-7 percent of the other forcing terms for the cross section rotation.

$$\begin{array}{c}
 \left. \begin{array}{cc}
 & \begin{array}{c} 0 \\ 0 \\ 0 \\ 0 \\ 0 \\ 0 \end{array} \\
 -1/4 \left[ \begin{array}{c} \\ \\ \\ \\ \\ \\ \\ \end{array} \right. & \begin{array}{c} 0 \\ 0 \\ l\rho I(-\cos(\varphi_i)\cos(\varphi_j) + \sin(\varphi_i)\sin(\varphi_j)) \\ 0 \\ 0 \\ 0 \\ 0 \end{array} \\
 & \left. \begin{array}{c} \\ \\ \\ \\ \\ \\ \\ \end{array} \right] \begin{array}{c} \phi_i^2 \\ \phi_j^2 \end{array} \\
 \end{array} \quad (110)
 \end{array}$$

### Potential contributions

The potential contribution from the elongation is the same as equation (77). The forces in the equation of motion due to the shear deformation are:

$$\begin{aligned}
 \frac{\delta L}{\delta x_i} &= -\frac{lAG\kappa \left( \text{atan}\left(\frac{dz}{dx}\right) - \frac{\varphi_j}{2} - \frac{\varphi_i}{2} \right)}{dx^2 \left( \frac{dz^2}{dx^2} + 1 \right)} dz \\
 \frac{\delta L}{\delta x_j} &= -\frac{\delta L}{\delta x_i} \\
 \frac{\delta L}{\delta z_i} &= \frac{lAG\kappa \left( \text{atan}\left(\frac{dz}{dx}\right) - \frac{\varphi_j}{2} - \frac{\varphi_i}{2} \right)}{dx \left( \frac{dz^2}{dx^2} + 1 \right)} \\
 \frac{\delta L}{\delta z_j} &= -\frac{\delta L}{\delta z_i} \\
 \frac{\delta L}{\delta \varphi_i} &= \frac{lAG\kappa \left( \arctan\left(\frac{z_j - z_i}{x_j - x_i}\right) - \frac{\varphi_j}{2} - \frac{\varphi_i}{2} \right)}{2} + EI \left( \frac{\varphi_j}{2} - \frac{\varphi_i}{2} \right) \\
 \frac{\delta L}{\delta \varphi_i} &= -\frac{\delta L}{\delta \varphi_j}
 \end{aligned} \quad (111)$$

## Appendix B Model verification

To verify the model that was implemented in MATLAB, several tests cases are checked for the different models. These are described below.

### B.1 2D geometrically non-linear Euler-Bernoulli model

#### B.1.1 Axial Stiffness

First of all, the implementation of the springs in axial direction was checked. This was done by inclining the pipe, implemented with the equations of motion for a set of catenary elements, given in equation (29). The maximum elongation was checked with the following formula for the elongation of a spring:

$$u = \frac{F}{k} = \frac{FL}{EA} \quad (112)$$

When the force was applied in different directions, the pipe/catenary consequentially turned in the correct orientation with the expected elongation. Appendix C discusses the implementation of the catenary equations, including material damping. Numerical values of the implementation can be found in Figure 95.

#### B.1.2 Bending Stiffness

The next step is to see whether the bending stiffness is implemented correctly, which is described by equation (34). An inclined section of the pipe is loaded on its tip, shown in Figure 85. The total static tip deflection is calculated by:

$$w_2 = \frac{Fl^3}{3EI} \quad (113)$$

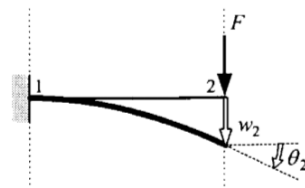


Figure 85: Inclined beam (Welleman, 2013)

The analytical solution for the natural frequency is calculated with equation (115).

$$f_1 = \frac{1.875^2}{2\pi L^2} \sqrt{\frac{EI}{\rho A}} \quad (114)$$

$$f_2 = \frac{4.694^2}{2\pi L^2} \sqrt{\frac{EI}{\rho A}}$$

$$f_3 = \frac{7.854^2}{2\pi L^2} \sqrt{\frac{EI}{\rho A}}$$

The numerical results are shown for a section of a pipe in Figure 86. In this figure, one can notice that the tip deflection oscillates in cycles with a natural period that is equal to the analytical solution. It is oscillating around the static tip deflection with an amplitude equal to the static tip deflection.

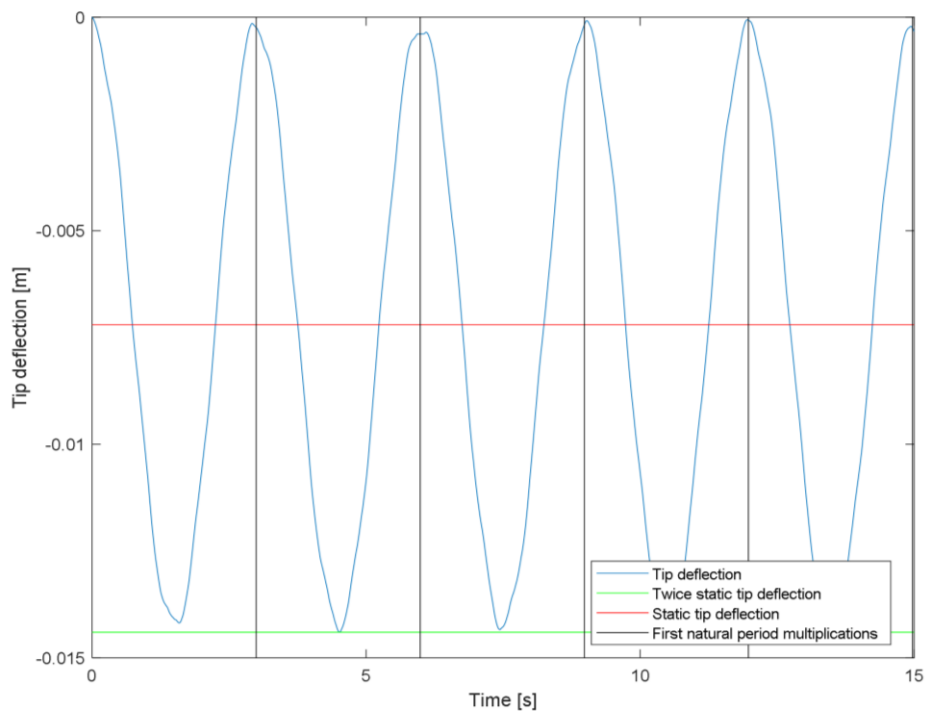


**Figure 86: Tip deflection cantilever EB beam. D=4.38m, L=50m, 15 nodes, E=1050MPa, F=1kN**

The oscillation is not a perfect sine. This is due to the fact that there is energy in multiple modes. To see what natural frequencies are present in the system, a fast Fourier transform (FFT) is applied to the tip deflection. Note that this is done because there is no linear stiffness matrix in the system. The results of the FFT is shown in Figure 87, which shows that there is energy in the system for the natural frequencies given in equation (115).

**Fast fourrier transform of the tip deflection of clamped 2d/3d Euler-Bernoulli beam model**

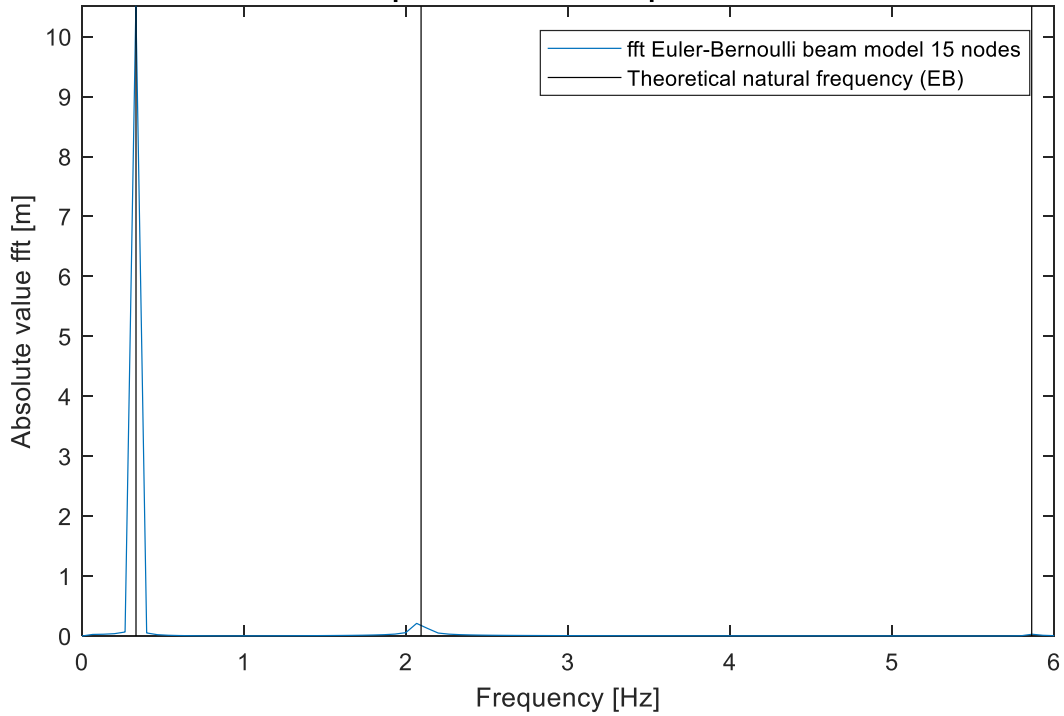


**Figure 87: Fast Fourier transform of tip deflection**

The reason for applying a geometrically non-linear Euler-Bernoulli model is that the pipe will experience large deflections. Therefore, it is verified whether the model is able to capture large deflections as intended. To do this, a cantilever pipe section is loaded on the tip by a moment given by equation (85). This should make the pipe roll up in a circle, which is verified in MATLAB and is shown in Figure 87.

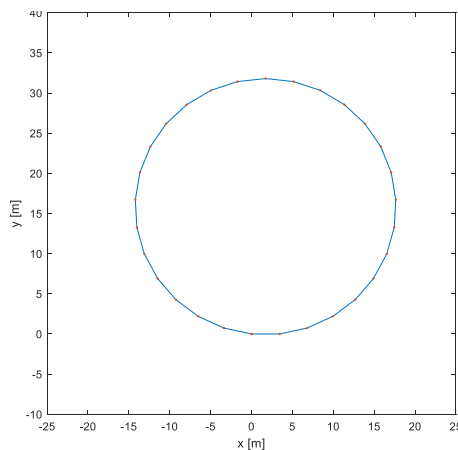


**Figure 88: Discretized pipe implemented in MATLAB and bent in full circle. L=100m, D=3m, 30 nodes**

### B.1.3 Hydrodynamic loading

The falling velocity of the pipe was checked as a step to check whether the hydrodynamic drag force was implemented correctly.

$$v_f = \sqrt{\frac{W_{sub}}{C_d D \frac{1}{2} \rho_w}} \quad (115)$$

## B.2 3D geometrically non-linear Euler-Bernoulli Beam Model

In order to verify the 3D implementation, the model is compared to the 2D implementation. A model run is performed with the following input for both the 2D and 3D model:

Table 6: Model input 2d/3d comparison

Seawater Density	$\rho_{sw}$	1026.6	kg/m <sup>3</sup>
Drag coefficient pipe	$C_d$	1.2	-
Pipe length	$L$	4000	m
Seabed slope	$s$	1/4	-
Inner pipe diameter	$D_i$	4	m
Outer pipe diameter	$D_o$	4.381	m
Modulus of elasticity	$E$	1050	MPa
Number of nodes	$nn$	25	-

Both the 2D and 3D model are used for a “freefall” pipe installation run where the pipe is sunk from the water surface without any external loading except for gravity and the hydrodynamic forces. In order to verify whether the three dimensional model is able to capture the dynamics in 3D, the pipe was model is ran with different three dimensional conditions:

- Gravity in z-direction
- Gravity in y-direction
- Gravity in z-direction, pipe initial conditions with an angle in x-y plane

Figure 89 shows the difference between the 2d and 3d geometrically non-linear Euler-Bernoulli model for a model run with 25 nodes. The difference between the 2D and 3D model are negligible. The small difference between the 2D and 3D models occurs due to numerical rounding of numbers and due to iteration precision during the solving procedure of the ODE.

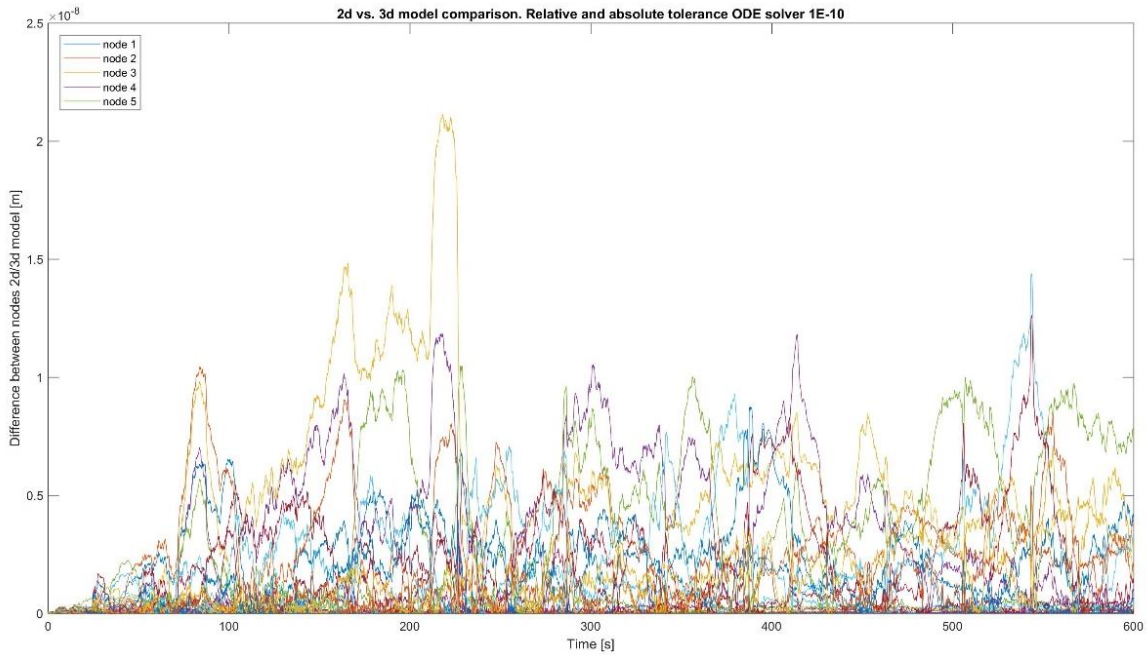


Figure 89: 2D and 3D model comparison for 600s freefall model run seabed. Relative and absolute tolerance ODE is 1E-4

### B.3 2D geometrically non-linear Timoshenko model

Similar to the Euler-Bernoulli model, the Timoshenko beam model is checked by inclining the beam and loading it with a tip load as shown in Figure 85. The tip deflection is shown in Figure 90, where the tip deflection for the Timoshenko model is compared to the Euler-Bernoulli model. Figure 91 shows the corresponding fast Fourier transform of the tip deflection. The results are similar and the models are comparable. The natural frequencies for the Timoshenko model are slightly lower than the analytical Euler-Bernoulli beam natural frequencies. This is due to the fact that both models are based on different assumptions. A Timoshenko beam is less stiff than an Euler-Bernoulli beam. This justifies the lower natural frequencies that were obtained with the Timoshenko beam model.

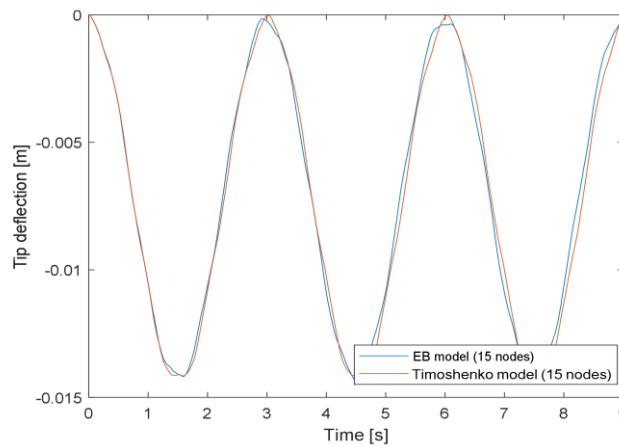


Figure 90: Tip deflection cantilever Timoshenko beam vs. Euler-Bernoulli beam.  $D=4.38\text{m}$ ,  $L=50\text{m}$ , 15 nodes,  $E=1050\text{MPa}$ ,  $F=1\text{kN}$

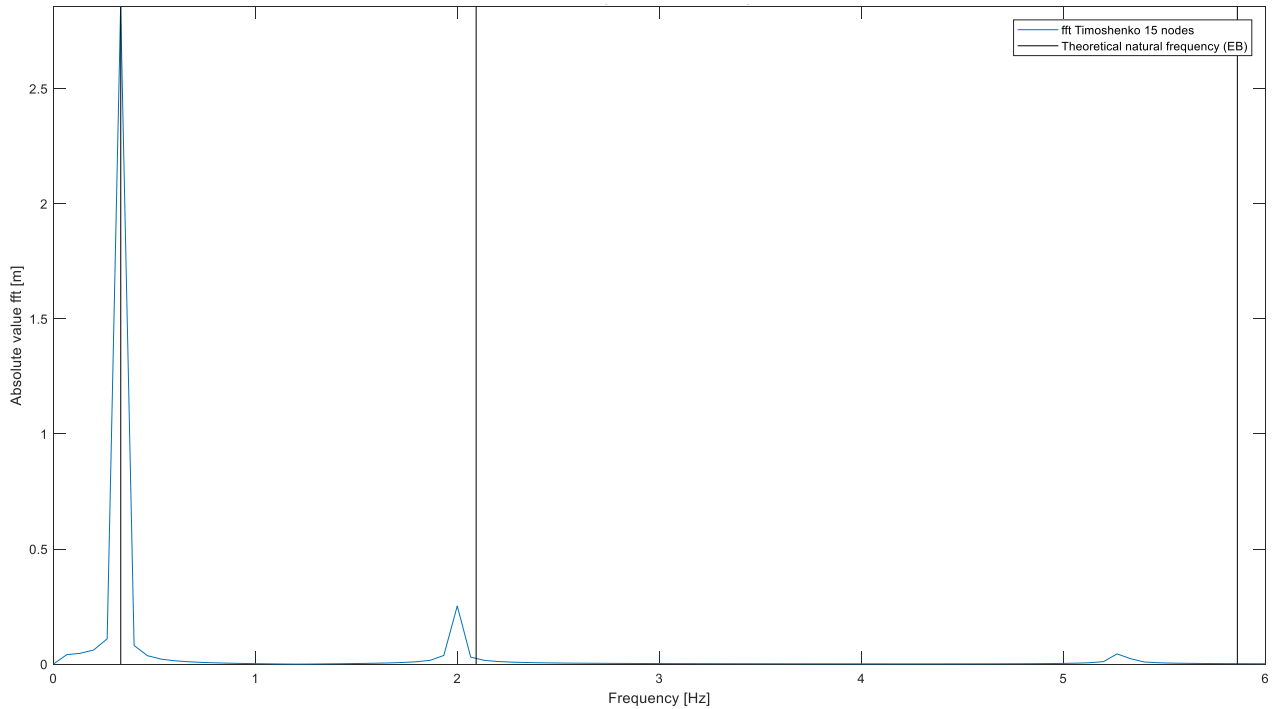


Figure 91: Fast Fourier transform tip deflection Timoshenko beam model

#### B.4 Hydrostatic pressure implementation

In order to check the implementation of the hydrostatic pressure, two cases are checked. Firstly the case where the pipe is vertical, which is also discussed in appendix E. A 200m long, vertically submerged pipe with a specific gravity of 5 is modeled. The initial conditions of the pipe is the original length, without taking elongation due to gravity into account. At  $t=0$ , the pipes mass is subjected to gravity and the hydrostatic pressure forces start acting on the pipe. The submerged weight of the pipe section is 9.2MN. Figure 92 shows a representation which is similar to the situation modeled. In this figure, the true wall stress is line DE, and the effective stress is BE. Now, as the stresses in the pipe are modeled, the true stress should be modeled in the axial direction. The theoretical stress at point E in Figure 92 should be 7.85MPa, for a submerged weight of 9.2MN. Also, length  $L_c$  is theoretically:

$$L_c = \frac{\rho_m}{\rho_s} L = \frac{1}{S_g} L \quad (116)$$

For a 200m long pipe, this length equals 40m. Figure 93 shows the true wall stress that was modeled by the 3D GNL EB model. This figure shows that the stress in the points of interest, discussed above, are fluctuating around the stress with the expected magnitude.

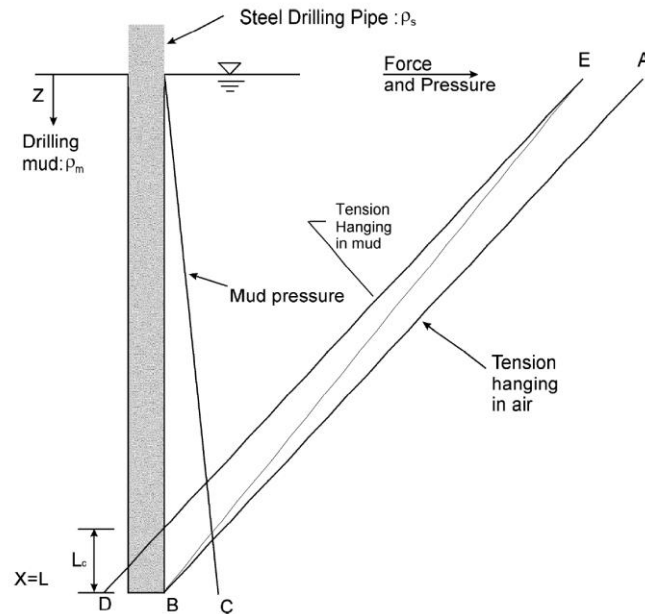


Figure 92: Forces and pressures on a vertical drill string in mud (Journée, 2001)

True wall stress in several points along a vertically submerged pipe,  $L=200\text{m}$ ,  $D=3\text{m}$ ,  $\text{SDR}=23$ ,  $S_g=5$

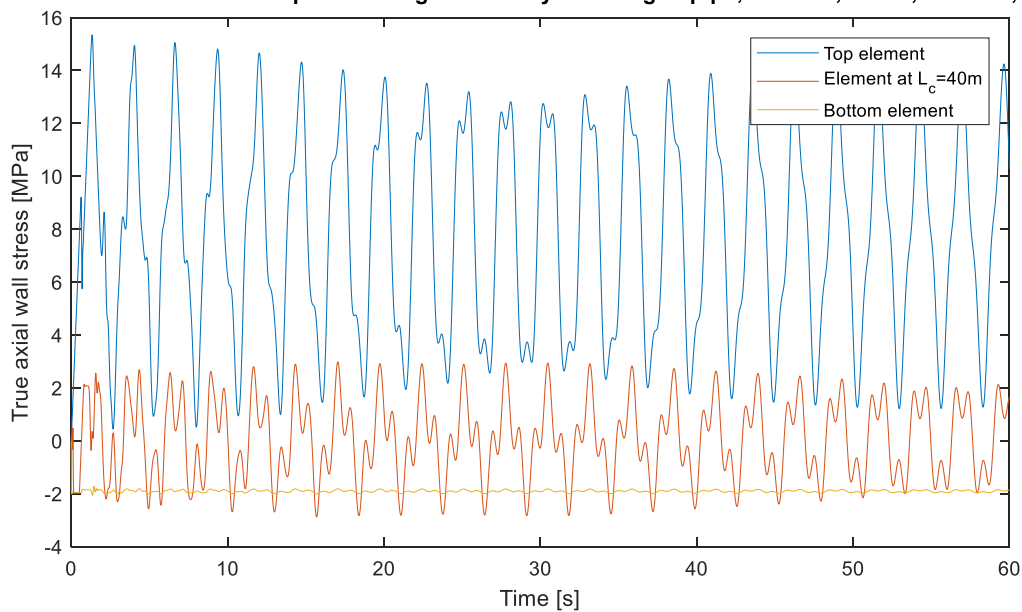


Figure 93: Modeled true wall stress plotted over time in several points along a vertically submerged pipe

Similarly, one could model a horizontally submerged pipe, where one end is fixed against a wall and the other end is free. When the pipe is exactly at the sea surface, ignoring that the pipe would be partially submerged, one would expect that the end cap force on the end of the pipe would be zero, because the hydrostatic pressure is zero. Only the submerged weight would act as a vertical load. When the pipe has a specific gravity of 1, the pipe would not experience any motion in the vertical and would not experience any axial stresses. This situation was modeled and verified. All three dimensional positions of the nodes stay the same and consequently the axial stresses are zero.

## Appendix C Material damping

The material damping is briefly discussed in section 3.2.4 in the main report. In this appendix, the derivation of the material damping is discussed. The implementation in the 2D geometrically non-linear Euler-Bernoulli model is shown. Model results with material damping are compared to results without material damping.

The mechanical loss coefficient  $\tan\delta$  is briefly discussed in section 3.2.4 in the main report. For linear dynamic systems, the stiffness matrix is often multiplied by the mechanical loss coefficient to obtain the damping matrix. However, there is no state independent stiffness matrix multiplication that can be used in order to obtain a similar damping matrix type of computation.

### C.1 Axial material damping

Material damping is added in the axial direction by implementing dashpots between the nodes, similarly to what would have been done if the pipe would be one-dimensional. In 1D, the difference in nodal velocities in a certain direction would be used in order to determine the material damping. For example, the equation of motion would look like equation (117).

$$\frac{\rho Al}{4} \begin{bmatrix} 1 & 1 \\ 1 & 1 \end{bmatrix} \begin{bmatrix} \ddot{u}_i \\ \ddot{u}_j \end{bmatrix} - \tan\delta \frac{EA}{l} \begin{bmatrix} 1 & -1 \\ -1 & 1 \end{bmatrix} \begin{bmatrix} \dot{u}_i \\ \dot{u}_j \end{bmatrix} - \frac{EA}{l} \begin{bmatrix} 1 & -1 \\ -1 & 1 \end{bmatrix} \begin{bmatrix} u_i \\ u_j \end{bmatrix} = \mathbf{F} \quad (117)$$

So the difference in velocities between the nodes in the direction of the neutral axis of the pipe are multiplied by  $\tan\delta \frac{EA}{l}$ . The same type of solution is sought for in the two dimensional case. Take an element in Figure 94 with two nodes with random velocities  $v_i$  and  $v_j$  with random magnitudes and random angles  $\gamma_i$  and  $\gamma_j$ . The element itself has an angle  $\alpha_n$  with respect to the global axis coordinate system.

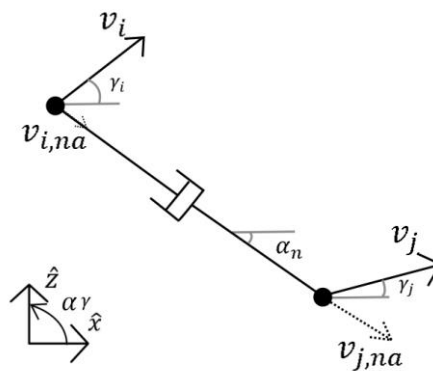


Figure 94: Element with dashpot and random velocities

The magnitude of the velocity of node i and j in the direction of the neutral axis is defined below.

$$v_{i,na} = v_i \cos(\gamma_i - \alpha_n) \quad (118)$$

$$\begin{aligned}
v_{j,na} &= v_i \cos(\gamma_j - \alpha_n) \\
v_{i,na} &= \sqrt{\dot{z}_i^2 + \dot{x}_i^2} (\cos(\alpha_n) \cos(\gamma_i) + \sin(\alpha_n) \sin(\gamma_i)) \\
&= \sqrt{\dot{z}_i^2 + \dot{x}_i^2} \left( \frac{\Delta x}{l_c} \frac{\dot{x}_i}{\sqrt{\dot{z}_i^2 + \dot{x}_i^2}} + \frac{\Delta z}{l_c} \frac{\dot{z}_i}{\sqrt{\dot{z}_i^2 + \dot{x}_i^2}} \right) \\
v_{j,na} &= \sqrt{\dot{z}_i^2 + \dot{x}_i^2} (\cos(\alpha_n) \cos(\gamma_j) + \sin(\alpha_n) \sin(\gamma_j)) \\
&= \sqrt{\dot{z}_i^2 + \dot{x}_i^2} \left( \frac{\Delta x}{l_c} \frac{\dot{x}_i}{\sqrt{\dot{z}_i^2 + \dot{x}_i^2}} + \frac{\Delta z}{l_c} \frac{\dot{z}_i}{\sqrt{\dot{z}_i^2 + \dot{x}_i^2}} \right)
\end{aligned}$$

So the damping force vector in the x-z plane at a node is:

$$\mathbf{F}_{c,i,na} = -\mathbf{F}_{c,j,na} = \tan\delta \frac{EA}{l} (v_{j,na} - v_{i,na}) \begin{bmatrix} \cos(\alpha) \\ \sin(\alpha) \end{bmatrix} \quad (119)$$

Now the full equations of motion for the axial elongation including material damping become:

$$\begin{aligned}
\frac{\rho Al}{4} (\ddot{x}_j + \ddot{x}_i) - \tan\delta \frac{EA}{l} (v_{j,na} - v_{i,na}) \frac{\Delta x}{l_c} - \frac{\Delta x EA (l_c - l)}{l * l_c} &= F_{\hat{x}_i} \\
\frac{\rho Al}{4} (\ddot{x}_j + \ddot{x}_i) + \tan\delta \frac{EA}{l} (v_{j,na} - v_{i,na}) \frac{\Delta x}{l_c} + \frac{\Delta x EA (l_c - l)}{l * l_c} &= F_{\hat{x}_j} \\
\frac{\rho Al}{4} (\ddot{z}_j + \ddot{z}_i) - \tan\delta \frac{EA}{l} (v_{j,na} - v_{i,na}) \frac{\Delta z}{l_c} - \frac{\Delta z EA (l_c - l)}{l * l_c} &= F_{\hat{z}_i} \\
\frac{\rho Al}{4} (\ddot{z}_j + \ddot{z}_i) + \tan\delta \frac{EA}{l} (v_{j,na} - v_{i,na}) \frac{\Delta z}{l_c} + \frac{\Delta z EA (l_c - l)}{l * l_c} &= F_{\hat{z}_j}
\end{aligned} \quad (120)$$

These equations of motion are implemented in MATLAB and compared to the 1D system in equation (117). The left of Figure 95 shows the x displacement of the last node over time for an arbitrary force at the end of the pipe in the axial direction. The initial conditions of the pipe are the undeformed state of a 10m long pipe section with zero nodal velocities. The x and y displacements and velocities of the first node are zero in order to take into account a hinged boundary condition. The same is done on the right hand side of Figure 95 but now for a 2D, 45 degree rotated pipe. The final elongation is equal and is consistent with formula (124).

$$F_{axial} = \frac{EA}{l} (l_{end} - l) \quad (121)$$

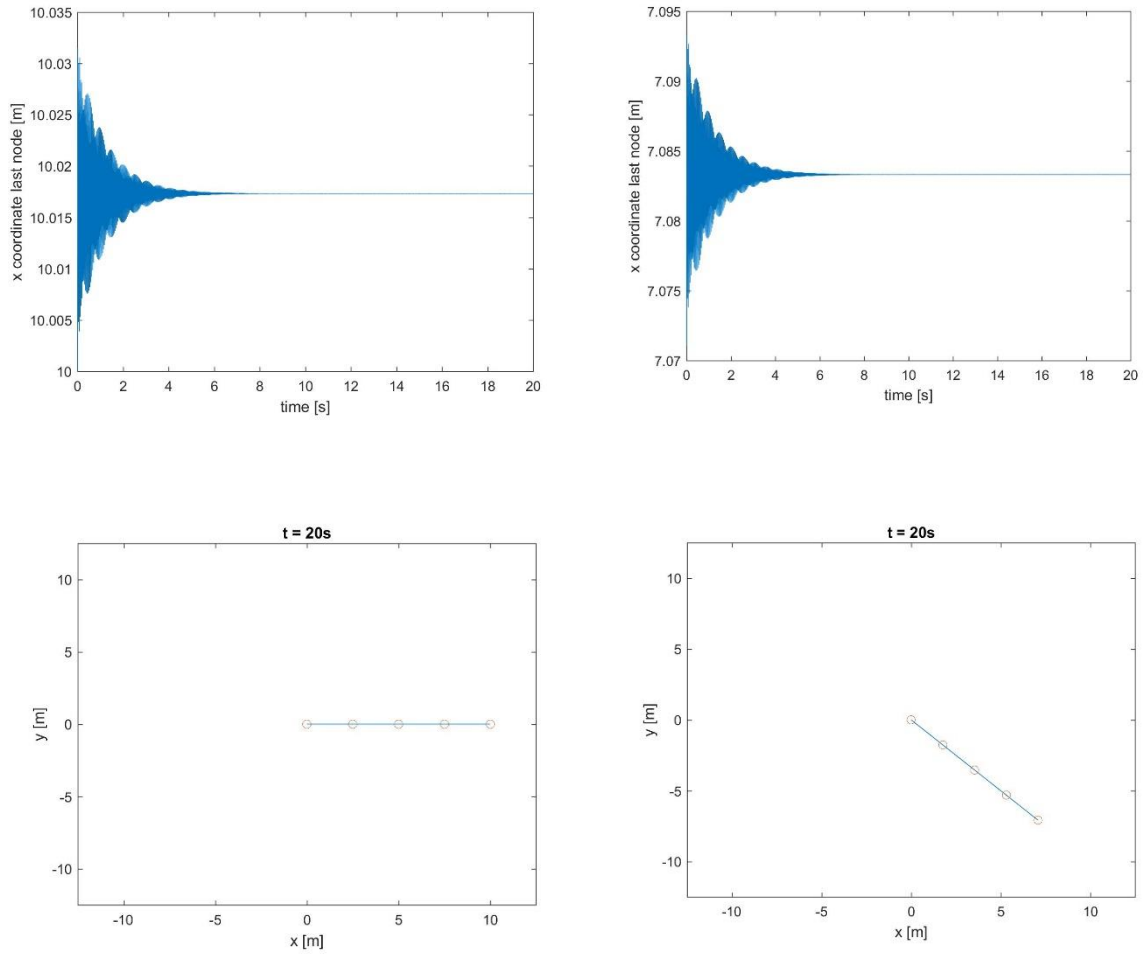


Figure 95: 1D rod (left) and 2D rod (right)

## C.2 Material damping due to bending

In a similar way to the damping in axial direction, damping can be derived in the lateral direction.

$$M_k = k_r \alpha = \frac{EI}{l} \alpha \quad (122)$$

$$M_c = \tan \delta \frac{EI}{l} \dot{\alpha}$$

Now,  $\dot{\alpha}$  should be written in terms of the nodal velocities. Similarly to what was done for the implementation of the bending stiffness above. Imagine an element where the nodes are moving through 2D space with random nodal velocities with random directions and magnitudes.

$$\dot{\alpha} = \frac{v_{i+1,p}}{l} + \frac{v_{i-1,p}}{l} \quad (123)$$

Where  $v_{i+1,p}$  is the velocity in node  $i + 1$  perpendicular to the element.

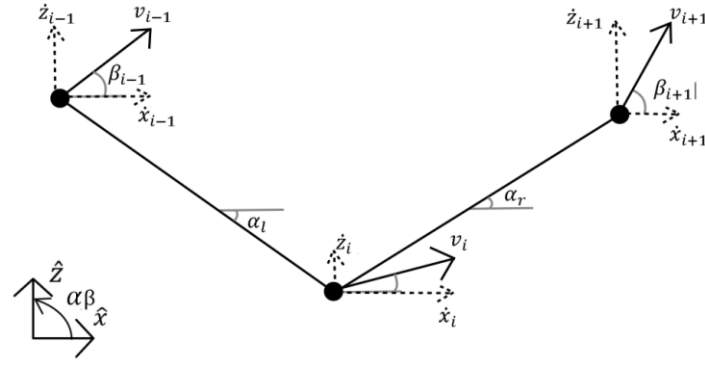


Figure 96: Three nodes with random velocities

In order to calculate the angular velocity in node  $i$ , the relative velocity to this node is calculated from:

$$\begin{aligned}
 \dot{x}_{rel,i-1} &= \dot{x}_{i-1} - \dot{x}_i \\
 \dot{z}_{rel,i-1} &= \dot{z}_{i-1} - \dot{z}_i \\
 \dot{x}_{rel,i+1} &= \dot{x}_{i+1} - \dot{x}_i \\
 \dot{z}_{rel,i+1} &= \dot{z}_{i+1} - \dot{z}_i
 \end{aligned} \tag{124}$$

The relative velocities in equation (124) can be decomposed in a velocity perpendicular to the element and a velocity in the axial direction (already used for the axial material damping). The velocity perpendicular to the element equals:

$$\begin{aligned}
 v_{p,i-1} &= \sqrt{\dot{x}_{rel,i-1}^2 + \dot{z}_{rel,i-1}^2} \sin(\beta_{i-1} - \alpha_l) \\
 &= \sqrt{\dot{x}_{rel,i-1}^2 + \dot{z}_{rel,i-1}^2} (\sin \beta_{i-1} \cos \alpha_l - \sin \alpha_l \cos \beta_{i-1}) \\
 &= \sqrt{\dot{x}_{rel,i-1}^2 + \dot{z}_{rel,i-1}^2} \left( \frac{\dot{z}_{rel,i-1}}{\sqrt{\dot{x}_{rel,i-1}^2 + \dot{z}_{rel,i-1}^2}} \frac{\Delta x_l}{l_{c,l}} \right. \\
 &\quad \left. - \frac{\Delta z_l}{l_{c,l}} \frac{\dot{x}_{rel,i-1}}{\sqrt{\dot{x}_{rel,i-1}^2 + \dot{z}_{rel,i-1}^2}} \right) \\
 v_{p,i+1} &= \sqrt{\dot{x}_{rel,i+1}^2 + \dot{z}_{rel,i+1}^2} \left( \frac{\dot{z}_{rel,i+1}}{\sqrt{\dot{x}_{rel,i+1}^2 + \dot{z}_{rel,i+1}^2}} \frac{\Delta x_r}{l_{c,r}} - \frac{\Delta z_r}{l_{c,r}} \frac{\dot{x}_{rel,i+1}}{\sqrt{\dot{x}_{rel,i+1}^2 + \dot{z}_{rel,i+1}^2}} \right)
 \end{aligned} \tag{125}$$

Now the velocities can be divided by the length which results in the angular velocity of node  $i$ :

$$\dot{\alpha}_i = \frac{v_{p,i+1}}{l} + \frac{v_{p,i-1}}{l} \tag{126}$$

Now the material damping related to bending is defined and can be decomposed in forces again similar to equation (90).

### C.3 Importance material damping

Adding the material damping to the model slows the model down. To see whether material damping is relevant, the model including material damping is compared to the model excluding material damping. The bending stress during a freefall run is given in Figure 97. This figure shows that the overall bending stress that is captured with and without material damping is the same. Figure 98 and Figure 99 show the relative error that is made by neglecting material damping. The relative error in this case stayed below 0.01 MPa and the relative error stayed below 0.35%. It is concluded that the damping due to hydrodynamic drag is dominating the damping and material damping does not play a significant role during installation.

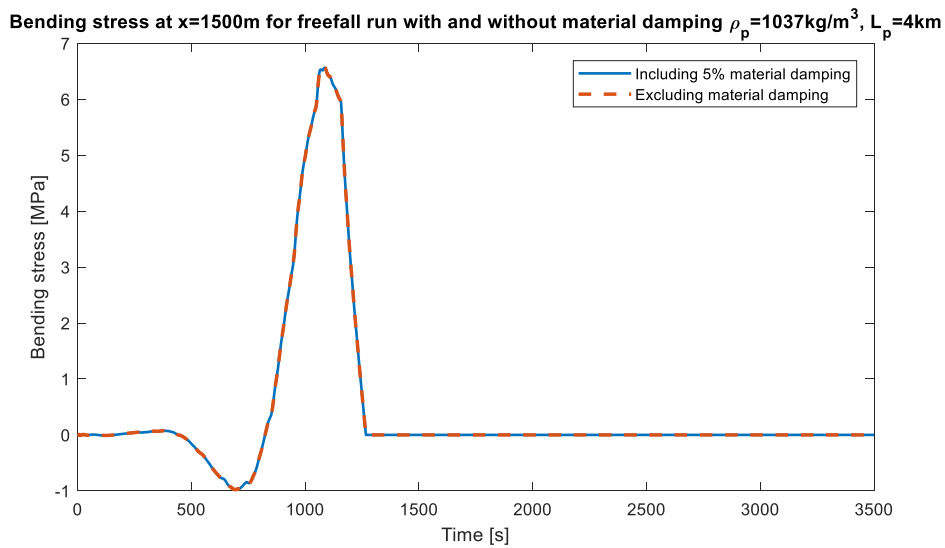


Figure 97: Bending stress during freefall run including and excluding material damping

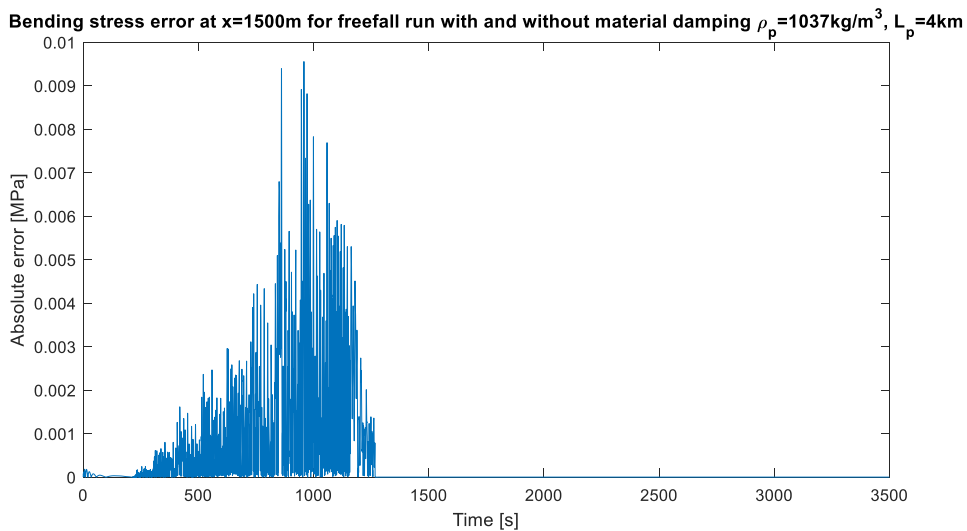
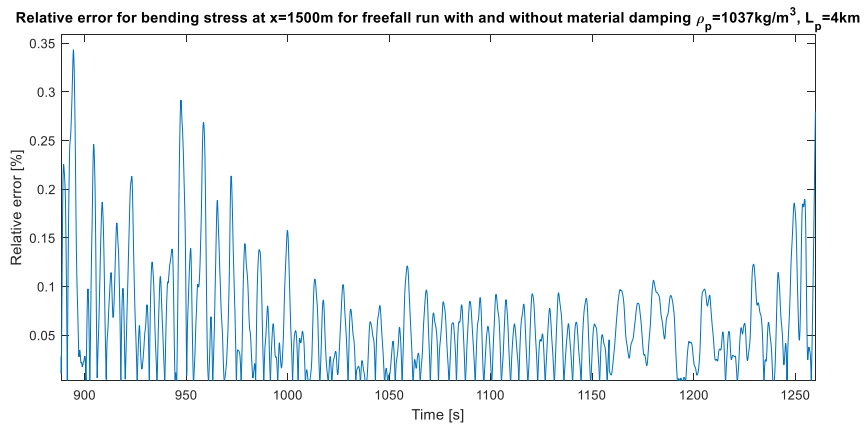


Figure 98: Bending stress error for neglecting material damping



**Figure 99: Relative bending stress error for neglecting material damping**

## Appendix E Interpretation of effective stress and derivation for 1D equation of motion vertical pipe subjected to hydrostatic pressure

In order to understand equation (18) better, the equations of motions for in the axial and lateral direction are derived below for a freely hanging pipe, when small angles are assumed. Imagine a pipe, for example for floating OTEC or a free hanging riser. A small section of the pipe with transverse motion in direction  $w$  is shown in Figure 100, where the right hand side is a differential element.

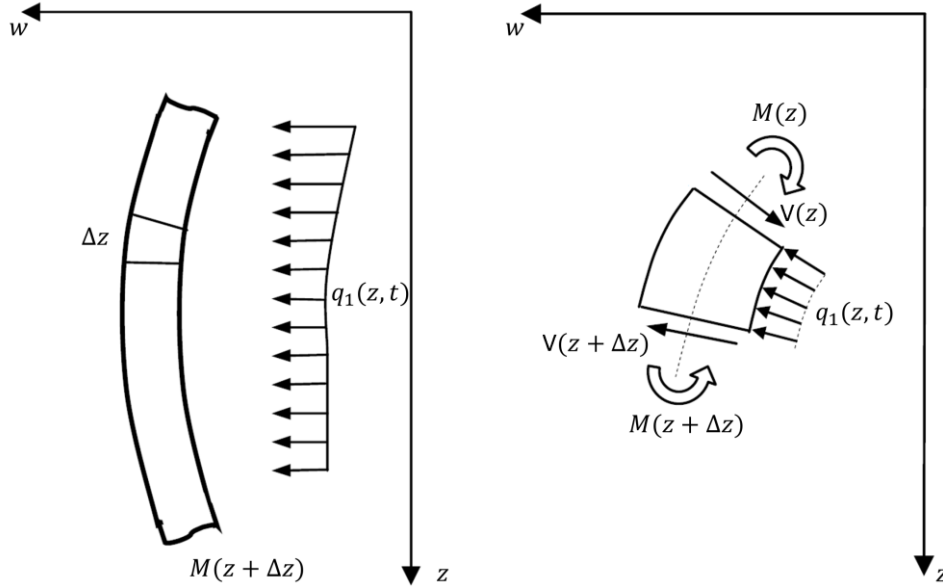


Figure 100: Section of a pipe subjected external load, moment and shear force

The equation of motion for the transverse motion of the section in Figure 100 is derived below, similarly to the procedure by A. V. Metrikine. Using the Euler-Bernoulli beam assumptions:

$$M = -EI \frac{\delta^2 w}{\delta z^2} \quad (127)$$

Assuming small slopes, the shear forces can be assumed to work horizontally. This leads to the following equation of motion:

$$\rho A \Delta z \frac{\delta^2 w}{\delta t^2} = -V(z) + V(z + \Delta z) + q_1 \Delta z \quad (128)$$

Applying a Taylor expansion, and neglecting the rotational inertia leads to:

$$\rho A \frac{\delta^2 w}{\delta t^2} + \frac{\delta}{\delta z^2} \left( EI \frac{\delta^2 w}{\delta z^2} \right) = q_1 \quad (129)$$

Now, the tension in a beam also influences the transverse motion of the beam. To derive the influence of the tension in the equation of motion, assume a piece of the pipe which is subjected to internal and external pressure, a distributed force  $q_1$  and tension  $T$ . Shear force and moments are neglected, as they were already taken into account in Figure 100.

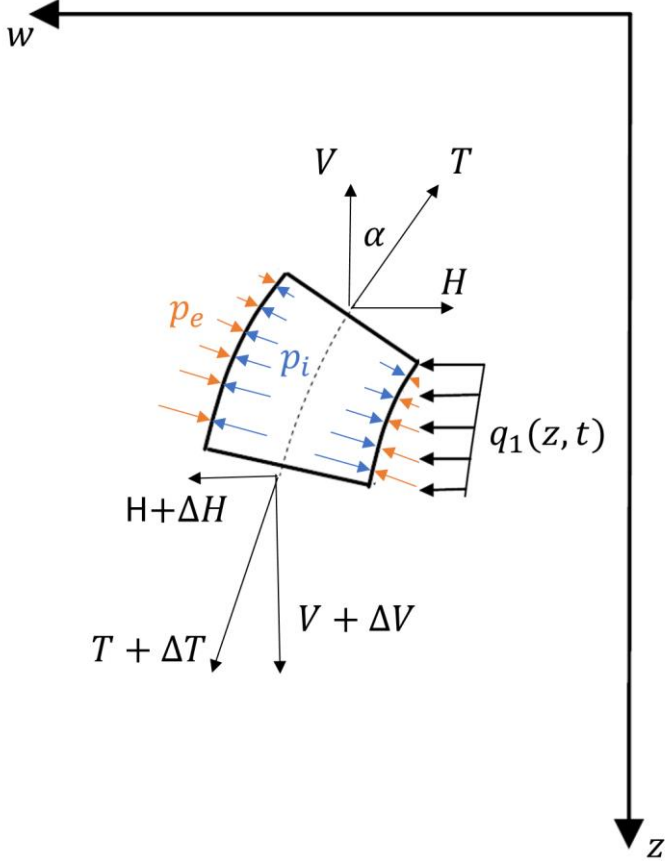


**Figure 101: Pipe section in tension with transverse loading  $q_1$  and internal (blue) and external (orange) hydrostatic pressures**

In Figure 101, the additional contribution due to the hydrostatic pressure, including is shown in blue and orange. So  $q_1$  represents all external loading in the horizontal, excluding hydrostatic pressure. Now, using the mechanical equivalence of the hydrostatic pressure according to Figure 102, one can decompose the pressure integration along the curved wall as the weight of the internal fluid plus the buoyancy of the external fluid (b) and the pressure field integrated over the end caps (c). Part (b) acts in the vertical direction and (c) acts perpendicular to the cross-section.

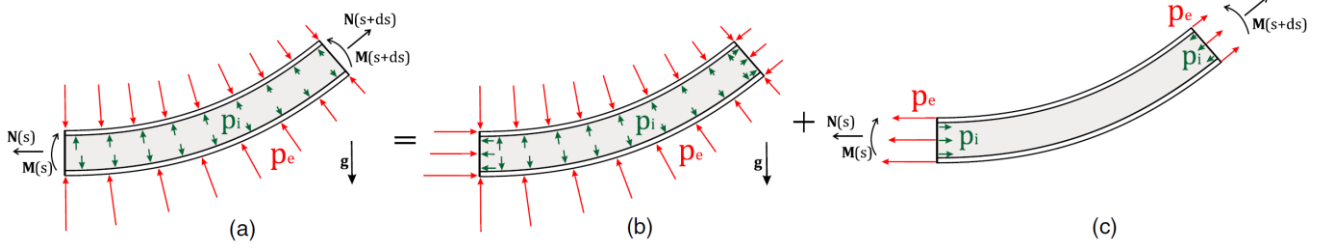


Figure 102: Mechanical equivalence of pressure along inside and outside pipe wall (Neto et al., 2017)

If one assumes that the vertical motion of the pipe is negligible, the pipe will only move horizontally. Newton's second law leads to:

$$\rho A \Delta z \frac{\delta^2 w}{\delta t^2} = H + \Delta H - H + q_1 \Delta z + E_H + \Delta E_H - E_H \quad (130)$$

Here,  $E_H$  is the horizontal component of the end-cap force. The lowercase  $H$  stands for the horizontal component of this force. Note that (b) in Figure 102, is not taken into account in this equation as its direction is vertical. This will not cause any horizontal deflection. The equation above can be simplified to:

$$\rho A \Delta z \frac{\delta^2 w}{\delta t^2} = \Delta H + q_1 \Delta z + \Delta E_H \quad (131)$$

For small deflections, the following holds:

$$H = V \tan(\alpha)$$

$$E_H = E_V \cos(\alpha) \quad (132)$$

$$\tan(\alpha) \approx \frac{\delta w}{\delta z}$$

Dividing equation (131) by  $\Delta z$ , implementing equation (132) in (131) and taking  $\lim_{\Delta z \rightarrow 0}$  leads to:

$$\rho A \frac{\delta^2 w}{\delta t^2} = \frac{\delta}{\delta z} \left( V \frac{\delta w}{\delta z} \right) + \frac{\delta}{\delta z} \left( E_V \frac{\delta w}{\delta z} \right) + q_1 \quad (133)$$

Where the following holds for small angles:

$$V = T \cos(\alpha) \approx T$$

$$E_V = E \cos(\alpha) \approx E \quad (134)$$

Which leads to:

$$\rho A \frac{\delta^2 w}{\delta t^2} = \frac{\delta}{\delta z} \left( T \frac{\delta w}{\delta z} \right) + \frac{\delta}{\delta z} \left( E \frac{\delta w}{\delta z} \right) + q_1 \quad (135)$$

Combining the tension and end cap forces, and combining equation (135) with equation (129) leads to the formula for a hanging riser or pipe that was for example also used by Brugmans (2005).

$$\rho A \frac{\delta^2 w}{\delta t^2} + EI \frac{\delta^4 w}{\delta z^4} - T_{eff} \frac{\delta^2 w}{\delta z^2} = +q_1 \quad (136)$$

Now, the usage of the effective tension in the equation of motion for transverse displacement of a vertically hanging pipe is clear. For the equation of motion in the longitudinal direction of the vertically hanging pipe, the vertical loading per unit length due to the external pressure will be zero. The reason is that the end cap pressures (c) on top and on the bottom of a small pipe section will result in a downward force, as a result of the different pressures at the different heights. Because this pressure difference times the area is exactly the same as the buoyancy in term (b), the vertical resultant of (b) and (c) in Figure 102 is zero. This makes sense as there are only horizontal pressures acting on a vertical area. This means that there is only an end cap force on the bottom of the pipe, meaning that the pipe could be in compression in the bottom of the pipe. So for small deflections in the horizontal, where the angle is small, the equation of motion in the longitudinal direction of the pipe is governed by the vertical loading per unit length. The internal and external pressure will only result in an end cap force on the bottom of the pipe.

In the same way as described above, the equations of motion for a completely submerged horizontal pipe with open ends can be understood. For the equation of motion in longitudinal horizontal direction, the end cap pressures of a pipe section in Figure 102 (c) are zero. As the pressures are exactly the same on the left and the right hand side of a small pipe section. The only force due to the hydrostatic pressure that is added in the longitudinal direction is a pressure dependent end cap force on the right and left and of the whole pipe. On the pipe ends, there is a vertical area where the pipe hydrostatic pressure can act. Now, for the transverse (vertical) deflections of the pipe, the loading in vertical direction is a result of the weight of the internal fluid plus the buoyancy of the external fluid. Together with the self-weight of the pipe this would result in the submerged weight of the pipe section. The end cap on a pipe section does not play an important role in the transverse direction of the beam if there are small deflections, because unlike in equation (130), there is no end cap difference  $\Delta E$ .

The equations of motion discussed above were for specific cases with small deflections. These cases give an insight in the effective axial stress and how it should be interpreted. In case of the pipe installation which is of interest in this thesis, the pipe could be randomly orientated. Therefore, with the latter in mind one could take a look at equation (18) in the main report. In the case of the equation of motion (136), the dot product in the second term for a vertically hanging pipe would be one, where the first two terms are cancelled. For any type of displacement or rotation of the pipe,  $\mathbf{t}(s)$  will not be parallel to  $\mathbf{g}$  and there will be a resultant horizontal force due to the dot product in the second term of equation (18). The third term in

this equation is often neglected, for example in equation (136). This term is dependent on the pressure, meaning that it will play an increasing role at increasing depths.

Again, a horizontal submerged pipe with open ends is considered, as discussed earlier in this appendix. In this case, the dot product in the second term in equation (18) will be zero. If there is no curvature the second and third term in equation (18) are zero and there will only be loading in the vertical in the considered pipe section, similarly to what has been discussed for the case of small deflections. Now for any other orientation of the pipe, equation (18) is used in order to implement the hydrostatic pressure correctly in the equation of motion of the Euler-Bernoulli beam in 3D Euclidean space.

## Appendix F Grid dependency

Due to the numerical discretization, there is an error introduced in the solution. One can imagine that discretizing a pipe with a few kilometres length into just a few sections leads to inaccurate results. For the Euler-Bernoulli model, it is important that the elements can capture the bending curvature with an appropriate accuracy. For the 3D model, the degrees of freedom per added node increases with 3. Therefore, one of the down sides of using more nodes is that the computation time increases significantly. During this thesis it is important that the bending stress is captured with an appropriate accuracy, however, it is also preferred that multiple scenarios are assessed without the computation time taking forever.

The position of the pipe during a freefall installation at a certain time step is shown in Figure 103. In this figure, the same installation is modelled with a different number of nodes. From the left hand side of the figure it can be seen that the overall behaviour of the pipe is not affected by the number of nodes. Looking at the bending on a smaller scale, one can see that the solution converges towards the dark blue line in the right hand side of the figure, which is the solution for 201 nodes. It is obvious that the black line, representing 41 nodes, cannot capture the bending effects appropriately.

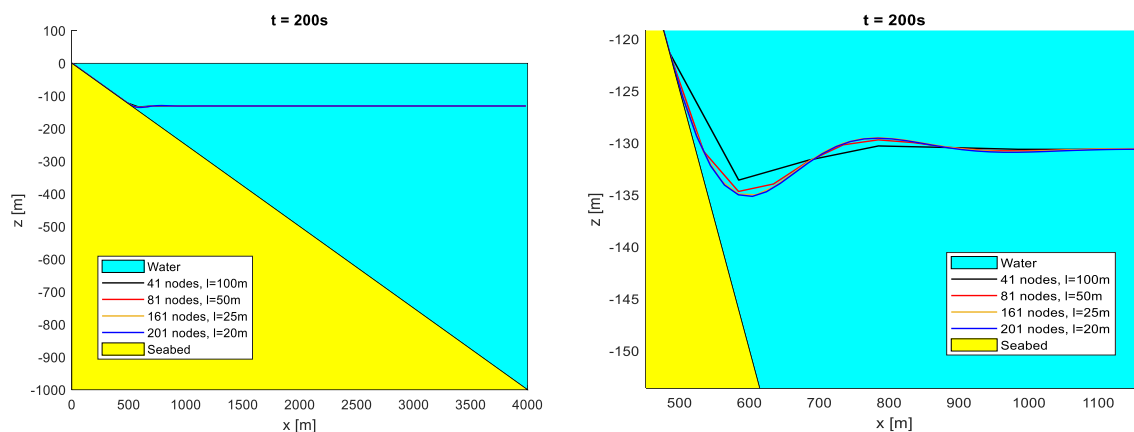


Figure 103: Pipe position at 200s during freefall installation.  $S_g=1.01$   $D=3m$   $SDR=23$

Bending is one of the most important factors to determine the amount of required nodes. Therefore, the bending stress in the pipe at  $s=1000m$  (local axis) is shown in Figure 104. Here it becomes more clear that decreasing the amount of nodes increases a significant error in the bending stress that is modelled. The red line, representing 81 nodes, does reasonably well but the solution converges to the yellow and purple lines. The bouncing lines are a result of the nodes hitting the seabed. For example, one can notice that in the blue line (41 nodes), there are multiple points where the bending stress experiences a sudden increase in the derivative with respect to time. At these points, one of the nodes around the node of interest hits the seabed which introduces a disturbance in the pipe. With an increasing amount of nodes, this disturbance happens more often due to the fact that there are more nodes that hit the seabed.

The magnitude of the disturbance is less because the element length is also decreased. One can imagine that for an infinitely small element length, the solution will become smoother and it will converge.

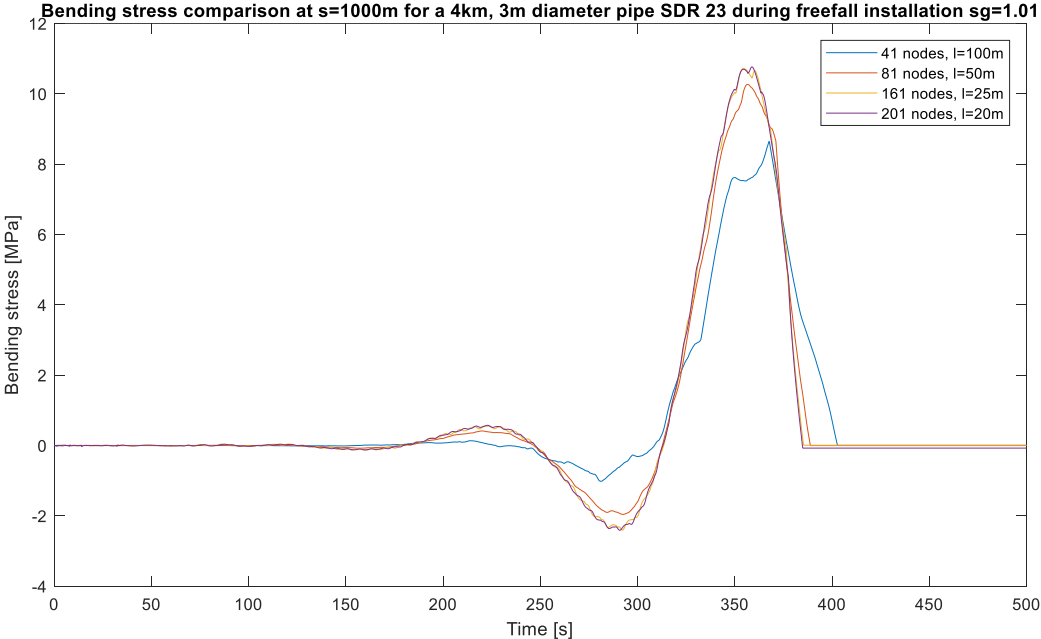


Figure 104: Bending stress at s=1000m for multiple model runs with a different number of nodes

The grid independency for bending stresses was not discussed in the thesis of Van Nauta Lemke (2017). The same sort of grid dependency was found in his model, from which one can conclude that the results for the bending stress in his model, using elements with a length of 117m, leads to significant errors in the results. For the same input parameters, the bending stress in his model was significantly lower than the bending stress that was computed by the EB and TS model.

## Appendix G Discussion on model Van Nauta Lemke (2017)

When taking a closer look at the model and Matlab code of Van Nauta Lemke (2017), it is concluded that there are some limitations to the applied model. Firstly, the geometrically linear Euler Bernoulli beam theory that was used, is only valid for small deflections and small rotations. Because the pipe is installed at a large water depth, the model was re-initialized in the ODE45 solver in MATLAB in order to estimate the large deflections. The model was reinitialized by taking using new initial conditions after every 8 simulated. The grey dashed line in Figure 105 was used to decompose the tension force due to the pulling tug vessel. The pipe deflection with respect to the grey dashed line is used as the new initial conditions for the re-initialization as can be seen on the right hand side of Figure 105.

The “assumed vertical loading” is added in the same direction as the gravity. This is a simplification that is not correct for larger deflections where the spatial derivative is larger. An error results from a misalignment between the direction of gravity and the “assumed vertical loading”. Furthermore, the grey dashed line was used to calculate the direction of the restoring force component due to the tension in the pipe. The stiffness matrix was re-initialized using the updated “assumed tension” force after each 8 seconds. ODE45 is used to calculate the deflection with respect to the grey dashed line for the time span of 8 seconds. Next, the elongation of the elements are calculated. The new x-locations are calculated according to the tension force in the pipe and the calculated deflections are added to the total deflection from the previous 8 seconds of modelling. The new deflection at the end of the re-initialization step was used for the next 8 seconds of modelling. This process is repeated until the installation modelling is completed. Furthermore, the drag force in this model is only in the vertical direction because only the velocity in the z direction is used. In reality, there is also a horizontal component of the drag force. Additionally, part of the gravity force will result in a tension in the axial direction of the pipe if the pipe is deflected and rotated. This is not taken into account in this model. Especially for larger seabed slopes, this model becomes less accurate. Due to the errors that follow from using a geometrically linear Euler Bernoulli model. Additionally, the hydrostatic pressure was not modeled correctly. No end cap force was added on the pipe end, and simply the submerged weight was used as vertical loading for each element. The tension that was applied in the 1D Euler-Bernoulli beam equation was simply the tension due to the pulling tug, where no influence of the hydrostatic pressure was taken into account. In the main report, the influence of the hydrostatic pressure is discussed in more detail.

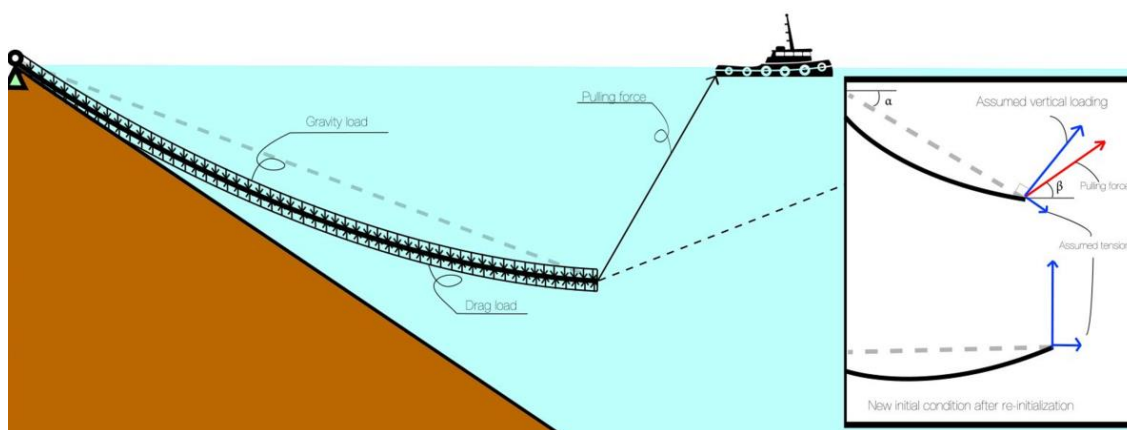


Figure 105: Explanation re-initialization step, model Van Nauta Lemke (2017)

# Appendix H Additional results

## Timoshenko vs. Euler-Bernoulli

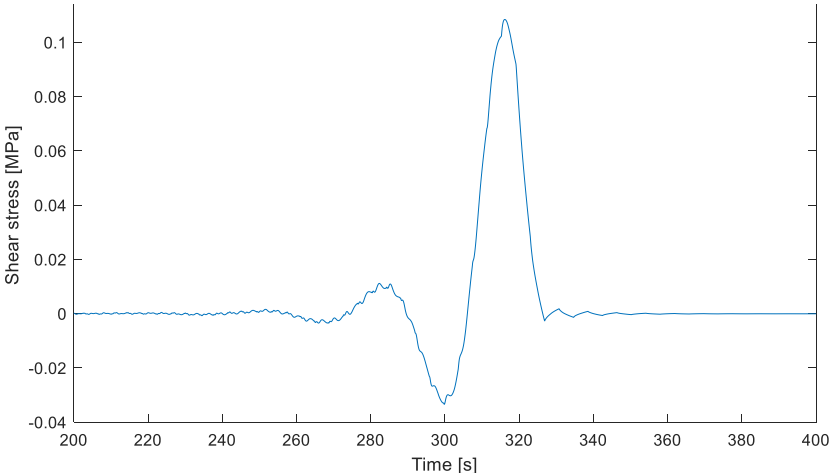


Figure 106: Shear stress in the pipe modeled by the Timoshenko beam model.  $s=2\text{km}$ ,  $L=4\text{km}$ , 161 nodes,  $D=3\text{m}$ ,  $\text{SDR}=23$ ,  $s_g=1.05$

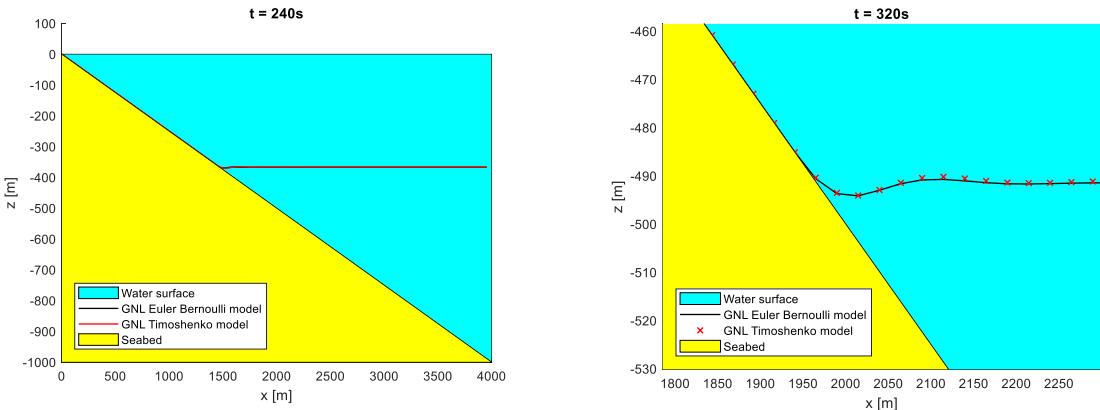
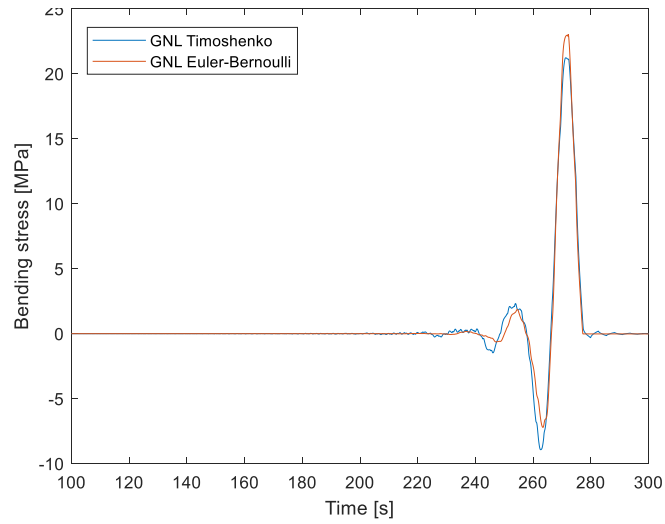
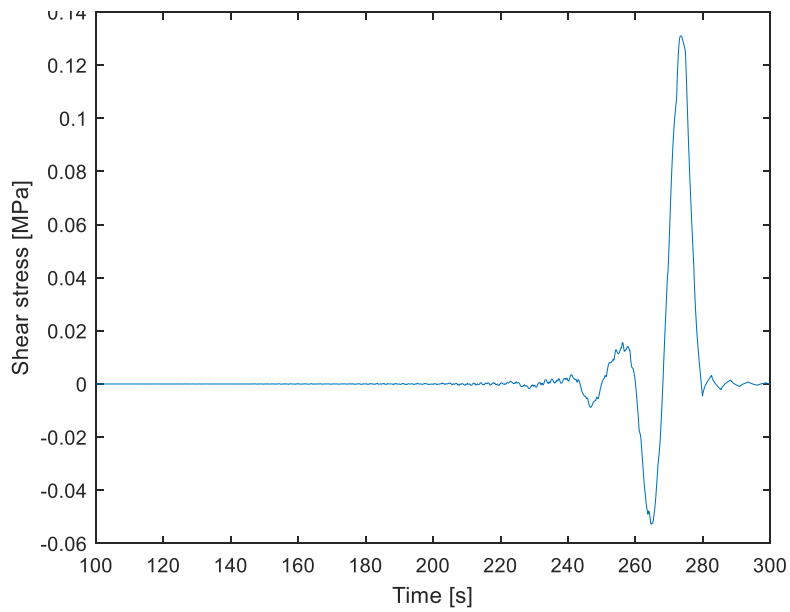


Figure 107: Global (left) and local (right) behaviour of the pipe modeled by the GNL Euler-Bernoulli beam model and the Timoshenko beam model.  $L=4\text{km}$ , 161 nodes,  $D=3\text{m}$ ,  $\text{SDR}=23$ ,  $s_g=1.01$



**Figure 108: Bending stress in the pipe modeled by the GNL Euler-Bernoulli beam model and the Timoshenko beam model. Location:  $s=2500\text{m}$ ,  $L=4\text{km}$ , 161 nodes,  $D=3\text{m}$ ,  $\text{SDR}=23$ ,  $s_g=1.1$**



**Figure 109: Shear stress in the pipe modeled by the Timoshenko beam model.  $L=4\text{km}$ , 161 nodes,  $D=3\text{m}$ ,  $\text{SDR}=23$ ,  $s_g=1.05$**

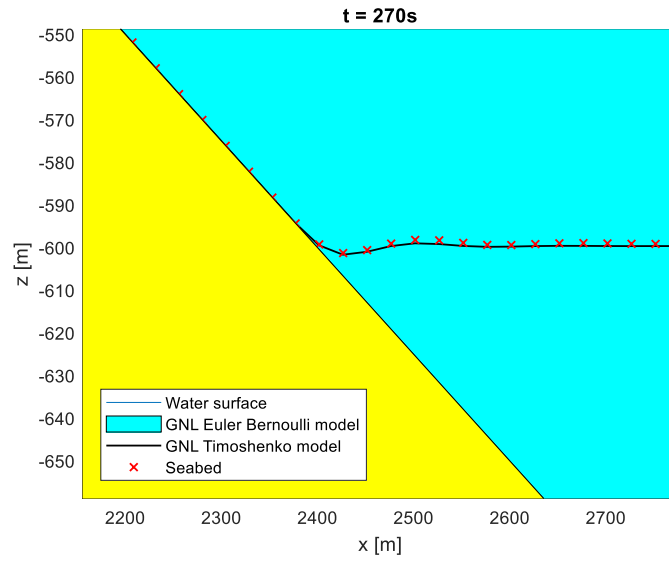


**Figure 110: Local behaviour of the pipe modeled by the GNL Euler-Bernoulli beam model and the Timoshenko beam model.  $L=4\text{km}$ , 161 nodes,  $D=3\text{m}$ ,  $\text{SDR}=23$ ,  $s_g=1.1$**

# Appendix I Model validation results

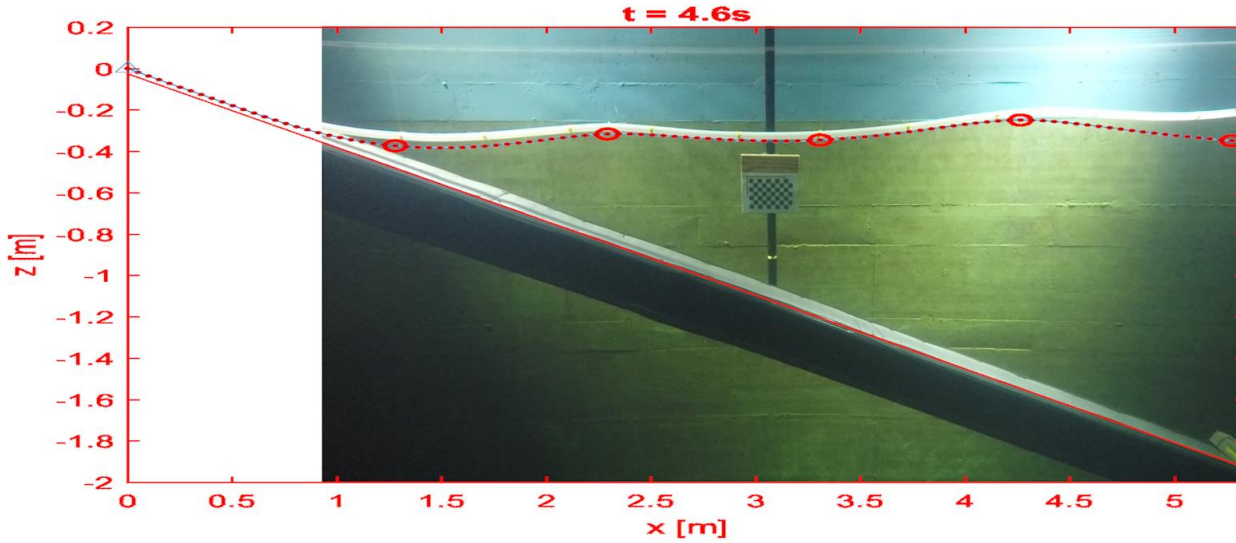


Figure 111: T.7.100.100

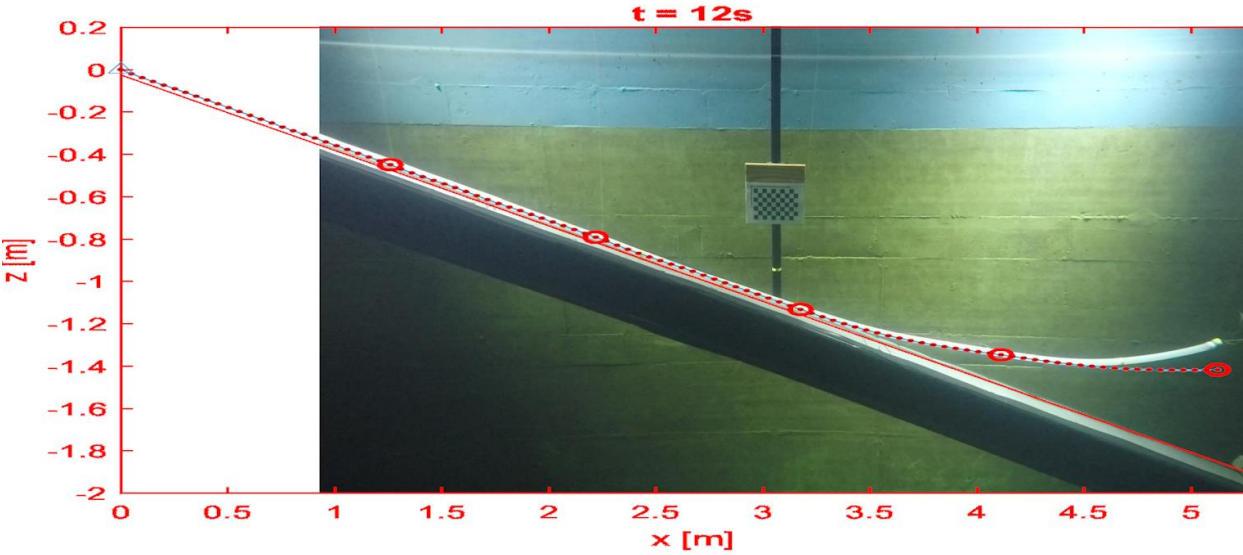


Figure 112: T.2.50.100

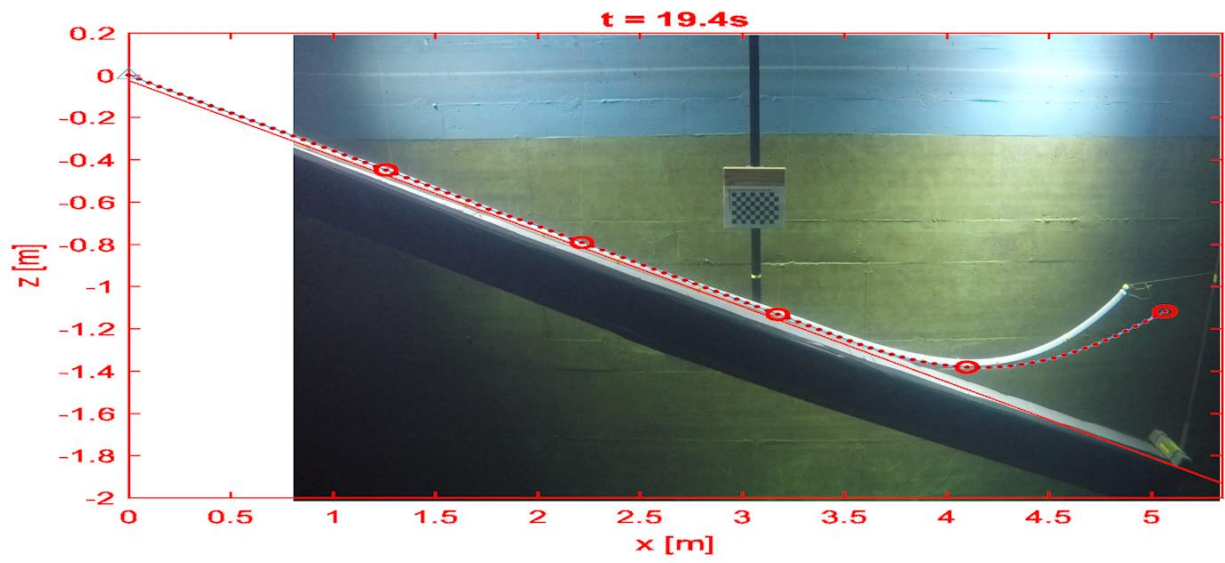


Figure 113: T.2.50.50

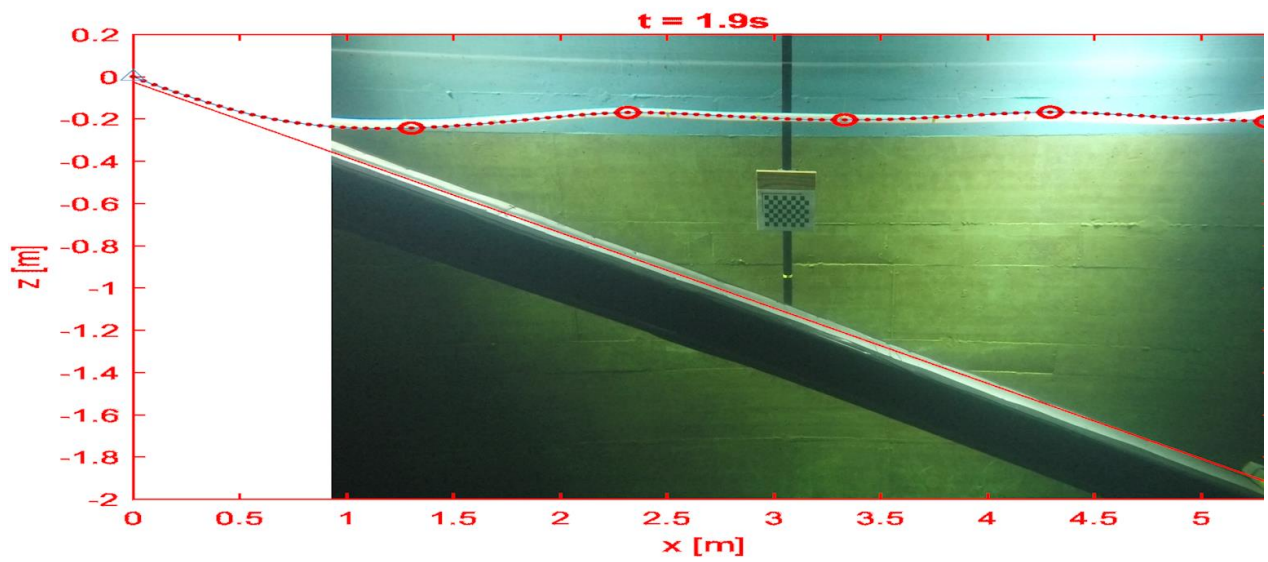


Figure 114: T.7.50.100

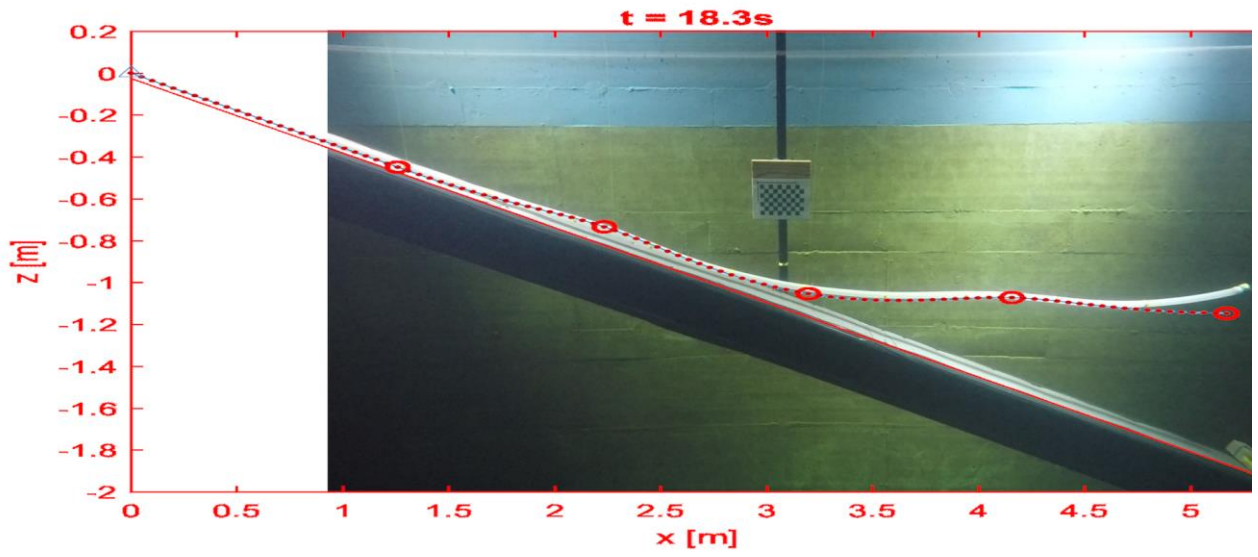


Figure 115: T.7.50.100

# Appendix J Additional results

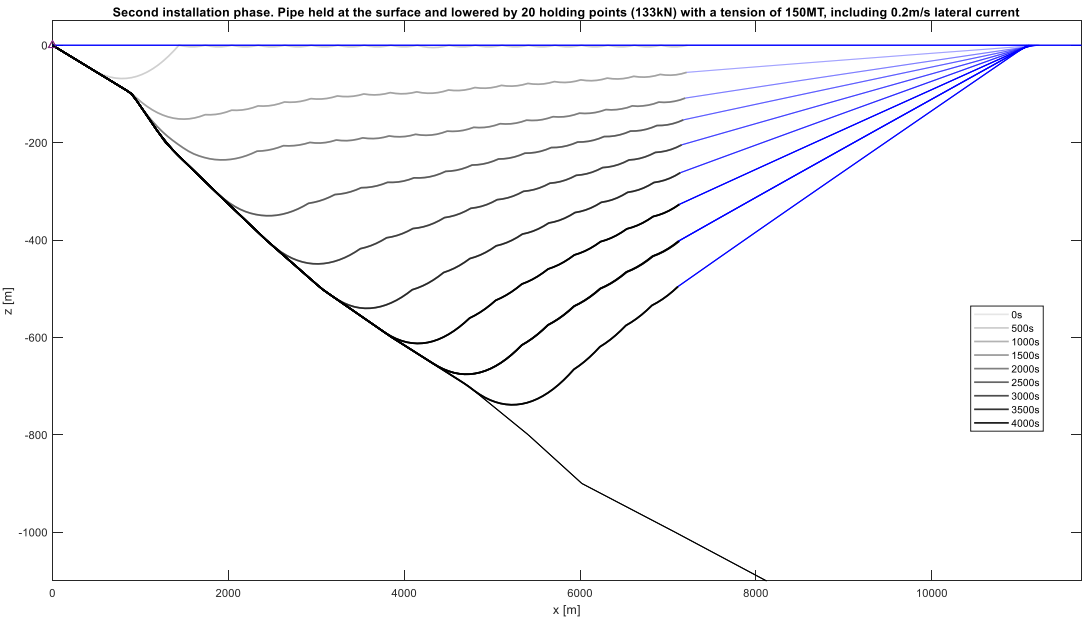


Figure 116: Vertical displacement at different time steps during hold and sink installation with uniform lateral current

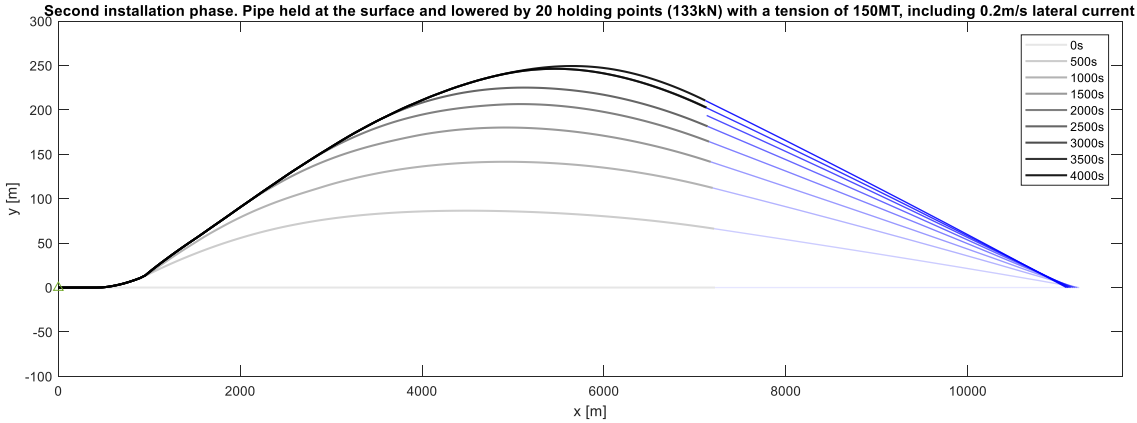


Figure 117: Lateral displacement at different time steps during hold and sink installation with uniform lateral current

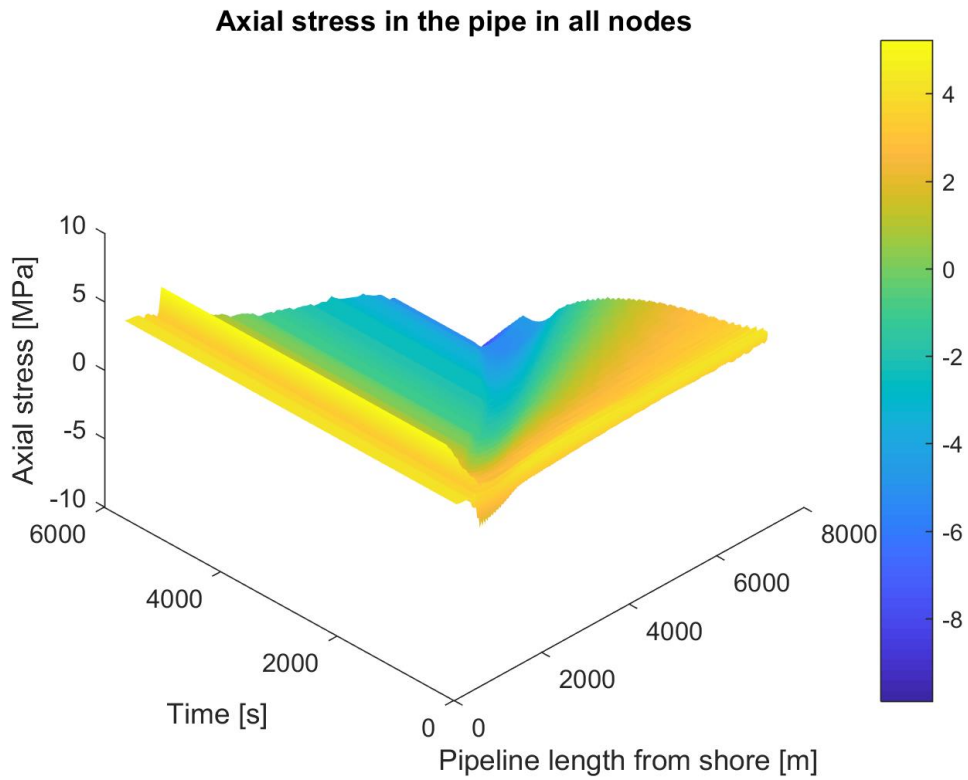


Figure 118: Axial stress in pipe during installation with current profile

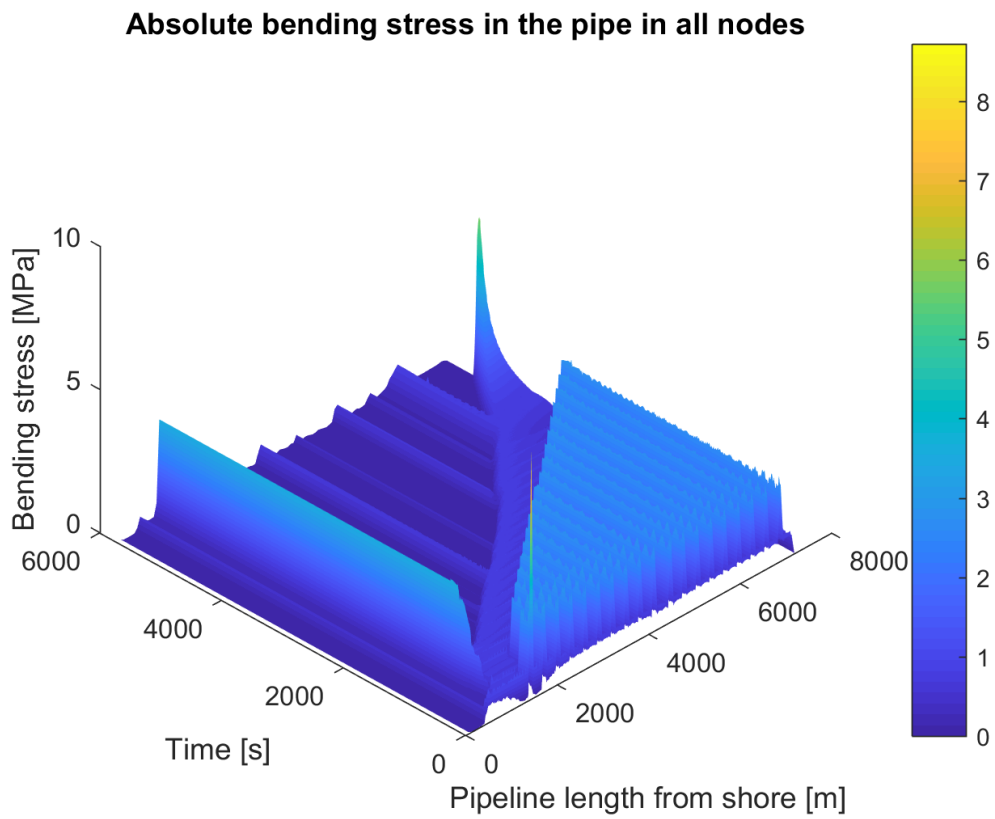


Figure 119: Bending stress in pipe during installation with current profile

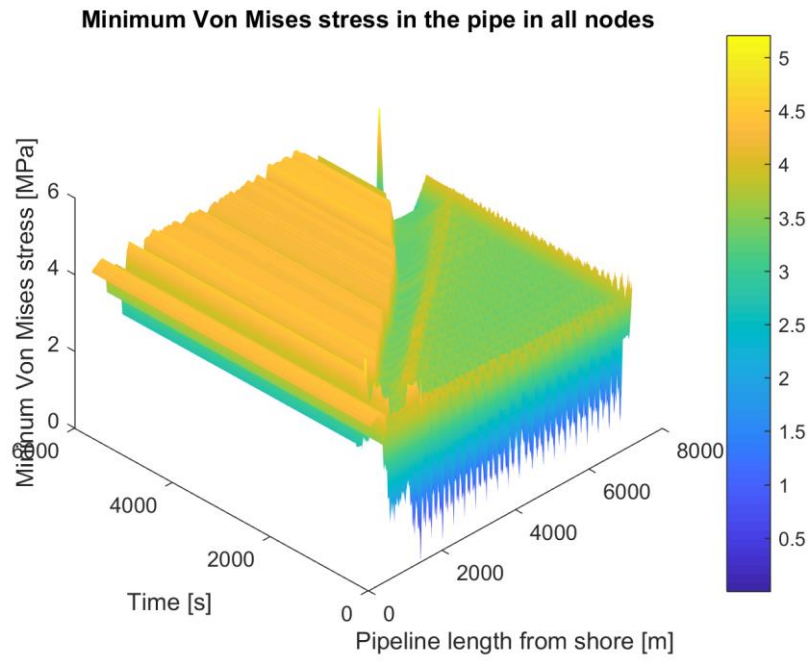


Figure 120: Minimum Von Mises stress in pipe during installation with current profile

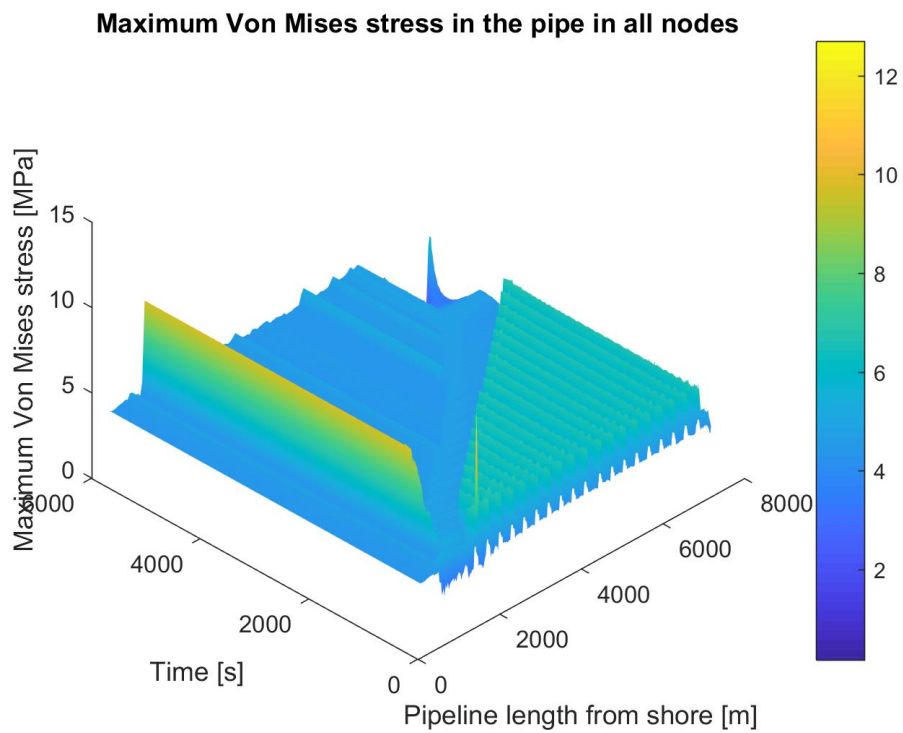


Figure 121: Maximum Von Mises stress in pipe during installation with current profile

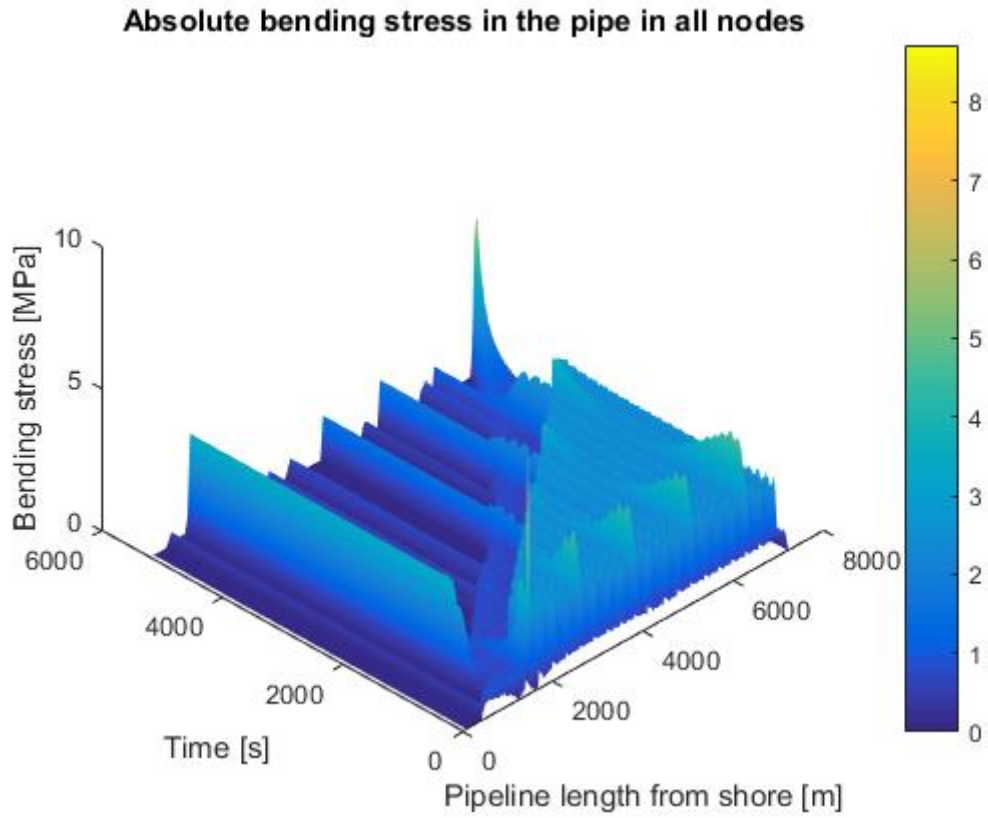


Figure 122: Bending stress in pipe during installation with current profile and 5 lateral holding points

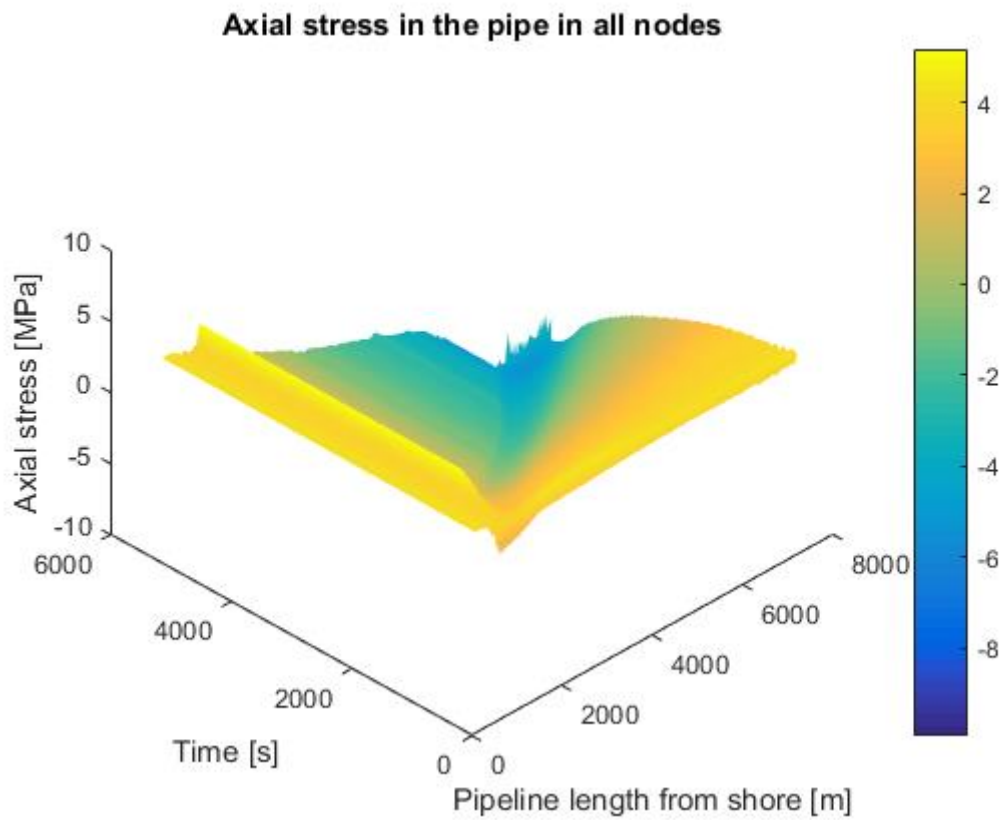


Figure 123: Axial stress in pipe during installation with current profile and 5 lateral holding points

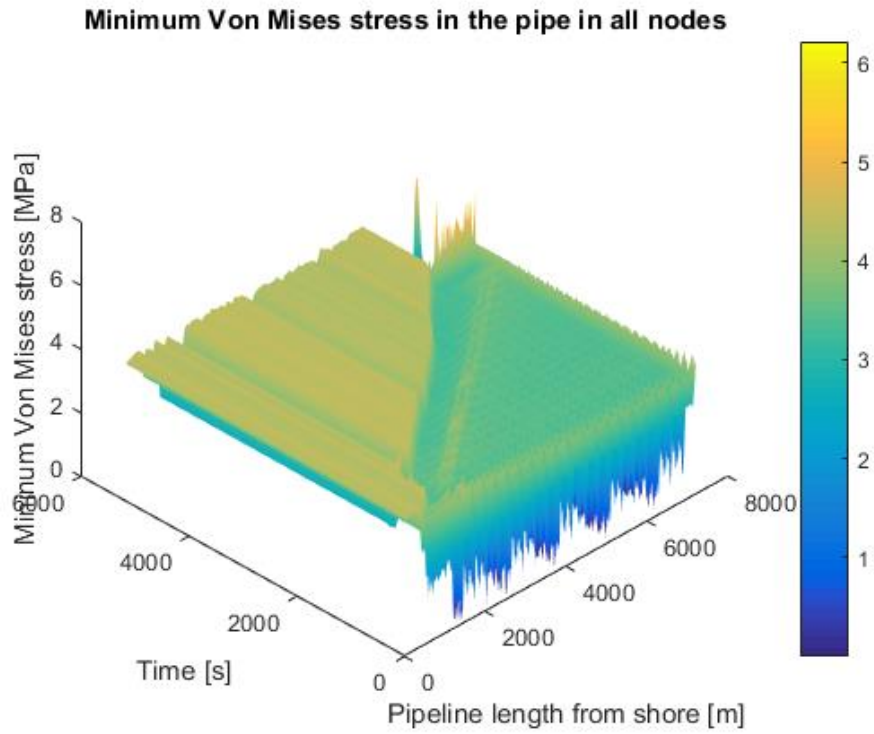


Figure 124: Minimum Von Mises stress in pipe during installation with current profile and 5 lateral holding points

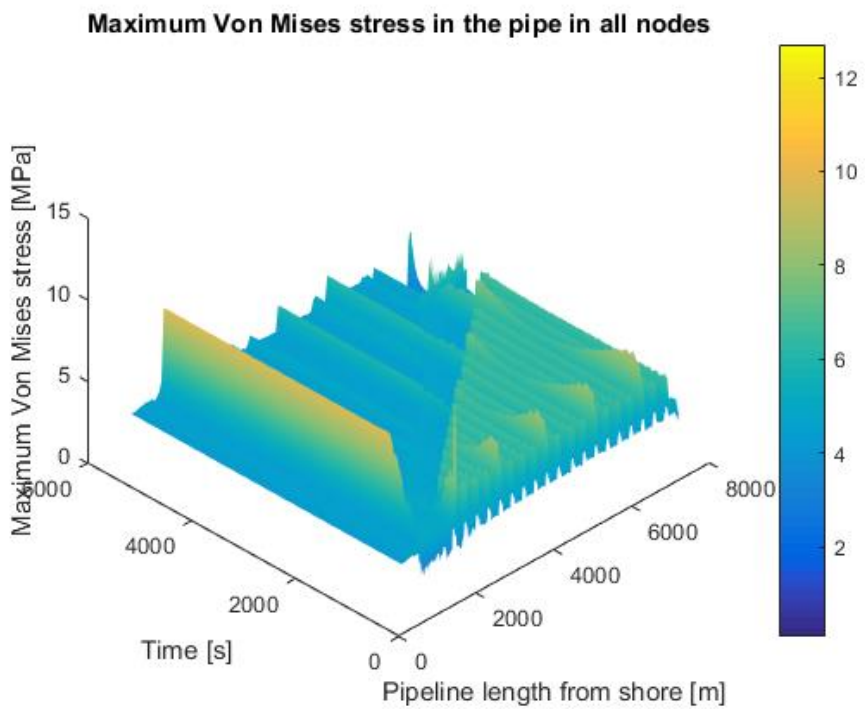


Figure 125: Maximum Von Mises stress in pipe during installation with current profile and 5 lateral holding points

## Appendix K Preliminary sensitivity study

In this appendix, some additional results are presented. Several model runs are performed in order to get a feel for the influence of certain parameters. Firstly, the influence of the specific gravity, SDR and pulling force is checked for the initial conditions similar to Figure 65 in the main report (see section 7.6.1). The stresses at the holding points for several cases are shown in Table 7. The base case is the same case as in the main report, which has a specific gravity that can handle current velocities up to 0.4m/s. As the SDR is lowered to 15 in case 2, the specific gravity is lowered as well as this is a function of the displaced volume of the pipeline. The same static equilibrium calculation was used as in equation (49) in the main report. The decreasing SDR means that the wall thickness increases. Therefore, a similar pulling force causes less stress. Case 2.1, 2.2 and 2.3 use different pulling forces. The results show that the maximum Von Mises stress does not change significantly, as a decreasing tension increases the bending and vice versa. Therefore, one could consider using a smaller pulling tug if it is cheaper and might cause lower local stresses at the connection between the pulling tug and the pipeline, however with increasing bending stress there is a higher risk of local buckling which must be taken into account. Case 3 allows the pipe to have a lower specific gravity, which could be the case in current velocities up to 0.2m/s in deep water. Case 3.1 shows that with 20 holding points, similar to the case study in the main report, the maximum Von Mises stress is lower than the Von Mises stress in the base case. As a result, one could use less holding points (case 3.2), which would make the installation cheaper.

Case	SDR	sg	Pulling force [MT]	holding points	Bending stress [MPa]	Axial stress [MPa]	Maximum Von Mises stress [MPa]
base	21	1.11	150	20	2.4	4.2	6.6
case 2.1	15	1.086	200	20	1.5	4	5.5
case 2.2	15	1.086	150	20	2.5	3	5.5
case 2.3	15	1.086	100	20	3.4	2.1	5.5
case 3.1	21	1.03	200	20	0.6	4	4.6
case 3.2	21	1.03	150	5	3.2	4	7.2

Table 7: Sensitivity on allowed stress for initial conditions when the pipeline is filled with water on the surface

These initial conditions are used to model the lowering procedure including the current profile. The most interesting case is the third case, with a lower specific gravity. The second case will only allow more stress and does not change the total weight of the pipeline in water as the specific gravity in this case is chosen based on the same outer dimensions of the pipe as the base case. Therefore, the lift and drag forces used in equation (49) are similar to the base case. Figure 126 shows the initial conditions for case 3.2. Figure 127 and Figure 128 show the deflections of the pipe after 2000s with two different current profiles. From this figure, one can

already see that the magnitude of the current velocity has a large impact on the lateral deflection of the pipe. However, still, for both cases the deflection is too large and measures are required to make sure that the pipe is installed at the appropriate location.

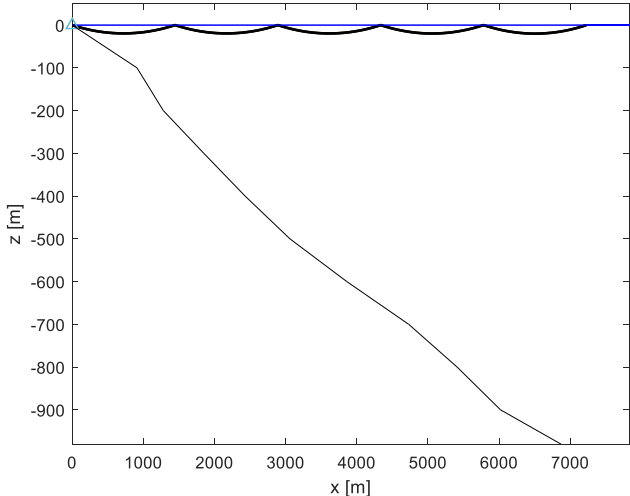


**Figure 126: Initial conditions case 3.2**

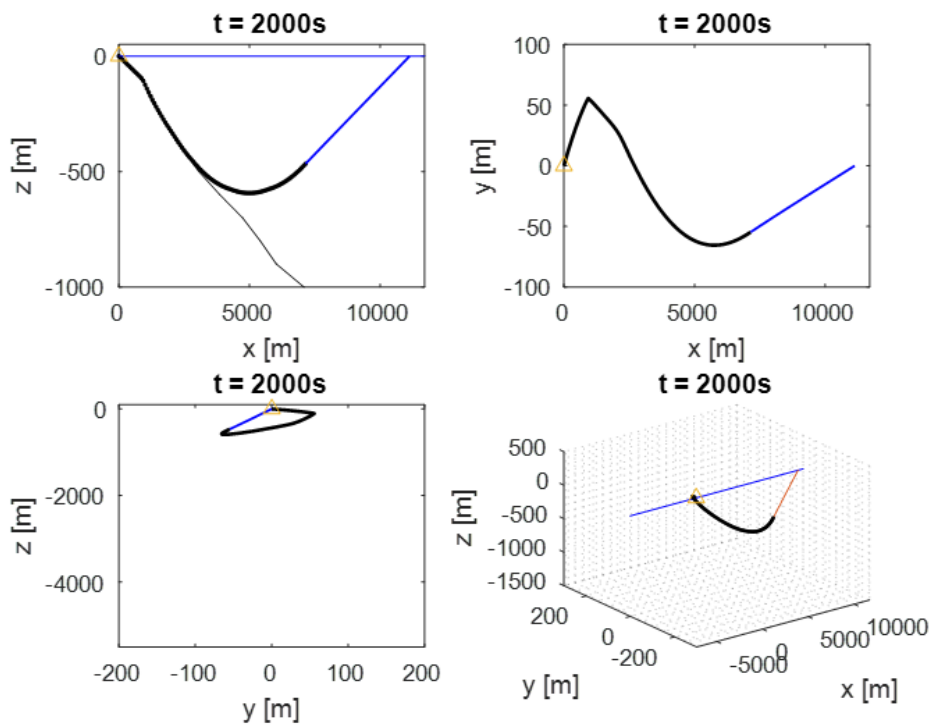


Figure 127: Pipe position at  $t=2000s$  for case 3.2 with current profile from figure 71 in the main report

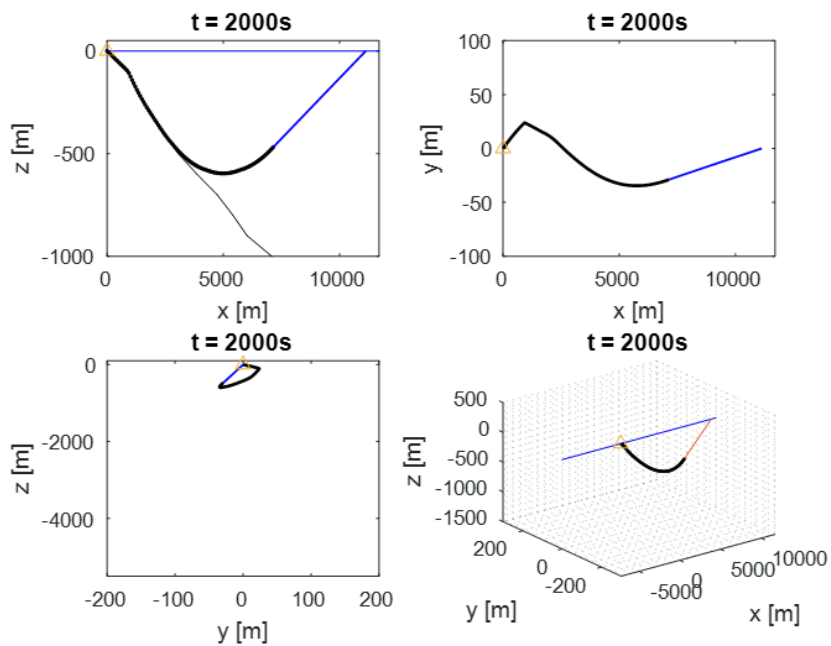


Figure 128: Pipe position at  $t=2000s$  for case 3.2 with the current profile from figure 71 in the main report multiplied by 0.5

For the base case, the current profile is also divided by two in order to get a feel for the sensitivity of the lateral deflection for different current velocities. The results are shown in Figure 129 and Figure 130, where one can see the deflection for the two cases after 500 seconds of lowering. This figure shows that the deflection without any lateral holding points in milder currents is still significant.

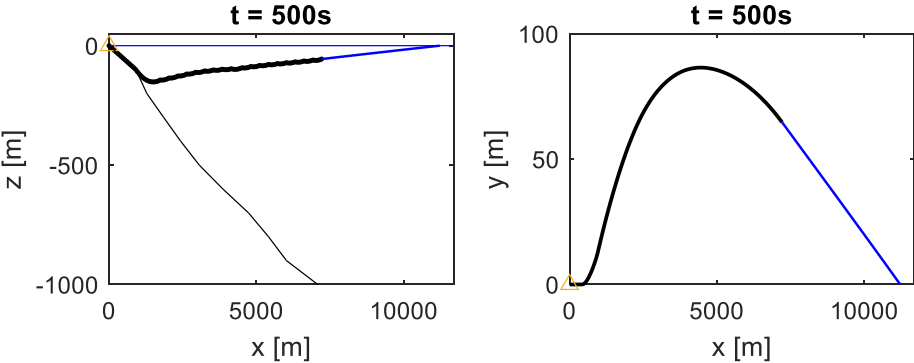


Figure 129: Pipe position at t=500s for base with the current profile from figure 71 in the main report

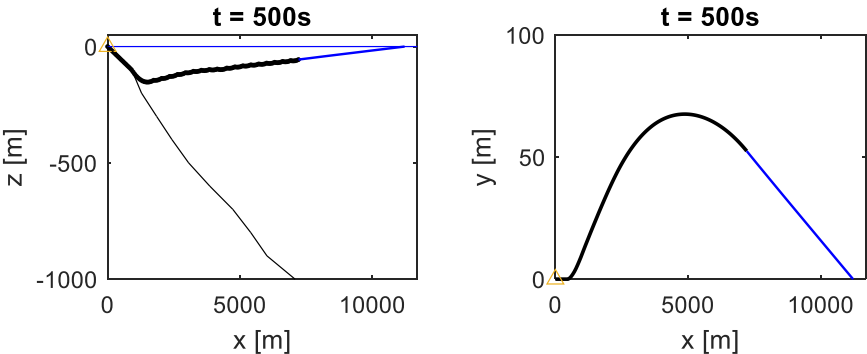


Figure 130: Pipe position at t=500s for base with the current profile from figure 71 in the main report multiplied by 0.5

